Development of Advanced Single-Molecule Fluorescence Microscopy Techniques and their Application for the Study of Protein-Protein Interactions in the Context of Immunological Signaling

Christian Niederauer

This thesis was reviewed by:

prof.dr. U. Endesfelder	University Bonn
dr. J.C. Hohlbein	Wageningen University and Research
dr. P. Jönsson	Lund University
prof.dr.ir. E. Peterman	Vrije Universiteit Amsterdam
dr. S. Schmid	Wageningen University and Research

The work described in this thesis was performed at AMOLF, Science Park 104, 1098 XG Amsterdam, The Netherlands, part of the Dutch Research Council (NWO). Financial support from the institute AMOLF for the printing of this thesis is gratefully acknowledged.

Cover image: Interacting proteins labeled using DNA-PAINT-SPT.
Printed by: Ipskamp Printing, Enschede

ISBN 978-94-6473-220-7

A digital version of this thesis is available online at www.ub.vu.nl and ir.amolf.nl. The DOI of this thesis is http://doi.org/10.5463/thesis.357. Printed copies can be obtained by request via library@amolf.nl.

One can indeed read a lot, but then one must once again discard everything and walk through the forest for a while, follow the weather and the flowers, the mists and winds, and rediscover within oneself the quiet point from which the world reveals itself as unity.

Man kann ja viel lesen, aber dann muss man einmal wieder alles wegwerfen und eine Weile durch den Wald laufen, dem Wetter und den Blumen, den Nebeln und Winden nachspüren und in sich den stillen Punkt wiederfinden, von wo aus die Welt zur Einheit wird.

Hermann Hesse, Lektüre für Minuten

VRIJE UNIVERSITEIT

DEVELOPMENT OF ADVANCED SINGLE-MOLECULE FLUORESCENCE MICROSCOPY TECHNIQUES AND THEIR APPLICATION FOR THE STUDY OF PROTEIN-PROTEIN INTERACTIONS IN THE CONTEXT OF IMMUNOLOGICAL SIGNALING

ACADEMISCH PROEFSCHRIFT

ter verkrijging van de graad Doctor of Philosophy aan
de Vrije Universiteit Amsterdam,
op gezag van de rector magnificus
prof.dr. J.J.G. Geurts,
in het openbaar te verdedigen
ten overstaan van de promotiecommissie
van de Faculteit der Bètawetenschappen
op donderdag 19 oktober 2023 om 11.45 uur
in een bijeenkomst van de universiteit,
De Boelelaan 1105

door

Christian Niederauer

geboren te Berlijn, Duitsland

promotor:	prof.dr. P.R. ten Wolde
copromotor:	dr. K. Ganzinger
promotiecommissie:	prof.dr. U. Endesfelder dr. J.C. Hohlbein dr. P. Jönsson prof.dr.ir. E.J.G. Peterman dr. S. Schmid

Contents

CONTENTS

1 Introduction

The essence of life is not about what we can gain for ourselves,
but about the connections we make with others
and the love we share.

The interactions and communication between living organisms and their environment are fundamental to the functioning of all life forms, from single-celled organisms to complex multicellular organisms such as humans. These interactions allow for the exchange of information, the coordination of physiological responses, and the maintenance of homeostasis, all of which are crucial for the survival and well-being of living organisms. Understanding these interactions is essential for comprehending the molecular mechanisms of life and the development of treatments for diseases.

1.1 General principles of signal transduction

Signaling in multicellular organisms is a complex and intricate process that involves the seamless coordination of millions of highly specialized cells. These cells must possess the ability to respond to a multitude of signals simultaneously and often initiate multiple diverse responses to the same signal, all while maintaining a remarkable degree of flexibility. This is achieved through the separation of signal detection and cellular response, facilitated by a series of signaling events as depicted in **Fig. 1.1**. A signal is detected at the extracellular space, e.g. by ligand-recognition, followed by signal transduction via intracellular signaling molecules, eventually leading to a cellular response, involving changes in cellular metabolism, gene expression or cytoskeletal organization. This separation allows for a high degree of adaptability, such as the ability of the

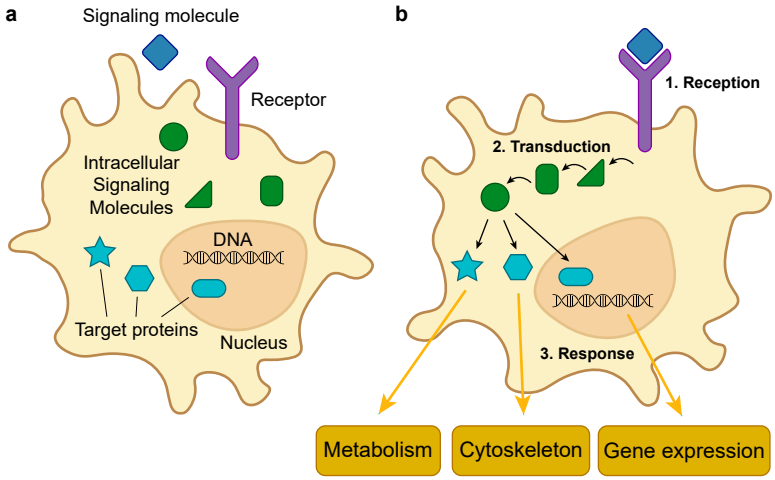

Figure 1.1 • Receptor-mediated signaling
General sequence of the complex molecular interactions occurring during receptor-mediated signaling: **(a)** Pre-activation state, where intracellular signaling molecules (green) and target proteins (blue) are present but not yet activated. **(b)** Signal transduction in three distinct stages: (1) Reception, where an extracellular signaling molecule binds to a plasma membrane-spanning receptor; (2) Transduction, where the binding of the signaling molecule triggers a cascade of intracellular signaling molecules via the receptor; (3) Response, where the intracellular signaling molecules activate target molecules, resulting in changes in cellular metabolism, the cytoskeleton, and gene expression.

same type of receptor to couple to different signaling pathways in different cell types, amplification or dampening of the signal as it travels along the pathway, activation of multiple pathways leading to diverse cellular responses, and integration of information from multiple receptors [1–3]. These processes are largely dependent on protein-protein interactions and protein regulatory mechanisms [4]. As signaling is such a universal feature of life, the basic model of signal transduction, as outlined in Fig. 1.1, is widely applicable across species and many signaling pathways are highly conserved, such as the mammalian target of rapamycin (mTOR) signaling pathway, found in all mammals [5].

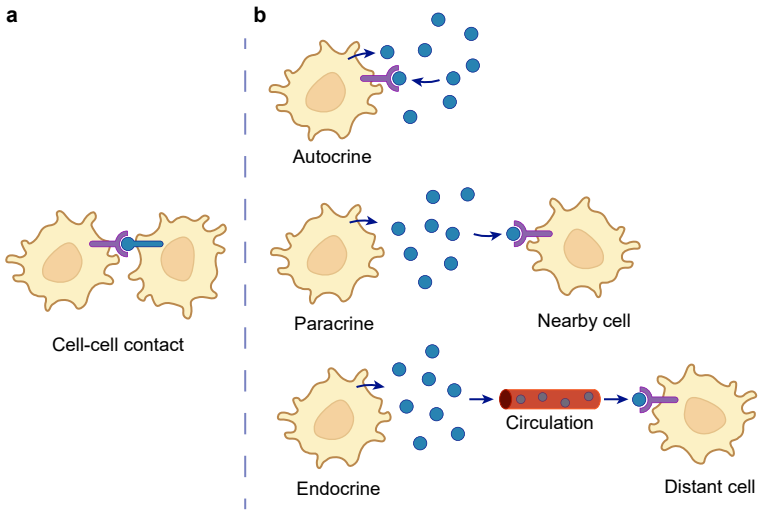

Figure 1.2 • Cell-cell signaling mechanisms
(a) Cell-cell contact-dependent signaling, in which a signaling molecule bound to the plasma membrane of the signaling cell interacts with a receptor on the surface of the target cell. **(b)** The three modes of cell-cell signaling via secreted molecules: paracrine, autocrine, and endocrine signaling.

1.1.1 Molecular basis of receptor-mediated signaling

The two main types of cell-cell signaling are depicted in **Fig. 1.2**: contact-dependent signaling, and signaling via secreted molecules. Typically, contact-dependent signaling involves the interaction of molecules bound to the plasma membrane of the signaling cell with a receptor on the surface of the target cell. This type of signaling is crucial in the initiation of the immune response (e.g. T cell activation by antigen/major histocompatibility complex (MHC)) [6, 7]. Secreted signaling molecules, on the other hand, diffuse through the extracellular environment to act on neighboring cells (paracrine), the secreting cells itself (autocrine), or, after release into the bloodstream, distant cells (endocrine). Often, signaling molecules can act in more than one fashion. Cytokines, for example, are involved in para-, auto- and endocrine signaling [8]. Hormones, on the other hand, are typically produced in glands distant from their targets, and therefore predominantly act in an endocrine way.

1.1.2 Transmembrane receptors feed extracellular signals into intracellular signaling cascades

On a molecular level, signal processing is accomplished through a variety of signaling pathways that allow cells to respond to their environment, communicate with one another, and coordinate their activities. These signaling pathways are initiated at the cell membrane, where specialized molecules, known as receptors, receive and transduce signals, allowing the cells to sense the outside world and respond accordingly. These receptors play a critical role in cell signaling and communication and their dysfunction is associated with many diseases, including cancer, neurological disorders, and immunological disorders [1, 2].

The extracellular molecules initiating these signaling pathways are often proteins. Proteins are advantageous as signaling molecules because they have complex structures with binding sites that allow for highly specific interactions with target molecules. This specificity enables proteins to perform sophisticated signaling functions and regulate cellular processes in a precise manner [4, 9, 10]. However, these proteins are unable to cross the cell membrane due to their size and polarity [11] and therefore act by binding to extracellular receptor proteins. These receptors have a distinct three-part structure (see **Fig. 1.3**) consisting of an extracellular domain (ectodomain) that interacts with the signaling molecule, a hydrophobic transmembrane domain, and an intracellular domain. Therefore, they act as the bridge between the signaling molecule and the target cell, transmitting the signal across the membrane and into the cell.

Receptors are generally categorized based on their signal transduction properties into three distinct groups of receptors:

1. **Receptors that directly produce an action to a stimulus:** One type of acetylcholine receptor, for example, serves as both a receptor and an ion channel, belonging to a family of receptors known as ion-channel receptors. Upon binding of acetylcholine, these receptors enable the passage of Na^+, K^+ and Ca^+ ions, leading to changes in the cell's membrane potential.

2. **Seven-helix transmembrane (7TM) receptors:** These receptors have seven membrane-spanning regions, an N-terminal extracellular region, and a C-terminal intracellular tail. The activation mechanism of most 7TM receptors involves coupling to G proteins, and thus they are also known as G protein-coupled receptors (GPCR), with serotonin receptors serving as an example.

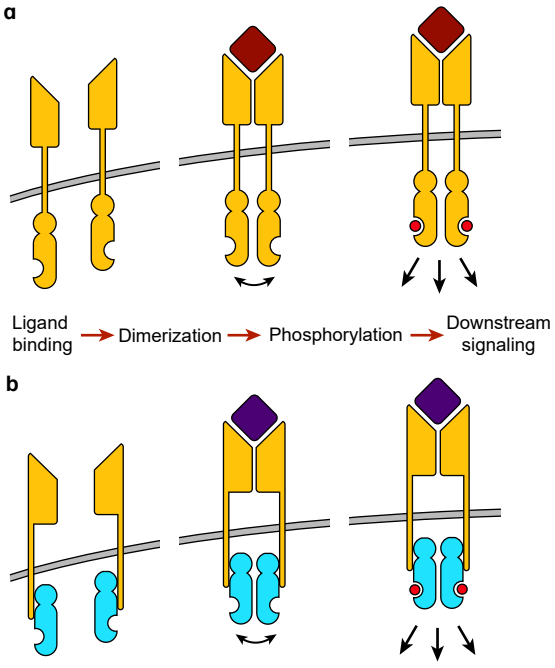

Figure 1.3 • Receptors with enzymatic activity

Enzyme-associated receptors utilize intrinsic or associated protein kinases for signaling. A ligand binding to the extracellular domains dimerizes the receptors, enabling autophosphorylation of protein kinases on the cytoplasmic side of the receptors (indicated by red dots), and eventually other downstream signaling proteins to transmit the signal. **(a)** Dimeric receptor with intrinsic kinase activity. **(b)** Dimeric receptor lacking intrinsic kinase activity. Association with intracellular non-receptor kinases conveys kinase activity to the receptor.

3. **Receptors with enzymatic activity:** This group of receptors has an intracellular tail that either contains an enzymatic domain (e.g. receptor tyrosine kinases), or that associates with enzymatic proteins (e.g. interleukin receptors, see **Chapter 3**). For interleukin receptors, Janus kinase (JAK) proteins constitutively associate with the intracellular domains of the receptors and provide them with kinase activity. Upon dimerization, JAK proteins phosphorylate each other and downstream proteins, leading to activation of the JAK-signal transducers and activators of transcription (STAT) pathway [12].

1.2 Theory of protein-protein interactions

Reversible protein-protein interactions form the basis of ligand-initiated signaling [13]. The chemical equation for a one-step, non-cooperative reaction with a one-to-one stoichiometry of receptor and ligand complex formation is given by:

$$\mathrm{R} + \mathrm{L} \rightleftharpoons \mathrm{RL}, \tag{1.1}$$

Biochemistry differentiates itself from traditional chemistry by its reliance on non-covalent and reversible binding. The immune system, for instance, depends on the body's ability to generate specific non-covalent binders that selectively recognize a diverse range of molecules.

with a ligand (L) binding to a receptor (R), transiently forming a ligand-receptor complex (RL).

The time-dependent rate equation for the formation and dissociation of the ligand-receptor complex, is:

$$\frac{\mathrm{d}[\mathrm{RL}]}{\mathrm{d}t} = k_{\mathrm{on}}[\mathrm{R}][\mathrm{L}] - k_{\mathrm{off}}[\mathrm{RL}] \tag{1.2}$$

with [R], [L] and [RL] representing the concentration of free receptors, free ligand and receptor-ligand complexes under equilibrium conditions, respectively, and k_{on} [$\mathrm{M}^{-1}\,\mathrm{s}^{-1}$] the forward reaction rate constant, or on-rate, and k_{off} [s^{-1}] the reverse reaction rate constant, or off-rate.

1.2.1 Equilibrium binding

In equilibrium, the reaction reaches a steady-state and [RL] remains constant:

$$\frac{\mathrm{d}[\mathrm{RL}]}{\mathrm{d}t} = 0 \Rightarrow k_{\mathrm{on}}[\mathrm{R}][\mathrm{L}] = k_{\mathrm{off}}[\mathrm{RL}] \tag{1.3}$$

This allows to define the equilibrium constants K_d (dissociation constant) and K_a (affinity constant):

$$K_{\mathrm{a}} = \frac{[\mathrm{RL}]}{[\mathrm{R}][\mathrm{L}]} = \frac{k_{\mathrm{on}}}{k_{\mathrm{off}}} \tag{1.4}$$

$$K_{\mathrm{d}} = \frac{[\mathrm{R}][\mathrm{L}]}{[\mathrm{RL}]} = \frac{k_{\mathrm{off}}}{k_{\mathrm{on}}} \tag{1.5}$$

The equilibrium constants provide a simple way of characterizing the strength of an interaction between two molecules, allowing to compare the binding between different ligands or receptor-ligand pairs [14]. It is worth noting that K_d is equal to the concentration of free ligand, at which half of the total receptor molecules $[\mathrm{R}_{\mathrm{tot}}] = [\mathrm{R}] + [\mathrm{RL}]$ are in complex with a ligand (half maximal binding):

$$[\mathrm{L}] = K_d \Rightarrow [L] = \frac{[\mathrm{R}][\mathrm{L}]}{[\mathrm{RL}]} \Rightarrow [\mathrm{R}]{=}[\mathrm{RL}] = \frac{1}{2}[\mathrm{R}_{\mathrm{tot}}] \tag{1.6}$$

1.2.2 Binding kinetics

Kinetic rate constants are important parameters characterizing the speed at which ligand-receptor binding events occur:

The reaction rate is given by the on-rate k_{on} and the concentrations of the reactants. As a first approximation, the on-rate can be considered to be diffusion-limited, i.e. molecular binding occurs as fast as diffusional collisions ($k_{\text{diff}} = 4\pi DR \approx 10^9$-$10^{10}\,\text{M}^{-1}\,\text{s}^{-1}$, with diffusion constant D and sum of the molecular radii R [15]). However, association rates can be significantly lower if orientational or conformational requirements for binding exist, or significantly enhanced in the case of binding surfaces with strong opposite electrostatic potentials [13, 16, 17].

The off-rate k_{off} represents the rate at which a complex dissociates. As binding processes follow exponential laws, the average half-life $\tau_{1/2}$ of a bi-molecular complex can directly be calculated from the off-rate: $\tau_{1/2} = \ln(2)/k_{\text{off}}$. This allows order-of-magnitude estimations of the stability of receptor-ligand complexes, assuming dissociation constants of 1 pM to 1 mM of biological interactions with typical sub-diffusion-limited on-rates [18]:

K_d	k_{off}	$\tau_{1/2}$
1 pM	10^{-6} to 10^{-4} s^{-1}	hours to days
1 nM	10^{-3} to 10^{-1} s^{-1}	seconds to hours
10 µM	10^{-1} to 10 s^{-1}	0.1 to 10 s
1 µM	1 to 100 s^{-1}	1 ms to 1 s
1 mM	10^{3} to 10^{5} s^{-1}	10 µs to 1 µs

Table 1.1 • Receptor-ligand complex half-lives
Estimated half-lives of receptor-ligand complexes assuming typical sub-diffusion-limited on-rates.

As shown in **Table 1.1**, high binding affinities correspond to the persistence of complexes for extended periods of time (hours), which, in the context of proteins involved in signaling, often implies the existence of a degradation pathway (e.g. endocytosis and subsequent degradation or recycling of the receptor [19]), since a long-lasting bound state effectively acts as a permanent on- or off switch and is therefore incompatible with the dynamic regulation of signaling [10, 13, 20]. Experimentally, high binding affinities require considerable incubation times before measurements ($\approx$ three to five times $\tau_{1/2}$), to reach sufficient equilibration of the exponential binding process [14].

1.2.3 Importance of studying kinetic rates

While determining equilibrium binding constants of protein-ligand interactions in solution is well-established and technically easier to achieve than measuring kinetic rates [21], the study of kinetic rates is essential for several reasons:

First, mathematically, equilibrium constants as the ratios of the dissociation- and association rates are ambiguous. Two processes may have equal equilibrium constants, but different rate constants [22, 23].

Second, in biological systems, protein-protein interactions rarely occur in equilibrium states, as proteins are produced, secreted, degraded and transported at varying rates and locations at all times [8, 23, 24].

Third, even in equilibrium, when different ligands compete for the same receptor, or one type of ligand may trigger different pathways, kinetic parameters rather than thermodynamic parameters become the determining factor for the outcome [13, 25].

Fourth, the lifetimes of ligand-receptor complexes (or residence time of the ligand) have been demonstrated to play a critical role in influencing the initiation and intensity of signaling cascades [25–34]. In epidermal growth factor receptor (EGFR) signaling, for example, it has been shown that the different ligands induce dimers with distinct lifetimes, with more short-lived dimers leading to more sustained EGFR signaling and different cellular responses [35]. Similarly, in drug development, viewing drug-target interactions not in terms of equilibrium affinity but focusing on the ligand-target lifetime, has been shown to drastically increase target selectivity and in vivo pharmacological activity [24, 25, 33, 36]. While it is possible to estimate these lifetimes coarsely, using **Eq. 1.5** and assuming (sub-)diffusion-limited on-rates, the resulting estimates span several orders of magnitude (see **Table 1.1**).

1.3 Binding in 3D versus 2D

A key factor in ligand-induced protein-protein interaction of receptors is the physical anchoring and arrangement of proteins on the plasma membrane. The two-dimensional topology and geometry greatly influence the protein-protein interactions that occur on these surfaces [37–39]. It is therefore essential to have a closer examination of the role that topological and dimensional features play in protein-protein interactions occurring on membranes. This understanding can provide valuable insights into the regulation of signal transduction [40, 41] and the design

of new drugs targeting these signaling pathways [20, 38, 42].

At its core, a membrane provides a physical platform for molecular interactions. The recruitment of molecular reactants onto the fluid membrane surface enhances their likelihood of interaction and increases their reaction kinetics, due to a local concentration effect [37, 43, 44]. Additionally, other factors such as constraints on molecular mobility and orientation, as well as spatiotemporal organization can also influence reaction rates [38, 42, 45–49]. Because of these largely undetermined, protein-specific factors, it remains difficult to translate three-dimensional (3D) binding kinetics to two-dimensional (2D) systems despite several attempts [44, 50–55]. As such, it is important to note that solution kinetics of protein-protein interactions that naturally would occur on membranes and hence a two-dimensional geometry, can only provide qualitative estimates but no quantitative insights [55–59].

1.3.1 Influence of receptor geometry

Dissociation constants of interactions occurring in 3D are expressed in units of molecules per volume whereas for interactions between surface-bound partners, the dissociation constants are expressed in molecules per unit area. Similarly, for reactions in 3D, the concentrations of ligands, receptors and ligand-receptor complexes are given in units of molecules per volume, whereas 2D counterparts are given in molecules per area. Depending on the exact geometry of the interaction, different 2D and 3D dissociation constants describe the ligand-receptor binding (see **Fig. 1.4**).

Ligand-induced receptor homodimerization (**Fig. 1.4b**), for example, is characterized by a 3D dissociation constant K_{B}, describing the interaction of the ligand from solution with the membrane-bound receptor, and a 2D dissociation constant K_{X}, describing the interaction of the membrane-bound free receptor with the membrane-bound ligand-carrying receptor [40, 41]. The fraction of dimerized receptor thus depends on the two dissociation constants, the receptor surface density, and the ligand concentration in solution. Generally, for every receptor geometry, the potential interactions and their geometrical implications need to be considered, to be able to properly characterize the interaction biophysically.

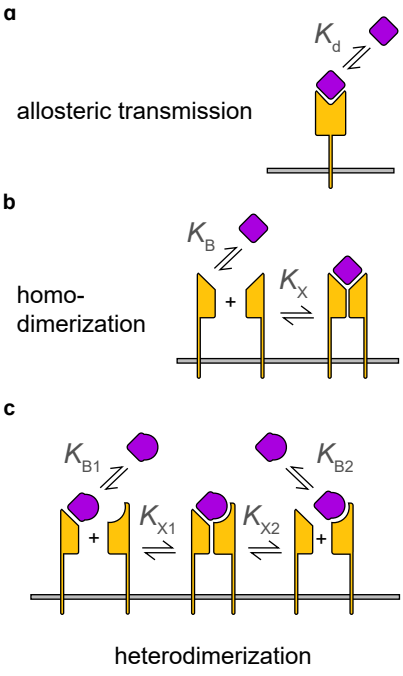

Figure 1.4 • Basic geometries of membrane-bound receptors

(a) Allosteric signal transmission through a membrane-bound receptor interacting with a ligand from solution. **(b)** Ligand-induced homodimerizing receptors, with dissociation constants for ligand-receptor, and receptor-receptor interaction. **(c)** Ligand-induced heterodimerizing receptors, with dissociation constants for ligand-receptor, and receptor-receptor interaction, separate for each receptor subunit.
Figure adapted from Binder *et al.*, 2021 [41].

1.3.2 Experimental approaches to characterize interactions

The key importance of the interaction between proteins and the binding of proteins to membranes or membrane proteins has led to the development of several techniques for measuring solution and surface binding constants [60].

Isothermal titration calorimetry (ITC), which measures the heat change produced upon binding

Microscale thermophoresis (MST), which measures the diffusion of fluorescently labeled proteins in solution in response to a temperature gradient, and the changes in diffusion that occur upon binding with another protein

Fluorescence anisotropy, which measures the rotational motion of fluorescently labeled proteins in solution taking place between photon absorption and subsequent fluorescence emission. Changes in rotational speed upon binding to another protein are detected and used to determine binding affinities

Quartz crystal microbalance (QCM), in which the change in resonance frequency of an acoustic reference signal reports on the binding of molecules to the surface [61]

Surface plasmon resonance (SPR), in which electrons in a thin metal film coated on a glass surface oscillate as a surface plasmon upon resonating with an evanescent field created by a light source shining onto the metal film. Small changes in the refractive index that occur when a protein in solution interacts with a protein immobilized on the metal film are detected by a shift in the resonance frequency

In addition to measuring affinity constants, it is important to note that QCM and SPR also allow for the measurement of binding kinetics. This is achieved through multiple rounds of ligand injection into a flow cell containing surface-immobilized proteins, followed by injection of a solution without the ligand. While this approach has been demonstrated in other methods, such as ITC [62], MST [63], and fluorescence anisotropy [64], it is not routinely performed due to the large protein quantities required - in QCM and SPR, surface-immobilized proteins can be reused during ligand titration experiments. While those methods are effective for irreversible reactions or perturbed systems returning to equilibrium, they are not well-suited for quasi-steady states where the rates of forward and backward reactions are approximately equal, and binding sites experience a constant turnover of binders. Furthermore, none of these methods can accurately replicate the translational and rotational freedom (or constraints) of membrane-bound proteins, as all binding partners are either free to diffuse in the solution or, as in the case of SPR and QCM, one partner is immobilized on the surface.

Consequently, the development of novel techniques is essential to investigate protein-protein interactions in 2D environments [55]. Fluorescence-based imaging techniques, such as total internal reflection fluorescence (TIRF) combined with labeled ligands [56, 57, 65, 66], Förster resonance energy transfer (FRET) [57, 58, 65, 67, 68], or fluorescence correlation spectroscopy (FCS) [69–71], allow the study of membrane-bound proteins and their interactions in biologically more relevant 2D environments, and have been used to extract binding constant and kinetic rates at the population-level. Specifically for measuring *trans*-interaction binding constants between two protein species in cell-cell or cell-supported lipid bilayer (SLB) interactions, the Zhu-Golan method has proven to be a valuable approach [55, 72–74]. This method quantifies the increase in fluorescence resulting from the accumulation of fluorescently-labeled binding partners in a cell-cell or cell-surface contact area, taking into account the lateral mobility of both binding partners.

While FCS is an ensemble technique in the sense that it measures the average behavior of a population of molecules, it's single-molecule sensitivity allows for the detection of subpopulations within the ensemble.

While fluorescence imaging in general is a powerful tool for investigating molecular interactions, single-molecule fluorescence imaging techniques such as single-molecule FRET (smFRET) and single-particle tracking (SPT) are required to fully harness its potential and gain a detailed view of molecular interactions on membranes. These techniques enable direct observation of molecular interactions in their biological context and even weak interactions are detected with high statistical significance by measuring the joint movement of two molecules over time. Additionally, quantitative measurements of colocalized particle fractions and interaction durations can be obtained. This offers a comprehensive view of the underlying mechanisms and dynamics of interactions and spatiotemporal organization occurring on membranes. As a result, single-molecule fluorescence imaging has emerged as a powerful tool for studying the behavior and function of proteins in complex environments, providing unparalleled sensitivity and spatial resolution.

1.4 Visualizing and tracking molecular interaction at the membrane

The demand for imaging techniques capable of visualizing the behavior of individual molecules in complex environments has led to the rapid growth of single-molecule microscopy, providing researchers access to a wealth of molecular information that is usually hidden in ensemble experiments [75–82]. This technology has revolutionized our understanding of cellular processes, providing unprecedented insights into the biomolecular mechanisms underlying many cellular functions [80, 82–88]. Single-molecule fluorescence techniques, such as smFRET [89, 90] and SPT [20, 31, 39, 90–98] revealed a surprising degree of complexity and flexibility of protein-protein interactions - the interactions between GPCRs and G proteins, for instance, when viewed from a single-molecule perspective, showed that the receptors and ligands are capable of adopting multiple conformations and forming dynamic nanodomains both on the plasma membrane and within cells [99]. In many cases, findings like these hold the potential to open up new avenues for drug development, allowing for modulation of signaling beyond the capabilities of currently available drugs [10, 20, 38, 100].

1.4.1 Single-molecule TIRF microscopy

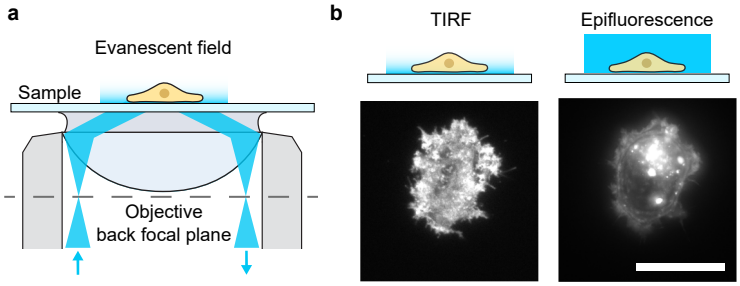

Figure 1.5 • Schematic representation of TIRF microscopy
A laser beam is focused off-center at the back focal plane of the objective, resulting in a steep angle of incidence on the glass-sample interface, which leads to total internal reflection of the laser beam. This results in an evanescent field that excites only a thin layer of fluorescently-labeled molecules in close proximity to the coverslip. **(b)** TIRF (left) and epifluorescence (right) images of the same cell with a fluorescently-labeled membrane. Scale bar is 20 µm.

TIRF microscopy is the most commonly used type of single-molecule imaging, since it allows to visualize biological processes at the single-molecule level, specifically at the cell membrane [76, 81, 89, 101–111]. As depicted in Fig. 1.5, it utilizes the total internal reflection (TIR) of a laser source to create an evanescent field [112]. As shown in Fig. 1.5, epifluorescence microscopy provides a view of the entire cell, while TIRF selectively illuminates the membrane while background fluorescence from the rest of the sample volume is minimized. This imaging mode allows for a signal-to background ratio sufficient for the imaging of individual fluorescently-labeled molecules, and at the same time reduces phototoxicity, allowing for extended imaging of live cells [113, 114]. Mathematically, the z-axial profile of the intensity of the evanescent field is given by:

$$I(z) = I_0 \exp\left(-\frac{z}{d}\right) \tag{1.7}$$

with d the distance to the interface, called the penetration depth, at which the evanescent field decays by a factor of $1/e \approx 37\%$ of I_0, the intensity at the interface. The penetration depth depends on the wavelength λ of the incident light, the refractive indices n_1 and n_2 of the glass slide and sample, respectively, and particularly on the incident angle θ:

$$d = \frac{\lambda}{4\pi\sqrt{n_1^2 \sin^2\theta - n_2^2}} \tag{1.8}$$

In TIRF microscopy, typically, the penetration depth ranges in between 50-200 nm.

While single-molecule microscopy techniques have revolutionized our understanding of cellular processes, the high costs and technical complexity of custom-built microscopes, as well as the lack of open-source documentation on how to build custom setups, limit the accessibility of these techniques.

1.4.2 Single-particle tracking of receptor proteins

The capability of TIRF microscopy to observe dynamic processes at the single-molecule level in real-time is often leveraged for a technique called single-particle tracking (SPT). SPT combined with TIRF microscopy to track individual molecules in living cells or reconstituted systems, researchers have gained valuable insights into the spatiotemporal organization of the plasma membrane [45, 77, 107, 115–119], the architecture and functional principles of the immunological synapse [81, 91, 96, 102, 120, 121], protein-protein interactions of receptors involved in signal transduction [20, 31, 89, 93, 97, 98, 105, 122–125], and many other complex molecular and cellular processes [59, 76, 79, 80, 82–84, 86, 126, 127].

In SPT-TIRF experiments, proteins situated on or close to the plasma membrane of live cells, or reconstituted proteins on SLBs, are tagged with fluorescent proteins, organic fluorescent dyes or quantum dots, and the position of molecules are tracked over time using a TIRF microscope. To do so, the positions of the proteins of interest are determined in each frame of a series of images using a localization algorithm (see **Fig. 1.6a**). Then, localizations across subsequent frames are connected using nearest neighbor algorithms [128, 129] or more advanced probabilistic methods [130, 131], reconstructing the protein's movement over time (see **Fig. 1.6b**). From these trajectories, diffusion properties and information about molecular interactions can be extracted (see **Fig. 1.6c**) [132, 133]. One of the most commonly studied properties is the mean squared displacement (MSD), which reflects the distance a particle has travelled in a given time interval (lag time). Analyzing the MSD for different lag times allows to extract information about the diffusion mode of a particle. Another important property is the diffusion coefficient, which is derived either from the MSD, or from the jump distance dis-

Diffusion modes include normal (Brownian) diffusion, confined diffusion, superdiffusion and subdiffusion, characterized by different shapes of the MSD-lag time curve.

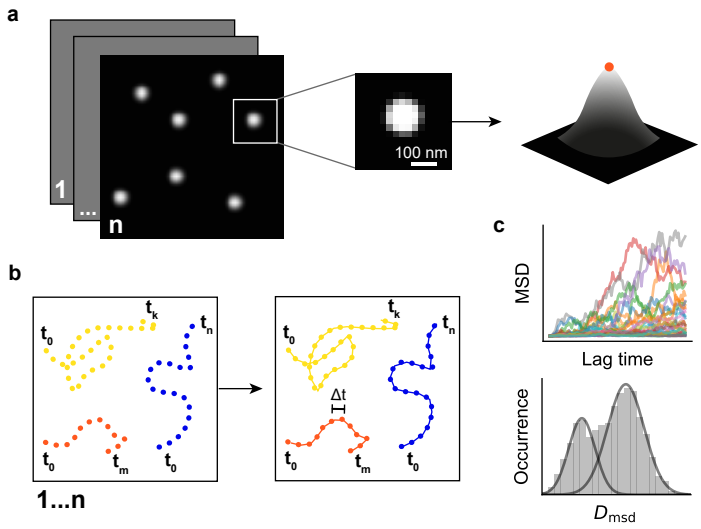

Figure 1.6 • Single-particle tracking and analysis
(a) Single-molecule data is recorded using TIRF microscopy and single emitters are localized frame-by-frame. **(b)** Individual localizations are connected over time, using nearest-neighbor or probabilistic algorithms. **(c)** Trajectories are analyzed to extract information about the motion and behavior of the tracked particles, such as the mean squared displacement (MSD), diffusion modes and coefficients, and interaction with other particles or cellular structures.

tribution [134]. By analyzing the distribution of diffusion coefficients for ensembles of trajectories, researchers can gain insight into the underlying physical processes that govern the particles' movement, such as interactions with the cytoskeleton, the formation of membrane microdomains, or the clustering of membrane proteins [71, 96, 103, 111, 116, 135–138]. In addition to diffusion, the colocalization of trajectories indicates protein-protein interactions [31, 92, 97, 110, 123, 139, 140] and the interactions of proteins with larger cellular structures [93, 110, 122].

While SPT is an effective technique for investigating the dynamic behavior of biomolecules, it is important to acknowledge the limitations of fluorescent labels. Primarily, their limited photostability restricts the duration for which molecules can be observed before fluorescent proteins or dyes bleach [126]. In contrast, photostable probes such as quantum dots offer improved longevity but present challenges in terms of chemical conjugation specificity to the target molecule and their large size, which can potentially interfere with molecular interactions [141].

1.4.3 Detecting protein-protein interaction via colocalization of single-molecule trajectories

Colocalization analysis in fluorescence microscopy refers to the process of determining the extent to which two or more species of fluorescently labeled molecules are found in the same spot in a sample. This can provide valuable information about the spatial and temporal relationships between different cellular components [142, 143] or the dynamics of molecules within subcellular compartments [122, 123, 144]. Typically, the analysis involves the quantification of the degree of overlap between the different fluorophores via correlation methods, and to generate images that depict the location and intensity of the various fluorescent signals [142, 145–147].

If performed at the single-molecule level, colocalization can often be interpreted as direct molecular interaction, revealing the nanoscale spatial organization and clustering of multi-protein complexes [10, 20, 38, 42, 90, 103, 122–124, 136, 148–154]. By tracking colocalizing molecules, even weak molecular interactions can be directly identified and characterized, due to the high spatiotemporal resolution in single-molecule microscopy that allows to discriminate between brief chance encounters and actual physical interaction [20, 57, 95, 98, 155–159].

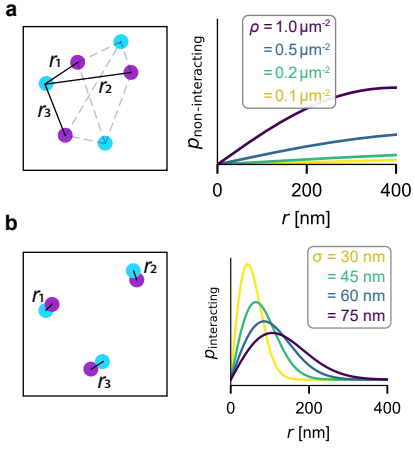

Figure 1.7 • Distance distribution of non-interacting and interacting particles

(a) Probability density function (PDF) of pairwise distances of non-interacting, randomly distributed molecules at surfaces densities between 0.1-1 µm^{-2}. **(b)** PDF of pairwise distances of physically interacting particles with an intermolecular distance of 10 nm. Distributions were calculated for localization uncertainties $\sigma_A = \sigma_B =$ 30 to 75 nm. Illustrations on the left clarify how pairwise distances are calculated.

Static single-molecule colocalization analysis

The pairwise distances of non-interacting molecules randomly distributed on a 2D surface follow a probability density function depending solely on the surface density (see **Fig. 1.7a**) [160]:

$$p_{\text{non-interacting}}(r) = 2\pi r\rho \exp\left(-\pi r^2 \rho\right) \tag{1.9}$$

For two physically interacting particles of species A and B, the distribution of pairwise distances when observed via dual-color single-molecule fluorescence microscopy, depends on the localization- and color-channel registration errors σ_{L} and σ_{C}, as well as the size of the interacting molecules and their fluorescent labels. With the overall localization error of a single molecule given by $\sigma = \sqrt{\sigma_{\text{L}}^2 + \sigma_{\text{C}}^2}$, the probability density $p_{\text{interacting}}(r)$ of distances r between interacting molecules with an intermolecular distance d_{mol}, is given by [155]:

$$p_{\text{interacting}}(r) = \frac{r}{2\sigma_{\overline{AB}}} \exp\left(-\frac{r^2 + d_{\text{mol}}^2}{4\sigma_{\overline{AB}}^2}\right) \cdot I_0\left(\frac{r \cdot d_{\text{mol}}}{2\sigma_{\overline{AB}}^2}\right) \tag{1.10}$$

with $\sigma_{\overline{AB}}^2 = \frac{1}{2}(\sigma_A^2 + \sigma_B^2)$, the respective overall localization errors of species A and B, and I_0 the modified Bessel function of order zero of the first kind. **Fig. 1.7b** shows the distance distributions of interacting particles for different values of localization errors.

The localization error σ_L of an individual fluorophore depends on the width of the diffraction-limited point spread function σ_{PSF} and scales with the inverse square root of the number of collected photons: $\sigma_L \sim \sigma_{\text{PSF}}/\sqrt{N}$ [161].

Two molecules are considered colocalized if their pairwise distance is smaller than a predefined threshold R (see **Fig. 1.8**). Specifically, for a molecule localized at the position (x_A, y_A), a molecule of species B is considered colocalizing if their position (x_B, y_B) falls within the threshold value, or search radius, R. Consequently, non-interacting molecules are also registered as colocalized, if their pairwise distance is smaller than R. Therefore, the threshold value R is usually a trade off between minimizing the false positive rate while still accurately identifying as many physically interacting particle pairs as possible. Generally, a reasonable starting point for choosing a threshold value is $R = 4\sigma$, yielding a false positive fraction of $\approx 2\%$ [156]. For denser samples or weakly interacting molecules, it can be beneficial to decrease this value to reduce the false positive rate.

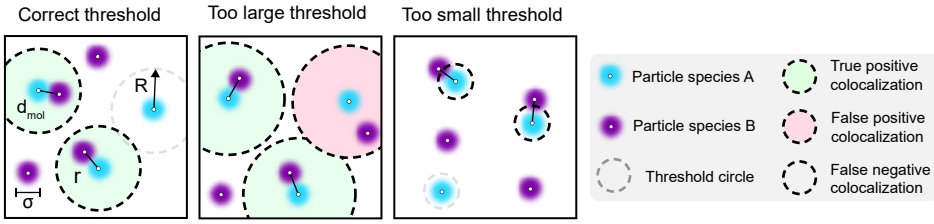

Figure 1.8 • Detection of colocalization via thresholding
Colocalization is detected by calculating pairwise distances r of particle species A and B. Single-molecule localizations are considered to be colocalizing (true positive) if their pairwise distance is below a pre-defined threshold R, which depends on the localization error σ and the intermolecular distance d_{mol} of interacting pairs. If the threshold chosen is too large, particles that are not physically interacting, are accidentally detected as colocalizing (false positive). Conversely, for too small thresholds, colocalizing particles may be missed (false negative), due to the localization errors and intermolecular distance.

For a bimolecular interaction in a dynamic equilibrium, with a fraction of particles associated at a given timepoint and the remaining particles diffusing freely, a typical pairwise distance distribution is depicted in **Fig. 1.9a**, calculated using **Eq. 1.9** and **Eq. 1.10** with parameter values resembling the experimentally detected distribution of pairwise distances of a sample of reconstituted inducible dimers (**Fig. 1.9b**). The contribution of interacting pairs (green area) features a pronounced peak at $r \approx \sqrt{2}\sigma$. A threshold value of $R = 180\,\mathrm{nm} \approx 4\sigma$ (dashed line) correctly identifies almost all true colocalizations (false negative rate of about 2%), while the false positive rate remains below 10% (see **Fig. 1.10** for the fractions of true positive, false positive and false negative colocalizations for different threshold values R).

While static colocalization analysis performed on the single-molecule level can yield important insights into the nanoscale spatial organization of cellular components, the dynamic nature of diffusing molecules on a membrane enables extending the colocalization analysis to incorporate temporal information. When tracking the observed molecules over time, only truly physically interacting molecules will remain associated, whereas non-interacting molecules separate over time due to their random motion [156]. Performing colocalization analysis frame-by-frame not only allows to reduce the rate of false positive detection of interaction, thereby drastically increasing statistical power [155, 156], but also allows to extract information about the duration of the interactions, therefore providing direct access to kinetic rates [31, 92, 95, 97, 110, 123, 139, 140, 158].

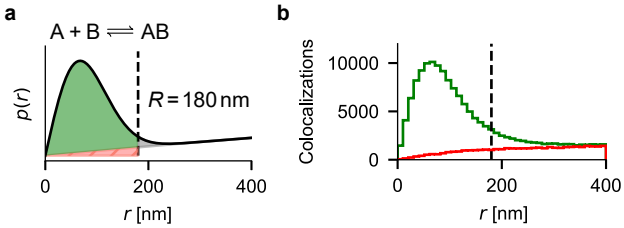

Figure 1.9 • Distance distributions of mixed populations
(a) Calculated probability density function of pairwise distances for particles interacting in a dynamic dimerization equilibrium (i.e. only a fraction of particles is dimerized at a given time) at a given surface density of 0.08 µm^{-2}. Colocalization is detected if the pairwise distance is smaller than the threshold value R, with the contribution of physically interacting particles shaded in green, and the contribution of non-interacting particles shaded in red (hatched). **(b)** Data from ligand-induced dimerization (green curve) and monomeric control (red curve) experiments. Pairwise distances between two molecule species A and B were calculated frame-by-frame and aggregated over a time period of 40 s.

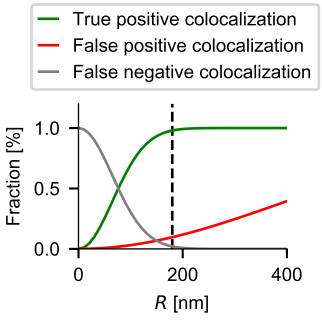

Figure 1.10 • Accuracy of colocalization analysis depends on threshold value choice

Fraction of accurately identified interacting pairs (green curve, true positive), false positive (red curve) and false negative (gray curve) colocalizations for a range of threshold values R. Dashed line is at threshold $R = 180$ nm. Curves were generated by integrating distance distributions from **Fig. 1.9a** in between $0 < r < R$.

Dynamic colocalization analysis

To perform dynamic colocalization analysis, colocalized pairs are identified by thresholding the pairwise distance in space, as described in the previous section, on a frame-by-frame basis. The resulting colocalization events can then either be associated with tracks generated separately for each molecular species, or, tracks are generated directly from colocalization events (see **Fig. 1.11**). Performing colocalization analysis on a frame-by-frame basis enables additional downstream analyses to very effectively differentiate random colocalizations from genuine interactions [152, 153, 155, 156, 158].

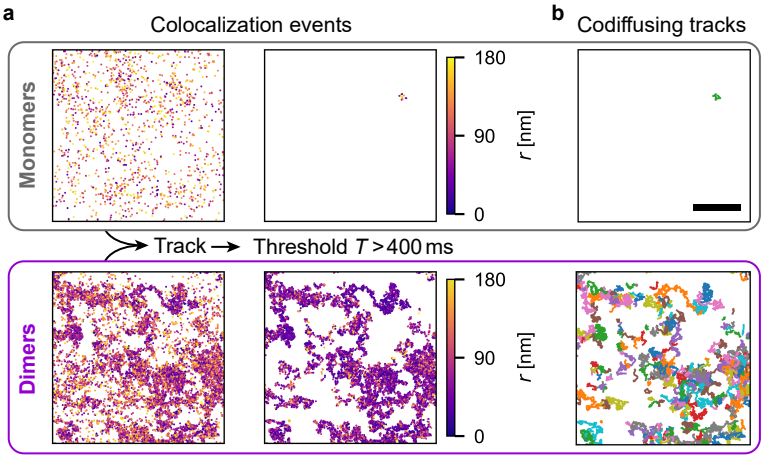

Figure 1.11 • Tracking colocalization events to obtain codiffusing trajectories
(a) Aggregated colocalization events over a period of 20 s, detected in a sample of monomers (top row) and induced dimers (bottom row), color-coded for the pairwise distance r. Colocalization events are tracked using a nearest-neighbor algorithm and trajectories containing less than 10 consecutive colocalizations ($T = 400$ ms) are rejected. **(b)** Codiffusing trajectories, generated from **(a)**, color-coded by track ID. Scale bar is 10 µm.

Since non-interacting particles are freely diffusing and the pairwise distance of a randomly colocalized pair of molecules generally increases over time, truly codiffusing molecules can easily be distinguished from non-interacting pairs (see **Fig. 1.11** and **Fig. 1.12**). The probability density function for two molecules with a pairwise distance r_t, that diffuse freely with diffusion constants $D_A = D_B = D$, to be observed at a pairwise distance $r_{t+\Delta t}$ after a timestep Δt, is given by [156, 162]:

$$p_{\text{non-interacting}}(r_{t+\Delta t}|r_t)\,\mathrm{d}r_{t+\Delta t} = \frac{1}{4D\Delta t} I_0\left(\frac{2r_t r_{t+\Delta t}}{8Dt}\right) r_{t+\Delta t} \exp\left(-(\frac{r_t^2}{+} r_{t+\Delta t})8Dt\right)\mathrm{d}r_{t+\Delta t}$$

with I_0 denoting the zeroth order modified Bessel function of the first kind.

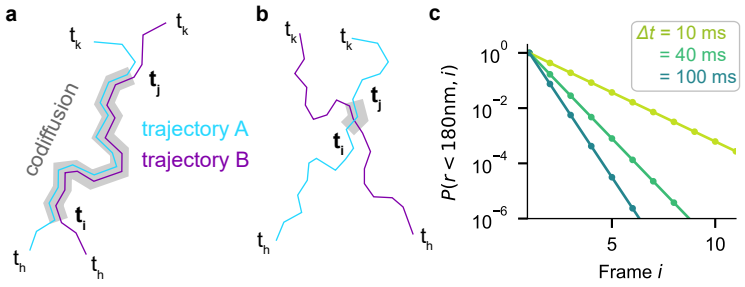

Figure 1.12 • Codiffusion analysis

(a) Trajectories of two molecules are shown in magenta and cyan, respectively. The molecules codiffuse for a period of time $(t_j - t_i)$ before eventually dissociating and diffusing independently. **(b)** Two freely diffusing molecules are detected as colocalizing at a time t if their pairwise distance is smaller than the colocalization threshold R. **(c)** $P(r < R, i)$ describes the probability that the pairwise distance of two non-interacting particles is smaller than colocalization threshold at frame i, after being registered as colocalized at frame 1. Calculations were performed with parameters $R = 180$ nm, $\rho = 0.5\,\mu\text{m}^{-2}$, $D = 0.5\,\mu\text{m}^2\,\text{s}^{-1}$ and frame rates of $1/\Delta t = 1/10$ ms to $1/100$ ms.

The chance of randomly colocalizing molecules to remain colocalized after n timesteps can be calculated recursively, using the known distribution of non-interacting molecules (**Eq. 1.9**), and integrating over all pairwise distances up to the predefined threshold value R. The result is depicted in **Fig. 1.12c** for parameter values $R = 180\,\text{nm}$, $\rho = 0.5\,\mu\text{m}^{-2}$, $D = 0.5\,\mu\text{m}^2\,\text{s}^{-1}$ and frame rates of $1/\Delta t = 1/5\,\text{ms}$ to $1/50\,\text{ms}$. The exponentially decreasing probability implies that we can introduce a threshold for the number of consecutive colocalizations that a molecular pair has to exceed, to be considered as truly interacting. This threshold duration T can be applied to detect molecular interaction with a high statistical certainty. In **Fig. 1.11b**, the threshold duration is set to 10 frames, at a $1/40\,\text{ms}$ framerate, and effectively removes all false positive colocalizations ($> 98\%$) in the non-interacting control sample (see **Fig. 1.11b**) [155, 156].

An appropriate choice of T depends on the timestep between frames Δt, the diffusion coefficient D, surface density ρ and the predefined colocalization threshold value R. Experimentally, many of the relevant parameters influence each other - the framerate of a measurement, for example, is determined by the technical possibilities of the microscope setup and the required localization precision, which in turn informs the choice of the colocalization threshold value, and itself is affected by the photophysics of the fluorescent labels and the diffusion constant of the molecules. Thus, choosing values for analysis parameters such as the colocalization and duration thresholds R, and T usually require some heuristics.

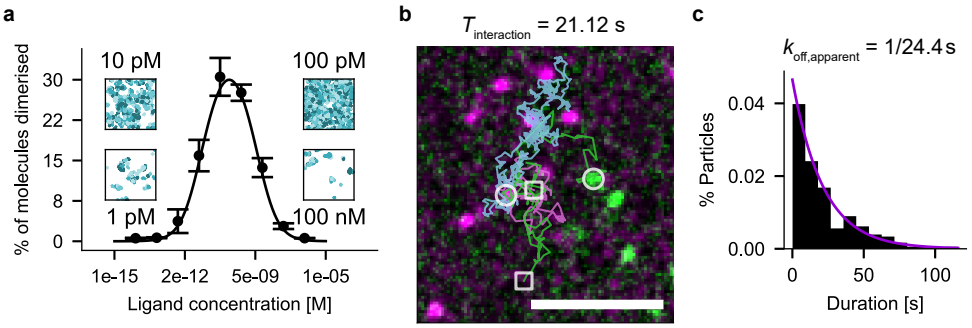

Figure 1.13 • Determining binding kinetics of molecular interactions
(a) Ligand-titration allows the determination of 2D binding constants by measuring the fraction of interacting ligand-induced homodimerizing molecules as a function of ligand concentration. **(b)** Directly observing both binding and unbinding events allows to extract off-rates based on the interaction duration. Two individual molecules labeled with spectrally different dyes (depicted in green and magenta tracks) associate, dimerize for 21.12 s (blue track) and dissociate. Beginning and end of trajectories are marked with circles and squares, respectively. Scale bar is 4 µm. **(c)** Example data of observed interaction durations, fitted with an exponential function with decay rate $k_{\text{off, app}} = 1/\tau_{\text{app}} = 1/24.4\,\text{s}$. Assuming mean trajectory lifetimes of $\tau_{\text{track, }A} = 48.4\,\text{s}$ and $\tau_{\text{track, }B} = 62.3\,\text{s}$, the corrected dissociation rate is $k_{\text{off}} = 1/233.3\,\text{s}$.

In addition to qualitative studies that identify whether interactions occur and which molecular species are involved [38, 42, 90, 124, 149, 150, 158], quantitative investigations that reveal binding kinetics can provide valuable insights [10, 20, 148, 158]. One such approach is ligand titration, which allows to extract 2D binding constants from the fraction of interacting molecules as a function of ligand concentration [20, 40, 163]. In **Chapter 4**, we use this approach to determine the 2D binding constants of a ligand-inducible homodimer (see also **Fig. 1.13a**). Furthermore, off-rates can be inferred by analyzing trajectories where both association and dissociation events are directly observed (see **Fig. 1.13b**)

[10, 94, 158, 164]. Alternatively, if full trajectories of association- and dissociation events are not available, the observed duration of interactions can be used to determine off-rates by fitting the histogram of durations to an exponential decay function and correcting for bleaching and tracking errors (see **Fig. 1.13c**) [10, 105, 164, 165]. The corrected off-rate is given as:

$$k_{\text{off}} = \tau_{\text{app}}^{-1} - \tau_{\text{tracks},A}^{-1} - \tau_{\text{tracks},B}^{-1} \tag{1.11}$$

with τ_{app} the dimer lifetime derived by fitting an exponential decay to the observed interaction duration histogram, and $\tau_{\text{tracks},A}$ and $\tau_{\text{tracks},B}$ the lifetime of trajectories of molecules A and B, derived by fitting an exponential decay to the histogram of trajectory lengths [164].

These possibilities make SPT with TIRF microscopes ideally suited for the study of protein-protein interactions on membranes, providing access to the spatial and temporal dynamics of interactions at the single-molecule level in a biologically relevant context.

Thesis outline

The overall aim of this thesis is to make single-molecule imaging accessible to a larger part of the research community by providing new tools and techniques that can be applied to a wide range of research questions in the field of protein-protein interactions and immunological signaling.

Chapter 2 of this thesis presents the design, construction, and characterization of a single-molecule TIRF microscope (K2 TIRF) that is optimized for live-cell and single-molecule imaging. Promoting open science principles, I provide comprehensive, step-by-step building instructions, a parts list, and CAD models to help other researchers construct their own systems or enhance their current setups. By sharing this information, I aim to reduce the barriers to entry for researchers seeking to use single-molecule TIRF microscopy in their work.

In **Chapter 3**, I present an experimental platform tailored for single-molecule analysis of ligand-induced binding involving purified interleukin-2 and -15 receptors, which are reconstituted on supported lipid bilayers. This chapter outlines the necessary steps for purifying and labeling protein receptor subunits, as well as their biophysical characterization using thermal shift assays and microscale thermophoresis. Furthermore, I provide comprehensive information on the reconstitution of the receptor subunits and the execution of simultaneous three-color tracking of these molecules. I also address the challenges encountered during the experiments, the impact they had on interpreting the data collected, and offer potential solutions to overcome these obstacles.

In **Chapter 4**, I present DNA points accumulation for imaging in nanoscale topography (DNA-PAINT) single-particle tracking (DNA-PAINT-SPT) as a novel DNA-PAINT based method to extend single-molecule trajectory lengths of membrane proteins in live cells and reconstitution experiments. We characterize protein-protein interactions using a model membrane protein that forms homodimers, achieving an unprecedented level of detail in the characterization of molecular interaction parameters in two-dimensional systems.

Lastly, in the outlook in **Chapter 5**, I explore prospective advancements and applications of the K2 TIRF microscope and DNA-PAINT-SPT, and discuss the optimal approach to continue investigating IL-2/IL-15 receptor binding kinetics in future studies.

References

[1] Bruce Alberts, ed. *Molecular Biology of the Cell*. 4th ed. New York: Garland Science, 2002.

[2] Harvey Lodish et al., eds. *Molecular Cell Biology*. Eighth edition, global edition. New York: W.H. Freeman Macmillan Learning, 2016.

[3] Catherine T Pawson and John D Scott. "Signal Integration through Blending, Bolstering and Bifurcating of Intracellular Information". In: *Nature Structural & Molecular Biology* 17.6 (2010), pp. 653–658.

[4] Tony Pawson and Piers Nash. "Protein–Protein Interactions Define Specificity in Signal Transduction". In: *Genes & Development* 14.9 (2000), pp. 1027–1047.

[5] Hisashi Tatebe and Kazuhiro Shiozaki. "Evolutionary Conservation of the Components in the TOR Signaling Pathways". In: *Biomolecules* 7.4 (2017), p. 77.

[6] David R. Fooksman et al. "Functional Anatomy of T Cell Activation and Synapse Formation". In: *Annual Review of Immunology* 28.1 (2010), pp. 79–105.

[7] Michael L. Dustin. "The Immunological Synapse". In: *Cancer Immunology Research* 2.11 (2014), pp. 1023–1033.

[8] Grégoire Altan-Bonnet and Ratnadeep Mukherjee. "Cytokine-Mediated Communication: A Quantitative Appraisal of Immune Complexity". In: *Nature Reviews Immunology* 19.4 (2019), pp. 205–217.

[9] Lucas M. P. Chataigner, Nadia Leloup, and Bert J. C. Janssen. "Structural Perspectives on Extracellular Recognition and Conformational Changes of Several Type-I Transmembrane Receptors". In: *Frontiers in Molecular Biosciences* 7 (2020), p. 129.

[10] Ignacio Moraga et al. "Instructive Roles for Cytokine-Receptor Binding Parameters in Determining Signaling and Functional Potency". In: *Science Signaling* 8.402 (2015), ra114–ra114.

[11] Nicole J. Yang and Marlon J. Hinner. "Getting Across the Cell Membrane: An Overview for Small Molecules, Peptides, and Proteins". In: *Site-Specific Protein Labeling*. Ed. by Arnaud Gautier and Marlon J. Hinner. Vol. 1266. New York, NY: Springer New York, 2015, pp. 29–53.

[12] Warren J. Leonard and John J. O'Shea. "JAKS AND STATS: Biological Implications". In: *Annual Review of Immunology* 16.1 (1998), pp. 293–322.

[13] G. Schreiber, G. Haran, and H.-X. Zhou. "Fundamental Aspects of Protein-Protein Association Kinetics". In: *Chemical Reviews* 109.3 (2009), pp. 839–860.

[14] Inga Jarmoskaite et al. "How to Measure and Evaluate Binding Affinities". In: *eLife* 9 (2020), e57264.

[15] M. v. Smoluchowski. "Versuch Einer Mathematischen Theorie Der Koagulationskinetik Kolloider Lösungen". In: Zeitschrift Für Physikalische Chemie 92U.1 (1918), pp. 129–168.

[16] H.X. Zhou. "Enhancement of Protein-Protein Association Rate by Interaction Potential: Accuracy of Prediction Based on Local Boltzmann Factor". In: *Biophysical Journal* 73.5 (1997), pp. 2441–2445.

[17] Maximilian Schlosshauer and David Baker. "Realistic Protein-Protein Association Rates from a Simple Diffusional Model Neglecting Long-Range Interactions, Free Energy Barriers, and Landscape Ruggedness". In: *Protein Science* 13.6 (2004), pp. 1660–1669.

[18] Sijia Peng, Wenjuan Wang, and Chunlai Chen. "Breaking the Concentration Barrier for Single-Molecule Fluorescence Measurements". In: *Chemistry - A European Journal* 24.5 (2018), pp. 1002–1009.

[19] Peter J. Cullen and Florian Steinberg. "To Degrade or Not to Degrade: Mechanisms and Significance of Endocytic Recycling". In: *Nature Reviews Molecular Cell Biology* 19.11 (2018), pp. 679–696.

[20] Stephan Wilmes et al. "Mechanism of Homodimeric Cytokine Receptor Activation and Dysregulation by Oncogenic Mutations". In: *Science* 367.6478 (2020), pp. 643–652.

[21] Xiaodong Pang and Huan-Xiang Zhou. "Rate Constants and Mechanisms of Protein–Ligand Binding". In: *Annual Review of Biophysics* 46.1 (2017), pp. 105–130.

[22] Gilbert J Kersh et al. "High- and Low-Potency Ligands with Similar Affinities for the TCR: The Importance of Kinetics in TCR Signaling". In: *Immunity* 9.6 (1998), pp. 817–826.

[23] Javier Corzo. "Time, the Forgotten Dimension of Ligand Binding Teaching". In: *Biochemistry and Molecular Biology Education* 34.6 (2006), pp. 413–416.

[24] Robert A. Copeland. “The Drug–Target Residence Time Model: A 10-Year Retrospective”. In: *Nature Reviews Drug Discovery* 15.2 (2016), pp. 87–95.

[25] Christofer S Tautermann. “Impact, Determination and Prediction of Drug–Receptor Residence Times for GPCRs”. In: *Current Opinion in Pharmacology* 30 (2016), pp. 22–26.

[26] K Matsui et al. “Kinetics of T-cell Receptor Binding to Peptide/I-Ek Complexes: Correlation of the Dissociation Rate with T-cell Responsiveness.” In: *Proceedings of the National Academy of Sciences* 91.26 (1994), pp. 12862–12866.

[27] Kelly J. Culhane et al. “Kinetic Model of GPCR-G Protein Interactions Reveals Allokairic Modulation of Signaling”. In: *Nature Communications* 13.1 (2022), p. 1202.

[28] Leon O. Murphy et al. “Molecular Interpretation of ERK Signal Duration by Immediate Early Gene Products”. In: *Nature Cell Biology* 4.8 (2002), pp. 556–564.

[29] Peter J. Tummino and Robert A. Copeland. “Residence Time of Receptor-Ligand Complexes and Its Effect on Biological Function”. In: *Biochemistry* 47.20 (2008), pp. 5481–5492.

[30] David A. Sykes et al. “Binding Kinetics of Ligands Acting at GPCRs”. In: *Molecular and Cellular Endocrinology* 485 (2019), pp. 9–19.

[31] Rinshi S. Kasai et al. “The Class-A GPCR Dopamine D2 Receptor Forms Transient Dimers Stabilized by Agonists: Detection by Single-Molecule Tracking”. In: *Cell Biochemistry and Biophysics* 76.1-2 (2018), pp. 29–37.

[32] Doug K Tischer and Orion David Weiner. “Light-Based Tuning of Ligand Half-Life Supports Kinetic Proofreading Model of T Cell Signaling”. In: *eLife* 8 (2019), e42498.

[33] Grant K Walkup et al. “Translating Slow-Binding Inhibition Kinetics into Cellular and in Vivo Effects”. In: *Nature Chemical Biology* 11.6 (2015), pp. 416–423.

[34] Luis F. Ponce, Karina García-Martínez, and Kalet León. “Quantitative Contribution of IL2Rγ to the Dynamic Formation of IL2-IL2R Complexes”. In: *PLOS ONE* 11.5 (2016), e0155684.

[35] Daniel M. Freed et al. “EGFR Ligands Differentially Stabilize Receptor Dimers to Specify Signaling Kinetics”. In: *Cell* 171.3 (2017), 683–695.e18.

[36] Robert A. Copeland, David L. Pompliano, and Thomas D. Meek. "Drug–Target Residence Time and Its Implications for Lead Optimization". In: *Nature Reviews Drug Discovery* 5.9 (2006), pp. 730–739.

[37] Boris N. Kholodenko, Jan B. Hoek, and Hans V. Westerhoff. "Why Cytoplasmic Signalling Proteins Should Be Recruited to Cell Membranes". In: *Trends in Cell Biology* 10.5 (2000), pp. 173–178.

[38] Ignacio Moraga et al. "Tuning Cytokine Receptor Signaling by Re-orienting Dimer Geometry with Surrogate Ligands". In: *Cell* 160.6 (2015), pp. 1196–1208.

[39] Jenny J. Lin et al. "Membrane Association Transforms an Inert Anti-TCRβ Fab' Ligand into a Potent T Cell Receptor Agonist". In: *Biophysical Journal* 118.12 (2020), pp. 2879–2893.

[40] Sepehr Fathi et al. "Absolute Ligand Discrimination by Dimeric Signaling Receptors". In: *Biophysical Journal* 111.5 (2016), pp. 917–920.

[41] Patrick Binder et al. "Optimal Ligand Discrimination by Asymmetric Dimerization and Turnover of Interferon Receptors". In: *Proceedings of the National Academy of Sciences* 118.37 (2021), e2103939118.

[42] Kritika Mohan et al. "Topological Control of Cytokine Receptor Signaling Induces Differential Effects in Hematopoiesis". In: *Science* 364.6442 (2019), eaav7532.

[43] D. Axelrod and M.D. Wang. "Reduction-of-Dimensionality Kinetics at Reaction-Limited Cell Surface Receptors". In: *Biophysical Journal* 66.3 (1994), pp. 588–600.

[44] Osman N. Yogurtcu and Margaret E. Johnson. "Cytosolic Proteins Can Exploit Membrane Localization to Trigger Functional Assembly". In: *PLOS Computational Biology* 14.3 (2018), e1006031.

[45] Jay T Groves and John Kuriyan. "Molecular Mechanisms in Signal Transduction at the Membrane". In: *Nature Structural & Molecular Biology* 17.6 (2010), pp. 659–665.

[46] Boris N. Kholodenko, John F. Hancock, and Walter Kolch. "Signalling Ballet in Space and Time". In: *Nature Reviews Molecular Cell Biology* 11.6 (2010), pp. 414–426.

[47] Steven M. Abel et al. "The Membrane Environment Can Promote or Suppress Bistability in Cell Signaling Networks". In: *The Journal of Physical Chemistry B* 116.11 (2012), pp. 3630–3640.

[48] William Y. C. Huang et al. “A Molecular Assembly Phase Transition and Kinetic Proofreading Modulate Ras Activation by SOS”. In: *Science* 363.6431 (2019), pp. 1098–1103.

[49] Lindsay B. Case et al. “Stoichiometry Controls Activity of Phase-Separated Clusters of Actin Signaling Proteins”. In: *Science* 363.6431 (2019), pp. 1093–1097.

[50] Yinghao Wu et al. “Transforming Binding Affinities from Three Dimensions to Two with Application to Cadherin Clustering”. In: *Nature* 475.7357 (2011), pp. 510–513.

[51] Zhong-Ru Xie, Jiawen Chen, and Yinghao Wu. “Linking 3D and 2D Binding Kinetics of Membrane Proteins by Multiscale Simulations: Linking 3D and 2D Binding Kinetics”. In: *Protein Science* 23.12 (2014), pp. 1789–1799.

[52] Jose Faro, Mario Castro, and Carmen Molina-París. “A Unifying Mathematical Framework for Experimental TCR-pMHC Kinetic Constants”. In: *Scientific Reports* 7.1 (2017), p. 46741.

[53] Victoria Junghans et al. “Effects of a Local Auxiliary Protein on the Two-Dimensional Affinity of a TCR-peptide MHC Interaction”. In: *Journal of Cell Science* (2020), jcs.245985.

[54] Bhavya Mishra and Margaret E. Johnson. “Speed Limits of Protein Assembly with Reversible Membrane Localization”. In: *The Journal of Chemical Physics* 154.19 (2021), p. 194101.

[55] Tommy Dam et al. “Supported Lipid Bilayers and the Study of Two-Dimensional Binding Kinetics”. In: *Frontiers in Molecular Biosciences* 9 (2022), p. 833123.

[56] Martynas Gavutis et al. “Lateral Ligand-Receptor Interactions on Membranes Probed by Simultaneous Fluorescence-Interference Detection”. In: *Biophysical Journal* 88.6 (2005), pp. 4289–4302.

[57] Martynas Gavutis et al. “Determination of the Two-Dimensional Interaction Rate Constants of a Cytokine Receptor Complex”. In: *Biophysical Journal* 90.9 (2006), pp. 3345–3355.

[58] Johannes B. Huppa et al. “TCR–Peptide–MHC Interactions in Situ Show Accelerated Kinetics and Increased Affinity”. In: *Nature* 463.7283 (2010), pp. 963–967.

[59] Adam O. Barden et al. “Tracking Individual Membrane Proteins and Their Biochemistry: The Power of Direct Observation”. In: *Neuropharmacology* 98 (2015), pp. 22–30.

[60] Panagiotis L. Kastritis and Alexandre M. J. J. Bonvin. “On the Binding Affinity of Macromolecular Interactions: Daring to Ask Why Proteins Interact”. In: *Journal of The Royal Society Interface* 10.79 (2013), p. 20120835.

[61] Jörg H. Kleinschmidt, ed. *Lipid-Protein Interactions: Methods and Protocols*. Vol. 2003. Methods in Molecular Biology. New York, NY: Springer New York, 2019.

[62] Kirk A. Vander Meulen et al. “Measuring the Kinetics of Molecular Association by Isothermal Titration Calorimetry”. In: *Methods in Enzymology*. Vol. 567. Elsevier, 2016, pp. 181–213.

[63] Julian A. C. Stein, Alan Ianeselli, and Dieter Braun. “Kinetic Microscale Thermophoresis for Simultaneous Measurement of Binding Affinity and Kinetics”. In: *Angewandte Chemie International Edition* 60.25 (2021), pp. 13988–13995.

[64] Kirsten N. Swonger and Anne S. Robinson. “Using Fluorescence Anisotropy for Ligand Binding Kinetics of Membrane Proteins”. In: *Current Protocols in Protein Science* 93.1 (2018).

[65] David Richter et al. “Ligand-Induced Type II Interleukin-4 Receptor Dimers Are Sustained by Rapid Re-Association within Plasma Membrane Microcompartments”. In: *Nature Communications* 8 (2017), p. 15976.

[66] Sara Löchte et al. “Live Cell Micropatterning Reveals the Dynamics of Signaling Complexes at the Plasma Membrane”. In: *The Journal of Cell Biology* 207.3 (2014), pp. 407–418.

[67] Damien Maurel et al. “Cell-Surface Protein-Protein Interaction Analysis with Time-Resolved FRET and Snap-Tag Technologies: Application to GPCR Oligomerization”. In: *Nature Methods* 5.6 (2008), pp. 561–567.

[68] Tomasz Żal, M.Anna Żal, and Nicholas R.J. Gascoigne. “Inhibition of T Cell Receptor-Coreceptor Interactions by Antagonist Ligands Visualized by Live FRET Imaging of the T-Hybridoma Immunological Synapse”. In: *Immunity* 16.4 (2002), pp. 521–534.

[69] Jonas Mücksch et al. “Quantifying Reversible Surface Binding via Surface-Integrated Fluorescence Correlation Spectroscopy”. In: *Nano Letters* 18.5 (2018), pp. 3185–3192.

[70] Jonas Ries et al. “Modular Scanning FCS Quantifies Receptor-Ligand Interactions in Living Multicellular Organisms”. In: *Nature Methods* 6.9 (2009), pp. 643–645.

[71] Tyler A. Jepson and Jean K. Chung. “Diffusion-Based Determination of Protein Homodimerization on Reconstituted Membrane Surfaces”. In: *BMB Reports* 54.3 (2021), pp. 157–163.

[72] De-Min Zhu et al. “Analysis of Two-Dimensional Dissociation Constant of Laterally Mobile Cell Adhesion Molecules”. In: *Biophysical Journal* 92.3 (2007), pp. 1022–1034.

[73] Cheng Zhu et al. “Insights from *in Situ* Analysis of TCR-pMHC Recognition: Response of an Interaction Network”. In: *Immunological Reviews* 251.1 (2013), pp. 49–64.

[74] Manto Chouliara et al. “Single-Cell Measurements of Two-Dimensional Binding Affinity across Cell Contacts”. In: *Biophysical Journal* 120.22 (2021), pp. 5032–5040.

[75] I. Tinoco and R. L. Gonzalez. “Biological Mechanisms, One Molecule at a Time”. In: *Genes & Development* 25.12 (2011), pp. 1205–1231.

[76] Nan Li et al. “Single-Molecule Imaging and Tracking of Molecular Dynamics in Living Cells”. In: *National Science Review* 4.5 (2017), pp. 739–760.

[77] Akihiro Kusumi et al. “Tracking Single Molecules at Work in Living Cells”. In: *Nature Chemical Biology* 10.7 (2014), pp. 524–532.

[78] Alexander Gust et al. “A Starting Point for Fluorescence-Based Single-Molecule Measurements in Biomolecular Research”. In: *Molecules* 19.10 (2014), pp. 15824–15865.

[79] Hao Shen et al. “Single Particle Tracking: From Theory to Biophysical Applications”. In: *Chemical Reviews* 117.11 (2017), pp. 7331–7376.

[80] Johan Elf and Irmeli Barkefors. “Single-Molecule Kinetics in Living Cells”. In: *Annual Review of Biochemistry* 88.1 (2019), pp. 635–659.

[81] Jenny J. Y. Lin et al. “Mapping the Stochastic Sequence of Individual Ligand-Receptor Binding Events to Cellular Activation: T Cells Act on the Rare Events”. In: *Science Signaling* 12.564 (2019), eaat8715.

[82] Alan P. Boka, Apratim Mukherjee, and Mustafa Mir. “Single-Molecule Tracking Technologies for Quantifying the Dynamics of Gene Regulation in Cells, Tissue and Embryos”. In: *Development* 148.18 (2021), dev199744.

[83] Takashi Funatsu et al. “Imaging of Single Fluorescent Molecules and Individual ATP Turnovers by Single Myosin Molecules in Aqueous Solution”. In: *Nature* 374.6522 (1995), pp. 555–559.

[84] Ronald D. Vale et al. “Direct Observation of Single Kinesin Molecules Moving along Microtubules”. In: *Nature* 380.6573 (1996), pp. 451–453.

[85] Akihiko Ishijima et al. “Simultaneous Observation of Individual ATPase and Mechanical Events by a Single Myosin Molecule during Interaction with Actin”. In: *Cell* 92.2 (1998), pp. 161–171.

[86] Ahmet Yildiz et al. “Myosin V Walks Hand-Over-Hand: Single Fluorophore Imaging with 1.5-Nm Localization”. In: *Science* 300.5628 (2003), pp. 2061–2065.

[87] G Mashanov. “Visualizing Single Molecules inside Living Cells Using Total Internal Reflection Fluorescence Microscopy”. In: *Methods* 29.2 (2003), pp. 142–152.

[88] Aaron A. Hoskins et al. “Ordered and Dynamic Assembly of Single Spliceosomes”. In: *Science* 331.6022 (2011), pp. 1289–1295.

[89] Wesley B. Asher et al. “Single-Molecule FRET Imaging of GPCR Dimers in Living Cells”. In: *Nature Methods* 18.4 (2021), pp. 397–405.

[90] Junel Sotolongo Bellón et al. “Four-Color Single-Molecule Imaging with Engineered Tags Resolves the Molecular Architecture of Signaling Complexes in the Plasma Membrane”. In: *Cell Reports Methods* 2.2 (2022), p. 100165.

[91] Geoff P O’Donoghue et al. “Direct Single Molecule Measurement of TCR Triggering by Agonist pMHC in Living Primary T Cells”. In: *eLife* 2 (2013), e00778.

[92] Alina Tabor. “Visualization and Ligand-Induced Modulation of Dopamine Receptor Dimerization at the Single Molecule Level”. In: *Scientific Reports* (2016), p. 16.

[93] Jan Möller et al. “Single-Molecule Analysis Reveals Agonist-Specific Dimer Formation of μ-Opioid Receptors”. In: *Nature Chemical Biology* 16.9 (2020), pp. 946–954.

[94] Titiwat Sungkaworn et al. “Single-Molecule Imaging Reveals Receptor–G Protein Interactions at Cell Surface Hot Spots”. In: *Nature* 550.7677 (2017), pp. 543–547.

[95] J. A. Hern et al. “Formation and Dissociation of M1 Muscarinic Receptor Dimers Seen by Total Internal Reflection Fluorescence Imaging of Single Molecules”. In: *Proceedings of the National Academy of Sciences* 107.6 (2010), pp. 2693–2698.

[96] Marcus J. Taylor et al. “A DNA-Based T Cell Receptor Reveals a Role for Receptor Clustering in Ligand Discrimination”. In: *Cell* 169.1 (2017), 108–119.e20.

[97] Ali Işbilir et al. “Advanced Fluorescence Microscopy Reveals Disruption of Dynamic CXCR4 Dimerization by Subpocket-Specific Inverse Agonists”. In: *Proceedings of the National Academy of Sciences* 117.46 (2020), pp. 29144–29154.

[98] Davide Calebiro and Titiwat Sungkaworn. “Single-Molecule Imaging of GPCR Interactions”. In: *Trends in Pharmacological Sciences* 39.2 (2018), pp. 109–122.

[99] Davide Calebiro et al. “G Protein-Coupled Receptor-G Protein Interactions: A Single-Molecule Perspective”. In: *Physiological Reviews* 101.3 (2021), pp. 857–906.

[100] Aron M. Levin et al. “Exploiting a Natural Conformational Switch to Engineer an Interleukin-2 ‘Superkine’”. In: *Nature* 484.7395 (2012), pp. 529–533.

[101] Damien Alcor, Géraldine Gouzer, and Antoine Triller. “Single-Particle Tracking Methods for the Study of Membrane Receptors Dynamics”. In: *European Journal of Neuroscience* 30.6 (2009), pp. 987–997.

[102] Ricardo A. Fernandes et al. “A Cell Topography-Based Mechanism for Ligand Discrimination by the T Cell Receptor”. In: *Proceedings of the National Academy of Sciences* 116.28 (2019), pp. 14002–14010.

[103] Christos Karathanasis et al. “Single-Molecule Imaging Reveals the Oligomeric State of Functional TNFα-induced Plasma Membrane TNFR1 Clusters in Cells”. In: *Science Signaling* 13.614 (2020), eaax5647.

[104] Derek Toomre and Joerg Bewersdorf. “A New Wave of Cellular Imaging”. In: *Annual Review of Cell and Developmental Biology* 26.1 (2010), pp. 285–314.

[105] D. Calebiro et al. “Single-Molecule Analysis of Fluorescently Labeled G-protein-coupled Receptors Reveals Complexes with Distinct Dynamics and Organization”. In: *Proceedings of the National Academy of Sciences* 110.2 (2013), pp. 743–748.

[106] Andreas Gahlmann and W. E. Moerner. “Exploring Bacterial Cell Biology with Single-Molecule Tracking and Super-Resolution Imaging”. In: *Nature Reviews Microbiology* 12.1 (2014), pp. 9–22.

[107] Xiaohua Wang et al. “Single-Molecule Fluorescence Imaging to Quantify Membrane Protein Dynamics and Oligomerization in Living Plant Cells”. In: *Nature Protocols* 10.12 (2015), pp. 2054–2063.

[108] Sarah R. Needham et al. “EGFR Oligomerization Organizes Kinase-Active Dimers into Competent Signalling Platforms”. In: *Nature Communications* 7.1 (2016), p. 13307.

[109] Limin Xiang et al. “Single-Molecule Displacement Mapping Unveils Nanoscale Heterogeneities in Intracellular Diffusivity”. In: *Nature Methods* 17.5 (2020), pp. 524–530.

[110] Juan A Torreno-Pina, Carlo Manzo, and Maria F Garcia-Parajo. “Uncovering Homo-and Hetero-Interactions on the Cell Membrane Using Single Particle Tracking Approaches”. In: *Journal of Physics D: Applied Physics* 49.10 (2016), p. 104002.

[111] Masataka Yanagawa et al. “Single-Molecule Diffusion-Based Estimation of Ligand Effects on G Protein–Coupled Receptors”. In: *Science Signaling* 11.548 (2018), eaao1917.

[112] Daniel Axelrod. “Chapter 7 Total Internal Reflection Fluorescence Microscopy”. In: *Methods in Cell Biology*. Vol. 89. Elsevier, 2008, pp. 169–221.

[113] A. L. Mattheyses, S. M. Simon, and J. Z. Rappoport. “Imaging with Total Internal Reflection Fluorescence Microscopy for the Cell Biologist”. In: *Journal of Cell Science* 123.21 (2010), pp. 3621–3628.

[114] Kalina L Tosheva et al. “Between Life and Death: Strategies to Reduce Phototoxicity in Super-Resolution Microscopy”. In: *Journal of Physics D: Applied Physics* 53.16 (2020), p. 163001.

[115] Akihiro Kusumi et al. “Paradigm Shift of the Plasma Membrane Concept from the Two-Dimensional Continuum Fluid to the Partitioned Fluid: High-Speed Single-Molecule Tracking of Membrane Molecules”. In: *Annual Review of Biophysics and Biomolecular Structure* 34.1 (2005), pp. 351–378.

[116] Alex J. B. Kreutzberger et al. “Rhomboid Distorts Lipids to Break the Viscosity-Imposed Speed Limit of Membrane Diffusion”. In: *Science* 363.6426 (2019), eaao0076.

[117] Adam D. Douglass and Ronald D. Vale. “Single-Molecule Microscopy Reveals Plasma Membrane Microdomains Created by Protein-Protein Networks That Exclude or Trap Signaling Molecules in T Cells”. In: *Cell* 121.6 (2005), pp. 937–950.

[118] Taka A. Tsunoyama et al. “Super-Long Single-Molecule Tracking Reveals Dynamic-Anchorage-Induced Integrin Function”. In: *Nature Chemical Biology* 14.5 (2018), pp. 497–506.

[119] Arnauld Sergé et al. “Dynamic Multiple-Target Tracing to Probe Spatiotemporal Cartography of Cell Membranes”. In: *Nature Methods* 5.8 (2008), pp. 687–694.

[120] Kiera B. Wilhelm et al. “Height, but Not Binding Epitope, Affects the Potency of Synthetic TCR Agonists”. In: *Biophysical Journal* 120.18 (2021), pp. 3869–3880.

[121] Catherine B. Carbone et al. “In Vitro Reconstitution of T Cell Receptor-Mediated Segregation of the CD45 Phosphatase”. In: *Proceedings of the National Academy of Sciences* 114.44 (2017), E9338–E9345.

[122] Marie-Lise Jobin et al. “Filamin A Organizes Γ-aminobutyric Acid Type B Receptors at the Plasma Membrane”. In: *Nature Communications* 14.1 (2023), p. 34.

[123] Shalini T Low-Nam et al. “ErbB1 Dimerization Is Promoted by Domain Co-Confinement and Stabilized by Ligand Binding”. In: *Nature Structural & Molecular Biology* 18.11 (2011), pp. 1244–1249.

[124] Stephan Wilmes et al. “Competitive Binding of STATs to Receptor Phospho-Tyr Motifs Accounts for Altered Cytokine Responses”. In: *eLife* 10 (2021), e66014.

[125] Davide Calebiro and Jak Grimes. “G Protein–Coupled Receptor Pharmacology at the Single-Molecule Level”. In: *Annual Review of Pharmacology and Toxicology* 60.1 (2020), pp. 73–87.

[126] Carlo Manzo and Maria F Garcia-Parajo. “A Review of Progress in Single Particle Tracking: From Methods to Biophysical Insights”. In: *Reports on Progress in Physics* 78.12 (2015), p. 124601.

[127] Kenichi Suzuki et al. “Rapid Hop Diffusion of a G-Protein-Coupled Receptor in the Plasma Membrane as Revealed by Single-Molecule Techniques”. In: *Biophysical Journal* 88.5 (2005), pp. 3659–3680.

[128] John C. Crocker and David G. Grier. “Methods of Digital Video Microscopy for Colloidal Studies”. In: *Journal of Colloid and Interface Science* 179.1 (1996), pp. 298–310.

[129] Daniel B. Allan et al. *Soft-Matter/Trackpy: Trackpy v0.5.0*. 2021.

[130] Khuloud Jaqaman et al. “Robust Single-Particle Tracking in Live-Cell Time-Lapse Sequences”. In: *Nature Methods* 5.8 (2008), pp. 695–702.

[131] M Endesfelder et al. “Swift – Fast, Probabilistic Tracking for Dense, Highly Dynamic Single-Molecule Data”. In: (2022).

[132] Michael J. Saxton and Ken Jacobson. “SINGLE-PARTICLE TRACKING:Applications to Membrane Dynamics”. In: *Annual Review of Biophysics and Biomolecular Structure* 26.1 (1997), pp. 373–399.

[133] Yannic Kerkhoff and Stephan Block. “Analysis and Refinement of 2D Single-Particle Tracking Experiments”. In: *Biointerphases* 15.2 (2020), p. 021201.

[134] Laura Weimann et al. “A Quantitative Comparison of Single-Dye Tracking Analysis Tools Using Monte Carlo Simulations”. In: *PLoS ONE* 8.5 (2013), e64287.

[135] Kevin Y. Chen et al. “Trapping or Slowing the Diffusion of T Cell Receptors at Close Contacts Initiates T Cell Signaling”. In: *Proceedings of the National Academy of Sciences* 118.39 (2021), e2024250118.

[136] Kenichi G.N. Suzuki et al. “Dynamic Recruitment of Phospholipase Cγ at Transiently Immobilized GPI-anchored Receptor Clusters Induces IP3–Ca2+ Signaling: Single-Molecule Tracking Study 2”. In: *Journal of Cell Biology* 177.4 (2007), pp. 731–742.

[137] Khuloud Jaqaman et al. “Cytoskeletal Control of CD36 Diffusion Promotes Its Receptor and Signaling Function”. In: *Cell* 146.4 (2011), pp. 593–606.

[138] Johanna V. Rahm et al. “Diffusion State Transitions in Single-Particle Trajectories of MET Receptor Tyrosine Kinase Measured in Live Cells”. In: *Frontiers in Computer Science* 3 (2021), p. 757653.

[139] Inhee Chung et al. “Spatial Control of EGF Receptor Activation by Reversible Dimerization on Living Cells”. In: *Nature* 464.7289 (2010), pp. 783–787.

[140] Carmen L. Krüger et al. “Quantitative Single-Molecule Imaging of TLR4 Reveals Ligand-Specific Receptor Dimerization”. In: *Science Signaling* 10.503 (2017), eaan1308.

[141] Yanqi Yu, Miao Li, and Yan Yu. “Tracking Single Molecules in Biomembranes: Is Seeing Always Believing?” In: *ACS Nano* (2019).

[142] Frédéric Jaskolski, Christophe Mulle, and Olivier J. Manzoni. "An Automated Method to Quantify and Visualize Colocalized Fluorescent Signals". In: *Journal of Neuroscience Methods* 146.1 (2005), pp. 42–49.

[143] Jesus Vega-Lugo et al. "Analysis of Conditional Colocalization Relationships and Hierarchies in Three-Color Microscopy Images". In: *Journal of Cell Biology* 221.7 (2022), e202106129.

[144] Paul D. Dunne et al. "DySCo: Quantitating Associations of Membrane Proteins Using Two-Color Single-Molecule Tracking". In: *Biophysical Journal* 97.4 (2009), pp. L5–L7.

[145] David L. Kolin and Paul W. Wiseman. "Advances in Image Correlation Spectroscopy: Measuring Number Densities, Aggregation States, and Dynamics of Fluorescently Labeled Macromolecules in Cells". In: *Cell Biochemistry and Biophysics* 49.3 (2007), pp. 141–164.

[146] Kenneth W. Dunn, Malgorzata M. Kamocka, and John H. McDonald. "A Practical Guide to Evaluating Colocalization in Biological Microscopy". In: *American Journal of Physiology-Cell Physiology* 300.4 (2011), pp. C723–C742.

[147] Thibault Lagache et al. "Statistical Analysis of Molecule Colocalization in Bioimaging". In: *Cytometry Part A* 87.6 (2015), pp. 568–579.

[148] Ah Ram Kim et al. "Functional Selectivity in Cytokine Signaling Revealed Through a Pathogenic EPO Mutation". In: *Cell* 168.6 (2017), 1053–1064.e15.

[149] Hua Leonhard Tan et al. "Determination of Oligomeric States of Proteins via Dual-Color Colocalization with Single Molecule Localization Microscopy". In: *eLife* 11 (2022), e76631.

[150] Caleb R Glassman et al. "Calibration of Cell-Intrinsic Interleukin-2 Response Thresholds Guides Design of a Regulatory T Cell Biased Agonist". In: *eLife* 10 (2021), e65777.

[151] Joshua D. Larson, Margaret L. Rodgers, and Aaron A. Hoskins. "Visualizing Cellular Machines with Colocalization Single Molecule Microscopy". In: *Chem. Soc. Rev.* 43.4 (2014), pp. 1189–1200.

[152] Hendrik Deschout et al. "Correlation of Dual Colour Single Particle Trajectories for Improved Detection and Analysis of Interactions in Living Cells". In: *International Journal of Molecular Sciences* 14.8 (2013), pp. 16485–16514.

[153] Franziska Fricke, Marina S. Dietz, and Mike Heilemann. “Single-Molecule Methods to Study Membrane Receptor Oligomerization”. In: *ChemPhysChem* 16.4 (2015), pp. 713–721.

[154] Ikuko Koyama-Honda et al. “Fluorescence Imaging for Monitoring the Colocalization of Two Single Molecules in Living Cells”. In: *Biophysical Journal* 88.3 (2005), pp. 2126–2136.

[155] Verena Ruprecht et al. “Measuring Colocalization by Dual Color Single Molecule Imaging”. In: *Advances in Planar Lipid Bilayers and Liposomes*. Vol. 12. Elsevier, 2010, pp. 21–40.

[156] Verena Ruprecht, Mario Brameshuber, and Gerhard J. Schütz. “Two-Color Single Molecule Tracking Combined with Photobleaching for the Detection of Rare Molecular Interactions in Fluid Biomembranes”. In: *Soft Matter* 6.3 (2010), pp. 568–581.

[157] W. Trabesinger et al. “Statistical Analysis of Single-Molecule Colocalization Assays”. In: *Analytical Chemistry* 73.6 (2001), pp. 1100–1105.

[158] Stephan Wilmes et al. “Receptor Dimerization Dynamics as a Regulatory Valve for Plasticity of Type I Interferon Signaling”. In: *Journal of Cell Biology* 209.4 (2015), pp. 579–593.

[159] Alexandra Tsirigotaki et al. “Mechanism of Receptor Assembly via the Pleiotropic Adipokine Leptin”. In: *Nature Structural & Molecular Biology* (2023), pp. 1–13.

[160] G.J. Schütz, W. Trabesinger, and T. Schmidt. “Direct Observation of Ligand Colocalization on Individual Receptor Molecules”. In: *Biophysical Journal* 74.5 (1998), pp. 2223–2226.

[161] Russell E. Thompson, Daniel R. Larson, and Watt W. Webb. “Precise Nanometer Localization Analysis for Individual Fluorescent Probes”. In: *Biophysical Journal* 82.5 (2002), pp. 2775–2783.

[162] Marija Vrljic et al. “Translational Diffusion of Individual Class II MHC Membrane Proteinsin Cells”. In: *Biophysical Journal* 83.5 (2002), pp. 2681–2692.

[163] Friedrich Roder et al. “Rapid Transfer of Transmembrane Proteins for Single Molecule Dimerization Assays in Polymer-Supported Membranes”. In: *ACS Chemical Biology* 9.11 (2014), pp. 2479–2484.

[164] Kenichi G.N. Suzuki et al. “Single-Molecule Imaging of Receptor–Receptor Interactions”. In: *Methods in Cell Biology*. Vol. 117. Elsevier, 2013, pp. 373–390.

[165] Rinshi S. Kasai et al. “Full Characterization of GPCR Monomer–Dimer Dynamic Equilibrium by Single Molecule Imaging”. In: *Journal of Cell Biology* 192.3 (2011), pp. 463–480.

2 The K2: Open-source simultaneous triple-color TIRF microscope for live-cell and single-molecule imaging

C. Niederauer, M. Seynen, J. Zomerdijk, M. Kamp and K. A. Ganzinger

Abstract

Imaging the dynamics and interactions of biomolecules at the single-molecule level in live cells and reconstituted systems has generated unprecedented knowledge about the biomolecular processes underlying many cellular functions. To achieve the speed and sensitivity needed to detect and follow individual molecules, these experiments typically require custom-built microscopes or custom modifications of commercial systems. The costs of such single-molecule microscopes, their technical complexity and the lack of open-source documentation on how to build custom setups therefore limit the accessibility of single-molecule imaging techniques. To advance the adaptation of dynamic single-molecule imaging by a wider community, we present the "K2": an open-source, simultaneous triple-color total internal reflection fluorescence (TIRF) microscope specifically designed for live-cell and single-molecule imaging. We explain our design considerations and provide step-by-step building instructions, parts list and full CAD models. The modular design of this TIRF microscope allows users to customize it to their scientific and financial needs, or to re-use parts of our design to improve the capabilities of their existing setups without necessarily having to build a full copy of the K2 microscope.

The following manuscript is reproduced as published. Supplementary materials are available in the online version of the publication [1].

2.1 Hardware in context

Commercially available fluorescence microscopes for state-of-the-art single-molecule and super-resolution microscopy are often expensive to acquire and lack the flexibility to incorporate custom features beyond already available add-ons. In recent years, a number of open-source projects originated within the super-resolution fluorescence microscopy community, facilitating the design and construction of custom microscopes from the bottom-up [2–8]. Additionally, stand-alone solutions for various sub-components of single-molecule microscopes have been published as open-source hardware projects (e.g. focus stabilization [9–11], laser sources [12–15], objective heaters [16, 17] and beam-shaping devices [13, 18–20]). Our microscope design builds on previous open-source projects and our in-house engineering expertise, to provide a cost-effective and flexible solution for single-molecule fluorescence microscopy.

Here, we present a single-molecule total internal reflection fluorescence (TIRF) microscope that is capable of acquiring dynamic single-molecule data with four-color excitation and simultaneous triple-color detection. The microscope uses a single sCMOS camera and projects the fluorescence emission coming from the sample onto different camera regions for each fluorescence channel. Together with homogeneous illumination from a beamshaping device, this enables simultaneous three-color imaging with large fields of view (73 µm x 73 µm) for each channel. The microscope further features objective heating, a plexiglass cover with an integrated LED array for brightfield illumination, and motorized switching of the angle of the excitation laser beam from TIRF to highly inclined and laminated optical sheet (HILO) and epifluorescence. Finally, the microscope also includes a flip-in lens for fluorescence recovery after photobleaching (FRAP) experiments and a focus stabilization system to correct axial sample drift in timelapse and multi-position measurements.

Documented imaging settings include: laser power, camera exposure time, camera bit-rate, sample stage position, TIR angle stage position, region of interest.

To ensure reliability and reproducibility of experiments, imaging settings are carefully documented for every dataset and saved as *.txt* metadata files. We also monitor and record environmental parameters (temperature, humidity) and axial sample drift when using the focus stabilization system. This allows us to precisely control and replicate our experiments under identical imaging conditions, which is essential for generating comparable and reproducible data with TIRF microscopes [21].

2.2 Hardware description

The K2 single-molecule TIRF microscope is comprised of a central cube with the sample stage, sample holder and objective (see **Fig. 2.1** and panel I in **Fig. 2.2**), as well as two enclosed boxes. The box on the right-hand side of the central cube houses the excitation path optics and the qgFocus parts (see **Fig. 2.1** and panel II and III in **Fig. 2.2**). The box to the left contains the detection pathway, where emitted fluorescence light from the sample is split in up to three spectrally separated channels (see **Fig. 2.1** and panel IV in **Fig. 2.2**). The excitation and detection pathways are enclosed in light-tight aluminum boxes to reduce background light levels, minimize laser safety issues, and prevent dust buildup. The entire setup is mounted on a vibration-damped optical table, with additional components (e.g. commercial multi-laser fiber-coupled source, panel V in **Fig. 2.2**) and the setup control computer located nearby.

Hardware name	K2: Open-source simultaneous triple-color TIRF microscope for live-cell and single-molecule imaging
Subject area	Single-molecule Biophysics, Fluorescence Microscopy
Hardware type	Imaging tool: Total Internal Reflection Fluorescence Microscope
Open-source license	CC-BY-NC-ND 4.0
Cost of hardware	100,000 € (excluding VAT)
Source file repository	Design files and data are available at doi.org/10.5281/zenodo.7380380. A ready-to-view model is available at https://autode.sk/3vdsOu0. Data analysis code is available at github.com/GanzingerLab. Up-to-date information about the setup is available at the K2 TIRF Github page: ganzingerlab.github.io/K2TIRF.

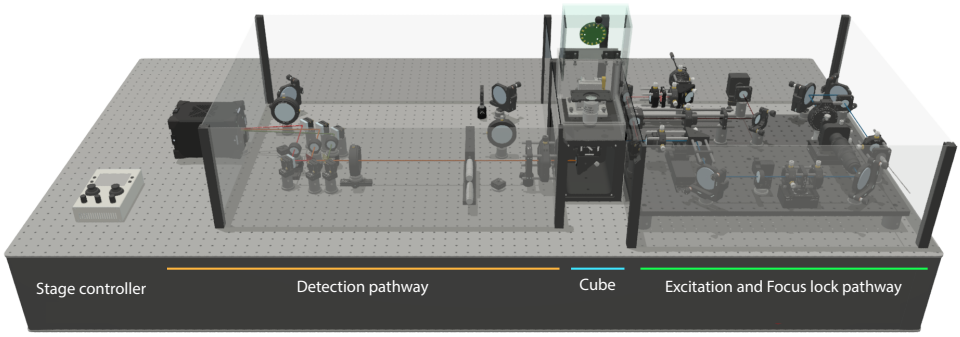

Figure 2.1 • Render of the K2 open-source simultaneous triple-color TIRF microscope for live-cell and single-molecule imaging

For illustration purposes, the two enclosure boxes to the left and right of the central cube are rendered transparent and their lids are removed. The handheld sample stage joystick controller is placed on the optical bench only for illustration purposes and usually located on the computer desk.

Microscope body

The K2 single-molecule TIRF microscope is a custom-designed instrument that does not use a conventional microscope body (see **Fig. 2.3**). The central part is a solid, CNC-milled aluminum block, based on the miCube project [4]. The cube houses the objective, sample stage, dichroic mirror and tube lens. Unlike traditional commercial microscopes, the K2 does not include an objective turret or ocular, as they are not required for our experiments. This design results in a smaller footprint and excellent mechanical stability.

A high numerical aperture oil-immersion objective (NA=1.49, CFI Apochromat TIRF, Nikon) with 60x magnification is mounted on a polyoxymethylene spacer to provide thermal isolation from the cube. A polyimide flexible heater, wrapped around the objective with Kapton foil, and a PT100 temperature sensor glued in place, enable precise temperature control via a proportional-integral-derivative (PID) controller (E5CC, Omron). The temperature data is transferred to the computer via a RS485-to-USB interface. This design is similar to other custom-made and commercial designs [16, 17, 22], and allows for active heating of the sample, which is thermally coupled to the objective via immersion oil. This enables live-cell imaging and in vitro experiments at physiological temperatures.

The sample stage of the K2 single-molecule TIRF microscope is equipped with a three-axis piezo stick-slip positioner (SLS-5252, Smaract) and a

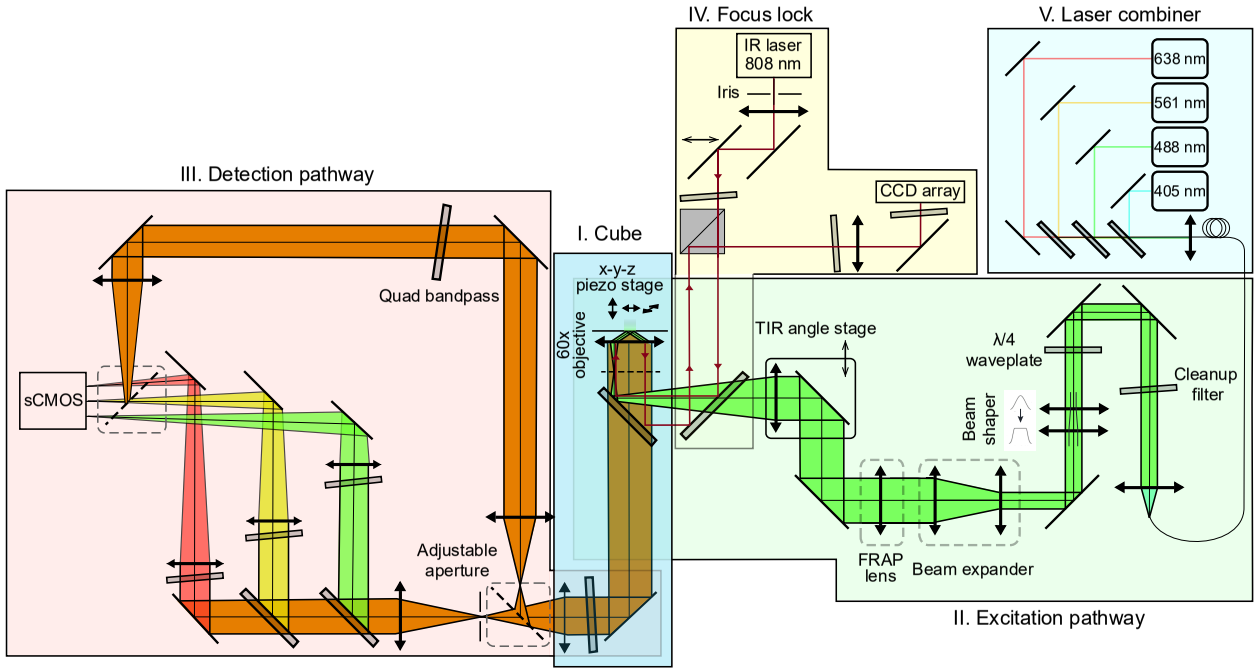

Figure 2.2 • Optical pathway of the K2 microscope

(I) The central cube houses the sample stage, objective, dichroic mirror for splitting excitation and emission light, and the tube lens. **(II)** The excitation pathway launches a four-color laser beam with circular polarization and flat-top beam shape into the central cube. The angle of incidence is controlled using a motorized stage to switch between epifluorescence, HILO- and TIRF-imaging. A flip-in lens can be used to focus the beam at the sample plane for bleaching experiments. **(III)** The detection pathway features a triple-color image splitter, projecting the field-of-view onto different regions of the sCMOS camera chip for simultaneous triple-color imaging. Two mirrors on magnetic mounts can be used to bypass the triple-color image splitter. **(IV)** The focus stabilization pathway uses an infrared laser to detect and compensate for axial drift of the sample. **(V)** A commercial multi-laser fiber-coupled source delivers the excitation laser beam via a single-mode fiber to the setup.

two-piece aluminum sample holder that accommodates square (18 mm to 26 mm side length), circular (25 mm to 37 mm diameter) and rectangular (62 mm to 80 mm length, up to 35 mm width) samples. Samples are held in place with magnets or an aluminum ring to minimize sample drift. The stage is controlled via the computer or a handheld joystick controller (see **Fig. 2.1**) and accurately positions samples with nanometer resolution and 30 mm travel range in all directions, allowing for high-throughput measurements of multi-well coverslides.

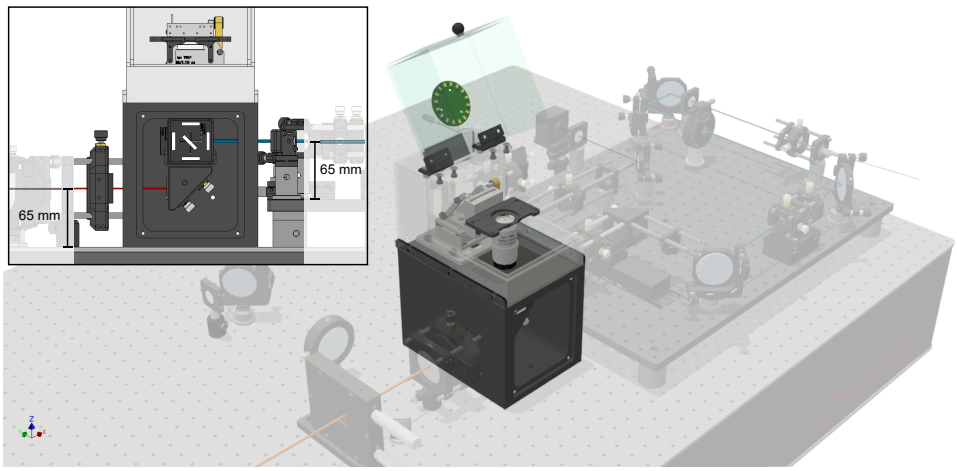

Figure 2.3 • Central cube
Central cube of the K2 microscope, showing the TIRF objective mounted on a thermal spacer, the sample stage with sample holder, and the dichroic mirror for splitting emitted fluorescence from excitation laser light inside the cube. The plexiglass cover encloses the objective and sample for added thermal stability and protection, and also provides a brightfield light source. Inset: The placement of the detection port on the central cube determines a beam height of 65 mm. The beam height of the excitation path is matched by placing the optical elements on an elevated breadboard, allowing the user to interchange alignment tools and pillar posts between the excitation and detection pathways.

The excitation laser beam enters the central cube through a port on the right-hand side and is reflected upwards towards the objective by a dichroic mirror. Residual transmitted laser light is absorbed by a neutral density filter mounted on the dichroic mirror cube. Emitted fluorescence collected by the objective is transmitted through the dichroic mirror and reflected via a mirror towards the exit port on the left-hand side of the cube. A four-bandpass emission filter on the mirror mount blocks remaining laser excitation light from reaching the detection pathway. The dichroic mirror and the right-angle mirror are accessible through a door on the front of the cube, which is held in place with magnets.

The central cube is enclosed by a plexiglass cover that protects the sample and objective from dust buildup and improves temperature stability by minimizing convective air transport. A sensor for temperature and humidity is placed inside the plexiglass box and records the environmental parameters during experiments. The lid of the plexiglass cover includes a LED ring for brightfield imaging of cellular targets. For laser safety considerations, potential adopters of our design may consider using a non-transparent cover.

Excitation pathway

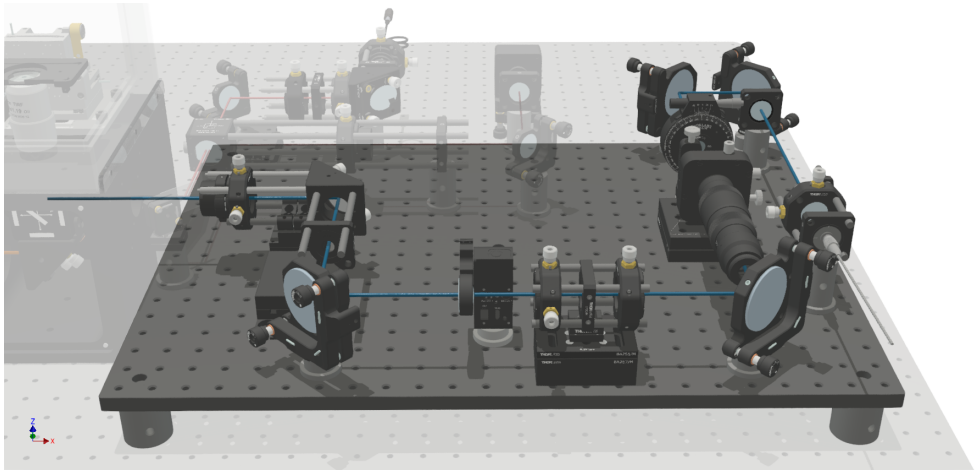

Figure 2.4 • Excitation pathway
Excitation pathway of the TIRF microscope, featuring (in the order of placement along the optical path) the fiber collimator, laser clean-up filter, quarter-wavelength waveplate, refractive beamshaper, beam expander, flip-in FRAP lens and motorized stage with TIR focusing lens. These components work together to shape and deliver the excitation laser beam to the sample stage, enabling precise control of the angle of incidence for different imaging modes (i.e. epifluorescence, HILO, and TIRF). All parts are mounted on an optical breadboard to match the height of the central cube's excitation port.

The excitation pathway is mounted on an elevated breadboard (see **Fig. 2.4**), which helps to keep the length of posts short for stability. Spacers (39.7 mm height) were used to raise the breadboard (12.7 mm thickness) to the required level, resulting in final beam heights of 65 mm in both the excitation pathway and the detection pathway. In principle, the beam can be brought up to the required height also by using long enough posts or a periscope-assembly.

We use a commercial multi-laser fiber-coupled source with a single-mode fiber output for delivering four excitation wavelengths (C-FLEX laser combiner, Hübner Photonics; 405 nm 140 mW, 488 nm 200 mW, 561 nm 220 mW, 638 nm 195 mW) to the excitation pathway. Laser excitation is controlled by a custom-made laser trigger box, that allows alternating and simultaneous excitation synchronized to the camera exposure. Other approaches to laser triggering include the open-source Ries lab laser engine, and the SMILE and NicoLase projects [12, 15, 23], as well as the commercial Triggerscope [24]. For potential adopters looking to replicate the setup in a more budget-friendly manner, using self-assembled solutions for both laser triggering and laser source could reduce costs by an additional 20 percent [12–15].

The TEM00 laser beam is re-collimated after exiting the fiber to a $1/e^2$ beam diameter of 6 mm (@ 561 nm), directed through a quad-line bandpass for spectral clean-up, and an achromatic quarter-wavelength waveplate to ensure circular polarisation. The Gaussian laser beam profile is transformed into a flat-top profile using a refractive beam shaping device (piShaper 6_6_VIS, AdlOptica, comparable alternative: TopShape TSM25-10-D-B-6, asphericon) [18–20]. A (removable) telescope magnifies the laser beam by a factor of 2.5, resulting in a beam diameter of 15 mm. The flat-top profile of the laser beam begins to distort as it propagates over longer distances, so we designed the setup to keep the distance between the beam shaper and the objective as short as possible.

For FRAP experiments, an additional lens on a motorized flip-mount can be inserted into the optical path after the telescope, focusing the excitation laser into a 30 µm diameter spot in the imaging plane.

To enable switching between imaging modes (epifluorescence, HILO- and TIRF-imaging, see **Fig. 2.12d**), the lens focusing the laser beam onto the back focal plane of the objective is mounted on a motorized stage that allows the beam to be translated off-axis while maintaining its parallel alignment with the objective's optical axis.

The lens that focuses the excitation beam onto the back focal plane of the objective is placed as close to the back focal plane as possible, which allows using a lens with a shorter focal length and therefore a bigger illuminated area at the sample plane. Using a telescope with a higher magnification to achieve an equally-sized illuminated area would result in clipping the laser beam, unless larger optics are used throughout the excitation path. To provide more flexibility in the arrangement of the optical elements, future versions of the central cube could be designed with a reduced distance between the objective port and excitation entry port. With the current design, our setup allows for a maximum homogeneously illuminated diameter of 190 µm.

Detection pathway

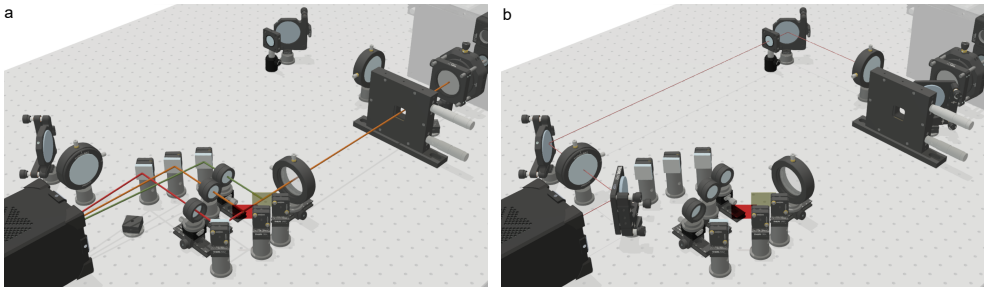

Figure 2.5 • Detection pathway options
Left: triple-color detection pathway with adjustable slit aperture and image splitter for simultaneous imaging of up to three color channels. **Right:** single-color full field-of-view path.

The detection pathway is designed under the assumption that the microscope will mostly be used in a triple-color simultaneous imaging mode (see **Fig. 2.5**). Using a single camera to capture three color channels simultaneously is more cost-effective than using three separate cameras, and combining a 60x objective without additional magnification with a 2048x2048 px sCMOS chip allows us to achieve large field-of-views (73.65 µm x 73.65 µm per color channel) nevertheless. To achieve even larger field-of-views, the triple-color detection pathway can be bypassed by placing two mirrors on pre-installed magnetic mounts, resulting in a circular field of view of 190 µm diameter. A commercial alternative for image splitting is the OptoSplit (Cairn Research [25]).

As described in the section about the central cube, fluorescence emission from the sample is collected by the objective, passes the quad-bandpass dichroic mirror in the cube and is reflected towards the detection pathway. A quad-line filter blocks residual excitation light from reaching the detection pathway. Emission fluorescence is directed through an infinity-corrected tube lens matching the objective, without further magnification (TTL200-A, Thorlabs). With the camera's physical pixel size of 6.5 µm, this results in an effective pixel size of $6.5\,\mu m/60 = 108.3\,nm$.

In the triple-color imaging mode, the image of the fluorescent sample is cropped horizontally by a custom razorblade slit aperture in an intermediate image plane. This is necessary to avoid overlapping of the color channels when imaging them side-by-side on the camera chip (see **??**). Splitting the fluorescence emission into three spectral channels and filtering them is done in infinity space in a 4f-configuration. This reduces aberrations and allows more mechanical freedom, since the distance of

the second to the first 4f-lens is not critical.

The first 4f-lens is positioned to have its focal plane aligned with the image plane formed by the tube lens. Then, the fluorescence emission is split into three colors by two low-pass dichroic mirrors, matched to the four-bandpass dichroic mirror in the cube, and one dielectric mirror. Furthermore, appropriate bandpass filters are placed in each color channel. Individual lenses mounted on rails and dovetail stages project the images of each color channel next to each other on the camera. The use of individual lenses allows precise co-alignment of the image planes and the correction of residual chromatic aberrations. A dielectric mirror is used in each color channel to project the spectrally-separated images onto the camera chip. Finally, three equally-sized square field-of-views are created by cropping the camera chip horizontally. By cropping in line with the scanning of the sCMOS chip, we are able to reduce the read-out time from 22.6 ms (full chip, 2048x2048) to 7.6 ms (central region, 2048x682). At a typical framerate of 25 fps, this approximately doubles the exposure time per frame (32.4 ms/17.1 ms $\approx$ 1.89).

The optical path for the image splitter was designed to be as compact as possible to minimize vignetting, while at the same time allowing component accessibility for alignment. Additionally, projecting the image onto the camera at an angle introduces aberrations, therefore the individual focusing lenses and the mirrors are placed as close to each other as possible. As a consequence, this maximizes the distance between the last mirror and the camera and hence decreases the angles at which images are projected from the left and right color channel.

In the single-color imaging mode, the full 190 µm diameter illuminated field-of-view is imaged with spatially unseparated color channels. This is accomplished by bypassing the slit aperture and the image splitting pathway using two mirrors, that are placed manually on magnetic mounts. The first mirror is placed after the tube lens and the second mirror before the camera. Two lenses relay the image in a 4f-system, which conveniently also allows the placement of additional components like filters or phase masks in the fourier plane (see **Fig. 2.5**, **??**).

Focus stabilization pathway

In microscopy in general, but specifically in super-resolution and time-lapse experiments, sample drift can significantly degrade the quality of the data [26]. In live-cell and single-molecule tracking, lateral sample drift usually does not interfere with the experiments as the typical drifting appears on much slower timescales than the molecular movement in

the sample (lateral sample drift in our setup: $\approx 1\,\mathrm{nm\,min^{-1}}$, diffusion of individual membrane receptors in cells: ≈ 0.1 to $1\,\mu\mathrm{m^2\,s^{-1}}$) [27–30].

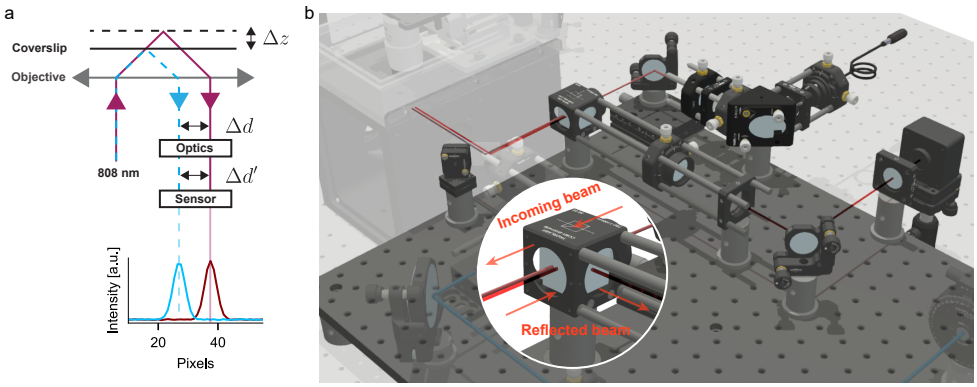

Figure 2.6 • qgFocus focus stabilization
(a) Schematic of the qgFocus focus stabilization system: an infrared laser beam is focused off-center at the back focal plane of the objective and is totally internally reflected at a coverslip. Upon an axial movement Δz of the coverslip, the reflection of the beam is shifted laterally by a distance Δd, which is translated into a distance $\Delta d'$ through downstream optics. A sensor registers the intensity profile of the back reflected beam and determines its center by a Gaussian fit. A control loop acting on the sample stage moves the sample such that the displacement of the currently measured intensity profile and of the referenced intensity profile is approaching zero. **(b)** Render of the focus stabilization pathway of the K2 TIRF, mounted alongside the excitation optics on an elevated breadboard. Inset: Separation of incoming infrared laser beam and back-reflected beam by a beamsplitter cube.

Movement of the sample along the optical axis (axial drift), however, leads to a shift of the focal plane. Since in TIRF microscopy, fluorescence is only emitted from a thin layer close to the coverslip, this shift leads to a decreased signal-to-background ratio due to the defocus blurring of the point spread function, or even the loss of the object that the user initially focused on. Therefore, keeping the sample in focus is crucial, especially when performing hour-long measurements and time-lapses, or repeated acquisitions on different areas on a sample.

One way to measure and control the distance of the sample from the objective is to use the back-reflection of the excitation laser, with the drawback that measuring and updating the z-position can only be done during the excitation cycle [9]. A dedicated infrared laser is a more versatile option, as it does not excite commonly used fluorescent proteins and dyes, allowing for continuous measurement and control of the sample's axial position without interfering with fluorescence measurements.

The principle of the focus stabilization is depicted in **Fig. 2.6a**. First, the sample is brought into focus manually and the position of the back-reflected beam is stored. Axial drift Δz of the sample leads to a lateral displacement Δd of the totally internally reflected infrared laser beam. The back-reflected laser beam is relayed through additional optics, resulting in a displacement $\Delta d'$, that is determined by comparing the center peaks of the previously saved reference and the currently measured laser profiles on a line-array sensor. To mechanically compensate for the axial drift, an active control mechanism reacts to the lateral displacement and moves the sample stage to keep the position of the back-reflected beam stable.

Our focus stabilization implementation (see **Fig. 2.6b**), qgFocus (short for **q**uite **g**ood Focus), is similar to other custom-built and commercial designs such as pgFocus [11] or CRISP [10]: A collimated infrared laser is coupled into the excitation path by a short pass dichroic mirror and attenuated with a neutral density filter so that it does not interfere with the fluorescence signals. A manual micrometer stage is used to shift the infrared laser beam off-axis, bringing it into total internal reflection. The infrared laser is then focused at the back focal plane, reflected at the glass-sample interface, and travels back towards a beamsplitter. The back-reflected laser beam is diverted by the beamsplitter towards a bandpass filter and finally focused onto a linescan sensor (TSL1401, Parallax). The signal is read-out and time-averaged internally, before it is sent to the computer (the update rate is adjustable, typically used rates are 10-30 Hz). A Gaussian function is fit to the intensity curve, and a control loop that locks onto the saved in-focus position of the Gaussian function center then moves the piezo-driven sample stage in the axial direction to maintain focus. In our system, manual sample travel in x-y during focus-controlled experiments is limited to $100\,\mu m\,s^{-1}$ to avoid jumps in the back-reflected beam position that cannot be followed by the control loop.

Scripts

Our microscope control software includes a script interface that allows users to control the setup and perform various tasks using C# commands. Examples of scripts that can be run using the interface are available at github.com/GanzingerLab/K2TIRF/tree/master/K2TIRF/scripts. The available examples include a simple x-y raster scanning script, a laser power calibration method that we used to calibrate the laser percentage settings (see **??**) and a script that continuously moves the sample stage up and down, which we used during the alignment process (see **??** and **??**).

2.3 Design files

A complete CAD assembly of the setup with all optical components has been uploaded to a public repository (doi.org/10.5281/zenodo.7380380). Please note that while we tried to reproduce the physical positions and distances of the optical components as faithfully as possible, this CAD model mainly serves illustration purposes and should not be used as an alignment guide.
For all custom-made mechanical components, CAD files and technical drawings are provided, following best practices for sharing reproducible microscope hardware [31]. For all custom-made electronic components, PCB layouts and electronic design files are provided. A ready-to-view CAD model is uploaded to Autodesk Drive (autode.sk/3vdsOu0). The source code of the software for the operation of the setup is uploaded to the Zenodo repository. Python code for processing and analyzing single-molecule imaging data is available at the Ganzinger group Github (github.com/GanzingerLab).

2.4 Bill of materials

The up-to-date bill of materials for the K2 TIRF project is available on the open-access Github page, providing detailed information on the components and materials needed to build the microscope:
ganzingerlab.github.io/K2TIRF/K2TIRF/component_table.html

2.5 Build instructions

For an overview of the layout of the optical components, see **Fig. 2.1** (CAD-model render), **Fig. 2.2** (schematic of the optical pathway) and **Fig. 2.7** (picture of the setup). The setup requires approximately 190 cm by 90 cm of optical bench space, as well as a similar area (e.g. above the optical bench) for the laser combiner, objective heating PID controller and laser trigger box, as well as space for the computer and screens.

When setting up the microscope, the most convenient approach is to start with building and aligning the excitation pathway and use the laser source for alignment. However, if this step needs to be deferred and another laser source is available (e.g. the Gustafsson alignment tool), it is possible to begin with the central cube and the detection pathway, since the excitation and detection pathways can largely be assembled

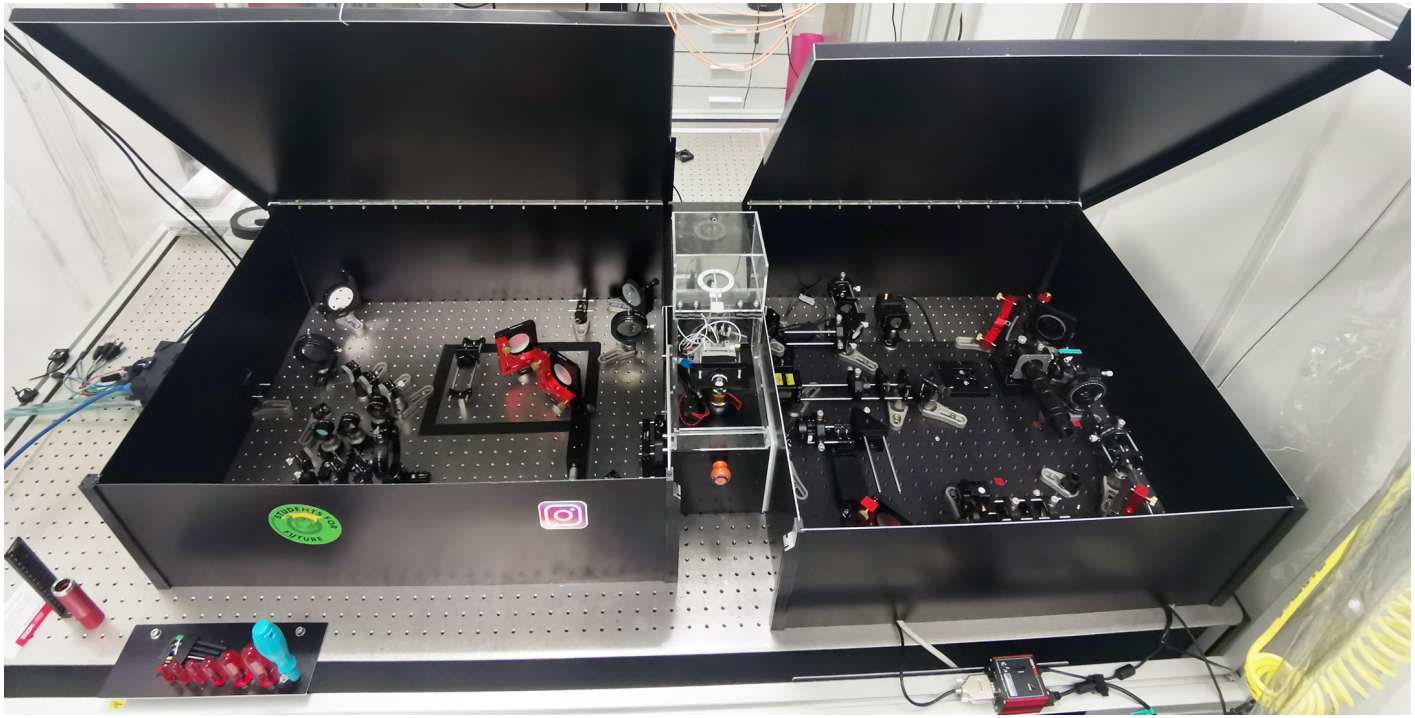

Figure 2.7 • Picture of the K2 TIRF microscope
From right to left, there are the excitation and focus stabilization pathways on an elevated breadboard, the central cube with the objective, sample stage and a plexiglass cover, and the triple- and single-color detection pathways with the camera on the left. The excitation and detection pathways are enclosed in light-tight aluminium boxes to reduce background light levels, minimize laser safety issues, and to prevent dust from building up.

and aligned independently of each other. In addition to commonly used alignment tools such as viewing disks, reticles, irises, and calibration slides, we use a cage system mounted on the objective port to simplify the alignment of the excitation path, and the Gustafsson alignment tool for the detection path alignment [32]. The Gustafsson alignment tool is a small diode laser aligned in a mount that is screwed into the objective thread. The wavelength should be situated within one of the fluorescence emission bands, e.g. in the GFP-like emission band between 500 nm and 550 nm. This allows the alignment laser to pass through the emission dichroic mirror, and, if alignment is performed in the correct order, the laser beam can be used to align the entire detection pathway. General approaches and recommendations for the alignment of optical parts are described in [33].

Detailed, step-by-step build instructions are provided in the supplementary information [1].

2.6 Operation instructions

To ensure optimal performance and data quality of the setup, it is important to verify the multicolor-channel alignment of the microscope regularly and update the correction map, as described in **Fig. 2.11**. Furthermore, drift in the alignment of the excitation path can be checked by confirming the stage positions at which the laser beam is in epifluorescence and entering the TIRF regimen. Additionally, it is essential to check the laser powers with a power meter to ensure they are within the specified range. Dust specks on optical surfaces can interfere with imaging, therefore it is recommended to carefully remove dust specks using oil-free air or nitrogen gas on the particular element. Any spilled immersion oil should immediately be removed with lint-free wipes and the contaminated surfaces cleaned with Ethanol. By following these guidelines, the microscope can be kept in optimal working condition, resulting in reliable and high-quality data.

K2 software

A software package for operating the setup was written in C#. It features a graphical user interface (GUI) that provides a simple and intuitive way to control and customize the microscope setup for different experiments. The GUI includes a number of panels for changing settings and directly controlling the various components of the microscope, such as the camera, stage, lasers, and qgFocus. **Fig. 2.8** and **Fig. 2.9** show some of the

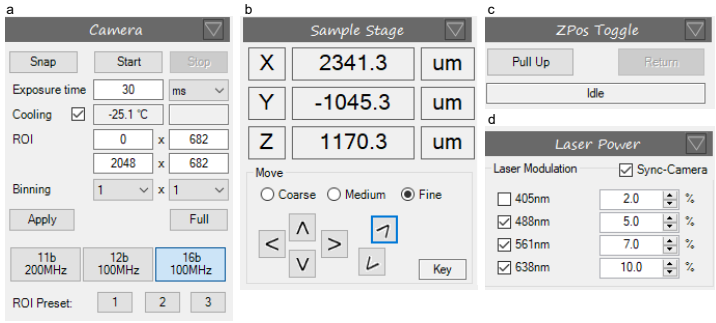

Figure 2.8 • Main control panels of the K2 software
(a) Camera: In this panel, the exposure time, manual/preset regions of interest (*ROI*), binning and bit-depth of the camera are configured, as well as live-viewing of the camera image (Start/Stop) and snapping a single frame (Snap). **(b)** Sample Stage: Piezo stage position readings, and arrow keys (operated via cursor click or with arrow keys on keyboard), complementary to the physical joystick, with three user-defined step sizes. **(c)** Zpos Toggle: Toggle for pulling up the sample away from the objective, and returning the sample to the initial z position (*Pull Up*, *Return*). **(d)** Laser powers: Laser power settings used during camera live-view, calibrated to achieve a linear percent-to-power relation. The synchronization of the lasers to the camera trigger can be switched off.

most important panels for controlling these components. The software also allows users to save experiment routines as templates, with a wide range of custom settings and options.

The source code has been uploaded to the public repository Zenodo (doi.org/10.5281/zenodo.7380380), excluding any third party software and internal libraries which are shared among other projects in the institute. Thus, this release will not compile into the final product but it can serve as an inspiration for other development efforts. For all commercial components (stage, camera, lasers, flip-in lens, TIR angle stage) LabView virtual instruments, python libraries, and/or micromanager plugins [34] exist and can be used alternatively for the setup control.

In the following, the operation of the setup is described using the K2 software.

Camera

The camera panel (**Fig. 2.8a**) provides access to all relevant camera settings, such as the exposure time, region of interest, pixel binning, and bit-depth. The Start/Stop buttons can be used to activate or stop the camera live-view streaming, and the Snap button takes a single frame snapshot.

Live-view and RGB viewing mode

The camera image is streamed in the live-view mode, allowing the user to position the sample and to search for a suitable region of interest, as well as to determine appropriate imaging conditions, such as laser power and exposure time. The contrast and colormap settings of the streamed image are set by the user (**??**). The K2 software also features a RGB viewing mode, that superpositions the triple-color separated camera channels as a red-green-blue overlay in the live-view (**??**). This allows to quickly assess colocalization in different channels and therefore speeds up screening for an interesting cell or region of interest on the sample, and is a convenient tool during the alignment of the triple-color image splitter (see **??**).

Sample stage

The piezo stick-slip stage is steered both with the software (**Fig. 2.8b**); either by clicking on the sample stage panel arrows, or using arrow keys on the keyboard) and by a handheld joystick controller. To ensure safe and efficient sample handling, the user can adjust the step sizes *Coarse*, *Medium* and *Fine* and define position limits (**??**).

A z-position toggle is available that improves the experimental workflow and reduces the amount of immersion oil needed for high-throughput measurements (**Fig. 2.8c**). It works by moving the sample upwards away from the objective, with x and y positions unchanged. The sample is first moved slowly (at 0.8 mm s^{-1} for 3 mm), to avoid introducing air bubbles into the immersion oil and to give the fluid time to draw back to the objective (see **??**). The sample can then be exchanged or moved horizontally, and returns to the previous z-position, again approaching the last millimeters towards the objective slowly. This considerably improves the handling when several samples are imaged and need to be exchanged often. When using multi-well samples, or when imaging many different regions on a single sample, the z-position toggle is used for removing the sample from the immersion oil, repositioning in x-y, and moving it

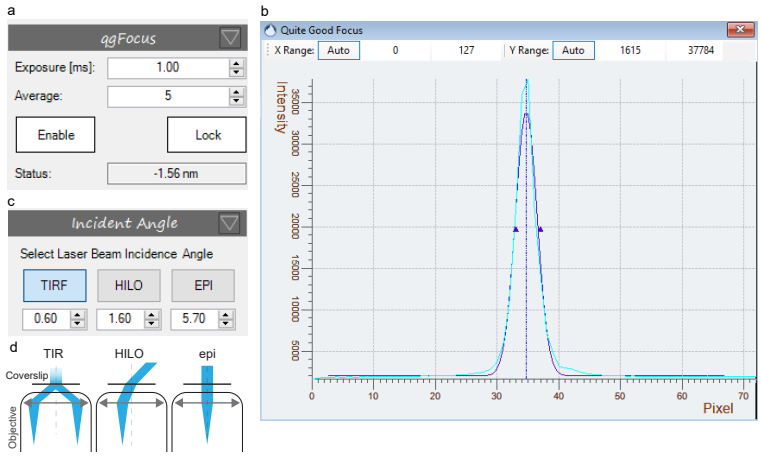

Figure 2.9 • qgFocus and TIR angle software panels
a) qgFocus control panel to switch on the focus stabilization sensor (*Enable*), to engage the focus stabilization (*Lock*) and to set the exposure time and number of averaging cycles. The *Status* reports on the current distance of the stage with respect to its initial z-position. **b**) qgFocus sensor output displaying the measured back-reflected laser intensity profile on qgFocus sensor (cyan line) and a Gaussian fit to the intensity profile (blue line). **c-d**) TIR stage panel: Stage positions for TIRF, HILO and epifluorescence imaging are set and can be called during the experiment to change the angle of incidence of the excitation laser beam.

back to the original z-position (see **??**). This reduces the amount of immersion oil that has to be reapplied and thus allows for high-throughput measurements with minimal user interaction. The exact values for the distance and speed limits are user-defined in the K2 software backend settings (**??**).

Laser powers

The laser powers panel controls laser on/off state and excitation power, and features the option to deselect synchronization of the excitation to the camera exposure (**Fig. 2.8**d). A linear relation between the power percentage set by the user and the actually delivered laser power is established in an initial calibration step (see **??**).

qgFocus

In the qgFocus panel, the focus stabilization sensor's exposure time and number of averaging cycles are set (**Fig. 2.9**). Within an axial range of about 5 µm around the samples' in-focus position, the back-reflected infrared laser is registered as a sharp peak on the qgFocus sensor and fit with a Gaussian function. For keeping the focus position stable, the center position of the Gaussian fit is saved and used as the setpoint for a control loop.

During the initial usage of the setup, determine the control loop variables to ensure that the focus position stabilizes within a few seconds after moving the sample in x-y (used values: proportional gain 0.7, integral time 2 s, integral limit 1×10^{10} s).

Once the qgFocus is engaged, the qgFocus panel displays the extent to which the stage has been shifted to maintain the sample in focus. The sample stage movement is restricted to a speed of 100 µm s^{-1} to allow the qgFocus to follow the sample's z-position continuously. This speed limit can be defined by the user in the K2 software backend settings (**??**).

Angle of incidence

The motorized TIR stage sets the angle of incidence of the excitation laser beam, allowing the user to switch between epifluorescence, HILO and TIRF imaging modes by calling user-defined positions on the Angle of Incidence panel (see **Fig. 2.9**).

When operating the setup the first time, the TIR stage positions corresponding to the different imaging modes are determined with a fluorescent sample (e.g. dye in solution) mounted: Starting from the epifluorescence position after setup alignment, the TIR stage is initially moved 4.5 mm, and then in steps of 0.1 mm. The transition from epifluorescence to TIRF imaging is easy to recognize (see [35] for a detailed description), as interference patterns caused by specs of dust scattering the coherent excitation laser beam, become visible. In sparse single-molecule type of samples, these interference patterns are not visible, but the transition is marked by a sharp increase in the signal-to-background ratio [6]. HILO imaging, where the laser beam penetrates the sample at an angle instead of being totally internally reflected, is typically performed close to the TIR setting (i.e. between 4 mm to 5 mm from the epifluorescence position).

Pre-configuring experiments

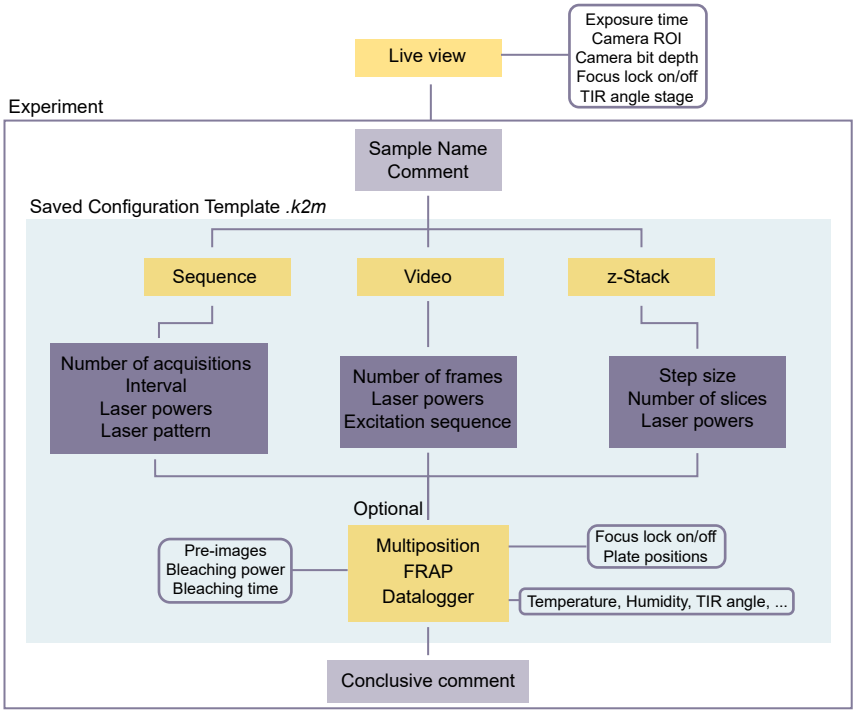

Figure 2.10 • Experiments configuration diagram
Experimental settings are optimized during live-view. An acquisition is then performed by configuring, or reusing a experiment configuration template and adding details about the sample and experimental conditions. For the acquisition itself, three options (*Sequence*, *Video* and *z-Stack*) are available and for each option, the necessary settings are configured. Optionally, the experiment can be performed at different sample positions (*Tiled acquisition*), as a *FRAP* experiment, and with additional recording of environmental parameters. After the experiment is performed, a comment may be added to the file.

Imaging conditions and sequences may be pre-configured as saveable experiment configuration file (**.k2m*) and can be reused as templates. The user can choose from three general modes: a) Sequence acquisitions, where a pre-programmed laser excitation sequence is looped through every timepoint - for a user-defined number of times, allowing for both alternating laser excitation style experiments and simple timelapses. b) Video acquisitions at the maximum camera framerate, with one or several lasers simultaneously activated. c) z-stacks, where images are taken at pre-defined axial positions, with one or several lasers switched on.

Each of these modes can be combined with a FRAP experiment at the beginning of the recording, or a tiled acquisition. During a tiled acquisition, the software performs the pre-configured acquisition at different, pre-defined stage positions.

The experiment configuration, sample name and optional comments are saved as a **.txt* file along with the microscopy data (**.raw* and **.yaml*.)

Sequence acquisition

For certain experiments (e.g. FRET), fluorophores need to be (alternatingly) excited by a single excitation wavelength at a time. This can be done by performing a Sequence Acquisition (see **??**). Any excitation sequence, with one or several lasers excited during a given camera frame, can be pre-programmed, and is looped through for every timepoint throughout the duration of the experiment. The interval between each timepoint can be set, which also allows for timelapse recordings (see **??**).

Video acquisition

The video acquisition mode allows the simultaneous imaging of multiple color channels, e.g. for multi-color single-molecule tracking experiments, at the maximum camera framerate without intervals between acquired frames. For every frame, the same pre-defined set of lasers at a certain power percentage will be used to excite the sample (see **??**). Additionally, there is the option to use in-frame alternating laser excitation. For simultaneous imaging of blue excitable dyes (e.g. ATTO488) and cyanine dyes (e.g. ATTO643), this was demonstrated to decrease the bleaching of red dyes induced by the 488 nm laser drastically [36]. The duration of the pulses is set to be at least ten times smaller than the total frame exposure time, and the triggering scheme is such that the 488 nm laser is pulsing anti-cyclic with respect to the others (see **??**).

zStack

Although TIRF microscopy implies collecting fluorescence from the sample surface plane, most TIRF setups allow changing the angle of incidence to HILO or epifluorescence imaging. In these imaging modes, a z-stack can deliver additional information along the axial dimension. The K2 software requires a starting z-position, the number of slices and z-step per slice and will record one frame per slice with a given laser

power and exposure time. During the acquisition, the focus stabilization is disengaged and the sample is moved back to the original z-position after the last slice.

FRAP

Fluorescence recovery after photobleaching (FRAP) is a method for studying diffusion dynamics by bleaching the sample locally and observing the recovery of fluorescence by diffusive exchange of unbleached fluorophores into the bleached area. A FRAP experiment in the K2 setup is performed by collecting a number of pre-bleaching frames (either in Sequence- or Video-mode), followed by a bleaching phase where the flip-in lens is flipped into the excitation path, the power of one or several lasers is increased. After the bleaching phase, the recovery is recorded using the Sequence- or Video-mode (see **??**). Between bleaching and the recovery phase, a short delay is introduced to account for the finite flipping time of the flip-in lens (flip-in: 0.5 s, flip-out: 1 s). The area and the position of the bleached spot is determined by the positioning and focal length of the flip-in lens.

Tiled acquisition

Coordinates (x,y and z) of stage positions can be generated (e.g. for a raster scanning of the sample, see **??**), saved in a list and called manually, or automated during an experiment where a pre-designed (sequence, video, and/or FRAP) acquisition is performed at each position of the coordinate list (see **??**). If the focus stabilization is engaged, the stored z-position is ignored.

Starting up the setup

Before turning on the lasers, verify that any removable optical component (beamshaper, beam expander, mirrors for bypassing the triple-color pathway) and filters are placed correctly depending on the experimental requirements. Make sure that the flip-in lens is flipped out, the TIR stage is in a safe position, the objective correction collar is in the correct position, and that the objective was cleaned properly by the last user. If heating is required, make sure to turn it on about 30 min before the experiment, to allow the temperature to stabilize (see **Fig. 2.15**).

Switch on the required power supplies (lasers, camera, camera cooling, motorized stages and mounts, computer) and mount the sample. Open the setup control software and initialize the motorized stages. Switch on the appropriate lasers at a low power and start the qgFocus and the live-view of the camera. Bring the sample into focus using the sample stage joystick controller. As described before, during the initial operation, the qgFocus control loop settings and the TIR stage positions for epifluorescence, HILO and TIRF imaging should be determined to ensure optimal imaging performance.

2.7 Validation and characterization

Multicolor channel alignment

Chromatic dispersion and misalignment of optical elements in the detection pathway lead to distortions across the different color channels, complicating the analysis and interpretation of multicolor microscopy data. Especially for (single-molecule) colocalization experiments, different color channels need to be precisely co-aligned. The physical alignment of the color-splitting optical path is done while imaging a calibration slide and superimposing the three color channels, as described in the supplementary build instructions (see **??**). In doing so, we achieve an average spatial variation across different color channels below 1 µm. The remaining spatial offset between the channels is then corrected computationally: first, accumulated bead positions from raster scanning the calibration slide are assigned throughout the corresponding channels (see **Fig. 2.11a-b**). A spatial correction map is then calculated (**Fig. 2.11c**) using a recently introduced method based on Zernike polynomial gradients [37]. Using this correction map, mean residual spatial variations are below 30 nm (**Fig. 2.11c-d**).

Sample drift and focus stabilization

Minimizing sample drift is crucial in (TIRF) microscopy to ensure optimal signal-to-background ratios and the reproducibility of measurements. Therefore, we evaluated the axial and lateral drift of our K2 TIRF microscope, with and without the focus stabilization, during a three hour experiment. Fluorescent beads (TetraSpeck Microspheres, 0.2 µm) mounted on the surface of a microscope slide were used as fiducials. The axial drift during experiments without focus stabilization (**Fig. 2.12a**) is observable as a slight blurring of the beads, which is not the case for

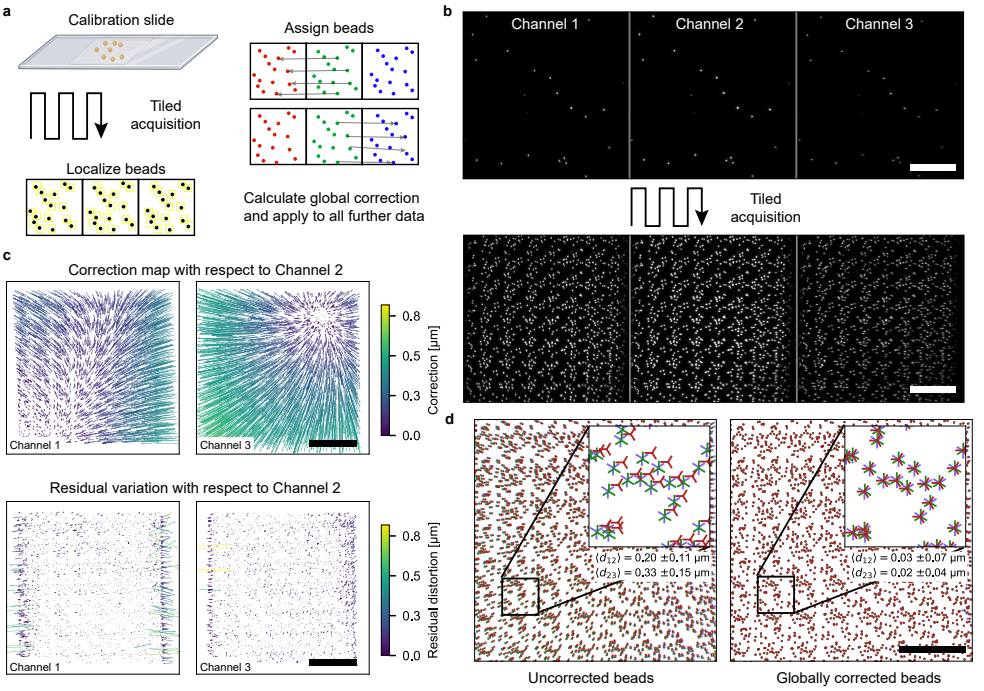

Figure 2.11 • Multicolor channel alignment

a) Multicolor-labeled Tetraspeck beads are deposited sparsely on a coverslide and imaged at multiple positions to collect a large number of $x-y$ sample points. Identical beads are identified in the three color channels and localized frame-by-frame. Variations of bead $x-y$ coordinates relative to the center channel are calculated pairwise, and used to compute a global correction map. This correction map is then used to correct single-molecule localizations acquired in further experiments. **b)** Top row: Image of Tetraspeck beads in the three color channels, for a given sample position. Lower row: Maximum projection of all bead images acquired during a tile raster-scan. **c)** Top row: Correction maps of left and right channel, with respect to the middle channel. Lower row: Residual spatial variation remaining after the correction is applied to the calibration data. Arrows indicate the direction of the necessary correction, with their length and color representing the amount of correction needed. **d)** Superimposed $x-y$ positions of Tetraspeck beads with uncorrected coordinates (left) and corrected coordinates (right), with average spatial variations $\langle d_{12} \rangle$ and $\langle d_{23} \rangle$ of identical beads in the left and right channel, with respect to the middle channel. Scale bars are 20 µm.

experiments with enabled focus stabilization. The axial sample drift was quantified by converting the lateral displacement of the back-reflected laser on the sensor into an axial distance. The displacement-to-pixel was determined in an initial calibration experiment (**??**, 1 px $\hat{=}$ 561 nm). **Fig. 2.12b** shows the axial drift throughout the three hour experiment exceeded 400 nm without focus stabilization, whereas virtually no residual drift was detectable when the focus stabilization was enabled (mean and standard deviation of the displacement from the in-focus position: –1.74 ± 2.41 nm).

Lateral drift was quantified by tracking the fiducial beads and calculating their euclidean distance from their original position at the start of the experiment. We found the lateral drift to be similar with and without focus stabilization enabled, which is expected since the focus stabilization only compensates the axial drift. In comparison to other setups [38–40], the lateral drift is extremely low ($\approx$ 200 nm in three hours), which is likely due to using a closed-loop piezo stage not only for the z-axis, but also for x- and y-axes. Most commercial and home-built setups use servomotors for the x- and y-axes, with at least one order of magnitude worse resolution and stability [38, 41, 42].

Field-of-view and illumination homogeneity

One of the key features of the K2 TIRF microscope is its large field-of-view that is flat and homogeneously illuminated, which facilitates conducting statistically sound and quantitative single-molecule fluorescence experiments. Using a refractive beamshaper and appropriate optics, we are able to evenly illuminate a large field of view up to 190 µm in diameter, providing a high signal-to-background ratio across the entire field of view. This is especially important for dynamic live-cell or single-molecule tracking experiments (e.g. cellular activation essays, kinetic studies of molecular interactions), because events may be non-recurrent and capturing as much data from a single field of view as possible with little to no spatial variation in imaging quality is essential (**Fig. 2.13**).

In addition, the large 2048 x 2048 px camera chip allows the imaging up to three color channels simultaneously side-by-side without the need to invest in multiple, synchronized cameras. Simultaneous capture of multi-color emission is important for accurately tracking fast dynamic processes of multiple species of fluorescently labeled molecules in cellular and artificial environments. For triple-color simultaneous imaging, the camera is cropped to produce three equal-sized fields of view of 682 x 682 pixels, or 73.656 µm x 73.656 µm (see **Fig. 2.13**).

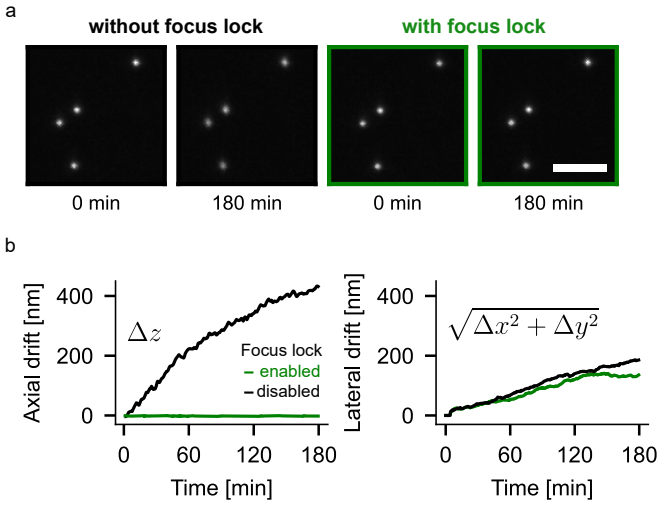

Figure 2.12 • Characterization of sample drift and focus stabilization

a) Still frames of a sample of fluorescent beads, imaged with and without qgFocus. For the experiment without focus stabilization, there is a slight blurring of beads observable over time, whereas the beads with the focus stabilization enabled stay in focus throughout the entire three hours experiment. For both experiments, the same sample was used, but before each acquisition, the sample was withdrawn from the immersion oil and re-positioned, to avoid biases due to non-identical settling times of the mounted sample. One frame was captured every 30 s for three hours. Scale bar is 5 µm. **b**) Representative axial and lateral sample drift during a three hour experiment with and without enabled focus stabilization. Left: Axial drift, right: lateral drift of tracked beads, given by the euclidean distance of their current position versus their position in the first frame.

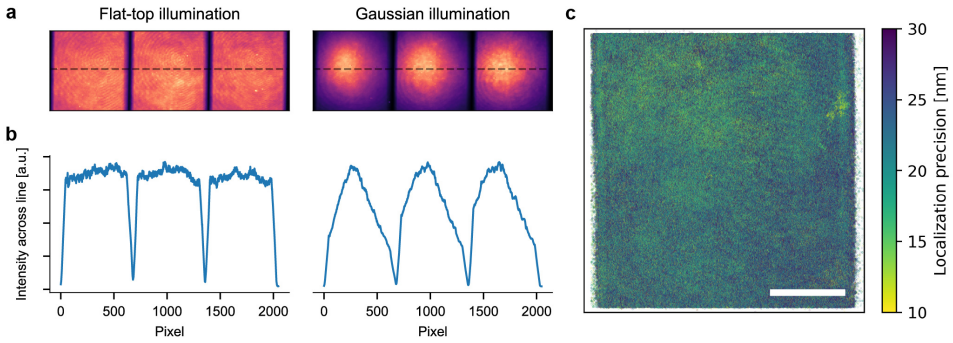

Figure 2.13 • Field-of-view and illumination homogeneity
Triple-color TIRF imaging of a multicolor fluorescently labeled bilayer, excited by a spatially homogeneous excitation field (**a**) versus a Gaussian beam (**b**). Laser intensities were adjusted for each color channel to produce similar peak intensities. Fields of view per color channel are 682x682 pixels, or 73.656 µm x 73.656 µm. **c)** Localization precision map computed from a total of 3,300,599 individual localizations of freely diffusing Cy3B-labeled reconstituted proteins on a supported lipid bilayer. The homogeneous excitation field allows precise localization of single-molecules across the entire field-of-view. Scale bar is 20 µm.

Furthermore, the homogeneous illumination of the field of view of the K2 microscope not only provides a high signal-to-background ratio across the entire field of view, but also enables seamless stitching of images acquired by raster-scanning the sample. This is because the lack of vignetting at the edges of the field of view allows the individual images to be easily combined into a single, large image without loss of quality (see **??**, 250 µm x 250 µm field of view). Furthermore, the focus stabilization system is able to compensate for coverslip tilt and inhomogeneities that can degrade the image quality during raster-scanning. This allows fully automated raster-scanned acquisitions without the need for manual intervention to maintain focus (see **??**).

2.7.1 Localization-based super-resolution performance

The performance of our setup in localization-based super-resolution microscopy was evaluated by imaging a commercially available DNA origami nanoruler sample (Gattaquant 2x 40 nm distance, 1 μm^{-2} surface density). The results, shown in **Fig. 2.14**, show well-resolved individual DNA binding sites and confirm the 40 nm distance between the binding sites. This demonstrates the capability of our setup in achieving high-resolution imaging at the nanoscale.

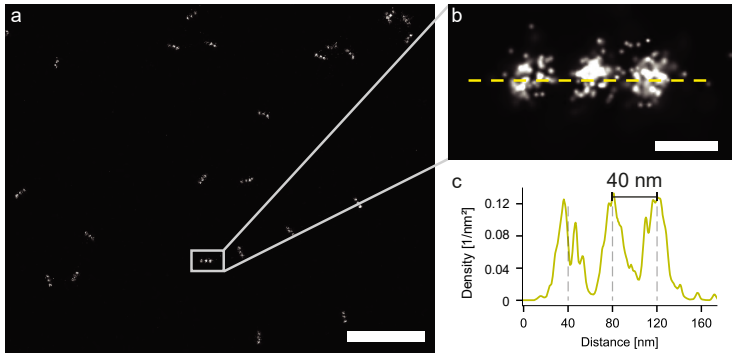

Figure 2.14 • DNA origami nanoruler benchmark sample
a) Rendered localizations of a 2 x 40 nm nanoruler sample, acquired over 10,000 frames (561 nm excitation wavelength, Cy3B imager strands). Scalebar: 500 nm **b)** Detailed view of one DNA origami nanoruler, with three docking sites distinctly visible. Scalebar: 40 nm **c)** Line profile of the localization density of the nanoruler shown in b), confirming the 40 nm distance between DNA binding sites on the DNA origami nanoruler.

2.7.2 Temperature stability and objective heating response time

We use an objective heater to maintain a stable, physiological temperature of the sample during extended live-cell imaging at 37 °C. The heater is controlled by a feedback loop that uses a temperature sensor at the objective to control the flow of current through a polyimide heater wrapped around the objective. Thermal decoupling of the objective and a plexiglass enclosure around the central cube help to maintain a constant temperature. The offset of objective temperature and the temperature directly at the sample was determined using a second sensor immersed in a test sample. At room temperature (21 °C), the system stabilizes at an objective temperature of 42.0 ± 0.1 °C (corresponding to 37 °C at the sample) after about 20 min (**Fig. 2.15**). Since there is no active cooling, it takes about 200 min for the system to return to room temperature. The thermal isolation and the mass of the central cube ensure minimal heating of the rest of the setup, which is important for maintaining alignment. In fact, the environmental sensor on the central cube showed an increase in temperature of less than 1 °C when the objective was heated to 42 °C (**??**). Overall, the objective heater is an effective and low-cost solution for maintaining a stable, physiological temperature of the sample during live-cell imaging.

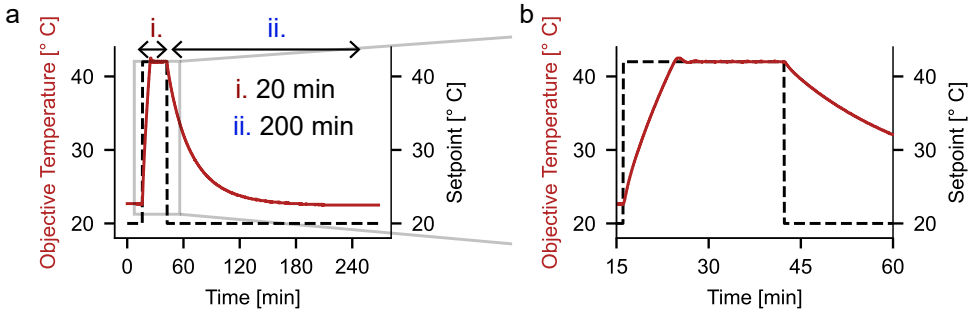

Figure 2.15 • Temperature control via objective heating
a) Heating phase, stabilized temperature and cooling phase during an objective heating cycle with a setpoint temperature of 42 ℃, corresponding to 37 ℃ sample temperature. **b)** Close-up showing stabilized temperature about 20 min after activating the objective heating.

2.7.3 Experimental applications: from live-cell imaging to single-molecule tracking

The K2 TIRF microscope can be used for a wide range of live-cell and single-molecule experiments [43]. **Fig. 2.16** showcases several such applications: dual-color single-molecule tracking of membrane proteins on live cells, with the third channel being used for detecting a transfection reporter (1) and dual-color single-molecule tracking of reconstituted membrane proteins transiently forming dimers on a supported lipid bilayer (2), as well as localization-based super-resolution microscopy like DNA-PAINT, demonstrated here by resolving a 2x 40 nm DNA origami nanoruler (3). Further applications are timelapse imaging of immune cell activation (4) and epifluorescence imaging of giant unilamellar vesicles (5), alongside brightfield imaging of an immune cell using the circular LED array. Combining epifluorescence imaging together with the z-stack function allows to capture 3D volumes of cells in suspension (6). The K2 TIRF microscope is also capable of performing fluorescence recovery after photobleaching (FRAP) experiments, here shown on a COS7 cell labeled with a fluorescent membrane marker (7).

In summary, the K2 TIRF microscope is a versatile instrument that allows the study of cellular and molecular dynamics in up to three fluorescence channels with an additional brightfield option. A large and homogeneously illuminated field-of-view, automated sample positioning and raster-scanning options enable the acquisition of high-quality, high-throughput microscopy data with comparatively little demand on user input. Furthermore, imaging experiments can be performed for extended durations (hours) due to the setup's excellent stability, active

focus stabilization and objective heating for live-cell compatibility. The extensive open-source documentation should allow researchers to easily recreate the setup, or parts of it, and adapt it to their specific requirements.

Current applications of the setup:

- (Single-molecule) TIRF microscopy with simultaneous detection of up to three colors
- Experiments with environmental control (temperature) or monitoring (temperature, humidity, sample drift)
- Video-rate recording with camera-triggered excitation (alternating or continuous)
- Timelapse- and tiled acquisitions with focus stabilization
- LED-based brightfield imaging
- Widefield epifluorescence imaging
- Fluorescence recovery after photobleaching (FRAP) experiments

Not performed currently but possible:

- Single-molecule Förster resonance energy transfer (FRET) microscopy
- Multi-color super-resolution microscopy: DNA-PAINT, photo-activated localization microscopy (PALM), stochastic optical reconstruction microscopy (STORM)

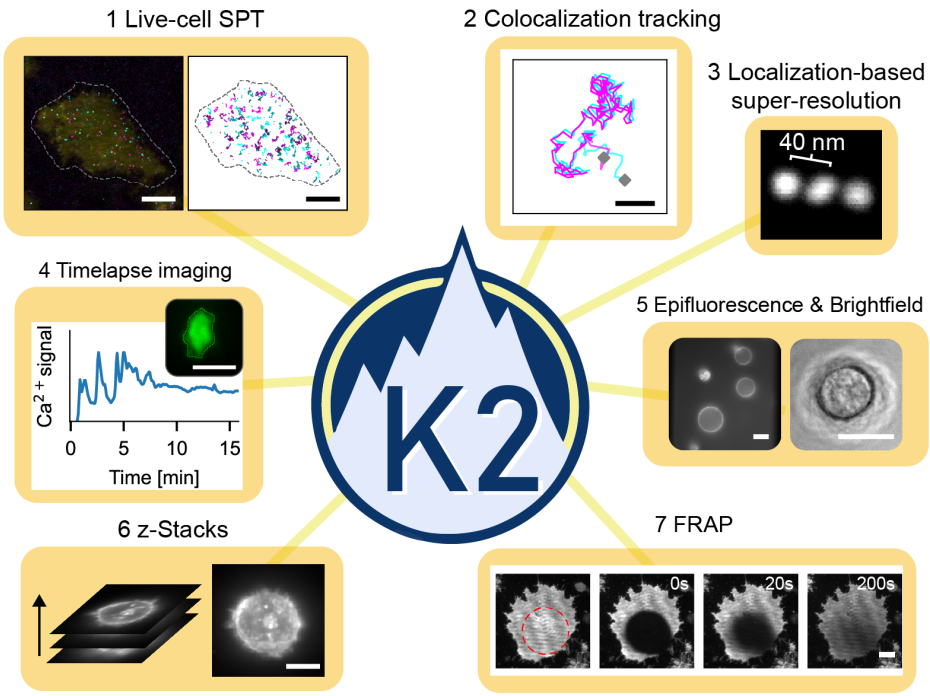

Figure 2.16 • Examples of the experiments that can be performed with the K2
(1) Dual-color single particle tracking on live Jurkat T-cells with a third channel used as a transfection reporter and (2) dual-color single-molecule tracking of reconstituted proteins on a supported lipid bilayer. Tracking the movement of two (or more) different fluorescently labeled molecules provides information about the interactions between different molecules by colocalization analysis. (3) Localization-based super-resolution microscopy, as demonstrated here by resolving a 2x 40 nm DNA origami nanoruler (structures averaged using Picasso Average [44]). (4) Live-cell timelapse imaging to measure immune cell activation: Jurkat T-cell outlines are tracked using cellpose [45] and TrackMate [46] and the mean intensity of the cell-permeable green fluorescent Ca^{2+} reporter Fluo4 is measured. (5) Epifluorescence imaging of giant unilamellar vesicles (left) and brightfield imaging of an adherent Jurkat T-cell (right). (6) Maximum projection of a z-stack of a Jurkat T-cell in suspension, imaged in epifluorescence mode.
(7) Timeseries of a fluorescence recovery after photobleaching measurements on a COS7 fibroblast cell: A reference image before the photobleaching step (left), directly after a bleaching pulse in the red circle (0 s, and the subsequent recovery after 20 s and 200 s, showing the mobility of the fluorescently labeled membrane. Scale bars are 10 µm.

References

[1] Christian Niederauer et al. “The K2: Open-source Simultaneous Triple-Color TIRF Microscope for Live-Cell and Single-Molecule Imaging”. In: *HardwareX* 13 (2023), e00404.

[2] Hongqiang Ma et al. “A Simple and Cost-Effective Setup for Super-Resolution Localization Microscopy”. In: *Scientific Reports* 7.1 (2017).

[3] Alexander Auer et al. “Nanometer-Scale Multiplexed Super-Resolution Imaging with an Economic 3D-DNA-PAINT Microscope”. In: *ChemPhysChem* (2018).

[4] Koen J. A. Martens et al. “Visualisation of dCas9 Target Search in Vivo Using an Open-Microscopy Framework”. In: *Nature Communications* 10.1 (2019), p. 3552.

[5] Benedict Diederich et al. “A Versatile and Customizable Low-Cost 3D-printed Open Standard for Microscopic Imaging”. In: *Nature Communications* 11.1 (2020), p. 5979.

[6] Mohammad Nour Alsamsam et al. “The miEye: Bench-top Super-Resolution Microscope with Cost-Effective Equipment”. In: *HardwareX* 12 (2022), e00368.

[7] John S. H. Danial et al. “Constructing a Cost-Efficient, High-Throughput and High-Quality Single-Molecule Localization Microscope for Super-Resolution Imaging”. In: *Nature Protocols* 17.11 (2022), pp. 2570–2619.

[8] Johannes Hohlbein et al. “Open Microscopy in the Life Sciences: Quo Vadis?” In: *Nature Methods* 19.9 (2022), pp. 1020–1025.

[9] Mad City Labs. *TIRF Lock™ — Keeps the Sample in the Focal Plane and Maintains TIRF Signal*. http://www.madcitylabs.com/tirf-lock.html. 2022.

[10] ASI Imaging. *CRISP Autofocus System*. https://www.asiimaging.com/products/focus-control-and-stabilization/crisp-autofocus-system/. 2022.

[11] Karl Bellve et al. “Design and Implementation of 3D Focus Stabilization for Fluorescence Microscopy”. In: *Biophysical Journal* 106.2 (2014), 606a.

[12] Daniel Schröder et al. “Cost-Efficient Open Source Laser Engine for Microscopy”. In: *Biomedical Optics Express* 11.2 (2020), p. 609.

[13] Jeff Y.L. Lam et al. “An Economic, Square-Shaped Flat-Field Illumination Module for TIRF-based Super-Resolution Microscopy”. In: *Biophysical Reports* 2.1 (2022), p. 100044.

[14] Andor. *Microscope Light Source — Integrated Laser Engine — ILE*. https://www.andor.oxinst.com/products/microscopy-components/integrated-laser-engine. 2022.

[15] John Philippi and Johannes Hohlbein. *SMILE: Single Molecule Imaging Laser Engine*. https://hohlbeinlab.github.io/miCube/LaserTrack_Arduino.html. 2022.

[16] Mohammed Mahamdeh and Erik Schäffer. “Optical Tweezers with Millikelvin Precision of Temperature-Controlled Objectives and Base-Pair Resolution”. In: *Optics Express* 17.19 (2009), p. 17190.

[17] Andy Maloney, Lawrence J. Herskowitz, and Steven J. Koch. “Effects of Surface Passivation on Gliding Motility Assays”. In: *PLOS ONE* 6.6 (2011), e19522.

[18] Khalid A. Ibrahim, Dora Mahecic, and Suliana Manley. “Characterization of Flat-Fielding Systems for Quantitative Microscopy”. In: *Optics Express* 28.15 (2020), p. 22036.

[19] Ian Khaw et al. “Flat-Field Illumination for Quantitative Fluorescence Imaging”. In: *Optics Express* 26.12 (2018), p. 15276.

[20] Florian Stehr et al. “Flat-Top TIRF Illumination Boosts DNA-PAINT Imaging and Quantification”. In: *Nature Communications* 10.1 (2019), p. 1268.

[21] Paula Montero Llopis et al. “Best Practices and Tools for Reporting Reproducible Fluorescence Microscopy Methods”. In: *Nature Methods* 18.12 (2021), pp. 1463–1476.

[22] Bioptechs. *Objective Heater – Bioptechs*. https://bioptechs.com/product/objective-heater/. 2022.

[23] Philip R. Nicovich et al. “NicoLase—An Open-Source Diode Laser Combiner, Fiber Launch, and Sequencing Controller for Fluorescence Microscopy”. In: *PLOS ONE* 12.3 (2017), e0173879.

[24] CAIRN Research. *Triggerscope 4 — Core And Analysis — Cairn Research Ltd*. https://www.cairn-research.co.uk/product/triggerscope-4/. 2022.

[25] Teledyne. *OptoSplit III — Teledyne Photometrics*. https://www.photometrics.com/products/imaging-splitters/optosplit-iii. 2022.

[26] Simao Coelho et al. “3D Active Stabilization for Single-Molecule Imaging”. In: *Nature Protocols* 16.1 (2021), pp. 497–515.

[27] Michael J. Saxton and Ken Jacobson. “SINGLE-PARTICLE TRACKING:Applications to Membrane Dynamics”. In: *Annual Review of Biophysics and Biomolecular Structure* 26.1 (1997), pp. 373–399.

[28] Laura Marchetti et al. “Ligand Signature in the Membrane Dynamics of Single TrkA Receptor Molecules”. In: *Journal of Cell Science* 126.19 (2013), pp. 4445–4456.

[29] Alex J. B. Kreutzberger et al. “Rhomboid Distorts Lipids to Break the Viscosity-Imposed Speed Limit of Membrane Diffusion”. In: *Science* 363.6426 (2019), eaao0076.

[30] Andres I. König et al. “Live Cell Single Molecule Tracking and Localization Microscopy of Bioorthogonally Labeled Plasma Membrane Proteins”. In: *Nanoscale* 12.5 (2020), pp. 3236–3248.

[31] Benedict Diederich et al. “CAD We Share? Publishing Reproducible Microscope Hardware”. In: *Nature Methods* 19.9 (2022), pp. 1026–1030.

[32] Sara Abrahamsson et al. “MultiFocus Polarization Microscope (MF-PolScope) for 3D Polarization Imaging of up to 25 Focal Planes Simultaneously”. In: *Optics Express* 23.6 (2015), p. 7734.

[33] Rainer Heintzmann. “Practical Guide to Optical Alignment”. In: *Fluorescence Microscopy*. Ed. by Ulrich Kubitscheck. Weinheim, Germany: Wiley-VCH Verlag GmbH & Co. KGaA, 2017, pp. 463–471.

[34] Arthur Edelstein et al. “Computer Control of Microscopes Using μManager”. In: *Current Protocols in Molecular Biology* 92.1 (2010).

[35] A. L. Mattheyses, S. M. Simon, and J. Z. Rappoport. “Imaging with Total Internal Reflection Fluorescence Microscopy for the Cell Biologist”. In: *Journal of Cell Science* 123.21 (2010), pp. 3621–3628.

[36] Junel Sotolongo Bellón et al. “Four-Color Single-Molecule Imaging with Engineered Tags Resolves the Molecular Architecture of Signaling Complexes in the Plasma Membrane”. In: *Cell Reports Methods* 2.2 (2022), p. 100165.

[37] Kaley A. McCluskey et al. “Global Correction of Optical Distortions in Multicolor Single-Molecule Microscopy Using Zernike Polynomial Gradients”. In: *Optics Express* 29.25 (2021), p. 42251.

[38] Sang Hak Lee et al. “Using Fixed Fiduciary Markers for Stage Drift Correction”. In: *Optics Express* 20.11 (2012), p. 12177.

[39] Ryan McGorty, Daichi Kamiyama, and Bo Huang. “Active Microscope Stabilization in Three Dimensions Using Image Correlation”. In: *Optical Nanoscopy* 2.1 (2013), p. 3.

[40] Yeoan Youn et al. “Thermal Nanoimprint Lithography for Drift Correction in Super-Resolution Fluorescence Microscopy”. In: *Optics Express* 26.2 (2018), p. 1670.

[41] Smaract. *Stick-Slip Drive Technology*. https://www.smaract.com/en/technology-introduction-and-options#position-sensors. 2022.

[42] ASI. *MS-2000 XYZ Automated Stage*. https://www.asiimaging.com/downloads/datasheets/MS-2000XY-Datasheet-Web.pdf. 2022.

[43] Christian Niederauer et al. “DNA-PAINT Single-Particle Tracking (DNA-PAINT-SPT) Enables Extended Single-Molecule Studies of Membrane Protein Interactions”. In: *bioRxiv* (2022), p. 503948.

[44] Joerg Schnitzbauer et al. “Super-Resolution Microscopy with DNA-PAINT”. In: *Nature Protocols* 12.6 (2017), pp. 1198–1228.

[45] Carsen Stringer et al. “Cellpose: A Generalist Algorithm for Cellular Segmentation”. In: *Nature Methods* 18.1 (2021), pp. 100–106.

[46] Dmitry Ershov et al. “TrackMate 7: Integrating State-of-the-Art Segmentation Algorithms into Tracking Pipelines”. In: *Nature Methods* 19.7 (2022), pp. 829–832.

3 Receptor assembly kinetics of interleukin-2/interleukin-15 receptors

3.1 Introduction

Single-molecule tracking has emerged as a powerful tool for the study of biomolecular interactions, particularly in the field of membrane receptor dynamics [1–12]. This technique allows for the visualization and tracking of individual receptor molecules as they move and interact within a cellular or artificial environment.

In this chapter, I describe the progress we made in developing the necessary experimental platform and analytical tools for studying the kinetic properties of interleukin-2 (IL-2) and interleukin-15 (IL-15) binding to their receptors using single-molecule tracking. These accomplishments include successful expression and labeling of all receptor subunits, verification of protein quality, optimization of the reconstitution protocol and programming of an analysis platform for single-molecule tracking data. Despite the limited quality of the single-molecule data obtained, making it unsuitable for detailed analysis in this thesis, the development of the experimental platform will pave the way for future investigations into cytokine-receptor interactions, building upon the advancements made in this chapter. Additionally, the chapter presents simulation results from enhanced Green's Function Reaction Dynamics (eGFRD) simulations that suggest new opportunities for accelerated targeted drug design, in combination with measurements of binding kinetics. Overall, the work presented in this chapter sets the stage for further investigations into the complex molecular mechanisms underlying cytokine signaling, with the potential to shed new light on the role of these molecules in health and disease.

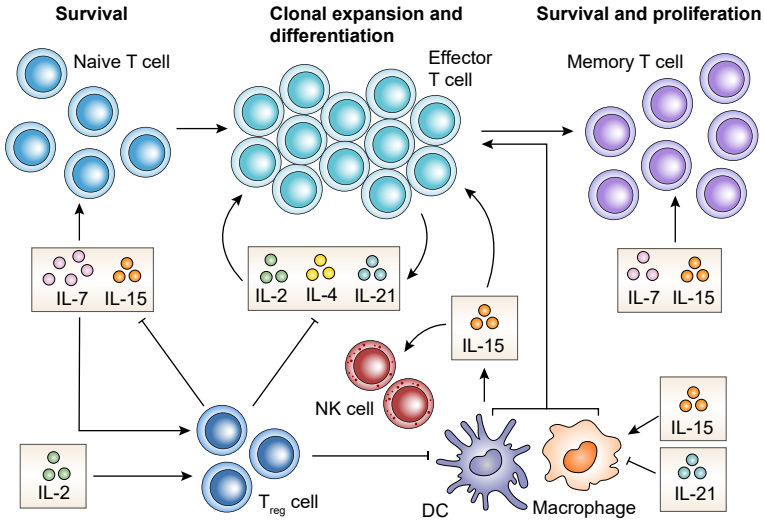

Figure 3.1 • Effects of γ_c family interleukins on T cell proliferation, homeostasis and differentiation

Cytokines of the γ_c family directly influence T cell survival, activation, proliferation, and differentiation, as well as indirectly affecting these processes through interactions with dendritic cells, macrophages, and regulatory T cells. IL-15, in particular, plays a crucial role in inducing the proliferation of natural killer cells, maintaining the homeostasis of CD8+ memory and CD4+ memory T cells, and promotes the recovery of naive CD8+ T cells in conditions of lymphopenia. Furthermore, IL-2 and IL-15 can enhance T cell proliferation following antigen stimulation. IL-7 is also essential for the survival of naive T cells. Additionally, IL-2, IL-4, and IL-21 play pivotal roles in T cell differentiation. Figure based to [13].

3.1.1 Interleukins and their role in the immune system

The word *cytokine* comes from the ancient Greek language: cyto, (cell) + kines (movement). The term interleukin derives from the combination of the Latin prefix inter (between) and the Greek adjective leukós (white), referring to white blood cells (leukocytes).

Interleukins are a group of cytokines that play a crucial role in mediating communication between cells of the immune system. They are small soluble proteins produced by a variety of immune cells, including T cells, monocytes and macrophages, and act as signal transmitters on a wide range of target cells, including T cells, B cells, natural killer cells, and other immune cells (see Fig. 3.1 for an overview of the γ_c family of interleukins). For instance, IL-2, which is the earliest cytokine produced by T cells after T cell receptor activation [14], helps stimulate the proliferation of other T cells, thereby enhancing the immune response

to invading pathogens. Since the immune system's function is primarily mediated by interleukins, dysfunctions in interleukin production have been linked to the development of autoimmune disorders and immune deficiencies [15, 16]. Fortunately, this also presents an opportunity to use interleukins to stimulate the activation of the immune system when it is failing to activate adequately, or for suppressing the immune system in cases of autoimmune overreaction. The therapeutic potential of interleukins is demonstrated by the increasing number of clinical trials utilizing interleukins to enhance the action and reduce side effects of cancer immunotherapies [13, 17–19].

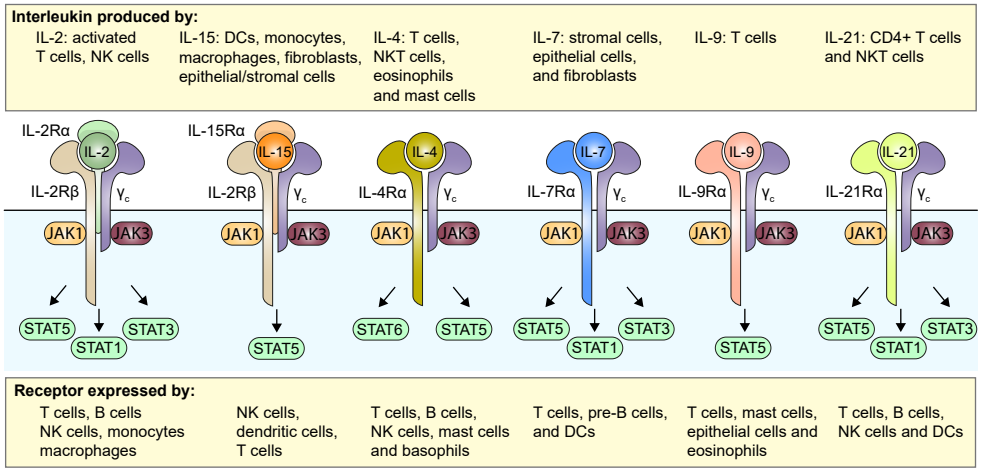

Figure 3.2 • Receptors of the γ_c family interleukins
Shown are the receptors for IL-2, IL-4, IL-7, IL-9, IL-15, and IL-21. The receptors for IL-2 and IL-15 share the common cytokine receptor γ_c and IL-2Rβ. Receptor assembly is induced by ligand binding, leading to the phosphorylation of Janus kinase 1 (JAK1) and JAK3, which then triggers downstream signaling by activating signal transducer and activator of transcription (STAT) proteins. Figure based on [13, 17].

Interleukins exert their effects by binding to their specific interleukin receptors on the surface of target cells, which leads to the activation of intracellular signaling pathways. Interleukin receptors are typically composed of several subunits that assemble upon ligand binding (see Fig. 3.2 for an overview of the γ_c family of interleukin receptors). Intracellularly, this brings the constitutively receptor-associated Janus kinases (JAKs) on the receptors' intracellular chains close to each other, allowing for their *trans*-phosphorylation and activation, followed by phosphorylation of receptor tails. Signal transducers and activators of transcription (STAT) proteins are recruited to the phosphorylated receptor tails and become activated by JAK phosphorylation. Upon activation, STATs dis-

sociate from the receptor, dimerize and subsequently translocate to the nucleus, where they modulate the transcription of genes involved in cell proliferation, differentiation and survival, as well as genes involved in the production of inflammatory molecules and the regulation of the immune response. Some specific examples of target genes activated by the STAT pathway in healthy immune cells include interferon-gamma, IL-2, and T-cell receptor genes. Besides the JAK/STAT pathway, other signaling pathways include RAS/Raf/MAPK, activating mitogenic target genes involved in cell growth, proliferation and differentiation, as well as the PI3K/AKT/mTOR pathway, promoting cell survival by inhibiting cell death pathways [15, 16, 20–22].

3.1.2 Interleukin-2 (IL-2) and interleukin-15 (IL-15)

Despite some interleukin receptor subunits being shared among different ligands, such as the cytokine receptor common subunit γ (γ_c) which partners with at least six other ligand-specific receptors, the various interleukins elicit vastly distinct signals [13, 15, 23]. IL-2 and IL-15, for example, are two crucial interleukins with differing function that both signal through a heterodimeric interleukin receptor consisting of γ_c and the IL-2 receptor beta chain (IL-2Rβ), with an additional private subunit, IL-2Rα and IL-15Rα, respectively (see **Fig. 3.3**). Signaling is transduced through the γ_c and IL-2Rβ subunits. While the IL-2Rα and IL-15Rα subunits were found to stabilize the respective receptor complexes, they are not directly involved with signal transduction as their cytoplasmic domains are rather short and dispensable for signaling (IL-2Rα: 11 amino acids, IL-15Rα: 37 amino acids) [24]. Despite signaling through the same heterodimeric receptor, IL-2 and IL-15 exhibit distinct differences in their actions and effects on the immune system, raising the question of how IL-2 and IL-15 can lead to different signals through the same receptor (see **Section 3.1.3**) [17, 26–42]. IL-2 and IL-15 both play vital roles in the development and homeostasis of the immune system [43, 44] (see **Fig. 3.1**). As a result, both IL-2 and IL-15 have emerged as interesting targets for therapeutic interventions aimed at modulating immune responses in diseases [18, 19, 45–50]. In the following sections, I will first briefly outline the function of both interleukins separately and then describe their potential as therapeutic targets for modulating immune responses.

In fact, the studies that reported interactions of IL15-Rα with signaling proteins like Syk kinase and TRAF2 have been retracted [25].

IL-2: IL-2 is an interleukin that plays a crucial role in the regulation of the immune system by stimulating the growth, activation and differentiation of T cells. Specifically, it promotes the expansion of CD4+ T helper

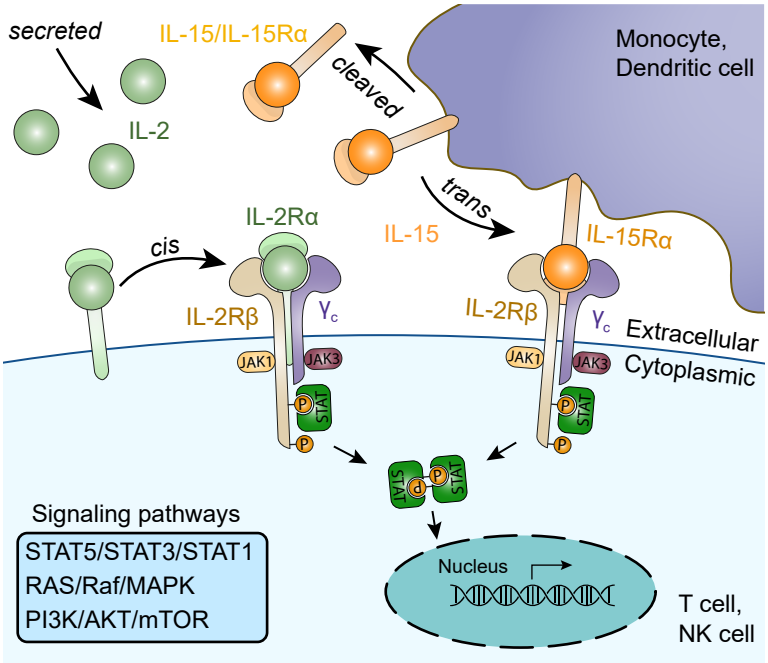

Figure 3.3 • IL-2 and IL-15 signaling pathways
Receptors for IL-2 and IL-15 share two subunits, the γ-chain (γ_c) and the IL-2Rβ chain. IL-2 (left, green) binds to pre-formed IL-2Rα-IL-2Rβ dimers or directly to its specific receptor subunit IL-2Rα, while IL-15 (right, orange) is predominantly *trans*-presented by monocytes or dendritic cells to NK cells or CD8+ T cells through binding with IL-15Rα. Both IL-2 and IL-15 mainly activate the JAK/STAT pathway, regulating the transcription of target genes involved in cell proliferation, differentiation, and survival, as well as genes involved in the production of inflammatory molecules and the regulation of the immune response. Other pathways including RAS/Raf/MAPK and PI3K/AKT are also activated by these interleukins, contributing to their complex effects on immune cells.

cells and CD8+ cytotoxic T cells, which are important in the body's defense against infections and cancer [44, 51, 52]. IL-2 also plays a key role in the regulation of the immune response by promoting the expansion of regulatory T cells (T_{reg} cells), which help to prevent overactive immune responses, such as in autoimmune diseases [53–55]. Furthermore, IL-2 also induces activation-induced cell death (AICD) of T cells, which is a process that helps to eliminate T cells that have been activated and are no longer needed, maintaining a balance of the T cells population [44, 51, 52, 56].

IL-15: Similarly to IL-2, IL-15 promotes the survival, activation, and proliferation of T cells and, importantly, natural killer cells [57–59]. In contrast to IL-2, it is also involved in the development of CD8+ memory and CD4+ memory T cells, which are important for long-term immunity [13].

Both interleukins have been utilized as therapeutic agents for the treatment of cancer and autoimmune diseases [17–19, 48, 51, 52, 58, 60–68]. Notably, IL-2 was the pioneering human cancer immunotherapy, demonstrated by its ability to elicit durable and complete tumor regressions in clinical trials involving patients with metastatic melanoma and renal cancer [69, 70].

Despite the initial excitement, interleukins as monotherapy have not lived up to expectations, and IL-2 remains the only interleukin to have been approved for the treatment of certain cancers [19]. This is in part due to the fact that interleukins typically act over short distances in their local environment, and therefore large quantities must be administered to patients to achieve effective local concentrations. This can lead to severe, potentially life-threatening toxicities, such as the capillary leak syndrome in the case of high-dose IL-2 treatment [71]. Additionally, the positive actions of these interleukins are often paralleled by the induction of immunological checkpoints, such as the secretion of inhibitory factors, the expression of inhibitors, and the induction of regulatory cells [18].

The limitations of using native forms of interleukins as monotherapy have led researchers to explore more sophisticated approaches. Recent studies have focused on strategies such as modifying the ligand-receptor affinities to target specific cell populations, or creating fusion constructs that target tumors specifically, in order to increase efficacy and decrease systemic toxic effects [18, 19, 47, 72–75]. In particular, there is a substantial body of research on the use of IL-2 and IL-15 in these types of approaches [67, 76–89]. However, in order to fully realize the potential of these sophisticated molecular engineering approaches, it is crucial to gain a deeper understanding of the underlying molecular signaling. Biophysical studies of receptor assembly and binding kinetics can provide valuable insights into the mechanism of action of these receptors and aid in the development of more effective and more tolerable therapies. In this context, we focused on understanding the molecular mechanism by which IL-2 and IL-15 signaling leads to similar yet distinct functional responses as this is not only an interesting biophysical question but also highly relevant to the design of new and specific IL-2 or IL-15 agonists for improved therapies.

3.1.3 The IL-2/IL-15 receptor dichotomy

IL-2 and IL-15 are structurally similar (see Fig. 3.4), but while they share some common functions in stimulating the generation and activation of immune cells, they also have distinct differences in their actions and effects on the immune system (see Table 3.1). IL-2 deficiency leads to autoimmune and inflammatory disorders, while IL-15 deficiency does not [49, 90, 91]. Conversely, most organ-specific autoimmune disorders are associated with IL-15 overexpression in the affected tissue [50, 92–98]. IL-15 also has a different effect on the differentiation of T_{reg} cells and AICD compared to IL-2: IL-15 blocks the differentiation of peripherally derived T_{reg} cells and is an anti-apoptotic factor [34, 99, 100], while IL-2 promotes the elimination of potentially harmful self-reactive T cells through AICD [101, 102].

Properties	**IL-2**	**IL-15**
Structure	15.5 kDa, four-helix bundle	14-15 kDa; four-helix bundle
Appearance	Soluble	IL-15 in complex with IL-15Rα
Receptor	IL-2Rα, IL-2Rβ, γ_c; K_D : 10 pM [103]	IL-15Rα (*cis/trans*), IL-2Rβ, γ_c; K_D < 10 pM [104, 105]
IL-producing	Activated T cells, NK cells	Dendritic cells, macrophages, monocytes, fibroblasts, epithelial/stromal cells
Receptor-expressing	T cells (CD4+ helper, CD8+ cytotoxic, T_{reg}) B cells, NK cells, monocytes, macrophages	NK cells, dendritic cells T cells (CD4+ memory, CD8+ cytotoxic)
Primary effects	Proliferation of activated T cells Promotes AICD T_{reg} development/survival Promotes B cell proliferation Inhibits CD8+ T cell division	Proliferation of activated T cells Inhibits AICD Promotes NK development/survival Promotes priming of NK cell activation Maintenance of naive/memory CD8+ T cells

Table 3.1 • Comparison of IL-2 and IL-15 ligands, their receptors and functions

Interestingly, the structures of the receptor-ligand complexes seem conserved between different ligands, ruling out models explaining specificity by different ligand-receptor conformations [27, 106–108] (see Fig. 3.4). IL-2 and IL-15 both signal through a shared receptor complex composed of the IL-2Rβ subunit and γ_c. Additionally, IL-2 and IL-15 associate with a third subunit (IL-2Rα and IL-15Rα, respectively; see Fig. 3.3). For both IL-2 and IL-15, however, signaling is solely transduced through the shared receptors IL-2Rβ/γ_c through the same adaptor proteins, while the interleukin-specific subunit is only stabilising the complex, raising the question of how the two interleukins can evoke differential responses [17, 26–42].

IL-2Rα is also known as CD25; IL-15Rα: CD215' IL-2Rβ: CD122; γ_c: CD132, or IL-2Rγ.

One hypothesis is that, while IL-2 functions as a soluble factor produced by activated T cells, IL-15 is primarily found in complex with IL-15Rα, binding to responding cells that express IL-2Rβ and γ_c either through cell contact-dependent *trans*-presentation, or as a soluble IL-15/IL-15Rα heterodimer, following the cleavage of the membrane-anchored complex [17, 30, 109, 111, 114–117] (see Fig. 3.3).

Interestingly, IL-15 signaling through *cis*-presentation, as well as IL-2 signaling through *trans*-presentation, have also been observed [109–113].

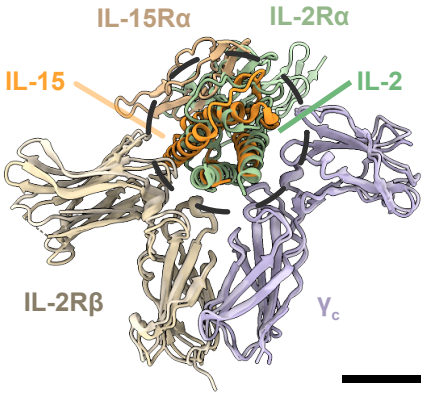

Figure 3.4 • Crystal structure overlay of IL-2 and IL-15 receptors

Crystal structure overlay of IL-2 (green) and IL-15 (orange) bound to the extracellular domains of their trimeric receptors. Bound ligands (in dashed circle) lead to identical geometrical arrangement of the two signaling subunits (IL-2Rβ in beige, γ_c in purple). α-subunits, specific to IL-2 and IL-15, respectively, exhibit a greater structural deviation, but are not involved directly with signaling. Protein database accession codes: 2ERJ (IL-2 quarternary complex [108]), 4GS7 (IL-15 quarternary complex [27]). Scale bar: 2 nm

Another hypothesis put forward is that the distinct roles of IL-2 and IL-15 can be attributed to them acting on T cells that have different activation statuses. This would be explained by the fact that IL-2 is not produced by antigen-presenting cells or non-hematopoietic cells such as epithelial or stromal cells. Instead, IL-2 is secreted at low levels and transiently by tissue-resident cytotoxic T cells, and rapidly consumed by activated T cells and T_{reg} cells in the tissue, making it unable to reach sufficient levels to signal through the constitutively expressed dimeric IL-2/IL-15Rβ-γ_c receptor that is shared with IL-15. This leads to IL-2 signaling mainly taking place through the high-affinity trimeric IL-2Rα-IL-2Rβ-γ_c receptor, which is only upregulated in response to T cell activation, while IL-15 can also signal through the dimeric receptor due to its higher affinity [59].

Non-hematopoietic refers to cells that are not involved in the formation or maturation of blood cells.

However, in vitro stimulation of T cells with sub-saturating concentrations of soluble IL-2 and IL-15 results in significantly different gene expression profiles. This indicates that the distinct roles of IL-2 and IL-15 are not solely governed by the local environment or cell activation states [27].

An alternative hypothesis that could potentially explain the distinct roles of IL-2 and IL-15 is that cells discriminate between different ligands based on their kinetic properties [118], through a mechanism known as kinetic proofreading [119–121]. This mechanism allows for high specificity by utilizing a series of energy-dependent intermediate steps, during each of which the reaction can be aborted. In the context of ligand-induced receptor signaling, the energy-dependent intermediate steps correspond to phosphorylation steps that occur intracellularly, while the abortion of the reaction corresponds to unbinding of the ligand, leading to receptor disassembly and the halt of *trans*-phosphorylation of the in-

tracellular receptor chains. Different affinities of IL-2 and IL-15 for their receptors have been determined in previous studies [27, 88, 103, 104, 122, 123], leading to large variations in receptor stability. This could result in the selective activation of certain signaling pathways based on the duration of ligand binding times, as suggested by combining molecular dynamics simulations and free energy calculations [42]. Additionally, similar mechanisms have been observed in other ligand-binding dependent receptors [72, 74, 121, 124–127]. This hypothesis also aligns with the observation of shared functions of the two interleukins, as both ligands would be able to initiate downstream signaling events, but the probability of reaching the progressive signaling steps may differ and influence the extent and specificity of their downstream signaling.

In conclusion, the molecular mechanisms underlying the distinct signaling of IL-2 and IL-15 remain to be fully understood. Further research is needed to better comprehend the clinical implications of these interleukins and optimize their therapeutic use [65].

3.2 Experimental approach

3.2.1 In vitro reconstitution

Interleukins and their effects on cells are usually studied in native-like environments within living cells, tissues or animal models [11, 21, 72, 128], but this approach has limitations. Studying receptors on live cells can be complicated by crosstalk with other cellular processes, making it difficult to isolate and understand the specific effects of the proteins of interest. Additionally, the environment within live cells is not well-defined and can vary between different cell types, making it challenging to compare results between different studies.

In vitro reconstitution experiments are a widely used technique in biophysics to study the kinetics of membrane proteins and their interactions with other molecules. In these experiments, purified, recombinantly expressed proteins are reconstituted in a controlled and well-defined environment. In particular, SLBs are an important experimental platform for reconstituting membrane proteins or membrane-associated proteins, since SLBs mimic the native lipid environment of cells, maintaining the two-dimensional geometry and diffusivity of the individual molecules [129–137]. In the case of interleukin receptor studies, the combination of in vitro reconstitution and single-molecule tracking allows to investigate the effect of different modes of presentation on receptor assembly, two-dimensional binding kinetics of (ligand-bound or not) receptor sub-

Reconstituting full-length membrane proteins is technically extremely challenging. Due to their hydrophobic regions, they are difficult to solubilize and keep stable.

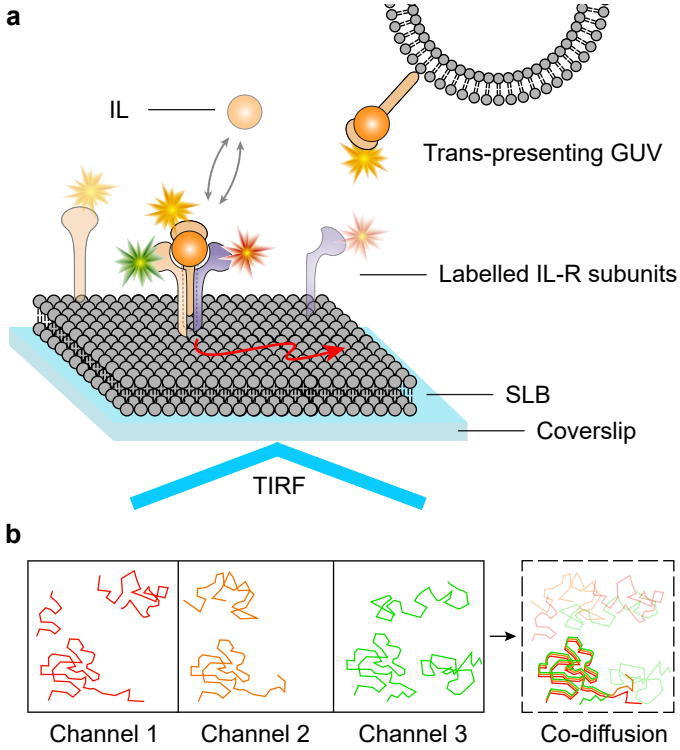

Figure 3.5 • Schematic of the experimental approach
(a) Fluorescently-labeled interleukin receptor ectodomains are reconstituted in vitro on a SLB. Interleukin ligands are added in solution or membrane-bound on giant unilamellar vesicles (GUVs) via *trans*-presentation through the α-receptor subunit. **(b)** Single-molecule trajectories are acquired simultaneously in different color channels and analyzed for co-diffusion to gather information about the nature and duration of interleukin receptor interactions.

units, the impact of receptor subunit ratios and densities on the receptor assembly [138] (see Fig. 3.5). Interleukin receptor activation is mediated by the extracellular binding of a ligand, and it has been shown that the receptor subunit ectodomains are well folded and bind the ligand in the assumed native conformation [27, 74, 108]. Consequently, the in vitro experiments could be simplified by expressing and reconstituting only the ectodomains of the receptor subunits on our SLBs. Labeling the receptor subunit species with spectrally distinct fluorescent dyes allowed to follow their individual dynamics and interactions by single-molecule tracking and colocalization analysis (see Chapter 4).

Reconstitution experiments in combination with single-molecule tracking offer a way to study several open questions in the context of IL-2 and IL-15 signaling:

Q1: How does the mode of ligand presentation (*cis* or *trans*) affect receptor assembly and stability?

Q2: How do the different binding kinetics of IL-2 and IL-15 and their mutated versions relate to the stability of the assembled receptor?

Q3: Do receptor subunits pre-assemble prior to ligand-binding?

Q4: How does the ratio of different receptor subunits affect ligand binding and receptor assembly?

In particular, Q1 and Q2 can not be addressed with conventional measurements of binding kinetics (see **Chapter 1**), as they do not reproduce the 2D-environment of the receptors. Q3 and Q4 can in principle be investigated with bulk methods, but single-molecule studies allow to follow receptor assembly directly, instead of only reporting on the equilibrium state. This is specifically relevant for multi-step receptor assembly, as it has been proposed for IL-2/IL-15 recruitment and receptor activation.

3.2.2 Protein preparation

Interleukin receptor constructs for recombinant expression were designed to contain the full extracellular domain (ectodomain) of each receptor subunit, a N-terminal polyglycine sequence for site-specific sortase-mediated fluorophore labeling [139], as well as a C-terminal His-tag (12x) to allow stable anchoring to nickelated lipids [140]. Detailed information about the protein constructs are given in **Section 3.6.2** of the appendix.

Expression and purification of interleukin receptor subunits

Protein expression using insect cell lines such as Sf-9 (derived from *Spodoptera frugiperda*) allows the large-scale production of recombinant protein with post-translational modifications. For the expression of the extracellular, interleukin-binding parts of the IL-2 and IL-15 receptor subunits, we used SF-9 cells in suspension culture and the baculovirus system for transfection. Dr. Patrick Celie at the Netherlands Cancer Institute (NKI) guided the initial protein expression rounds. Subsequently, we established our own insect cell culture facility at AMOLF.

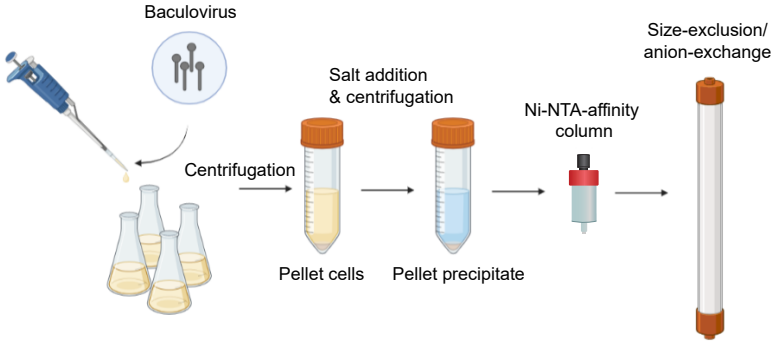

Figure 3.6 • Protein production in insect cell culture
Steps involved in baculovirus-mediated protein expression and purification using Sf-9 cells: Sf-9 cells are cultivated in suspension and infected with baculovirus solution carrying the sequence of the protein to be expressed. Three days after transfection, cells are pelleted and discarded, the supernatant is treated with calcium and nickel salts and tris(hydroxymethyl)aminomethane (TRIS) buffer to form a precipitate which is also discarded. After filtering, the solution is loaded onto a nickel-nitrilotriacetic acid (Ni-NTA) affinity column. Proteins are eluted and further purified via size-exclusion chromatography and ion-exchange chromatography, before used for further steps.

Dr. Ricardo Fernandes from the lab of K. Christopher Garcia at Stanford University (now at University of Oxford) kindly provided baculovirus samples with IL-2Rα, IL-15Rα, IL-2Rβ, and γ_c ectodomain sequences, with N-terminal sortase-tags and C-terminal 12x His-tags.

The expression and purification process is depicted in Fig. 3.6: Sf-9 cells were cultured in suspension and infected with the respective baculovirus solution to induce protein expression. Insect cells secrete the recombinant proteins into the medium, which are subsequently harvested and purified. Cells were removed by centrifugation, and components present in the medium that would also bind to Ni-NTA and hence interfere, were removed by salting-out and centrifugation. Recombinant protein in the supernatant was purified using Ni-NTA affinity, followed by size-exclusion and, if deemed necessary, anionic exchange chromatography, on a fast protein liquid chromatography (FPLC) system.

3.2.3 Protein quality control

In typical bulk biochemistry experiments, the behavior of a large number of proteins is measured at once, and the overall result is the ensemble average of molecular properties of many individual proteins. In such experiments, the loss of activity of even a small fraction of proteins can significantly affect the outcome of the experiment. As a result, it is essential to maximize and also quantify the functional fraction of the population of proteins to obtain accurate and reliable results, which often poses a significant challenge.

In single-molecule experiments, it is not as critical that all proteins are functional as individual molecules can be monitored for their activity, and non-functional molecules can in principle be excluded from the analysis. However, it is still essential to confirm the purity, identity and functionality of proteins used for single-molecule experiments to ensure that the results obtained are reliable and reproducible [141, 142].

We assessed the identity and purity of the recombinant proteins using sodium dodecylsulfate polyacrylamide gel electrophoresis (SDS-PAGE) and mass spectrometry. First, purified proteins were separated using SDS-PAGE according to their size and visualized using Coomassie Blue staining. The resulting gel bands were compared to known protein standard ladders and the expected molecular weight of the purified protein to confirm their identity and purity. Since post-translational modifications such as glycosylation can lead to deviations of the expected molecular weight, we cut out stained bands and additionally performed mass spectrometry for IL-2Rβ and γ_c purification batches (done by the lab of Jennifer Geddes-McAlister, Molecular and Cellular Biology Department, University of Guelph).

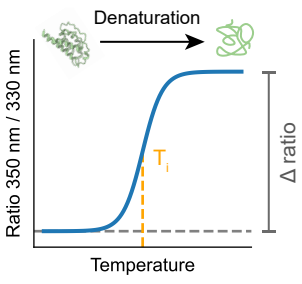

Figure 3.7 • Thermal shift assay

The change in intrinsic fluorescence upon heating is quantified to determine the protein quality. When the protein denatures and unfolds during heating, the amino acids' immediate environment changes, leading to a different emission spectrum of autofluorescent amino acids.

To test the structural integrity of the receptor subunits, we measured changes in the intrinsic fluorescence of tryptophan and tyrosine residues using a thermal shift assay (TSA) machine (Prometheus, Nanotemper). As shown in Fig. 3.7, while the sample is heated, changes in fluores-

cence signal reveal transitions in the folding state of the protein. The fluorescence data collected during the thermal run were plotted as a ratio and used to calculate the inflection temperature T_i and the change in signal during the run (Δ ratio). These results provide insight into the stability and folding of the purified protein and help ensure its quality across different batches of expression, purification and labeling.

Additionally, to evaluate the functionality of the proteins, we conducted microscale thermophoresis (MST). This technique measures interactions between fluorescently-labeled and unlabeled biomolecules, based on the detection of a temperature-induced change in diffusive behaviour called thermophoresis (see **Fig. 3.8**). Since the temperature change is locally confined, a change in fluorescence in that region can be measured and used to quantify molecular interactions. In contrast to single-molecule experiments of protein-protein interactions, MST is a bulk method and reported molecular properties reflect the ensemble average.

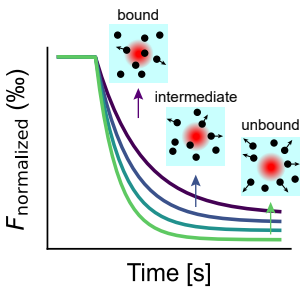

Figure 3.8 • Microscale thermophoresis (MST)

Fluorescently labeled molecules respond to a thermal gradient produced by an infrared laser, displaying different diffusion behavior depending on their molecular interactions (thermophoresis). The degree of their movement is observed by fluorescence, enabling the determination of parameters such as binding affinity in titration experiments.

Fluorescent labeling of recombinant proteins

One of the essential requirements in single-molecule tracking experiments is the use of bright and photostable fluorescent labels on the proteins of interest. Furthermore, for multicolor single-molecule tracking experiments, the selection of fluorophores with distinct emission spectra is crucial to track multiple molecular species within a single sample.

Fluorophore and filter selection Fluorophores were selected based on their spectral characteristics, photostability, quantum yield and extinction coefficients, using the fluorophore database `fpbase.org`. Additionally, the spectral characteristics and the filter sets of the fluorescence microscope need to be matched to minimize potential issues such as

bleedthrough and cross-excitation. The excitation and detection efficiencies for the different fluorophores in the three color channels, considering all dichroic mirrors and filters in the excitation and emission paths, as well as the quantum efficiency of the used camera and the quantum yields of the fluorophores are shown in Fig. 3.9, with integrated values stated in Table 3.2. Absorption spectra and detailed bleedthrough characteristics of the selected fluorophores are shown in Section 3.6.3.

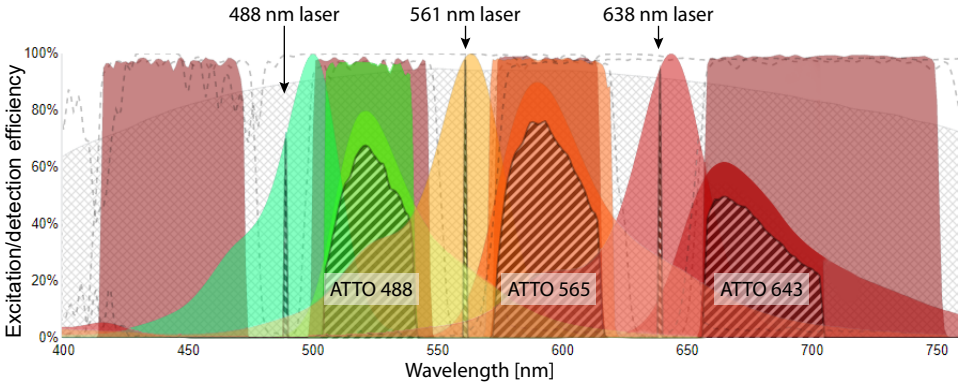

Figure 3.9 • K2 excitation and detection efficiencies for spectrally distinct dyes
The excitation and detection efficiencies of the K2 setup for the fluorophores ATTO 488, ATTO 565 and ATTO 643 are displayed, with three lasers exciting the fluorophores at 488 nm, 561 nm and 638 nm. All filters and dichroic mirrors, as well as the quantum efficiency of the camera are considered. Emission spectra are scaled to quantum yields. An interactive brightness and efficiency calculator for the K2 TIRF setup is available at fpbase.org/microscope/jKJ82bXWwME8ZLMmYfack8.

Bleedthrough and cross-excitation are two related phenomena that can result in unwanted signals and a compromised signal-to-noise background. Bleedthrough occurs when the fluorescence emission from one fluorophore is detected in a channel where it is not expected to emit, due to spectral overlap between the emission spectrum of the fluorophore and the detection window of the channel (see Fig. 3.30). In single-molecule experiments, this can result in a false-positive colocalization signal. Cross-excitation, on the other hand, occurs when the excitation light for one fluorophore also excites another fluorophore that emits at a different wavelength (see Fig. 3.29). This can result in a false-positive signal in a channel where no fluorophore is expected to emit, due to the cross-excitation of a different fluorophore. In the context of the experiments presented in this chapter, cross-excitation is not problematic as the fluorophores are simultaneously excited.

Channel	488 nm	561 nm	638 nm
ATTO 488	42.6%	1.1%	0.004%
ATTO 565	-	42.2%	0.9%
ATTO 643	-	-	35.2%

Table 3.2 • Bleedthrough assessment
Integrated detection efficiencies for the different fluorophores for all three color channels. Calculated using `fpbase.org` [143].

Site-specific labeling of interleukin receptor subunits Genetically encoded peptide tags allow for the site-specific, enzyme-mediated covalent labeling of proteins, and, due to their small size ,minimize the potential perturbation of protein functionality [144]. We chose a sortase-mediated approach to covalently label the interleukin receptor subunits at their N-terminus. Sortase is an enzyme that catalyzes transpeptidation reactions by recognizing a short peptide tag (sequence: LPETGG), to which a fluorophore can be conjugated. Sortase cleaves the threonine-glycine bond of the peptide and forms an acyl intermediate with the threonine. A N-terminally genetically encoded polyglycine tag at the protein resolves the intermediate and a covalent bond between the fluorescently labeled peptide and the protein is formed [139]. Using this approach, we labeled the subunits of IL-2 and IL-15 receptor complexes with bright, photostable organic dyes (ATTO 488, ATTO 565, ATTO 643). Additionally, we introduced a Strep-tag sequence (WSHPQFEK) in the labeling peptide, which allowed the removal of unlabeled protein by Strep-Tactin affinity chromatography (see Fig. 3.10).

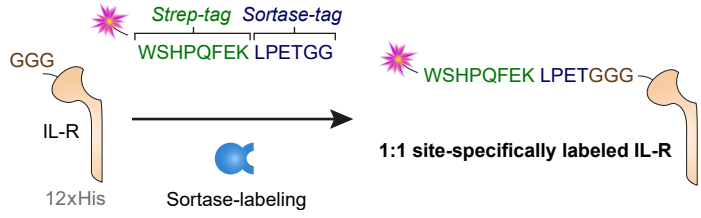

Figure 3.10 • Site-specific, sortase-mediated covalent labeling
Sortase specifically recognizes the sortase-tag peptide sequence and cleaves it, forming an intermediate that is resolved by nucleophilic attack of the polyglycine-tag of the protein of interest. Sortase, unreacted peptide and cleavage products are removed via Ni-NTA affinity chromatography. The additionally introduced Strep-tag in the peptide sequence allows the removal of unlabeled protein via Strep-Tactin affinity chromatography.

3.2.4 Preparation of SLBs

The reconstitution of recombinant proteins on a two-dimensional support that maintains lateral diffusivity typically involves using polyhistidine-tagged proteins binding to nickelated lipids embedded in a SLB. Nickelated lipids are lipids that have been modified to contain nickel ions chelated by nitrilotriacetic acid (NTA). The histidine residues on the protein bind to the nickel ions through coordination bonds in a specific interaction, as histidine residues have a high affinity for metal ions, especially nickel. This specificity of interaction makes Ni-NTA affinity a reliable method for the reconstitution of His-tagged proteins on SLBs in densities appropriate for single-molecule experiments [140].

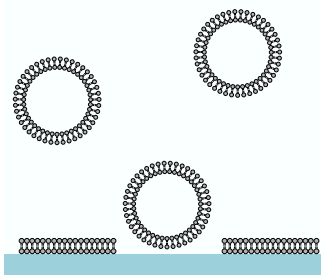

Figure 3.11 • Supported lipid bilayer formation

Schematic representation of small unilamellar vesicle fusion leading to the formation of a SLB. After lipid vesicles adsorb to the hydrophilic substrate, bilayer patches form and merge to a continuous lipid bilayer.

A common method for creating SLBs is the vesicle fusion technique, which entails the adsorption and bursting of small unilamellar vesicle (SUV)s onto a target surface, usually glass slides (see Fig. 3.11). The adsorption of the vesicles to the surface and eventually their rupture and formation of a homogeneous SLB is determined by attractive forces such as Van der Waals and electrostatic forces between the vesicle and substrate, and the interaction between vesicles [145]. To facilitate the adsorption and rupture of vesicles, we used hydroxylated glass slides as substrates. These glass slides were prepared using piranha cleaning and plasma cleaning.

3.2.5 Single-molecule tracking and colocalization analysis

The experimental design for this project focuses on using single-molecule tracking and colocalization analysis to investigate receptor interactions and dynamics. Specifically, we track up to three species of fluorescently labeled receptor chains and analyze their individual diffusion dynamics. Additionally, we use statistical analysis methods to quantify the degree and frequency of receptor subunit colocalization, and explore the po-

tential implications of receptor density, ligand concentration, mode of ligand presentation, and the effect of modified ligands.

To analyze the single-molecule tracking data, we developed a Python software package called SPIT (**s**ingle-**p**article **i**nteraction and **t**racking, see github.com/GanzingerLab/SPIT). It provides fully automated analysis of single-molecule data, including chromatic correction of multi-channel images (based on *naclib* [146]), localization (based on *Picasso* [147]), tracking (based on *TrackPy* [148] and *Swift* [149]), and colocalization analysis.

3.3 Results

3.3.1 Protein identity and quality

All four interleukin receptor subunits were successfully expressed in insect cells and purified using a combination of affinity, size-exclusion and anionic-exchange chromatography. The purity of the subunits was assessed by SDS-PAGE (see Fig. 3.12). The amount of purified protein obtained for each subunit was in the milligram range, which is suitable for the subsequent labeling and purification steps.

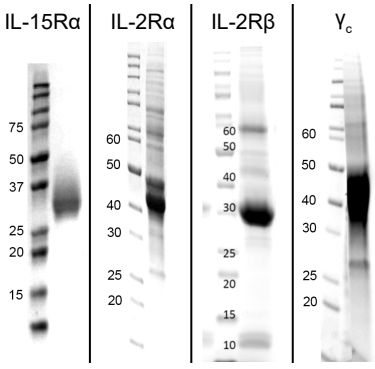

Figure 3.12 • SDS-PAGE gel of purified interleukin receptor subunits

The gel shows the four different purified interleukin receptor subunits, stained with Coomassie Blue. The molecular weights of each interleukin receptor subunit can be estimated based on their migration on the gel compared to protein standard ladder of known size.

Mass spectrometry analysis was performed for initial purification batches of IL-2Rβ and γ_c to confirm the identity of the bands on the SDS-PAGE gel. The results demonstrated that our transfection and expression system effectively expressed the target proteins as intended. One of the non-attributable bands was identified as elongation factor-1α, which was co-purified along with the target proteins during the affinity purification steps, and removed by subsequent purification steps.

Furthermore, we observed shifted and smeared bands on the SDS-PAGE gel, which deviated from the expected molecular weight based on the amino acid weight of the interleukin receptor subunits. We associated this observation with different glycosylation states of the expressed proteins, as glycosylation is a common post-translational modification in eukaryotic cells. To confirm this hypothesis, a deglycosylation assay was conducted (see Fig. 3.13 and Section 3.6.1), which revealed the disappearance of higher molecular weight bands and the appearance of lower molecular weight bands, suggesting that the shifted and smeared bands are caused by the presence of various glycosyl groups of different sizes. For a complete removal of all glycosyl groups, a more comprehensive screening of different deglycosylation enzymes and conditions would likely be necessary.

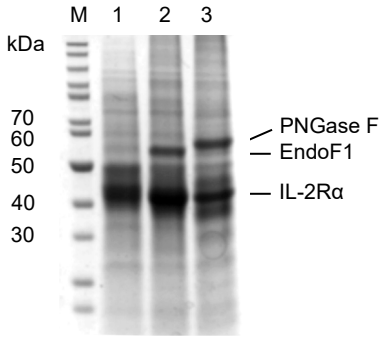

Figure 3.13 • Deglycosylation assay

SDS-PAGE gel showing the effect of deglycosylation enzymes on recombinantly expressed IL-2Rα. Lane 1 is the untreated protein, lanes 2 and 3 show IL-2Rα incubated with two different deglycosylation enzymes, endoglycosidase F1 and Peptide:N-glycosidase F. The shifted and smeared bands observed in the native protein are less pronounced in the deglycosylated samples, indicating partial removal of glycosyl groups. Molecular weight markers are shown on the left for reference.

Thermal stability of the in-house recombinantly expressed interleukin receptor subunits and commercially obtained IL-2 and IL-15 ligands was evaluated on a thermal shift assay (TSA) device (Prometheus, Nanotemper). The recombinantly expressed interleukin receptor subunits showed a clear transition from folded to unfolded, indicating that they were properly folded and stable (see Fig. 3.14a). In contrast, the commercially obtained interleukin ligands generally did not show a clear transition from folded to unfolded, suggesting that they are less stable or less properly folded. Notably, thermal stability data varied significantly between the commercially obtained interleukin ligands, indicating differences in the quality of the protein preparation among different manufacturers (see Fig. 3.14b).

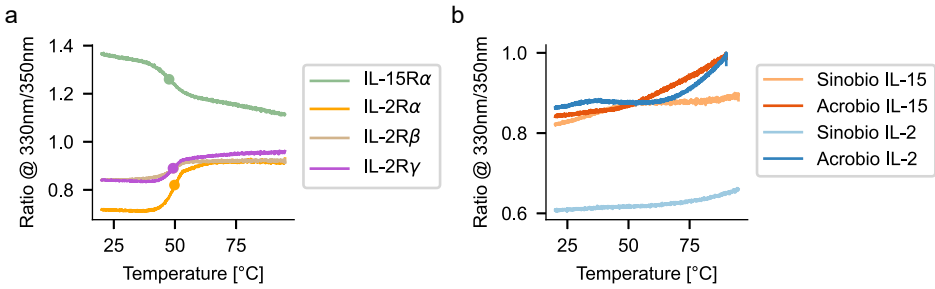

Figure 3.14 • Thermal shift assay of interleukin receptor subunits and ligands
Intrinsic fluorescence ratio change during a TSA for **(a)** recombinantly expressed interleukin receptor ectodomains (folding state transition temperatures T_i for the receptor subunits were in the range between 47.6 °C and 49.8 °C), and **(b)** commercially obtained recombinantly expressed interleukin ligands (folding state transition temperatures T_i for IL-15 were in the range between 37.9 °C and 39.2 °C and not detectable for IL-2).

To further investigate the functional quality of the proteins, microscale thermophoresis (MST) was performed (see Fig. 3.15). MST is a bulk assay to measure protein-protein interaction, which means that any non-functional proteins will lead to an overestimation of the dissociation constant. In fact, we measured a dissociation constant $K_D = 263 \pm 53\,\text{nM}$, which is several orders of magnitude above the reported literature values in the 1-10 pM range [43, 150]. Combined with the TSA experiments, these findings provide further evidence for potential issues with the functional quality of the interleukin ligands.

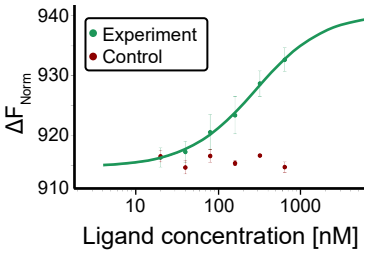

Figure 3.15 • Microscale thermophoresis analysis of interleukin receptor-ligand binding

Titration curve displaying the change in the fluorescence ratio F_{Norm} at different concentrations of IL-15Rα, IL-2Rβ, IL-15, with a fixed concentration of fluorescently labeled γ_c-ATTO 643 (40 nM). $K_{\text{D, fit}} = 263 \pm 53\,\text{nM}$ (green curve). The control experiment without IL-15 is shown in red, with no detectable K_D.

3.3.2 Sortase-mediated labeling of interleukin receptor chains

The labeling of interleukin receptor chains was assessed using a combination of SDS-PAGE and fluorescence imaging. To ensure accurate interpretation of the results, samples of the labeling reaction were taken at different timepoints and ran on a gel together with several controls. In particular, it was critical to include controls for the fluorescently-labeled peptides, as some peptides ran at unexpected molecular weights on the SDS-PAGE, which could lead to misinterpretation. As shown in Fig. 3.16 for IL-2Rβ, successful sortase-mediated labeling was observed, as evident by the fluorescent band at the same height as the IL-2Rβ receptor subunit. The addition of the peptide tag increased the molecular weight of the protein by approximately 2 kDa, resulting in the appearance of a second band above the original IL-2Rβ band in the Coomassie Blue stained gel.

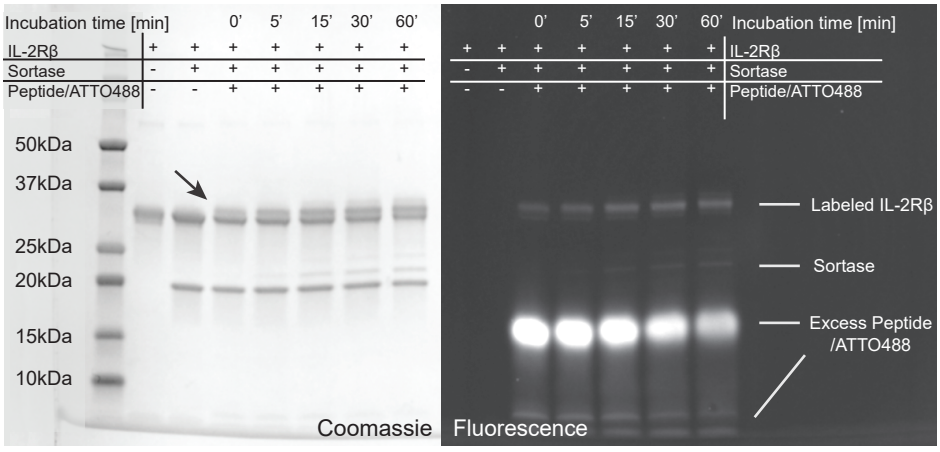

Figure 3.16 • SDS-PAGE and fluorescence imaging of sortase labeling reaction
SDS-PAGE image showing the results of a sortase-mediated labeling reaction for IL-2Rβ. Multiple aliquots of the labeling reaction were taken at different timepoints and run on the gel, along with several controls and a protein ladder of known molecular weights for reference. The gel was stained with Coomassie Blue and imaged on a bright-field and fluorescent gel imager. The appearance of fluorescently-labeled IL-2Rβ bands indicate successful labeling. The Coomassie Blue-stained gel (left) shows a shift in molecular weight of the target protein due to the conjugation of the fluorophore-labeled peptide (red arrow). The unreacted excess peptide runs at an apparent molecular weight higher than expected (right gel, at around 15 kDa), which may be attributed to the charge or chemical structure of the fluorophore, and is not visible in the Coomassie Blue staining due to the peptide's small actual molecular weight (2 kDa).

The degree of labeling (DOL) was determined for preparative batches of labeled and purified proteins by analyzing the absorbance spectra measured with a photospectrometer (see Section 3.6.1).

Protein	IL-15Rα	IL-2Rα	IL-2Rβ	γ_c
ATTO 488	90%	-	-	-
ATTO 565	-	61% (*)	117% (**)	-
ATTO 643	-	-	-	81%

Table 3.3 • Degree of labeling
Degree of labeling after sortase-labeling and Ni-NTA and Strep-Tactin affinity chromatography for different combinations of fluorophore-conjugated peptide and interleukin receptor subunits. (*) Only Ni-NTA affinity purified. (**) $>$ 100% likely due to unknown residual concentration of desthiobiotin in the sample.

3.3.3 Supported lipid bilayer preparation

The fluidity and homogeneity of the SLBs are critical factors for the successful execution of reconstitution experiments. By providing a two-dimensional surface, the SLB enables the receptor subunits to diffuse freely, thereby facilitating lateral interactions among each other and with their ligands. The homogeneity, defect-free nature, and mobility of the SLBs were assessed by incorporating fluorescently labeled lipids into the DOPC/Ni-NTA lipid mix and optimized by testing different surface and SUV preparation protocols, and different protein incubation times and concentrations (see Fig. 3.17).

The mobility of the SLB was quantified using FRAP, which involved photobleaching a small region of the SLB containing fluorescently labeled lipids, followed by monitoring the recovery of fluorescence over time. Analysis of the recovery kinetics (see Section 3.6.4) demonstrated that properly prepared SLBs were highly mobile ($D > 2\,\mu m^2\,s^{-1}$), and enabled free diffusion of reconstituted proteins (see Fig. 3.18).

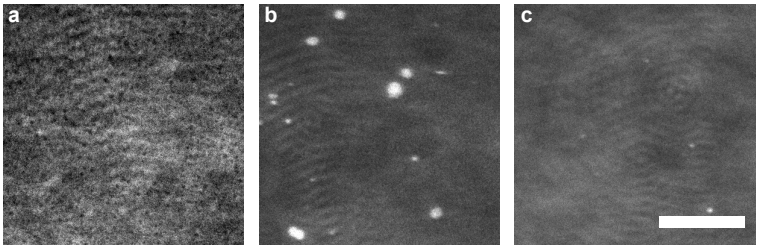

Figure 3.17 • Optimizing SLB quality
The quality of SLBs can be improved by optimizing surface preparation and small unilamellar vesicle generation. **(a)** Insufficiently cleaned coverslips can result in immobile bilayers, that show no or impaired recovery during fluorescence recovery after photobleaching (FRAP) experiments, or defects in the bilayer, as seen by dark spots. **(b)** Excess lipid vesicles or liposomes can attach to the bilayer even after thorough washing, due to incorrect preparation of small unilamellar vesicles, such as not drying the lipid-in-chloroform solution adequately towards a thin film before re-suspending, or insufficient sonication of liposomes. **(c)** A properly formed homogeneous bilayer. Scale bar is 15 µm.

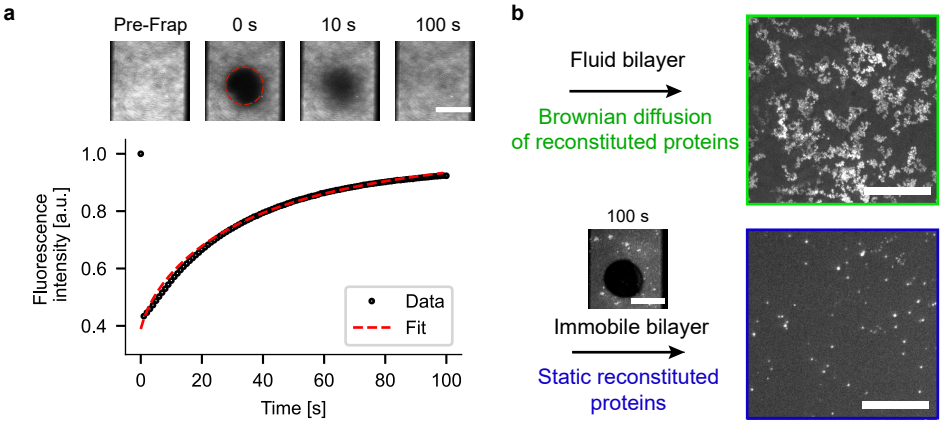

Figure 3.18 • SLB quality assessment via FRAP
(a) Top: A circular spot (red circle) on a SLB with fluorescently labeled lipids is bleached, and the subsequent recovery of intensity due to the diffusion of unbleached lipids into the bleached area is recorded. Bottom: The mobility of the bilayer, represented by the diffusion constant of the fluorescently labeled lipids is derived by fitting the data: $D = 2.11\ \mu m^2\ s^{-1}$. The recovery of intensity, compared to the value before bleaching, was 92.3% after 100 s. Scale bar is 30 µm. **(b)** Top: Reconstituted proteins on a fluid bilayer show Brownian diffusion, as displayed by a maximum projection of 50 frames of a movie (25 Hz framerate). Bottom: Immobile bilayer with impaired recovery during a FRAP experiment, with the bleached area still distinctly visible after 100 s. Reconstituted proteins on a immobile bilayer remain static. Scale bar is 30 µm.

3.3.4 Protein reconstitution

To achieve reproducible reconstitution of individual, diffusive His-tagged proteins at single-molecule densities on SLBs, it was necessary to optimize the experimental protocol. We tested various buffer compositions, protein incubation concentrations and durations. Even in seemingly homogeneous SLBs, nanoscopic defects lead to immobilization (and likely denaturation) of proteins and impair single-molecule tracking. Additionally, denatured and aggregated proteins, as a result of the freezing-thawing of protein aliquots, bind unspecifically to the bilayer surface. To suppress unspecific binding and block bilayer defects, blocking agents such as bovine serum albumin (BSA) and casein are commonly used in reconstitution experiments [127, 134, 151]. After formation of the SLB, we incubated the bilayer with 10 mg mL^{-1} BSA and kept BSA present at 1 mg mL^{-1} in all subsequent steps. Fig. 3.19 shows the effects of different BSA concentrations on the reconstitution of His-tagged proteins.

To test the specific interaction between His-tagged proteins and nickelated lipids, we added imidazole, a molecule that competes with histidine residues for nickel binding, to a sample of reconstituted proteins. The addition of imidazole led to the immediate unbinding of the majority of proteins, as shown in Fig. 3.20.

For a given molar amount of nickelated lipids in the SLB, both the protein concentration during incubation and the incubation duration itself affect the density of reconstituted proteins. His-tagged proteins form more stable interactions when incubated for longer [140], but over time also degrade. Therefore, we chose a compromise of 1 h for incubation, and found that protein concentrations in the range of 100 pM to 1 nM resulted in a density appropriate for single-molecule tracking (see Fig. 3.21). With increasing densities ($> 0.3\,\mu m^{-2}$, tracking algorithms become unreliable as particle trajectories overlap and cross each other [152]. Eventually, point spread functions of individual particles overlap and single-molecule localization becomes unfeasible.

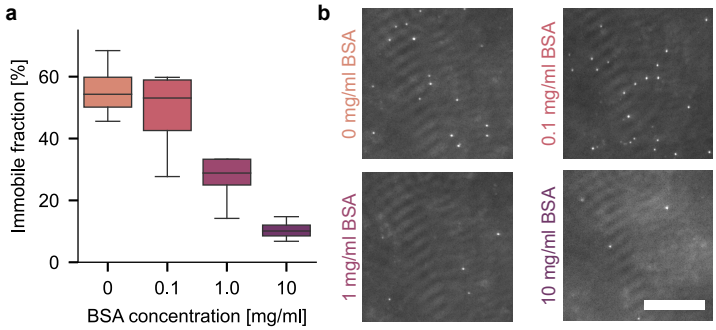

Figure 3.19 • Blocking of bilayer defects with BSA
The effect of BSA concentration on reconstitution of His-tagged proteins on SLB is quantified in **(a)**. Immobile proteins were identified by averaging the first 100 frames of TIRF movies of reconstituted proteins of SLBs that have been blocked with different amounts of BSA. As the concentration of BSA increases, the fraction of immobile molecules decreases. **(b)** Representative images of reconstituted proteins on the SLB at different BSA concentrations, averaged across the first 100 frames to identify immobile proteins. Scale bar is 5 µm.

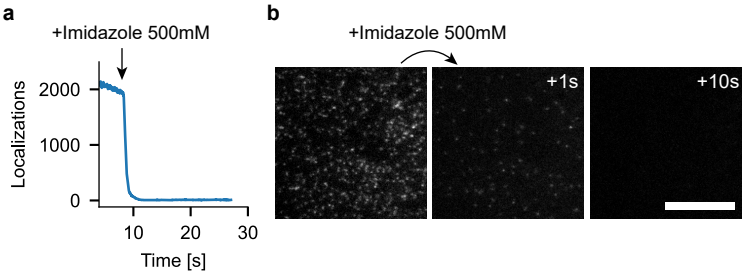

Figure 3.20 • Imidazole-induced dissociation of His-tagged proteins from nickelated SLB
(a) Number of His-tagged reconstituted proteins present in a given field of view during the addition of 500 mM imidazole. Proteins to dissociate promptly by acting as a competitive agent, confirming the specificity of the histidine-nickel interaction. **(b)** Still frames of a section of the field of view before, 1 s after and 10 s after addition of 500 mM imidazole to the sample chamber. Scale bar is 15 µm.

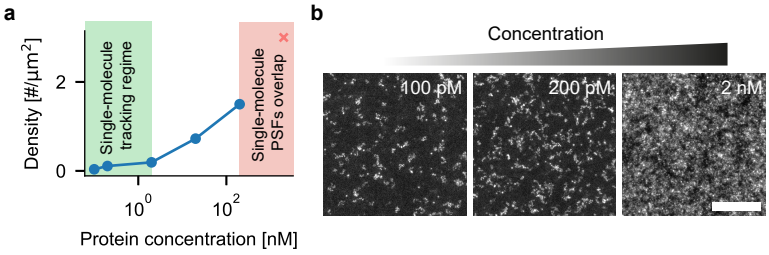

Figure 3.21 • Density of reconstituted His-tagged IL-15Rα at different incubation concentrations

(a) Density of IL-15Rα for increasing protein incubation concentrations on a SLB containing 1 mol% Ni-NTA lipids after 1 h incubation.
(b) Corresponding maximum projections (initial 10 frames) of TIRFM videos of reconstituted IL-15Rα with different incubation concentrations. Scale bar is 15 µm.

3.3.5 Tracking and colocalization experiments

As described in Chapter 1, the photostability of the fluorescent labels has an impact on the analysis of single-molecule tracking data. Therefore, we evaluated the photostability of the fluorescently labeled receptor subunits by recording single-molecule bleaching curves of fluorescently labeled reconstituted interleukin receptor subunits. We observed distinct bleaching kinetics for each fluorophore, as determined by their respective bleaching constants, representing the time for the number of trajectories to decay to $1/e \approx 37\%$ (ATTO488: 5.5 ± 2.2 s, ATTO565: 17.7 ± 5.5 s, ATTO643: 99.8 ± 8.8 s; see Fig. 3.22). This variation in bleaching rates can be attributed to the unique photophysics of each fluorophore [153].

Subsequently, we reconstituted the full IL-15 receptor and added varying amounts of ligands to investigate the formation of dimers (IL-2Rβ and

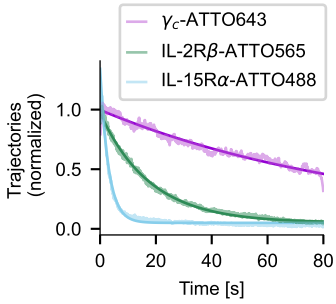

Figure 3.22 • Photostability of fluorescent labels

Number of trajectories against time showing distinct bleaching kinetics of fluorescently-labeled receptor subunits. Bleaching constants were obtained by fitting exponential functions to the bleaching curves.

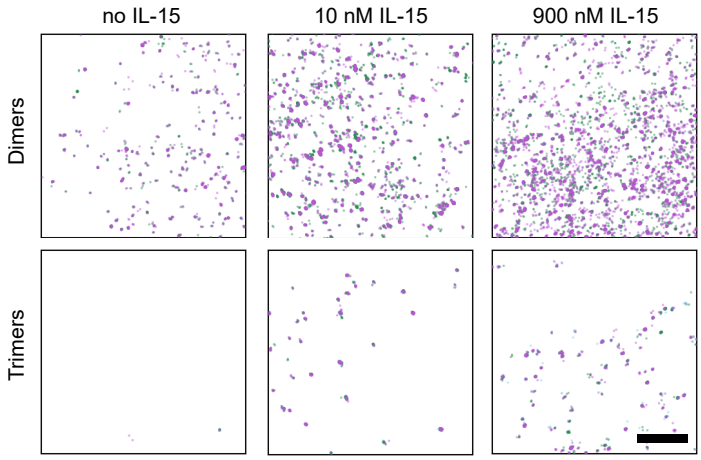

Figure 3.23 • Formation of interleukin receptor complexes
Reconstituted IL-15 receptors show (limited) interaction in response to varying amounts of IL-15 ligand added. Top row: Colocalization events between IL-2Rβ (green) and γ_c (magenta) for different ligand concentrations. Lower row: Trimeric colocalization events involving IL-15Rα (blue), IL-2Rβ and γ_c. No trimers were observed for ligand concentrations below 1 nM. Scale bar is 10 µm.

γ_c subunits) and trimers (IL15-Rα, IL-2Rβ, γ_c subunits). For ligand concentrations below 1 nM, the assembly of the trimeric receptor could not be observed. In line with the MST measurements, we observed dimers and trimers at increased ligand concentrations (see **Fig. 3.23**, **Fig. 3.24a**).

However, the fraction of interaction molecules and their duration was much lower than what could be expected based on the stability of the trimeric receptor (K_D in the low picomolar range, see **Table 3.1**). The observed lifetimes of trimeric receptors were $\tau_{\text{obs}} \approx 2.6\,\text{s}$. After correcting for bleaching (see **Chapter 1**, [154]) we obtain:
$\tau_{\text{corrected}} = \left(\tau_{\text{obs}}^{-1} - \tau_{\text{ATTO488}}^{-1} - \tau_{\text{ATTO565}}^{-1} - \tau_{\text{ATTO643}}^{-1}\right)^{-1}$
$= (1/2.6\,\text{s} - 1/5.5\,\text{s} - 1/17.7\,\text{s} - 1/99.8\,\text{s})^{-1} \approx 7.3\,\text{s}.$
This is more than 100 times shorter than a conservative estimation of the expected interaction duration based on the solution dissociation constant:$1/10^{-3}/\text{s} = 1000\,\text{s} \approx 17\,\text{min}$ (see **Table 1.1**).

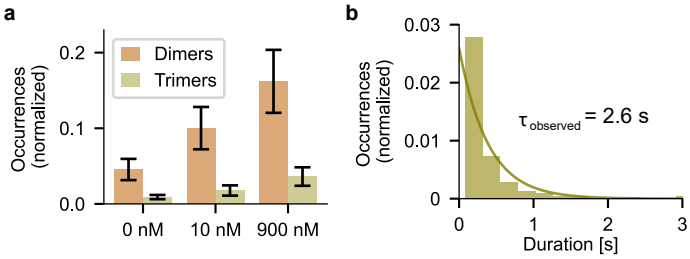

Figure 3.24 • Frequency and lifetime of dimers and trimers
(a) The occurrence of IL-2Rβ-γ_c dimers (orange) and IL-15Rα-IL-2Rβ-γ_c trimers (green) at different IL-15 ligand concentrations. **(b)** Duration of trimer interactions fitted with an exponential decay curve, yielding a bleaching-uncorrected lifetime of 2.6 s for the trimeric receptor.

These results prompted us to assess ligand-receptor interaction in a simplified system involving only IL-15 and IL-15Rα, in conjunction with an antibody against IL-15 (see **Fig. 3.25**). We observed short-lived colocalizations lasting only a few seconds, which again did not align with our initial expectations. The reported K_D of 38 pM of IL-15 to the IL-15Rα subunit [88] would result in interaction durations in the order of 30 s to 45 min (see **Table 1.1** in **Chapter 1**).

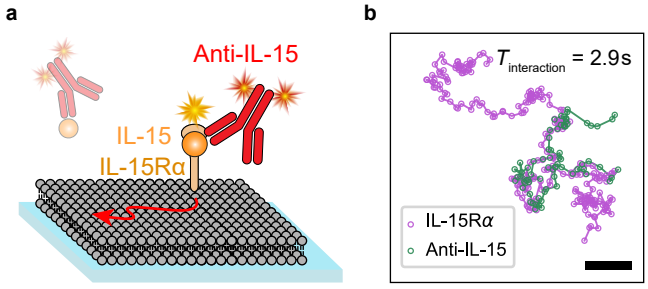

Figure 3.25 • IL-15-IL-15Rα binding functionality
(a) Experimental design where IL-15 (orange) binds to IL-15Rα receptor subunits (orange) and anti-IL-15 antibody (red) targeting IL-15. **(b)** Co-diffusion tracks of IL-15Rα (magenta) and anti-IL-15 antibody (green), providing indirect evidence for the binding of IL-15 to IL-15Rα. Scale bar is 2 µm.

3.3.6 eGFRD simulations of IL-2/IL-15 receptor assembly

In close exchange with our group, Tom Clement and Prof. Dr. Pieter Rein ten Wolde (AMOLF, Amsterdam) conducted enhanced Green's Function Reaction Dynamics (eGFRD) simulations to investigate the binding dynamics of IL-2 and IL-15 to their receptors [155]. Their findings suggested that preformed IL-2Rα-IL2-Rβ complexes provide the main entry point for IL-2 to bind to receptor subunits on the membrane, due to the interaction between IL-2Rα and IL-2Rβ receptor subunits (see **Fig. 3.26**, [103]).

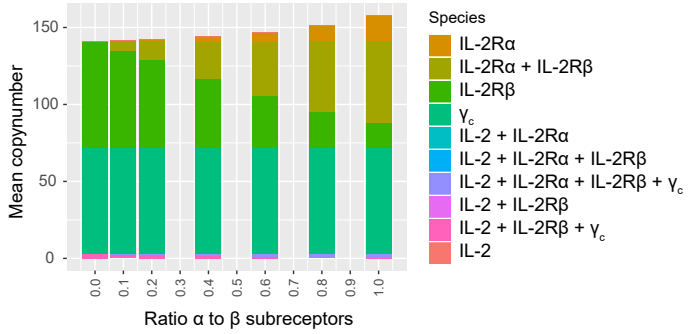

Figure 3.26 • IL-2 recruitment via preformed IL-2Rα-IL-2Rβ dimers
Average particle numbers of ligand and receptor subunits at different IL-2Rα surface densities. Without IL-2Rα, IL-2 only binds to IL-2Rβ-γ_c. With increasing IL-2Rα concentration, IL-2 recruitment shifts towards preformed IL-2Rα-IL-2Rβ complexes. Figure adapted from Clement *et al.*, 2021 [155].

The simulations also showed that even in high IL-2Rα surface density regimes, a significant ratio of IL-2-bound receptors remain in the low-affinity IL-2Rβ-γ_c form (see **Fig. 3.27**). This suggests that the intermediate-affinity IL-2Rβ-γ_c receptor may work as a dampening factor on the signal of the high-affinity trimeric receptor.

These findings have important implications when it comes to drug development: IL-2 analogues with greater specificity for the IL-2Rβ-γ_c receptors could shift the IL-2 balance towards effector T cells instead of regulatory CD25+ (IL-2Rα) T cells, potentially leading to superior antitumor properties [76, 85]. Besides enhancing the affinity of IL-2 for IL-2Rβ-γ_c, our findings suggest that reducing IL-2Rα-IL-2 affinity, or blocking the interaction of IL-2Rα-IL-2Rβ may be promising options to differentially attenuate IL-2 recruitment to CD25+ T cells by weaken-

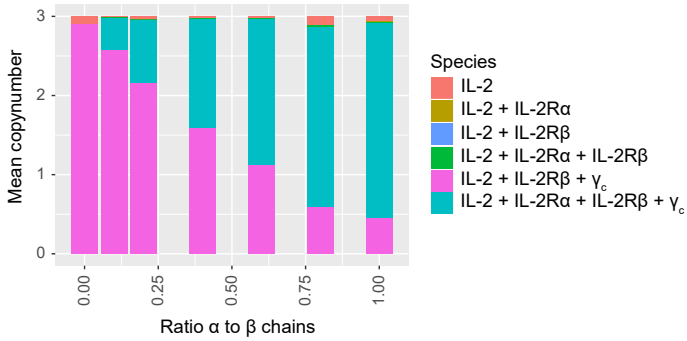

Figure 3.27 • IL-2Rβ-γ_c in complex with IL-2 maintains significant fractions even at high IL-2Rα densities
Average particle numbers of free IL-2 and IL-2 containing subreceptor units at different IL-2Rα surface densities. Even at equal densities of IL-2Rα, IL-2Rβ and γ_c, IL-2 in complex with IL-2Rβ-γ_c remains significant ($\approx$ 15%). Figure adapted from Clement *et al.*, 2021 [155].

ing the IL-2Rα-IL-2 recruitment pathway. Combining these simulations and the corresponding (single-molecule) binding kinetics measurements have the potential to drastically accelerate the targeted development of drugs with superior therapeutic activity [42, 76, 77].

3.4 Discussion

By using single-molecule tracking techniques, the binding and dissociation of individual interleukin receptor-ligand complexes, as well as the effect of different ligand-presentation modes or receptor subunit compositions can be observed. These parameters are critical for understanding the specificity and selectivity of receptor-ligand interactions and their roles in immune responses. Moreover, a better understanding of the underlying molecular mechanisms of interleukin receptor signaling has the potential to accelerate the development of targeted drugs, as promising recent studies have shown [42, 76, 77].

The focus of this chapter was on the development of an experimental platform and analytical tools for investigating the kinetic properties of IL-2 and IL-15 binding to their receptors through single-molecule tracking. The accomplishments of this research include the successful expression and site-specific labeling of receptor subunits, the optimization of the reconstitution protocol, and the development of an analysis platform for single-molecule tracking data (see **Section 3.6.4**, **Fig. 3.31**).

Using TSA and MST, we found hints that the quality of the commercially available ligands were inferior. No clear unfolding transitions were observed in TSA measurements, suggesting that a large fraction of the protein is misfolded or unfolded. Binding constants measured with MST were several orders of magnitude higher than expected, consistent with the presence of non-functional ligands. As a result, the obtained single-molecule data was of limited quality and not suitable for detailed analysis in this thesis. Additionally, the data quality was limited by photobleaching of the fluorescent dyes. For IL-2/IL-15 receptor studies, this is specifically limiting, since the high stability of the ligand-receptor complexes require prolonged observation [103–105]. Despite these challenges, we were able to observe some instances of receptor colocalization - although not enough to draw any meaningful conclusions from these observations. Further improvements in labeling techniques (see **Chapter 4**) and sourcing of higher quality interleukin ligands, or in-house expression, will be necessary to overcome these challenges. Nevertheless, the experimental platform and the protocols established in this chapter will provide a vantage ground for further single-molecule tracking studies.

It is our hope that this research will not only deepen our understanding of interleukin receptors, but also pave the way for future studies that aim to leverage single-molecule tracking to gain insights into the dynamics of other biomolecular interactions. These strategies can help advance our general understanding of receptor signaling pathways and contribute to the development of new therapeutic approaches.

3.5 Methods

Expression and purification of interleukin receptor subunits

Sf-9 cells were obtained from ATCC (ATCC number CRL-1711) and cultured in suspension in Insect Xpress medium (Lonza) at a density of around 1E06/ml at 28 °C in a bench top orbital shaker (New Brunswick Innova 40, Eppendorf), with total volumes of up to 3 L. Cells were infected with 1 mL of baculovirus per 500 mL of cell suspension. Baculovirus solution (P2 generation), carrying the respective sequences of the extracellular domains of IL-2Rα, IL-15Rα, IL-2Rβ and γ_c with N-terminal sortase-tags and C-terminal His-tags (12x His), were a kind gift of Ricardo Lopes Fernandes (Garcia Lab, Stanford University). Three days after transfection, cells were pelleted by centrifugation (15 minutes, 1500 rpm). In order to precipitate components present in the medium

that would also bind to Ni-NTA and hence interfere, calcium- and nickel salts and TRIS buffer (pH 8) were added to the supernatant to final concentrations of 4 mM $CaCl_2$, 0.8 mM $NiCl_2$ and 40 mM TRIS. Precipitate formed after stirring for 15 minutes was removed by centrifugation (20 minutes, 4000 rpm). The supernatant was collected, filtered through a 0.45 µm-filter and loaded onto a 1 mL HisTrap excel affinity column at a flow rate of 3 mL/min on a FPLC system (Biorad NGC or ÄKTA pure). Bound protein was eluted using 200 mM imidazole. Depending on the purity of the eluted protein, further purification steps such as size-exclusion chromatography (ENrich SEC70, ENrich SEC650, HiLoad Superdex 16/600 75 pg) or ion-exchange chromatography (ResQ anion exchange column) were performed. Protein was upconcentrated using centrifugal filter units (Amicon Ultra 15, 10 kDa cutoff) to concentrations of 30 to 150 µM and aliquoted in 100 µL volumes, flash-frozen in liquid nitrogen and stored at −80 °C until further use.

Nickel ions are more strongly bound to the Ni Sepharose excel resin compared to conventional resins, preventing the stripping of nickel ions by chelating and reducing agents present in the insect cell medium.

Thermal shift assay and microscale thermophoresis

TSA were performed by Dr. Alex Fish at NKI. Ectodomains of IL-15Rα, IL-2Rα, IL-2Rβ and γ_c, as well as commercially obtained IL-2 and IL-15 were loaded into capillaries at concentrations of 0.1 mg mL^{-1}, supplemented with 0.05% Tween-20 to prevent adsorption to capillary walls. Capillaries were heated from 20 °C to 95 °C in a Prometheus TSA machine (Nanotemper). A temperature slope of 1 °C min^{-1} and a UV excitation power of 100% was used for all experiments. MST experiments were performed by Dr. Alex Fish at NKI. Ectodomains of IL-15Rα, IL-2Rβ and commercial IL-15 (Sinobiological) were titrated from 20 nM to 640 nM into individual samples containing 40 nM ATTO 643-γ_c and 0.05% Tween-20. Samples were loaded into capillaries and microscale thermophoresis was measured on a Monolith machine (Nanotemper), using 50% excitation power (red laser) and 40% heating power. A control experiment was performed by titrating ectodomains of IL-15Rα, IL-2Rβ without the IL-15 ligand into individual samples containing 40 nM ATTO 643-γ_c and 0.05% Tween-20.

Deglycosylation assay

The deglycosylation assay was performed by Dr. Patrick Celie (NKI). IL-2Rα (1 mg mL^{-1}) were incubated overnight with endoglycosidase F1 (0.5 mg mL^{-1}) and Peptide:N-glycosidase F (0.5 mg mL^{-1}) for 45 min at 37 °C. IL-2Rα and glycosidase enzymes were expressed at NKI. Samples were ran on a SDS-PAGE gel together with a IL-2Rα-only control.

Protein labeling

For the labeling of receptor subunits with spectrally different dyes, HPLC-purified N-terminally fluorophore-conjugated peptides (Peptide Specialty Laboratories GmBH) were obtained with the fluorophores ATTO 488, ATTO 565 or ATTO 643. Peptides were dissolved towards 40 mM in DMSO (Sigma-Aldrich) and stored at −20 °C until further usage. The sortase plasmid (tetramutant construct with deleted N-terminal flexible region) was a kind gift of Prof. Sattler, and the expression was performed as described [156]. Briefly, a 4 mL overnight culture in 2xYT medium containing 50 mg mL^{-1} Kanamycin was prepared and diluted 100-fold on the next day. Protein expression was induced by adding 0.5 mM IPTG at an OD of 0.6-0.7. After overnight incubation at 25°, cells were pelleted (5000 rpm, 20 min) and resuspended in lysis buffer (50 mM TRIS pH7.5, 150 mM NaCl, 5 mM $MgCl_2$, 10% glycerol, 10 mM imidazole) at a concentration of 0.2 g mL^{-1}, homogenized in a Dounce homogenizer and passed through a French pressure cell press three times. The lysate was centrifuged (27000 rpm, 50 min) and the supernatant was loaded onto Ni-NTA beads or a Ni-NTA affinity column, and washed with 50 mM TRIS buffer at pH8, 150 mM NaCl, 25 mM imidazole. Bound protein was eluted using 250 mM imidazole and loaded onto a Hi-Load Superdex 75 16/60 size-exclusion chromatography column. Three peaks were identifiable in the chromatograms, of which the first and second were identified as sortase (monomer and dimer), pooled, and subjected to Tobacco Etch virus (TEV) protease cleavage, to remove the His-tag that would otherwise interfere with the purification of the labeled interleukin proteins: The concentration of the sortase was measured using a spectrophotometer (Nanodrop 2000) and 100U of His-tagged TEV protease were added per 1 mg of sortase. After overnight incubation at 4 °C, the solution was loaded onto a Ni-NTA affinity column without imidazole present. The flow through containing cleaved sortase was concentrated to 100 µM using centrifugal filter units (Amicon Ultra 15, 10kDA cutoff), flash-frozen in liquid nitrogen in 100 µL aliquots and stored at −80 °C.

In trial purifications where the size-exclusion chromatography step was omitted, aggregation of sortase was observed, likely due to the presence of misfolded sortase which is removed by the SEC.

Sortase-mediated labeling The sortase-mediated labeling of interleukin receptor subunits was performed following a previously described protocol [139]. In brief, a reaction mix containing 50 µM interleukin receptor subunits, 100 µM Sortase, and 500 mM fluorophore-conjugated peptide dissolved in DMSO was prepared in buffer containing 10 mM $CaCl_2$ and 100 mM $NaHCO_3$. The reaction was allowed to proceed at room temperature for 4 hours in the dark, after which it was loaded onto a HisTrap HP 1 mL Ni-NTA column (29051021, Cytiva) equili-

brated in HEPES-buffered saline (HBS buffer, 20 mM HEPES pH 7.6, 140 mM NaCl) using a FPLC system (ÄKTA pure). Bound protein was eluted using 200 mM imidazole, and loaded onto a StrepTrap HP 1 mL StrepTactin column (29048653, Cytiva) equilibrated in HBS buffer. Labeled protein was eluted using 2.5 mM desthiobitin (D1411, Sigma-Aldrich), dialyzed against HBS buffer and up-concentrated to a concentration of 1 to 50 µM using Amicon Ultra 15 centrifugal filter units (10 kDa cutoff). The labeled protein was then split into 3-5 µL aliquots, flash-frozen in liquid nitrogen, and stored at −80 °C until further use. It is important to note that, as a lower boundary, 1 mg protein was used per labeling round, corresponding to 0.5 to 1 mL of reaction mix. This was due to the inevitable loss of protein during purification and up-concentration, which would take up a large fraction when handling even smaller starting amounts and volumes.

Supported lipid bilayer formation

SUVs were prepared by sonicating an aqueous solution of liposomes. To this end, lipids dissolved in chloroform were mixed in the desired molar ratios: 89.5 mol% DOPC (850375, Avanti), 1 mol% DGS-NTA-Ni (790404, Avanti) and 0.5 mol% DOPE-ATTO 390 (AD 390-161, ATTO-TEC. Since chloroform is volatile and damages standard micropipettes, positive-displacement pipettes were used. Typical final lipid preparation amounts were 1-10 mg in about 200 µL to 2 mL of chloroform. The lipids were dried to a thin film on the walls of a flask in a chemical flow hood. The mixture was continuously swirled, while gently blowing a stream of nitrogen into the flask. Residual chloroform was removed by placing the flask in a desiccator overnight, wrapped in aluminium foil to prevent bleaching of fluorescent lipids. Lipids were resuspended to a final concentration of 2 mg mL^{-1} in HBS. Successful resuspension of the lipids was indicated by the formation of a milky suspension of liposomes in buffer. Liposomes were aliquoted in PCR tubes in volumes of 10-20 µL and stored at −20 °C until further usage, for up to three months. SUVs were prepared on the day of the reconstitution experiment by wrapping individual PCR tube aliquots in Parafilm to prevent water entering the tube, and subjecting them to 30 min of sonication in an ice-cooled water-bath sonicator shielded from light. The aliquot was positioned such that the liquid inside was visibly agitated.

Using a round-bottom flask for this process is recommended to facilitate the formation of homogeneous thin lipid layers.

Microscopy glass slides (1.5H, 631-0851, VWR) were pre-treated using piranha solution, a 3:1 mixture of 95%-98% sulfuric acid (258105, Sigma-Aldrich) and 30% hydrogen peroxide (216763, Sigma-Aldrich). To reduced the risk of chemical accidents, piranha cleaning was performed in a chemical flow hood. Sulfuric acid and hydrogen peroxide

were stored in small amounts (<20 mL) and distributed on the glass slides drop-wise, using individual Pasteur pipettes. Microscopy glass slides were distributed on a large Petri dish, to provide an inert surface and to facilitate picking up the glass slides with tweezers afterwards. For 22 x 22 mm glass slides, six drops of sulfuric acid were distributed on the center of the slide, before the addition of two drops of hydrogen peroxide. During incubation, glass slides were covered by a glass Petri dish for additional safety. The activity of reagents was ensured by keeping the hydrogen peroxide at 4 °C, and replacing reagents monthly. After one hour, slides were picked up with metal tweezers, thoroughly washed with milliQ water and dried using a gentle flow of nitrogen. Then, sample chambers were created by glueing 0.5 mL Eppendorf tubes with the conical part removed onto the glass slides, using UV-curable optical adhesive (NOA68, Thorlabs). The slides were cured in three minutes using a 36 W UV nail dryer (B00R4M0TI0, Nailstar). The cured sample chambers were then subjected to air-plasma cleaning for 10 minutes (Harrick Plasma Cleaner PDC-002-HPCE). Afterwards, the sample chambers were immediately filled with 50 µL HBS, followed by 50 µL of sonicated SUV solution, diluted to 0.2 mg mL^{-1}. After 30 min incubation in a dark, moisturized box, excess SUVs were removed by careful washing with 1 mL of HBS.

Based on our experience, the piranha solution was active enough as long as some of the glass slides misted up or even produced smoke when the hydrogen peroxide was added.

The quality of the SLBs was assessed using FRAP and visual inspection for homogeneity and macroscopic defects on a TIRF microscope. Microscopic defects were blocked by incubating the SLB with 10 mg mL^{-1} BSA (A9418, Sigma-Aldrich, supernatant after centrifugation at 4 °C for 60 min at 16.100 g) for 30 min, followed by careful washing with 1 mL of HBS.

Reconstitution of His-tagged interleukin receptors

Recombinantly expressed His-tagged interleukin receptor subunits were thawed, diluted to 100 µL in HBS supplemented with 1 mg mL^{-1} BSA (HBSB), and centrifuged using a Beckman Coulter Airfuge Ultracentrifuge (4 °C,30 min, 199000 g). Supernatants were diluted in HBSB and added to the sample chamber at final concentrations of 100 pM to 1 nM. After 1 h incubation, unbound protein was removed by careful washing with 1 mL HBSB. After 30 min, the buffer was exchanged with HBSB supplemented with an oxygen-scavenging and triplet-quenching system consisting of 3.7U/mL pyranose oxidase (P4234, Sigma-Aldrich), 200U/mL catalase (C40, Sigma-Aldrich), 0.8% glucose and 2 mM Trolox-Trolox-quinone (238813, Sigma-Aldrich; Trolox to Trolox-quinone ratio 10% to 20%, see Section 3.6.1).

Fluorescence microscopy

Single-molecule tracking experiments were performed on the K2 TIRF setup described in detail in Chapter 2. Experiments were performed at room temperature (20-22 °C). The camera exposure was set to 40 ms at 12-bit, recording a region of interest of 682 x 2048 pixels. The number of frames recorded at a single sample position ranged from 1000 to 50000 frames (40 s to ≈ 7 min). Focus stabilization was used during the recordings. Multicolor channel data was aligned by following the Tetraspeck bead calibration protocol described in Chapter 2.

SLB quality was assessed by FRAP experiments. A typical FRAP experiment was performed by recording several frames, followed by the bleaching sequence where a 150 mm achromatic lens was flipped into the excitation path, upstream of the lens focusing the laser beam onto the back focal plane of the objective. This focuses the laser power towards a circle of 30 µm diameter at the sample plane. Simultaneously, the laser power was increased to the maximum value, achieving an irradiance of about 20 kW cm^{-2}. After 2 s, the lens was flipped out of the excitation path, and the recovery was recorded over a duration of 100 s in 1 s intervals.

3.6 Supplemental Information

3.6.1 Supplemental Methods

Trolox/Trolox-quinone formation protocol

The antifading agent Trolox (TX) acts by quenching triplet states of fluorescent molecules through electron transfer and subsequently recovering the resulting radical ion through a complementary redox reaction. This process requires partial oxidation of Trolox to form a Trolox-quinone (TQ) derivative with strong oxidizing properties. The formation of this oxidized form is achieved via (photo-) reaction with molecular oxygen. For commonly used fluorescent dyes, a molar fraction of TQ in the range of 2-30% was shown to be most efficient at triplet quenching when used at total TX/TQ concentrations of 1-2.5 mM [157].

The preparation of TX/TQ in the appropriate ratio involves dissolving Trolox (at 1 - 2.5 mM, 238813, Sigma-Aldrich) in HBS and illuminating it with a LED lamp on a rotary disk for 10 to 30 hours. Photoinduced oxidation is monitored by measuring the absorption using a Nanodrop 2000 UV-Vis spectrophotometer (see Fig. 3.28). Using the known initial

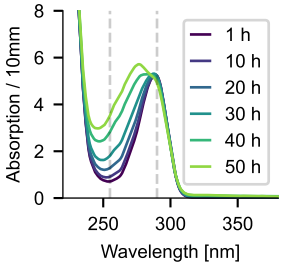

Figure 3.28 • Absorption spectra of Trolox/Trolox-quinone

Trolox/Trolox-quinone absorption spectra after different durations of illumination. Increasing oxidation of Trolox to Trolox-quinone results in a shift of the absorption spectrum.

concentration and the absorption value at 255 nm, the ratio of TX to TQ can then easily be calculated [157].

The absorption A_λ of the Trolox-sample at a specific detection wavelength λ is the combined absorption of both TX and TQ. The extinction coefficients of TX and TQ at the wavelength λ are denoted as $\epsilon_{\lambda(\mathrm{TX})}$ and $\epsilon_{\lambda(\mathrm{TQ})}$, respectively, and d represents the optical path length over which the absorption is measured:

$$A_\lambda = (\epsilon_{\lambda(\mathrm{TX})} \cdot [\mathrm{TX}] + \epsilon_{\lambda(\mathrm{TQ})} \cdot [\mathrm{TQ}]) \cdot d \tag{3.1}$$

Assuming that each TX molecule transforms into one TQ molecule, the starting concentration $[\mathrm{TX}]_0$ is equivalent to [TX], and [TQ] equals 0. The sum of the concentrations of both [TX] and [TQ] equals $[\mathrm{TX}]_0$:

$$[\mathrm{TX}]_0 = [\mathrm{TX}] + [\mathrm{TQ}] \tag{3.2}$$

The concentration of TQ can be determined as a function of the absorbance at a specific detection wavelength by combining **Eq. 3.1** and **Eq. 3.2**.

$$[\mathrm{TQ}] = \frac{\frac{A_\lambda}{d} - \epsilon_{\lambda(\mathrm{TX})} \cdot [\mathrm{TX}]_0}{\epsilon_{\lambda(\mathrm{TQ})} - \epsilon_{\lambda(\mathrm{TX})}} \tag{3.3}$$

Using the absorption value at 255 nm is particularly advantageous in practice, as there is a large difference in extinction at these wavelengths: $\epsilon_{255\mathrm{nm},\,(\mathrm{TX})} = 400\,\mathrm{mol^{-1}\,cm^{-1}}$, $\epsilon_{255\mathrm{nm},\,(\mathrm{TQ})} = 11\,600\,\mathrm{mol^{-1}\,cm^{-1}}$, allowing the detection even of small amounts of TQ.

The initial concentration $[\mathrm{TX}]_0$ is determined by the amount of TX that is dissolved in a given volume of buffer. To minimize errors resulting from the uncertainty when weighing small amounts of TX powder, $[\mathrm{TX}]_0$ can alternatively be determined by measuring the absorption of TX at 290 nm, with the extinction coefficient $\epsilon_{290\mathrm{nm}(\mathrm{TX})} = 2350\,\mathrm{mol^{-1}\,cm^{-1}}$:

$$[\mathrm{TX}]_0 = \frac{\frac{A_{290\mathrm{nm}}}{d}}{\epsilon_{290\mathrm{nm(TX)}}} \tag{3.4}$$

To enable rapid on-the-spot estimation of the TQ fraction, a Python-based web application was deployed on an online integrated development environment, allowing the convenient access from the lab computer located at the Nanodrop spectrophotometer.

Degree of labeling

The degree of labeling was determined for the labeled and purified proteins by analyzing the absorbance spectra measured with a photospectrometer, making use of the Lambert-Beer law:

$$A = \epsilon \cdot c \cdot d, \tag{3.5}$$

with A: absorbance, ϵ: extinction coefficient, c: molar concentration, d: path length.

The concentration of the dye c_{dye} was calculated using its extinction coefficient at the absorption maximum ϵ_{max}:

$$c_{\mathrm{dye}} = \frac{A_{\mathrm{max}}}{\epsilon_{\mathrm{max}} \cdot d} \tag{3.6}$$

The concentration of protein c_{protein} was calculated using its extinction coefficient at 280 nm, corrected for the contributions of the dye and peptide:

$$c_{\mathrm{protein}} = \frac{A_{280} - A_{\mathrm{max}} \cdot \mathrm{CF}_{280,\mathrm{dye}} - c_{\mathrm{dye}} \cdot \epsilon_{\mathrm{peptide}} \cdot d}{\epsilon_{\mathrm{protein}} \cdot d} \tag{3.7}$$

Values for the absorbance A_{max} at the respective absorption maximum λ_{abs} of the dye and correction factor to calculate its absorbance at 280 nm were obtained from the manufacturer. Protein and peptide extinction coefficients were obtained by entering the respective amino acid sequences into the ProtParam tool `web.expasy.org/protparam`.

By combining equations (2.2) and (2.3), it follows for the DOL:

$$\mathrm{DOL} = \frac{c_{\mathrm{dye}}}{c_{\mathrm{protein}}} = \frac{A_{\mathrm{max}}\epsilon_{\mathrm{protein}}}{A_{280}\epsilon_{\mathrm{max}} - A_{\mathrm{max}}\mathrm{CF}_{280,\mathrm{dye}}\epsilon_{\mathrm{max}} - A_{\mathrm{max}}\epsilon_{\mathrm{peptide}}} \tag{3.8}$$

3.6.2 Protein constructs

IL-2Rα

```
         10         20         30         40         50         60
GGGELCDDDP PEIPHATFKA MAYKEGTMLN CECKRGFRRI KSGSLYMLCT GNSSHSSWDN

        70         80         90        100        110        120
QCQCTSSATR NTTKQVTPQP EEQKERKTTE MQSPMQPVDQ ASLPGHCREP PPWENEATER

       130        140        150        160        170        180
IYHFVVGQMV YYQCVQGYRA LHRGPAESVC KMTHGKTRWT QPQLICTGEM ETSQFPGEEK

       190        200        210        220        230
PQASPEGRPE SETSCLVTTT DFQIQTEMAA TMETSIFTTE YQAAAHHHHH HHHHHHH
```

signal peptide 1-21, **22-240 extracellular**, 241-259 transmembrane, 260-272 cytoplasmic

IL-2Rβ

```
        10         20         30         40         50         60
GGGAVNGTSQ FTCFYNSRAN ISCVWSQDGA LQDTSCQVHA WPDRRRWNQT CELLPVSQAS

        70         80         90        100        110        120
WACNLILGAP DSQKLTTVDI VTLRVLCREG VRWRVMAIQD FKPFENLRLM APISLQVVHV

       130        140        150        160        170        180
ETHRCNISWE ISQASHYFER HLEFEARTLS PGHTWEEAPL LTLKQKQEWI CLETLTPDTQ

       190        200        210        220        230
YEFQVRVKPL QGEFTTWSPW SQPLAFRTKP AALGKDTAAA HHHHHHHHHH HH
```

signal peptide 1-27, **27-240 extracellular**, 241-265 transmembrane, 266-551 cytoplasmic

γ_c

```
        10         20         30         40         50         60
GGGLNTTILT PNGNEDTTAD FFLTTMPTDS LSVSTLPLPE VQCFVFNVEY MNCTWNSSSE

        70         80         90        100        110        120
PQPTNLTLHY WYKNSDNDKV QKCSHYLFSE EITSGCQLQK KEIHLYQTFV VQLQDPREPR

       130        140        150        160        170        180
RQATQMLKLQ NLVIPWAPEN LTLHKLSESQ LELNWNNRFL NHCLEHLVQY RTDWDHSWTE

       190        200        210        220        230        240
QSVDYRHKFS LPSVDGQKRY TFRVRSRFNP LCGSAQHWSE WSHPIHWGSN TSKENPFLFA

       250
LEAAAAHHHH HHHHHHHH
```

signal peptide 1-23, **23-262 extracellular**, 263-283 transmembrane, 284-369 cytoplasmic

IL-15Rα

```
        10         20         30         40         50         60
GGGITCPPPM SVEHADIWVK SYSLYSRERY ICNSGFKRKA GTSSLTECVL NKATNVAHWT

        70         80         90        100        110        120
TPSLKCIRDP ALVHQRPAPP STVTTAGVTP QPESLSPSGK EPAASSPSSN NTAATTAAIV

       130        140        150        160        170        180
PGSQLMPSKS PSTGTTEISS HESSHGTPSQ TTAKNWELTA SASHQPPGVY PQGHSDTTAA

       190
AHHHHHHHHH HHH
```

signal peptide 1-30, **31-205 extracellular**, 206-228 transmembrane, 229-267 cytoplasmic

IL-2

```
        10         20         30         40         50         60
APTSSSTKKT QLQLEHLMSD LQMILNGINN YKNPKLTRML TFKFYMPKKA TELKHLQCLE

        70         80         90        100        110        120
EELKPLEEVL NLAQSKNFHL RPRDLISNIN VIVLELKGSE TTFMCEYADE TATIVEFLNR

       130
WITFAQSIIS TLT
```

Accession number P60568.1 (Ala21-Thr153)

IL-15

```
        10         20         30         40         50         60
NWVNVISDLK KIEDLIQSMH IDATLYTESD VHPSCKVTAM KCFLLELQVI SLESGDASIH

        70         80         90        100        110
DTVENLIILA NNSLSSNGNV TESGCKECEE LEEKNIKEFL QSFVHIVQMF INTS
```

Accession number P40933.1 (Asn49-Ser162)

Protein	kDa	kDa (*SDS PAGE*)	OD (*)	Abs 0.1 (**)	Uniprot ID	Nr. of amino acids	Source
IL2Ra	26.9	30-35	27555	1.026	P01589	258	in-house
IL2Rb	26.7	30-35	59970	2.244	P14784	232	in-house
IL2Rg	30.3	-	61795	2.039	P31785	258	in-house
IL15Ra	20.4	-	22710	1.113	Q13261	193	in-house
IL-2	15.5	13-18	10095	0.656	Q0GK43	133	commercial supplier
IL-15	13	9-14			P40933	114	commercial supplier

Table 3.4 • Interleukin receptor construct details

(*) Extinction coefficients are in units of $M^{-1}cm^{-1}$, at 280 nm measured in water.
(**) Abs 0.1% (=1 g L^{-1}) and assuming all pairs of cystine residues form cystines.

3.6.3 Emission and absorption spectra

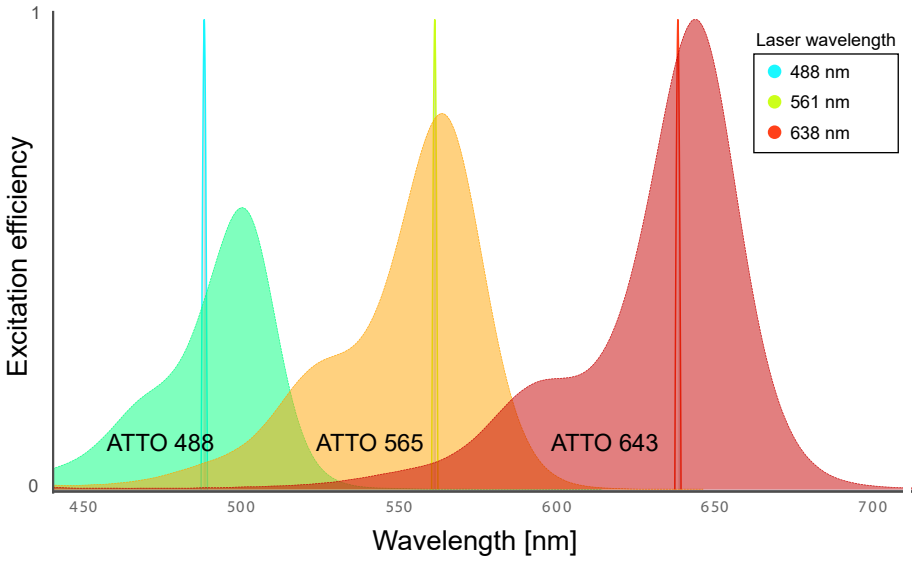

Figure 3.29 • Absorption spectra of spectrally distinct dyes
The absorption spectra of the fluorophores ATTO 488, ATTO 565 and ATTO 643 are displayed, with three lasers exciting the fluorophores at 488 nm, 561 nm and 638 nm. Absorption spectra are scaled to the respective extinction coefficient.

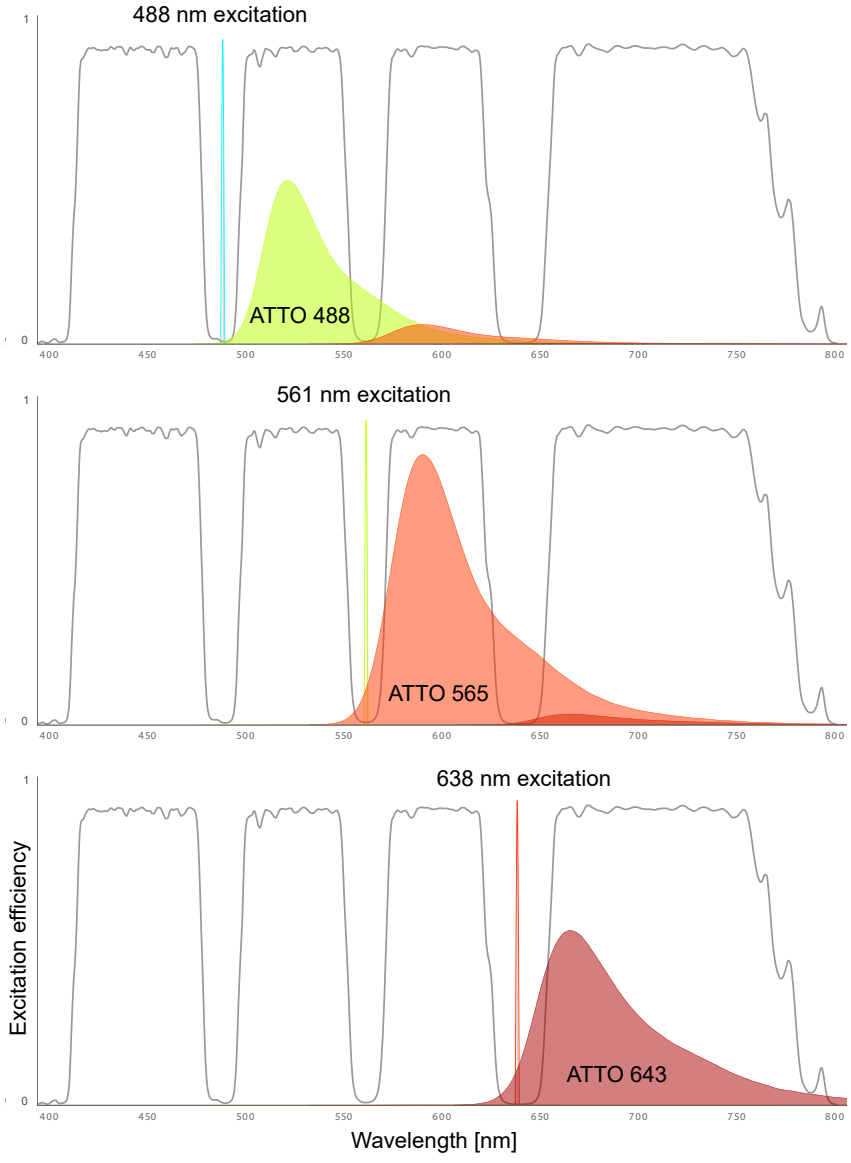

Figure 3.30 • Comparison of emission spectra for different fluorophores to illustrate bleedthrough and cross-excitation effects

Emission spectra, normalized to the respective laser excitation and scaled with respect to the fluorophore quantum yields for ATTO 488, ATTO 565 and ATTO 643 when excited at 488 nm, 565 nm and 638 nm wavelengths, at identical laser intensity. Detection windows given by the dichroic mirror are displayed to assess bleedthrough.

3.6.4 Analysis

Single-molecule tracking and FRAP data is analyzed using SPIT, a Python module developed for batch processing of single molecule tracking and colocalization data. The initial framework was developed by Miles Wang-Henderson specifically for our analysis needs. It integrates the input and output of various pre-existing modules (*picasso* [147], *trackpy* [148], *Swift* [149]) into a coherent framework for batch processing. SPIT provides a command-line interface that allows users to perform localization of single molecules, linking of trajectories, identification of colocalizations and FRAP analysis.

SPIT *localize* performs spot localization using Picasso by loading the movie files, identifying spots, fitting spots with a 2D-Gaussian function, and performing color-correction of multi-color data if required. The color-correction uses a transformation matrix produced by the module *naclib* [146]. The final results are saved to a *.csv* file and a *.yaml* file containing additional information. Optionally, plots of the results (number of localizations per frame, nearest neighbor distribution, localization precision) are generated.

SPIT *link* loads the localization data and uses *trackpy* or *Swift* for linking the localizations. After linking, the function performs particle-wise diffusion analysis and filters out short tracks and immobile particles. The resulting dataframes of linked localizations and trajectory-wide parameters are then saved to *.csv* and *.hdf* files, respectively. The number of trajectories per frame, the jump distance distribution, the mean square displacement curves, a histogram of diffusion coefficients and sample trajectories are plotted.

SPIT *colocalize* loads localized files, checks for corresponding second channel files and calculates mutual distances between individual localizations. Mutual distances below a predefined threshold are registered as colocalization events, aggregated over all frames, and saved as a *.csv* file. This analysis can be performed on localized files, or localized and tracked files. A histogram of mutual distances, the number of colocalizations per frame, as well as a map of all colocalization events, color-coded by mutual distance, are generated. Colocalization events can then be linked using SPIT link.

SPIT *frap* performs FRAP analysis by registering the bleached spot using a Canny edge algorithm to detect the perimeter of the spot. It then applies a Hough circle transform to find the best fitting circle, determining the radius and xy-position of the circle's center.

Using the circle coordinates and radius, it creates a Boolean array to divide the movie data into inside and outside of the bleached spot. Finally, the code fits the Soumpasis recovery function to the fluorescence intensity ratio of the outside and inside of the spot, accounting for overall photobleaching:

$$F_{\text{ratio}} = a_0 + a_1 \cdot \exp\left(-\frac{2 \cdot t_d}{t}\right) \cdot \left[I_0\left(\frac{2 \cdot t_d}{t}\right) + I_1\left(\frac{2 \cdot t_d}{t}\right)\right]$$

where a_0 and a_1 are constants, t_d is the decay time, t is a fitting parameter, and I_0 and I_1 are the modified Bessel functions of the first kind of order 0 and 1, respectively [158].

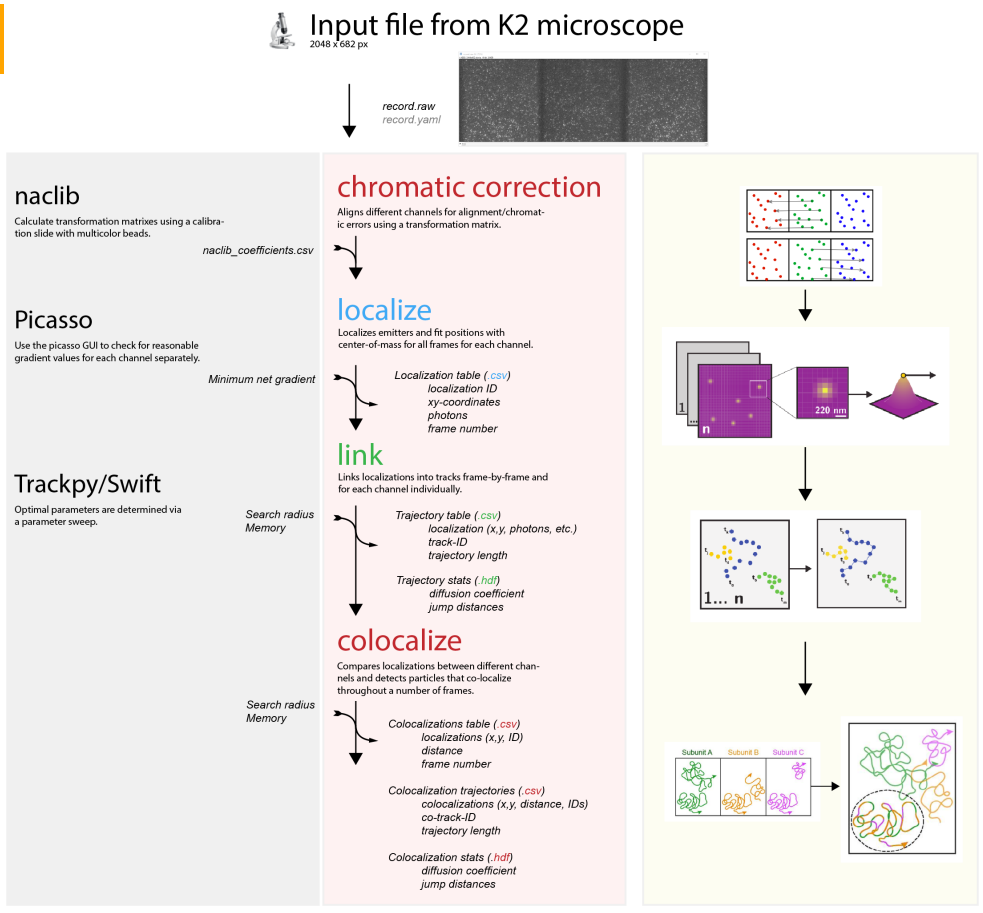

Figure 3.31 • SPIT workflow for SPT and colocalization analysis

After chromatic correction, accounting for the shift in the position between different imaging channels, particles are localized, using the *picasso* module. Then, coordinates are linked over time to generate trajectories, using either *Swift* or *TrackPy*. The colocalization analysis module calculates pairwise distances of localizations between the different channels. Distances below a given threshold are marked as colocalizations. Colocalizations are then linked, or compared to the trajectories linked in the previous step, and consecutive colocalizations are identified as interacting pairs if they exceed a given duration threshold.

References

[1] D. Calebiro et al. “Single-Molecule Analysis of Fluorescently Labeled G-protein-coupled Receptors Reveals Complexes with Distinct Dynamics and Organization”. In: *Proceedings of the National Academy of Sciences* 110.2 (2013), pp. 743–748.

[2] Junel Sotolongo Bellón et al. “Four-Color Single-Molecule Imaging with Engineered Tags Resolves the Molecular Architecture of Signaling Complexes in the Plasma Membrane”. In: *Cell Reports Methods* 2.2 (2022), p. 100165.

[3] Marie-Lise Jobin et al. “Filamin A Organizes Γ-aminobutyric Acid Type B Receptors at the Plasma Membrane”. In: *Nature Communications* 14.1 (2023), p. 34.

[4] Jerome Jatzlau et al. “A Versatile Halo- and SNAP-tagged BMP/TGFβ Receptor Library for Quantification of Cell Surface Ligand Binding”. In: *Communications Biology* 6.1 (2023), p. 34.

[5] Juan A Torreno-Pina, Carlo Manzo, and Maria F Garcia-Parajo. “Uncovering Homo-and Hetero-Interactions on the Cell Membrane Using Single Particle Tracking Approaches”. In: *Journal of Physics D: Applied Physics* 49.10 (2016), p. 104002.

[6] Titiwat Sungkaworn et al. “Single-Molecule Imaging Reveals Receptor–G Protein Interactions at Cell Surface Hot Spots”. In: *Nature* 550.7677 (2017), pp. 543–547.

[7] Davide Calebiro and Titiwat Sungkaworn. “Single-Molecule Imaging of GPCR Interactions”. In: *Trends in Pharmacological Sciences* 39.2 (2018), pp. 109–122.

[8] Masataka Yanagawa et al. “Single-Molecule Diffusion-Based Estimation of Ligand Effects on G Protein–Coupled Receptors”. In: *Science Signaling* 11.548 (2018), eaao1917.

[9] Jenny J. Y. Lin et al. “Mapping the Stochastic Sequence of Individual Ligand-Receptor Binding Events to Cellular Activation: T Cells Act on the Rare Events”. In: *Science Signaling* 12.564 (2019), eaat8715.

[10] Davide Calebiro and Jak Grimes. “G Protein–Coupled Receptor Pharmacology at the Single-Molecule Level”. In: *Annual Review of Pharmacology and Toxicology* 60.1 (2020), pp. 73–87.

[11] Stephan Wilmes et al. “Mechanism of Homodimeric Cytokine Receptor Activation and Dysregulation by Oncogenic Mutations”. In: *Science* 367.6478 (2020), pp. 643–652.

[12] Wesley B. Asher et al. “Single-Molecule FRET Imaging of GPCR Dimers in Living Cells”. In: *Nature Methods* 18.4 (2021), pp. 397–405.

[13] Yrina Rochman, Rosanne Spolski, and Warren J. Leonard. “New Insights into the Regulation of T Cells by Γ_c Family Cytokines”. In: *Nature Reviews Immunology* 9.7 (2009), pp. 480–490.

[14] Dorothy K. Sojka et al. “IL-2 Secretion by CD4+ T Cells In Vivo Is Rapid, Transient, and Influenced by TCR-Specific Competition”. In: *The Journal of Immunology* 172.10 (2004), pp. 6136–6143.

[15] Jian-Xin Lin and Warren J. Leonard. “The Common Cytokine Receptor γ Chain Family of Cytokines”. In: *Cold Spring Harbor Perspectives in Biology* 10.9 (2018), a028449.

[16] Grégoire Altan-Bonnet and Ratnadeep Mukherjee. “Cytokine-Mediated Communication: A Quantitative Appraisal of Immune Complexity”. In: *Nature Reviews Immunology* 19.4 (2019), pp. 205–217.

[17] Thomas A. Waldmann. “The Biology of Interleukin-2 and Interleukin-15: Implications for Cancer Therapy and Vaccine Design”. In: *Nature Reviews Immunology* 6.8 (2006), pp. 595–601.

[18] Thomas A. Waldmann. “Cytokines in Cancer Immunotherapy”. In: *Cold Spring Harbor Perspectives in Biology* 10.12 (2018), a028472.

[19] Daria Briukhovetska et al. “Interleukins in Cancer: From Biology to Therapy”. In: *Nature Reviews Cancer* 21.8 (2021), pp. 481–499.

[20] David E. Levy and J. E. Darnell. “STATs: Transcriptional Control and Biological Impact: Signalling”. In: *Nature Reviews Molecular Cell Biology* 3.9 (2002), pp. 651–662.

[21] Stephan Wilmes et al. “Competitive Binding of STATs to Receptor Phospho-Tyr Motifs Accounts for Altered Cytokine Responses”. In: *eLife* 10 (2021), e66014.

[22] Xiaoyi Hu et al. “The JAK/STAT Signaling Pathway: From Bench to Clinic”. In: *Signal Transduction and Targeted Therapy* 6.1 (2021), p. 402.

[23] Katsutoshi Ozaki and Warren J. Leonard. “Cytokine and Cytokine Receptor Pleiotropy and Redundancy”. In: *Journal of Biological Chemistry* 277.33 (2002), pp. 29355–29358.

[24] Dirk M. Anderson et al. “Functional Characterization of the Human Interleukin-15 Receptor αChain and Close Linkage of IL15RA and IL2RA Genes”. In: *Journal of Biological Chemistry* 270.50 (1995), pp. 29862–29869.

[25] Quirin Schiermeier. “German Research Centre Widens Misconduct Probe”. In: *Nature* (2010), news.2010.671.

[26] Brad H. Nelson, James D. Lord, and Philip D. Greenberg. “Cytoplasmic Domains of the Interleukin-2 Receptor β and γ Chains Mediate the Signal for T-cell Proliferation”. In: *Nature* 369.6478 (1994), pp. 333–336.

[27] Aaron M Ring et al. “Mechanistic and Structural Insight into the Functional Dichotomy between IL-2 and IL-15”. In: *Nature Immunology* 13.12 (2012), pp. 1187–1195.

[28] J. Barlic. “IL-15 and IL-2 Oppositely Regulate Expression of the Chemokine Receptor CX3CR1”. In: *Blood* 102.10 (2003), pp. 3494–3503.

[29] Jana Barlic et al. “Interleukin (IL)-15 and IL-2 Reciprocally Regulate Expression of the Chemokine Receptor CX3CR1 through Selective NFAT1- and NFAT2-dependent Mechanisms”. In: *Journal of Biological Chemistry* 279.47 (2004), pp. 48520–48534.

[30] Brian Becknell and Michael A. Caligiuri. “Interleukin-2, Interleukin-15, and Their Roles in Human Natural Killer Cells”. In: *Advances in Immunology*. Vol. 86. Elsevier, 2005, pp. 209–239.

[31] Donald M. Eicher. “IL-2 and IL-15 Manifest Opposing Effects on Activation of Nuclear Factor of Activated T Cells”. In: *Cellular Immunology* 223.2 (2003), pp. 133–142.

[32] Xian Chang Li et al. “IL-15 and IL-2: A Matter of Life and Death for T Cells in Vivo”. In: *Nature Medicine* 7.1 (2001), pp. 114–118.

[33] D. M. Mitchell, E. V. Ravkov, and M. A. Williams. “Distinct Roles for IL-2 and IL-15 in the Differentiation and Survival of CD8+ Effector and Memory T Cells”. In: *The Journal of Immunology* 184.12 (2010), pp. 6719–6730.

[34] T Waldmann. “Contrasting Roles of IL-2 and IL-15 in the Life and Death of Lymphocytes Implications for Immunotherapy”. In: *Immunity* 14.2 (2001), pp. 105–110.

[35] T. A. Waldmann. “The Shared and Contrasting Roles of IL2 and IL15 in the Life and Death of Normal and Neoplastic Lymphocytes: Implications for Cancer Therapy”. In: *Cancer Immunology Research* 3.3 (2015), pp. 219–227.

[36] Abhinav Arneja et al. “Qualitatively Different T Cell Phenotypic Responses to IL-2 versus IL-15 Are Unified by Identical Dependences on Receptor Signal Strength and Duration”. In: *The Journal of Immunology* 192.1 (2014), pp. 123–135.

[37] Iris Castro et al. “The Basis of Distinctive IL-2– and IL-15–Dependent Signaling: Weak CD122-Dependent Signaling Favors CD8 $^{+}$ T Central-Memory Cell Survival but Not T Effector-Memory Cell Development”. In: *The Journal of Immunology* 187.10 (2011), pp. 5170–5182.

[38] Averil Ma, David L. Boone, and James P. Lodolce. “The Pleiotropic Functions of Interleukin 15: Not so Interleukin 2–Like after All”. In: *The Journal of Experimental Medicine* 191.5 (2000), pp. 753–756.

[39] Dihia Meghnem et al. “Cutting Edge: Differential Fine-Tuning of IL-2– and IL-15–Dependent Functions by Targeting Their Common IL-2/15Rβ/Γ_c Receptor”. In: *The Journal of Immunology* 198.12 (2017), pp. 4563–4568.

[40] Anne-Hélène Pillet et al. “A Programmed Switch from IL-15- to IL-2-Dependent Activation in Human NK Cells”. In: *The Journal of Immunology* 182.10 (2009), pp. 6267–6277.

[41] Anne-Hélène Pillet, Jacques Thèze, and Thierry Rose. “Interleukin (IL)-2 and IL-15 Have Different Effects on Human Natural Killer Lymphocytes”. In: *Human Immunology* 72.11 (2011), pp. 1013–1017.

[42] Luis F. Ponce et al. “Differential Effects of IL2Rα and IL15Rα over the Stability of the Common Beta-Gamma Signaling Subunits of the IL2 and IL15 Receptors”. In: *Journal of Chemical Information and Modeling* 61.4 (2021), pp. 1913–1920.

[43] T. A. Fehniger. “Interleukin 15: Biology and Relevance to Human Disease”. In: *Blood* 97.1 (2001), pp. 14–32.

[44] Onur Boyman and Jonathan Sprent. “The Role of Interleukin-2 during Homeostasis and Activation of the Immune System”. In: *Nature Reviews Immunology* 12.3 (2012), pp. 180–190.

[45] Jian Qiao and Yang-Xin Fu. “Cytokines That Target Immune Killer Cells against Tumors”. In: *Cellular & Molecular Immunology* 17.7 (2020), pp. 722–727.

[46] Piera Filomena Fiore et al. “Interleukin-15 and Cancer: Some Solved and Many Unsolved Questions”. In: *Journal for ImmunoTherapy of Cancer* 8.2 (2020), e001428.

[47] Ivan S. Pires, Paula T. Hammond, and Darrell J. Irvine. “Engineering Strategies for Immunomodulatory Cytokine Therapies: Challenges and Clinical Progress”. In: *Advanced Therapeutics* 4.8 (2021), p. 2100035.

[48] Shoubao Ma, Michael A. Caligiuri, and Jianhua Yu. “Harnessing IL-15 Signaling to Potentiate NK Cell-Mediated Cancer Immunotherapy”. In: *Trends in Immunology* 43.10 (2022), pp. 833–847.

[49] John J. O’Shea, Averil Ma, and Peter Lipsky. “Cytokines and Autoimmunity”. In: *Nature Reviews Immunology* 2.1 (2002), pp. 37–45.

[50] Thomas A. Waldmann. “The Biology of IL-15: Implications for Cancer Therapy and the Treatment of Autoimmune Disorders”. In: *Journal of Investigative Dermatology Symposium Proceedings* 16.1 (2013), S28–S30.

[51] Abul K. Abbas et al. “Revisiting IL-2: Biology and Therapeutic Prospects”. In: *Science Immunology* 3.25 (2018), eaat1482.

[52] Rosanne Spolski, Peng Li, and Warren J. Leonard. “Biology and Regulation of IL-2: From Molecular Mechanisms to Human Therapy”. In: *Nature Reviews Immunology* 18.10 (2018), pp. 648–659.

[53] Brad H. Nelson. “IL-2, Regulatory T Cells, and Tolerance”. In: *The Journal of Immunology* 172.7 (2004), pp. 3983–3988.

[54] Takatoshi Chinen et al. “An Essential Role for the IL-2 Receptor in Treg Cell Function”. In: *Nature Immunology* 17.11 (2016), pp. 1322–1333.

[55] Congxiu Ye, David Brand, and Song G. Zheng. “Targeting IL-2: An Unexpected Effect in Treating Immunological Diseases”. In: *Signal Transduction and Targeted Therapy* 3.1 (2018), p. 2.

[56] Zhenhua Dai et al. “The Role of the Common Cytokine Receptor γ-Chain in Regulating IL-2-Dependent, Activation-Induced CD8+ T Cell Death”. In: *The Journal of Immunology* 163.6 (1999), pp. 3131–3137.

[57] Tiffany Horng, Jelena S Bezbradica, and Ruslan Medzhitov. “NKG2D Signaling Is Coupled to the Interleukin 15 Receptor Signaling Pathway”. In: *Nature Immunology* 8.12 (2007), pp. 1345–1352.

[58] Xinquan Wang et al. “Structural Biology of Shared Cytokine Receptors”. In: *Annual Review of Immunology* 27.1 (2009), pp. 29–60.

[59] Bana Jabri and Valérie Abadie. “IL-15 Functions as a Danger Signal to Regulate Tissue-Resident T Cells and Tissue Destruction”. In: *Nature Reviews Immunology* 15.12 (2015), pp. 771–783.

[60] Manoj Patidar, Naveen Yadav, and Sarat K. Dalai. “Interleukin 15: A Key Cytokine for Immunotherapy”. In: *Cytokine & Growth Factor Reviews* 31 (2016), pp. 49–59.

[61] Pin-Yu Perera et al. “The Role of Interleukin-15 in Inflammation and Immune Responses to Infection: Implications for Its Therapeutic Use”. In: *Microbes and Infection* 14.3 (2012), pp. 247–261.

[62] Thomas A Waldmann. “The IL-2/IL-15 Receptor Systems: Targets for Immunotherapy”. In: *Journal of Clinical Immunology* 22.2 (2002), p. 6.

[63] Thomas R. Malek and Iris Castro. “Interleukin-2 Receptor Signaling: At the Interface between Tolerance and Immunity”. In: *Immunity* 33.2 (2010), pp. 153–165.

[64] Natalia Arenas-Ramirez, Janine Woytschak, and Onur Boyman. “Interleukin-2: Biology, Design and Application”. In: *Trends in Immunology* 36.12 (2015), pp. 763–777.

[65] Ying Yang and Andreas Lundqvist. “Immunomodulatory Effects of IL-2 and IL-15; Implications for Cancer Immunotherapy”. In: *Cancers* 12.12 (2020), p. 3586.

[66] Yeshuang Yuan et al. “Therapeutic Potential of Interleukin-2 in Autoimmune Diseases”. In: *Trends in Molecular Medicine* (2022), S147149142200106X.

[67] Cristina Bergamaschi et al. “Heterodimeric IL-15 in Cancer Immunotherapy”. In: *Cancers* 13.4 (2021), p. 837.

[68] Jai Rautela and Nicholas D Huntington. “IL-15 Signaling in NK Cell Cancer Immunotherapy”. In: *Current Opinion in Immunology* 44 (2017), pp. 1–6.

[69] Steven A Rosenberg. “Interleukin 2 for Patients with Renal Cancer”. In: *Nature Clinical Practice Oncology* 4.9 (2007), pp. 497–497.

[70] Steven A. Rosenberg. “IL-2: The First Effective Immunotherapy for Human Cancer”. In: *The Journal of Immunology* 192.12 (2014), pp. 5451–5458.

[71] Rowena N Schwartz, Lori Stover, and Janice P Dutcher. “Managing Toxicities of High-Dose Interleukin-2”. In: *Oncology* 16.11 Suppl 13 (2002), pp. 11–20.

[72] Kritika Mohan et al. “Topological Control of Cytokine Receptor Signaling Induces Differential Effects in Hematopoiesis”. In: *Science* 364.6442 (2019), eaav7532.

[73] Ignacio Moraga et al. “Instructive Roles for Cytokine-Receptor Binding Parameters in Determining Signaling and Functional Potency”. In: *Science Signaling* 8.402 (2015), ra114–ra114.

[74] Ignacio Moraga et al. “Tuning Cytokine Receptor Signaling by Re-orienting Dimer Geometry with Surrogate Ligands”. In: *Cell* 160.6 (2015), pp. 1196–1208.

[75] Jürgen Scheller et al. “Immunoreceptor Engineering and Synthetic Cytokine Signaling for Therapeutics”. In: *Trends in Immunology* 40.3 (2019), pp. 258–272.

[76] Daniel-Adriano Silva et al. “De Novo Design of Potent and Selective Mimics of IL-2 and IL-15”. In: *Nature* 565.7738 (2019), pp. 186–191.

[77] Junming Ren et al. “Interleukin-2 Superkines by Computational Design”. In: *Proceedings of the National Academy of Sciences* 119.12 (2022), e2117401119.

[78] M. P. Rubinstein et al. “Converting IL-15 to a Superagonist by Binding to Soluble IL-15R”. In: *Proceedings of the National Academy of Sciences* 103.24 (2006), pp. 9166–9171.

[79] Eric J. Hsu et al. “A Cytokine Receptor-Masked IL2 Prodrug Selectively Activates Tumor-Infiltrating Lymphocytes for Potent Antitumor Therapy”. In: *Nature Communications* 12.1 (2021), p. 2768.

[80] Fei Mo et al. “An Engineered IL-2 Partial Agonist Promotes CD8+ T Cell Stemness”. In: *Nature* 597.7877 (2021), pp. 544–548.

[81] Alfredo Quijano-Rubio et al. “A Split, Conditionally Active Mimetic of IL-2 Reduces the Toxicity of Systemic Cytokine Therapy”. In: *Nature Biotechnology* (2022).

[82] Stefanie U. Frick et al. “Interleukin-2 Functionalized Nanocapsules for T Cell-Based Immunotherapy”. In: *ACS Nano* 10.10 (2016), pp. 9216–9226.

[83] Lenka V. Hurton et al. “Tethered IL-15 Augments Antitumor Activity and Promotes a Stem-Cell Memory Subset in Tumor-Specific T Cells”. In: *Proceedings of the National Academy of Sciences* 113.48 (2016), E7788–E7797.

[84] Liliane Khoryati et al. “An IL-2 Mutein Engineered to Promote Expansion of Regulatory T Cells Arrests Ongoing Autoimmunity in Mice”. In: *Science Immunology* 5.50 (2020), eaba5264.

[85] Aron M. Levin et al. “Exploiting a Natural Conformational Switch to Engineer an Interleukin-2 ‘Superkine’”. In: *Nature* 484.7395 (2012), pp. 529–533.

[86] Suman Mitra et al. “Interleukin-2 Activity Can Be Fine Tuned with Engineered Receptor Signaling Clamps”. In: *Immunity* 42.5 (2015), pp. 826–838.

[87] Michael R. Mortensen et al. “Targeting an Engineered Cytokine with Interleukin-2 and Interleukin-15 Activity to the Neovasculature of Solid Tumors”. In: *Oncotarget* 11.44 (2020), pp. 3972–3983.

[88] Erwan Mortier et al. “Soluble Interleukin-15 Receptor α (IL-15Rα)-Sushi as a Selective and Potent Agonist of IL-15 Action through IL-15Rβ/γ: HYPERAGONIST IL-15 - IL-15Rα FUSION PROTEINS”. In: *Journal of Biological Chemistry* 281.3 (2006), pp. 1612–1619.

[89] Jonathan T. Sockolosky et al. “Selective Targeting of Engineered T Cells Using Orthogonal IL-2 Cytokine-Receptor Complexes”. In: *Science* 359.6379 (2018), pp. 1037–1042.

[90] Benjamin Sadlack et al. “Ulcerative Colitis-like Disease in Mice with a Disrupted Interleukin-2 Gene”. In: *Cell* 75.2 (1993), pp. 253–261.

[91] Dennis M. Willerford et al. “Interleukin-2 Receptor α Chain Regulates the Size and Content of the Peripheral Lymphoid Compartment”. In: *Immunity* 3.4 (1995), pp. 521–530.

[92] Iain B. McInnes et al. “The Role of Interleukin–15 in T–Cell Migration and Activation in Rheumatoid Arthritis”. In: *Nature Medicine* 2.2 (1996), pp. 175–182.

[93] M. Aringer et al. “Serum Interleukin-15 Is Elevated in Systemic Lupus Erythematosus”. In: *Rheumatology* 40.8 (2001), pp. 876–881.

[94] Bertrand Meresse et al. “Coordinated Induction by IL15 of a TCR-Independent NKG2D Signaling Pathway Converts CTL into Lymphokine-Activated Killer Cells in Celiac Disease”. In: *Immunity* 21.3 (2004), pp. 357–366.

[95] Adi Vaknin-Dembinsky et al. “Membrane Bound IL-15 Is Increased on CD14 Monocytes in Early Stages of MS”. In: *Journal of Neuroimmunology* 195.1-2 (2008), pp. 135–139.

[96] R. W. DePaolo et al. “Co-Adjuvant Effects of Retinoic Acid and IL-15 Induce Inflammatory Immunity to Dietary Antigens”. In: *Nature* 471.7337 (2011), pp. 220–224.

[97] Jing Chen et al. “Insulin-Dependent Diabetes Induced by Pancreatic Beta Cell Expression of IL-15 and IL-15Rα”. In: *Proceedings of the National Academy of Sciences* 110.33 (2013), pp. 13534–13539.

[98] Valérie Abadie et al. “IL-15, Gluten and HLA-DQ8 Drive Tissue Destruction in Coeliac Disease”. In: *Nature* 578.7796 (2020), pp. 600–604.

[99] Noriyuki Ohta et al. “IL-15-Dependent Activation-Induced Cell Death-Resistant Th1 Type CD8$\alpha\beta$+NK1.1+ T Cells for the Development of Small Intestinal Inflammation”. In: *The Journal of Immunology* 169.1 (2002), pp. 460–468.

[100] P T Saligrama et al. “IL-15 Maintains T-cell Survival via S-nitrosylation-mediated Inhibition of Caspase-3”. In: *Cell Death & Differentiation* 21.6 (2014), pp. 904–914.

[101] Michael Lenardo et al. “MATURE T LYMPHOCYTE APOPTOSIS—Immune Regulation in a Dynamic and Unpredictable Antigenic Environment”. In: *Annual Review of Immunology* 17.1 (1999), pp. 221–253.

[102] J. Marks-Konczalik et al. “IL-2-induced Activation-Induced Cell Death Is Inhibited in IL-15 Transgenic Mice”. In: *Proceedings of the National Academy of Sciences* 97.21 (2000), pp. 11445–11450.

[103] Mathias Rickert et al. “Compensatory Energetic Mechanisms Mediating the Assembly of Signaling Complexes Between Interleukin-2 and Its α, β, and γ Receptors”. In: *Journal of Molecular Biology* 339.5 (2004), pp. 1115–1128.

[104] Sriram Balasubramanian et al. “Ligand Binding Kinetics of IL-2 and IL-15 to Heteromers Formed by Extracellular Domains of the Three IL-2 Receptor Subunits”. In: *International Immunology* 7.11 (1995), pp. 1839–1849.

[105] Erwan Mortier et al. “Natural, Proteolytic Release of a Soluble Form of Human IL-15 Receptor α-Chain That Behaves as a Specific, High Affinity IL-15 Antagonist”. In: *The Journal of Immunology* 173.3 (2004), pp. 1681–1688.

[106] Mami Chirifu et al. “Crystal Structure of the IL-15–IL-15Rα Complex, a Cytokine-Receptor Unit Presented in Trans”. In: *Nature Immunology* 8.9 (2007), pp. 1001–1007.

[107] Xinquan Wang, Mathias Rickert, and K. Christopher Garcia. "Structure of the Quaternary Complex of Interleukin-2 with Its α, ß, and γ_c Receptors". In: *Science* 310.5751 (2005), pp. 1159–1163.

[108] D. J. Stauber et al. "Crystal Structure of the IL-2 Signaling Complex: Paradigm for a Heterotrimeric Cytokine Receptor". In: *Proceedings of the National Academy of Sciences* 103.8 (2006), pp. 2788–2793.

[109] Erwan Mortier et al. "IL-15Rα Chaperones IL-15 to Stable Dendritic Cell Membrane Complexes That Activate NK Cells via Trans Presentation". In: *The Journal of Experimental Medicine* 205.5 (2008), pp. 1213–1225.

[110] Simone C Wuest et al. "A Role for Interleukin-2 Trans-Presentation in Dendritic Cell–Mediated T Cell Activation in Humans, as Revealed by Daclizumab Therapy". In: *Nature Medicine* 17.5 (2011), pp. 604–609.

[111] Cristina Bergamaschi et al. "Circulating IL-15 Exists as Heterodimeric Complex with Soluble IL-15Rα in Human and Mouse Serum". In: *Blood* 120.1 (2012), e1–e8.

[112] Naruhisa Ota et al. "No Requirement of *Trans* Presentations of IL-15 for Human CD8 T Cell Proliferation". In: *The Journal of Immunology* 185.10 (2010), pp. 6041–6048.

[113] Ivan Zanoni et al. "IL-15 Cis Presentation Is Required for Optimal NK Cell Activation in Lipopolysaccharide-Mediated Inflammatory Conditions". In: *Cell Reports* 4.6 (2013), pp. 1235–1249.

[114] Sigrid Dubois et al. "IL-15Rα Recycles and Presents IL-15 In Trans to Neighboring Cells". In: *Immunity* 17.5 (2002), pp. 537–547.

[115] Spencer W. Stonier and Kimberly S. Schluns. "Trans-Presentation: A Novel Mechanism Regulating IL-15 Delivery and Responses". In: *Immunology Letters* 127.2 (2010), pp. 85–92.

[116] F. Tamzalit et al. "IL-15.IL-15R Complex Shedding Following Trans-Presentation Is Essential for the Survival of IL-15 Responding NK and T Cells". In: *Proceedings of the National Academy of Sciences* 111.23 (2014), pp. 8565–8570.

[117] Agnès Quéméner et al. "IL-15Rα Membrane-Anchorage Either in *Cis* or in *Trans* Is Required for Stabilization of IL-15 and Optimal Signaling". In: *Journal of Cell Science* (2019), jcs.236802.

[118] Patrick Binder et al. “Optimal Ligand Discrimination by Asymmetric Dimerization and Turnover of Interferon Receptors”. In: *Proceedings of the National Academy of Sciences* 118.37 (2021), e2103939118.

[119] T. W. McKeithan. “Kinetic Proofreading in T-cell Receptor Signal Transduction.” In: *Proceedings of the National Academy of Sciences* 92.11 (1995), pp. 5042–5046.

[120] W. S. Hlavacek et al. “Kinetic Proofreading Models for Cell Signaling Predict Ways to Escape Kinetic Proofreading”. In: *Proceedings of the National Academy of Sciences* 98.13 (2001), pp. 7295–7300.

[121] Daniel M. Freed et al. “EGFR Ligands Differentially Stabilize Receptor Dimers to Specify Signaling Kinetics”. In: *Cell* 171.3 (2017), 683–695.e18.

[122] Theodore R. Sana et al. “Expression and Ligand Binding Characterization of the .Beta.-Subunit (P75) Ectodomain of the Interleukin-2 Receptor”. In: *Biochemistry* 33.19 (1994), pp. 5838–5845.

[123] Stefano F. Liparoto and Thomas L. Ciardelli. “Biosensor Analysis of the Interleukin-2 Receptor Complex”. In: *Journal of Molecular Recognition* 12.5 (1999), pp. 316–321.

[124] Leon O. Murphy et al. “Molecular Interpretation of ERK Signal Duration by Immediate Early Gene Products”. In: *Nature Cell Biology* 4.8 (2002), pp. 556–564.

[125] Surojit Paul et al. “NMDA-mediated Activation of the Tyrosine Phosphatase STEP Regulates the Duration of ERK Signaling”. In: *Nature Neuroscience* 6.1 (2003), pp. 34–42.

[126] Rinshi S. Kasai et al. “The Class-A GPCR Dopamine D2 Receptor Forms Transient Dimers Stabilized by Agonists: Detection by Single-Molecule Tracking”. In: *Cell Biochemistry and Biophysics* 76.1-2 (2018), pp. 29–37.

[127] William Y. C. Huang et al. “A Molecular Assembly Phase Transition and Kinetic Proofreading Modulate Ras Activation by SOS”. In: *Science* 363.6431 (2019), pp. 1098–1103.

[128] Caleb R Glassman et al. “Calibration of Cell-Intrinsic Interleukin-2 Response Thresholds Guides Design of a Regulatory T Cell Biased Agonist”. In: *eLife* 10 (2021), e65777.

[129] Martin Loose et al. “Min Protein Patterns Emerge from Rapid Rebinding and Membrane Interaction of MinE”. In: *Nature Structural & Molecular Biology* 18.5 (2011), pp. 577–583.

[130] Katja Zieske and Petra Schwille. “Reconstitution of Self-Organizing Protein Gradients as Spatial Cues in Cell-Free Systems”. In: *eLife* 3 (2014), e03949.

[131] Phuong A. Nguyen et al. “Using Supported Bilayers to Study the Spatiotemporal Organization of Membrane-Bound Proteins”. In: *Methods in Cell Biology*. Vol. 128. Elsevier, 2015, pp. 223–241.

[132] Edward Jenkins et al. “Reconstitution of Immune Cell Interactions in Free-Standing Membranes”. In: *Journal of Cell Science* 132.4 (2019), jcs219709.

[133] Markus Axmann, Gerhard J. Schütz, and Johannes B. Huppa. “Single Molecule Fluorescence Microscopy on Planar Supported Bilayers”. In: *Journal of Visualized Experiments* 104 (2015).

[134] Xiaolei Su et al. “Reconstitution of TCR Signaling Using Supported Lipid Bilayers”. In: *The Immune Synapse*. Ed. by Cosima T. Baldari and Michael L. Dustin. Vol. 1584. New York, NY: Springer New York, 2017, pp. 65–76.

[135] Kristina A. Ganzinger and Petra Schwille. “More from Less – Bottom-up Reconstitution of Cell Biology”. In: *Journal of Cell Science* 132.4 (2019), jcs227488.

[136] Pablo F. Céspedes et al. “Model Membrane Systems to Reconstitute Immune Cell Signaling”. In: *The FEBS Journal* 288.4 (2021), pp. 1070–1090.

[137] Tommy Dam et al. “Supported Lipid Bilayers and the Study of Two-Dimensional Binding Kinetics”. In: *Frontiers in Molecular Biosciences* 9 (2022), p. 833123.

[138] Andrea Bodnár et al. “A Biophysical Approach to IL-2 and IL-15 Receptor Function: Localization, Conformation and Interactions”. In: *Immunology Letters* 116.2 (2008), pp. 117–125.

[139] Christopher S Theile et al. “Site-Specific N-terminal Labeling of Proteins Using Sortase-Mediated Reactions”. In: *Nature Protocols* 8.9 (2013), pp. 1800–1807.

[140] Jeffrey A. Nye and Jay T. Groves. “Kinetic Control of Histidine-Tagged Protein Surface Density on Supported Lipid Bilayers”. In: *Langmuir* 24.8 (2008), pp. 4145–4149.

[141] I. Tinoco and R. L. Gonzalez. “Biological Mechanisms, One Molecule at a Time”. In: *Genes & Development* 25.12 (2011), pp. 1205–1231.

[142] Inga Jarmoskaite et al. “How to Measure and Evaluate Binding Affinities”. In: *eLife* 9 (2020), e57264.

[143] Talley J. Lambert. “FPbase: A Community-Editable Fluorescent Protein Database”. In: *Nature Methods* 16.4 (2019), pp. 277–278.

[144] Philipp Wolf et al. “Strategies for Site-Specific Labeling of Receptor Proteins on the Surfaces of Living Cells by Using Genetically Encoded Peptide Tags”. In: *ChemBioChem* 22.10 (2021), pp. 1717–1732.

[145] Ralf P. Richter, Rémi Bérat, and Alain R. Brisson. “Formation of Solid-Supported Lipid Bilayers: An Integrated View”. In: *Langmuir* 22.8 (2006), pp. 3497–3505.

[146] Kaley A. McCluskey et al. “Global Correction of Optical Distortions in Multicolor Single-Molecule Microscopy Using Zernike Polynomial Gradients”. In: *Optics Express* 29.25 (2021), p. 42251.

[147] Joerg Schnitzbauer et al. “Super-Resolution Microscopy with DNA-PAINT”. In: *Nature Protocols* 12.6 (2017), pp. 1198–1228.

[148] Daniel B. Allan et al. *Soft-Matter/Trackpy: Trackpy v0.5.0*. 2021.

[149] M Endesfelder et al. “Swift – Fast, Probabilistic Tracking for Dense, Highly Dynamic Single-Molecule Data”. In: (2022).

[150] J. G. Giri et al. “Identification and Cloning of a Novel IL-15 Binding Protein That Is Structurally Related to the Alpha Chain of the IL-2 Receptor.” In: *The EMBO Journal* 14.15 (1995), pp. 3654–3663.

[151] Pradeep M Nair et al. “Using Patterned Supported Lipid Membranes to Investigate the Role of Receptor Organization in Intercellular Signaling”. In: *Nature Protocols* 6.4 (2011), pp. 523–539.

[152] Nicolas Chenouard et al. “Objective Comparison of Particle Tracking Methods”. In: *Nature Methods* 11.3 (2014), pp. 281–289.

[153] Laura D. Hughes, Robert J. Rawle, and Steven G. Boxer. “Choose Your Label Wisely: Water-Soluble Fluorophores Often Interact with Lipid Bilayers”. In: *PLoS ONE* 9.2 (2014), e87649.

[154] Kenichi G.N. Suzuki et al. “Single-Molecule Imaging of Receptor–Receptor Interactions”. In: *Methods in Cell Biology*. Vol. 117. Elsevier, 2013, pp. 373–390.

[155] Tom Clement, Pieter Rein ten Wolde, and Anton Feenstra. "Simulation of Multiplexing in Immune Cell Receptors Using eGFRD". 2021.

[156] Lee Freiburger et al. "Efficient Segmental Isotope Labeling of Multi-Domain Proteins Using Sortase A". In: *Journal of Biomolecular NMR* 63.1 (2015), pp. 1–8.

[157] Thorben Cordes, Jan Vogelsang, and Philip Tinnefeld. "On the Mechanism of Trolox as Antiblinking and Antibleaching Reagent". In: *Journal of the American Chemical Society* 131.14 (2009), pp. 5018–5019.

[158] D.M. Soumpasis. "Theoretical Analysis of Fluorescence Photobleaching Recovery Experiments". In: *Biophysical Journal* 41.1 (1983), pp. 95–97.

4 DNA-PAINT single-particle tracking (DNA-PAINT-SPT) enables extended single-molecule studies of membrane protein interactions

Christian Niederauer, Chikim Nguyen, Miles Wang-Henderson, Johannes Stein, Sebastian Strauss, Alex Cumberworth, Florian Stehr, Ralf Jungmann, Petra Schwille, Kristina Anne Ganzinger

Abstract

DNA-PAINT based single-particle tracking (DNA-PAINT-SPT) has recently significantly enhanced observation times in in vitro SPT experiments by overcoming the constraints of fluorophore photobleaching. However, with the reported implementation, only a single target can be imaged and the technique cannot be applied straight to live cell imaging. Here we report on leveraging this technique from a proof-of-principle implementation to a useful tool for the SPT community by introducing simultaneous live cell dual-color DNA-PAINT-SPT for quantifying protein dimerization and tracking proteins in living cell membranes, demonstrating its improved performance over single-dye SPT.

The following manuscript is reproduced essentially as preprinted. Supplementary movies SM1-SM6 are available in the online version of the manuscript [1].

4.1 Introduction

Single-particle tracking (SPT) is a powerful method to investigate the orchestration of biomolecular processes at cell membranes or in reconstituted systems [2, 3]. To detect and follow the molecules of interest, these are usually fluorescently labeled, with observation times and localization precision depending on label brightness and photostability. Furthermore, labels have to be conjugated with the target molecule in one-to-one stoichiometry to obtain meaningful data [4]. Due to their small size, brightness and ease of chemical addressability, organic dyes conjugated to genetically encoded protein tags are currently the preferred labeling strategy for SPT of membrane proteins [5–8]. However, observations are typically only possible for a few seconds at 20–50 nm spatial precision before the dyes photobleach [3]. Short trajectories particularly hamper quantitative studies of molecular association by multi-color SPT, as they reduce the dynamic range of these experiments and make it hard to distinguish true co-diffusion events from chance encounters.

Recently, we have demonstrated how DNA-PAINT-SPT can increase trajectory lengths by circumventing the limited photon budget of single dyes [9]. In DNA-PAINT-SPT, short dye-labeled DNA oligonucleotides (imager strands) transiently bind to a target-bound complementary docking strand that contains several repeating and speed-optimised sequences [10, 11]. As multiple imager strands can thus bind simultaneously and are designed to exchange on a time scale similar to that of dye photobleaching, this allowed us to follow the motion of DNA-origami on a supported lipid bilayer (SLB) for minutes rather than seconds [9]. While the concept of a continuous turnover of fluorophores to circumvent photobleaching has gained traction in the field of single-molecule fluorescence [12, 13], it is yet to be implemented in more complex biological samples.

Here, we introduce a new motif for dual-color DNA-PAINT-SPT for measuring protein-protein interactions at the single-molecule level, and use it to reliably quantify ligand-induced protein dimerization in membranes. We further extend our new dual-color DNA-PAINT-SPT implementation to live cell imaging applications and demonstrate its improved performance over single-dye SPT.

4.2 Results

4.2.1 Orthogonal docking strands for reliable detection of protein-protein interactions in dual-color SPT

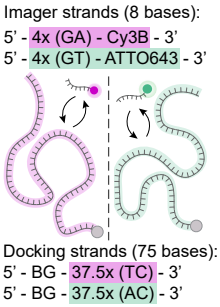

Figure 4.1 • Multicolor sequence design

Sequence design for dual-color DNA-PAINT-SPT. Imager strands are 8 nucleotide long fluorescently labeled single-stranded DNA consisting of nucleotide-pair repeats (GA and GT). Docking strands are 75 nucleotide long single-stranded DNA, consisting of repeats of the respective complementary nucleotide-pairs (TC and AC) and a benzylguanine (BG) moiety for covalent labeling of proteins with a SNAPtag. A single docking strand can be occupied by several imager strands at the same time, with binding times tuned to match bleaching kinetics, allowing for the continuous observation of labeled proteins.

To apply DNA-PAINT-SPT in dual-color experiments of molecular interactions, we designed orthogonal docking-imager strand pairs (**Fig. 4.1**, **Section 4.5.1**) that exhibited negligible crosstalk (localization densities of poly(TC)- and poly(AC)-labeled FKBP proteins, with complementary GA- and GT-imager strands in solution: $0.11\,\mu m^{-2}$; localization density of poly(TC)- and poly(AC)-labeled FKBP proteins, with non-complementary GT- and GA-imager strands in solution: $0.000\,64\,\mu m^{-2}$ and $0.0013\,\mu m^{-2}$, respectively; (**Fig. 4.2**). This ensured that we could use the co-diffusion of single-molecules in two different color channels as a means of detecting their molecular interaction.

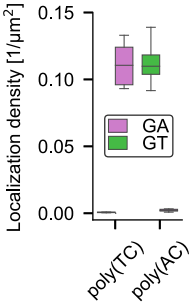

Figure 4.2 • Sequence orthogonality

Density of tracks of reconstituted SNAPtag fusion proteins labeled with BG-conjugated orthogonal docking strand sequences and their respective imager strands conjugated to ATTO643 or Cy3B fluorophores. Boxes, line and whiskers show, respectively, 25–75 quartiles, median, and minimum and maximum values of data pooled from three fields of view of duplicate samples per condition.

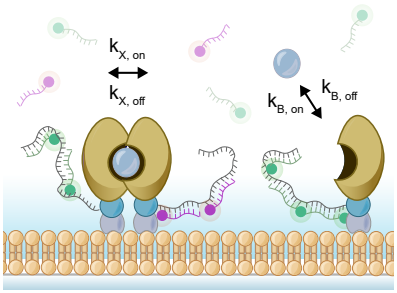

Figure 4.3 • Homodimerization experimental design

Schematic of the in vitro dimerization assay. FKBP-proteins (yellow) are reconstituted on a supported lipid bilayer and labeled via their SNAPtag (blue) with orthogonal DNA oligonucleotide docking strands. Complementary (8 nucleotides) imager strands, conjugated to Cy3B (magenta) and ATTO643 (green) fluorophores transiently bind to the docking strand and allow for dual-color single-particle tracking. Dimerization of FKBP-proteins is induced by adding a dimerization agent (grey sphere).

We employed our dual-color DNA-PAINT-SPT method to investigate ligand-induced FK506 binding protein (FKBP) homodimerization by anchoring His-tagged FKBP to nickel-nitrilotriacetic acid (NTA-Ni)-containing supported lipid bilayers (SLBs). This system enables the study of 2D protein-protein interaction, preserving diffusive mobility and rotational freedom of the protein. We labeled the proteins via their SNAPtag using two orthogonal sets of benzylguanine (BG)-modified DNA docking strands, and reconstituted the labeled proteins in equimolar amounts. When we added the respective imager strands without the dimerization agent, no co-diffusion was detected (**Fig. S4.1**), suggesting that the DNA-PAINT-SPT label itself does not introduce interactions. When adding the dimerization agent AP20187 in solution [14, 15] (**Fig. 4.3**, we reliably detected co-diffusion events and hence protein dimerization (**Fig. 4.4**, **Fig. S4.2**, **Fig. S4.3**, **??**, **??**) using a total internal reflection fluorescence microscope (TIRFM).

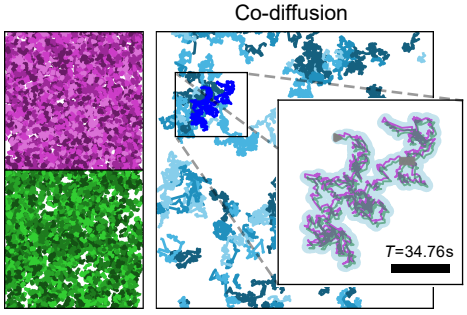

Figure 4.4 • Detection of codiffusing homodimers

Single-molecule trajectories collected during a 40 seconds recording (left, magenta and green) and detected dimerization events (right, blue). Fields of view are 70 x 70 µm. Inset: Tracks of two monomers (magenta and green) co-diffusing for 34.76 seconds (869 frames). For display purposes, tracks were moved in opposite x and y directions by 0.2 µm. Co-diffusion as detected by the tracking algorithm is presented as a blue-shaded track. Scale bar: 5 µm.

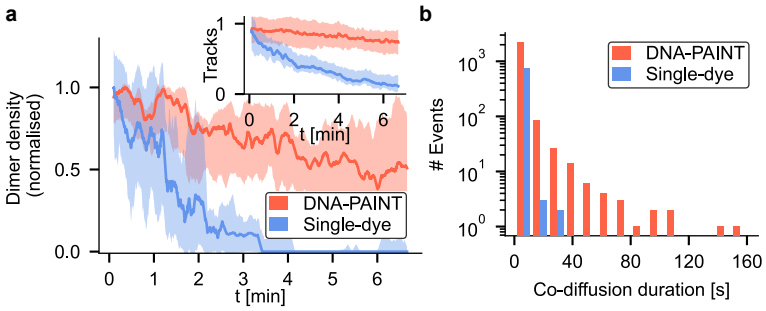

Figure 4.5 • Comparison of DNA-PAINT-SPT and single-dye control in detecting dimers and interaction durations

(a) Mean number of dimers per frame observable using Cy3B- and ATTO643 DNA-PAINT-SPT (red) or Cy3B- and ATTO643 single-dye control (blue), normalised to their respective initial values. Inset: Number of tracks using DNA-PAINT-SPT (red) or single-dye control (blue), normalised to their respective initial values. Curves represent the median with shaded areas indicating the 25-75 quartiles of data collected from three samples per condition. **(b)** Histogram of interaction durations for ligand-induced dimerization as detected using Cy3B- and ATTO643 DNA-PAINT-SPT (red, mean = 24.2 ± 3.8 s) or Cy3B- and ATTO643 single-dye labeling (blue, mean = 3.3 ± 1.3 s). Data collected during measurements of six minutes each from three samples per condition.

Individual dimers could routinely be followed for tens of seconds, often even for several minutes (**Fig. 4.5a-b**; **??**, **Fig. S4.4**), in stark contrast to various single-dye labeled controls, including state-of-the-art fluorophores developed for single-molecule imaging [16] (**Fig. 4.5a-b**; **Fig. S4.5**). Similarly, the number of observable DNA-PAINT labeled proteins remained more stable than the single-dye controls: not only does the number of detected dimers rapidly decrease over time for single-dye labeling, but also the apparent dimer lifetime is shortened as a consequence, resulting in a systematic underestimation of dimer stability (medians of co-diffusion durations measured with DNA-PAINT and single-dye labeling: $T_{\text{DNA-PAINT-SPT}} = 24.2 \pm 3.8$ s, and $T_{\text{single-dye}} = 4.1 \pm 1.3$ s; **Fig. 4.5b**).

As a result of the frictional drag incurred by the increased membrane footprint of the dimers, we observed slowing down of diffusion of dimerized proteins by 28 % (**Fig. 4.6**).

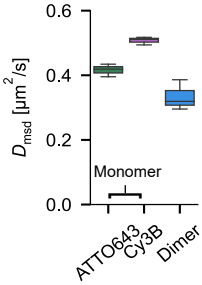

Figure 4.6 • Diffusion constants of FKBP monomers and dimers

Diffusion constants of monomers and dimers labeled with DNA-PAINT-SPT. Boxes, line and whiskers show, respectively, 25–75 quartiles, median, and minimum and maximum values of data collected from three samples per condition.

4.2.2 Obtaining 2D dissociation constants for homodimerization from ligand-titration experiments

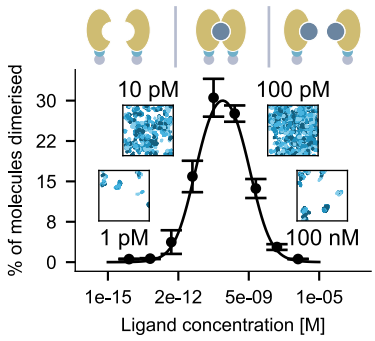

Figure 4.7 • DNA-PAINT-SPT allows quantitative single-molecule studies of FKBP homodimerization

Fraction of dimerized molecules as detected using DNA-PAINT-SPT during ligand-titration experiments. Fitting the data with an analytical homodimerization model results in dissociation constants $K_X = 5.9 \pm 0.5 \times 10^{-3}\,\mu m^{-2}$, $K_B = 33 \pm 5\,pM$. Insets: Trajectories of detected dimers for selected ligand concentrations, collected during 40 seconds measurements. Fields of view are 70 70 µm. Error bars denote mean and standard deviation of data collected on five fields of view per condition, samples were prepared independently as duplicates.

When titrating the ligand from low to increasingly higher concentrations, we could follow the onset of dimerization at around 1 pM, detected a maximal interaction level at concentrations around 100 pM and eventually the diminishing of dimerization due to the saturation of monomers with ligands at >10 nM (**Fig. 4.3a**, **Fig. S4.2**). From these measurements, we were able to extract 2D dissociation constants K_B (ligand from solution binding to FKBP monomer; [M]) and K_X (cross-linking of a ligand-bound monomer with a free monomer; [µm^{-2}]), by fitting an analytical homodimerization model to our DNA-PAINT single-molecule data ($K_B = 0.85 \pm 0.17$ nM, $K_X = 2.6 \pm 0.2 \times 10^{-2}\,\mu m^{-2}$; coefficient of determination $R^2 = 0.9914$; **Fig. 4.7**, **Section 4.5.2**, [17]). Inducing dimerization with an anti-SNAPtag antibody instead of the AP20187 ligand was reflected in a two-fold reduction of diffusion upon dimerization,

compared to AP20187-induced dimers (see **Fig. S4.6**, **Fig. S4.7**) and larger dissociation constants (**Fig. S4.8**, **Fig. S4.9**; $K_B = 136 \pm 41\,\mathrm{nM}$, $K_X = 0.12 \pm 0.02\,\mu\mathrm{m}^{-2}$), in line with the expectations from solution kinetics predicting weaker affinities for the antibody.

4.2.3 Orthogonal DNA-PAINT-SPT of two membrane proteins in live cells using SNAPligand- and nanobody-modified docking strands

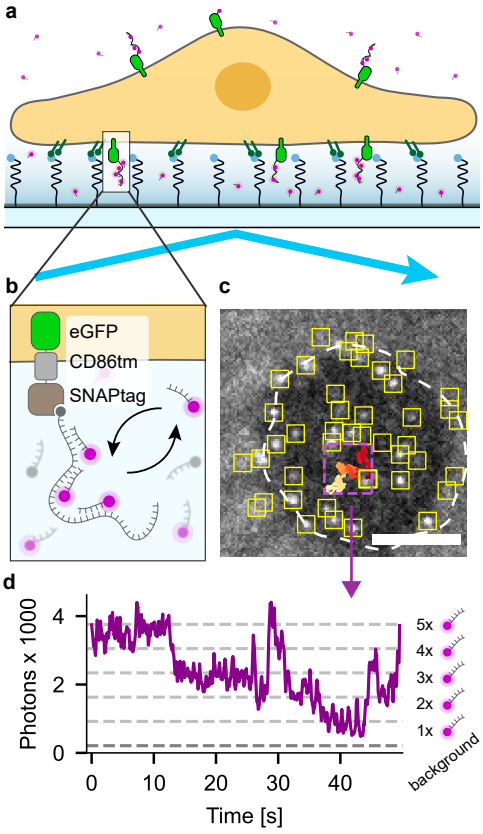

Figure 4.8 • Live-cell implementation of DNA-PAINT-SPT

(a) Schematic of DNA-PAINT-SPT experiment: cells rest on PEG-cushioned SLBs decorated with RGD peptides for optimal cell attachment, imager access and surface passivation. **(b)** Membrane proteins of interest are labeled with a oligonucleotide (docking strand) using protein tags (SNAPtag) or nanobodies, allowing continuous binding and unbinding of several fluorescently-labeled, complementary imager strands from solution. **(c)** Video frame of TIRFM video showing single-molecule trajectories of DNA-PAINT labeled membrane proteins expressed on a Jurkat T cell. Localized molecules (yellow boxes) and trajectory of an individual molecule (magenta box, trajectory is color-coded in time from red to yellow). Scale bar: 5 µm. **(d)** Intensity of single molecule trajectory displayed in **Fig. 4.8c**, magenta box) over time. Dashed dark gray line is the background level, light gray lines are guides to the eye indicating multiples of the lowest photon intensity, corresponding to the number of imager strands bound to the docking strand.

Having developed dual-color DNA-PAINT-SPT, we next sought to establish DNA-PAINT-SPT for live cell SPT experiments. Since DNA-PAINT-SPT relies on the diffusive exchange of fluorescent imager strands from solution, a surface-restricted excitation geometry (i.e. TIRFM) is required to suppress the background signal from free imager strands. However, the implementation of TIRFM for DNA-PAINT-SPT on live

cells is not trivial: the glass surface properties need to be tuned to facilitate cell adhesion while allowing imagers to diffuse underneath the cell (**Fig. 4.8a**). At the same time, unspecific binding of free imagers has to be minimal. Out of all passivation methods screened, we found that SLBs containing lipids modified with an integrin-recognition peptide (DSPE-PEG2000-RGD) suppressed nonspecific binding the best while promoting cell attachment and imager strand diffusion underneath the cells (**Fig. 4.8a** and **Section 4.5.3**, **Fig. S4.10**, **??**). During the live-cell imaging time scales typical for SPT experiments (minutes to max. two hours), we observed no significant effects on cell viability or morphology beyond the differences in cell adhesion to the surfaces. For Cy3B-conjugated imager strands, passivation For selected fluorophores, passivation using a non-covalent PLL-PEG/PLL-PEG-RGD coating was also sufficient (**Section 4.5.3**).

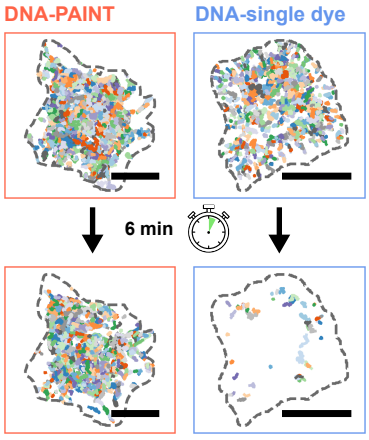

Figure 4.9 • DNA-PAINT-SPT enables extended tracking of individual membrane proteins on live cells

Membrane protein (SNAPtag-CD86tm-FKBP-GFP) trajectories collected during the first (top) and last (bottom) 20 seconds of a six minute recording; Left: membrane proteins labeled with DNA-PAINT (BG-DNA, nine repeats of eight nucleotides complementary to Cy3B-labeled imager strand). Right: membrane proteins labeled with DNA single-dye control (BG-DNA, 35 nucleotides complementary to Cy3B-labeled imager strand). Scale bar: 10 µm.

After surface optimisation, we labeled a model transmembrane protein (SNAP-CD86tm-FKBP-GFP) via its extracellular SNAPtag with a BG-DNA docking strand for DNA-PAINT-SPT (**Fig. 4.8b**): after addition of complementary imager strands carrying Cy3B fluorophores, individual membrane proteins on the cell surface were visible as diffusing bright fluorescent spots with step-wise fluctuating intensity, as expected from the continuous binding and unbinding of imager strands (**Fig. 4.8b-d**; **??**). We note cells appear as dark shadows surrounded by elevated background (**Fig. 4.8c**) in our TIRFM videos, indicating that diffusion of imager strands into the space between cells and glass coverslips is restricted. However, using a 75 nucleotides DNA docking strand and 40 nM of imager strands, we could achieve continuous exchange as indicated by the step-wise intensity fluctuations (**Fig. 4.8d**). Comparing DNA-PAINT-SPT on these cells to single-dye controls, we found that

the number of observable DNA-PAINT labeled membrane proteins remained stable ($> 85\%$ after six minutes) compared to the single-dye control, where this number decreased to less than a fifth of the initial value ($< 15\%$ after six minutes), with most of the remaining observable molecules diffusing in from the cell boundaries (**Fig. 4.9**, **Fig. 4.10a**, **Fig. S4.11**). As a combined measure for average trajectory length and number, we plot the number of tracks that are longer than a given threshold time T, normalised to the number of molecules initially detected per cell, for DNA-PAINT and single-dye labeled membrane proteins (**Fig. 4.10b**, **Fig. S4.12**). This shows that also for live cell imaging, DNA-PAINT-SPT not only keeps the number of observable molecules constant for long durations (>6 min), but also increases the duration of individual trajectories (Cy3B-DNA-PAINT-SPT: $\tau_{1/2} = 31 \pm 13$ s; Cy3B-single-dye: $\tau_{1/2} = 17 \pm 3$ s).

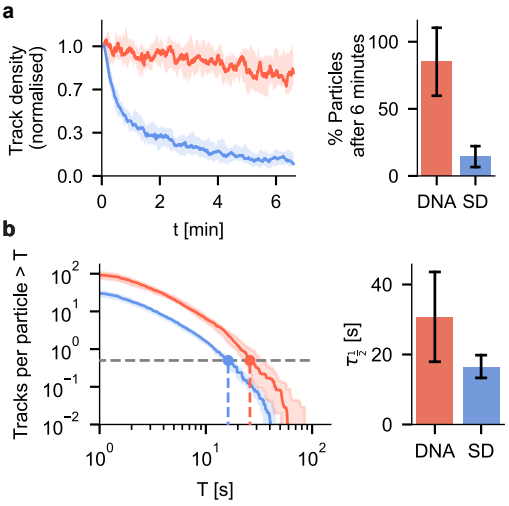

Figure 4.10 • DNA-PAINT-SPT and single-dye SPT trajectory numbers and durations

(a) Number of trajectories per frame on individual cells labeled with DNA-PAINT (red, $n_{\text{cells}} = 25$) or single dyes (blue, $n_{\text{cells}} = 32$), normalised to initial number of trajectories. **(b)** Single-molecule trajectories on individual cells labeled with DNA-PAINT (red, $n_{\text{cells}} = 25$) or single dyes (blue, $n_{\text{cells}} = 32$) with a duration longer than T, normalised to the initial number of trajectories per cells. In **(b)** and **(c)**, curves represent the median with shaded areas indicating the 25-75 quartiles of data collected from three samples per condition. Bars and error bars denote mean and standard deviation.

Diffusion constants of proteins labeled with DNA-PAINT, single-dye DNA or BG-conjugated organic fluorophores were similar: DNA-PAINT with Cy3B-labeled imager strands: 0.093 ± 0.017 µm^2/s, single-dye DNA labeled with Cy3B: 0.085 ± 0.014 µm/s, BG-JF549i: 0.082 ± 0.020 µm/s, BG-AF647: 0.107 ± 0.016 µm/s; **Fig. 4.11**, **Fig. S4.13**). This suggests that DNA-PAINT-labeling *per se* influences diffusion to a lesser extent than the choice of fluorophore [18]. We also note that we did not observe any exclusion effects of DNA-labeled proteins from cell-surface contacts (**Fig. 4.8c**, **Fig. S4.14**, **Fig. S4.15**).

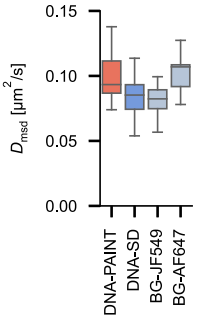

Figure 4.11 • Diffusion constants of differently labeled membrane proteins on live cells

Diffusion constants of SNAPtag-CD86tm-FKBP-GFP cell membrane proteins labeled with DNA-PAINT ($n_{\text{cells}} = 28$), DNA single-dye control ($n_{\text{cells}} = 43$) and organic fluorophores JF549 ($n_{\text{cells}} = 21$) and AF647 ($n_{\text{cells}} = 7$). Boxes, line and whiskers show, respectively, 25–75 quartiles, median, and minimum and maximum values of data.

Using dual-color DNA-PAINT-SPT, we were able to track FKBP-dimers on live cells for minutes, a substantial improvement over interaction tracking durations of mere seconds that are typically attainable with conventional single-dye labeling (see **Fig. S4.16**, **??**). Notably, DNA-PAINT-SPT worked equally well with a second, non-covalent labeling approach, using a docking strand conjugated to an antiGFP-nanobody (**Fig. 4.8b**, **Fig. 4.12**). Thus, we can use two orthogonal labeling approaches (BG-conjugated docking strands or antiGFP-nanobodies) in combination with the orthogonal docking-imager pairs for dual-color DNA-PAINT-SPT on live cells (**Fig. 4.12**; **??**).

4.3 Discussion

In this work we present DNA-PAINT-SPT as a new promising technique for simultaneous dual-color tracking of proteins on SLBs and live cells. We developed docking strands with orthogonal sequences and show that our method outperforms current state-of-the-art labeling in both colour channels. The marked improvement in trajectory lengths makes DNA-PAINT-SPT an ideal tool to study 2D binding kinetics quantitatively with unprecedented ease: to the best of our knowledge, this is the first time that 2D dissociation constants could be reliably extracted from single-molecule measurements using an analytical dimerization model. We quantified 2D-K_D constants of two dimerization agents (AP20187 and monoclonal anti-SNAPtag antibodies) in our FKBP protein homodimer-system, showing that we can clearly differentiate between the two using our DNA-PAINT-SPT approach. Moreover, since in both cases, dimerization was induced by a soluble ligand, we could also verify that the DNA-PAINT-SPT labels do not induce interactions or crosslinking by themselves. The absence of these artifacts and the convenient one-to-one targeting of molecules via standard tagging approaches

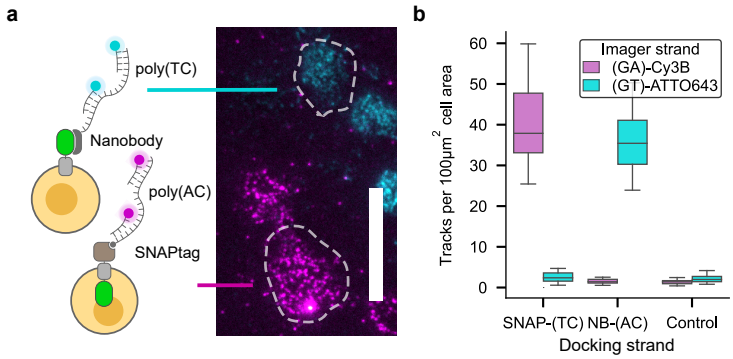

Figure 4.12 • Multicolor DNA-PAINT-SPT and conjugation strategies on live cells

(a) Cells expressing either GFP-CD86tm-FKBP-HALOtag (cyan) or SNAPtag-CD86tm-FKBP-GFP (magenta) fusion proteins labeled with GFP-nanobody-conjugated docking strands (nanobody-DNA, nine repeats of eight nucleotides complementary to Cy3B-labeled imager strand) or with BG-DNA (BG-DNA, nine repeats of eight nucleotides complementary to ATTO643-labeled imager strand). Scale bar: 20 µm. **(b)** Density of tracks detected on cells expressing extracelullar SNAPtag- ($n_{\text{cells}} = 38$) or GFP-fusion proteins ($n_{\text{cells}} = 35$) and non-transfected controls ($n_{\text{cells}} = 30$), when labeled in parallel with BG- or nanobody-conjugated docking strands with orthogonal sequences and their respective imager strands. Boxes, line and whiskers show, 25–75 quartiles, median, and minimum and maximum values.

make DNA-PAINT-SPT superior over other photostable labelling approaches, such as quantum dots or gold particles [4].

Protein-protein interactions in membranes are vital to many aspects of cellular function, including cellular signalling. Hence, experimental techniques that can measure these interactions *in situ* are highly desirable [19]. We note that in contrast to DNA-PAINT-SPT, most traditional affinity measurement techniques, such as surface plasmon resonance, only give 3D-K_D constants and on-rates that cannot easily be converted into their 2D counterparts which are the relevant measures of protein-protein interactions in membranes [17, 19–21].

In a next step, we established dual-color DNA-PANT-SPT on live cells and for labelling membrane proteins with two orthogonal approaches; either via an extracellular SNAPtag that binds benzylguanine-conjugated docking strands, or with an extracellular GFP tag that was labeled by docking strands conjugated to antiGFP-nanobodies. These orthogonal

tagging methods allow the labelling of two sets of proteins simultaneously and specifically with different colors. We expect DNA-PAINT-SPT to work with a wide range of other common tagging approaches in addition to those tested in this study [22–24]. While we carefully examined the orthogonality of our DNA-PAINT-SPT labels and employed widely-used tags that have been shown in many cases not to interfere with receptor function [25–28], it is crucial to validate experimentally that the chosen labeling method does not significantly affect the biological function of the receptors under study. To minimize the impact of the label on the protein function and interactions, smaller peptide tags such as the ALFA-tag [23] or the incorporation of unnatural amino acids to enable bio-orthogonal attachment of DNA-docking strands via click chemistry [29] could be employed. For reducing the background and unspecific binding of free imager strands, we found bilayers decorated with PEGylated lipids conjugated to integrin-ligands to provide a highly-passivating, cell-attachment promoting surface. As an alternative, we demonstrated that reconstituting the adhesion protein ICAM on nickelated bilayers yields comparable surface passivation and cell attachment properties. Since the vast majority of cell lines express integrins, we expect this method to be widely applicable [30–32]. Moreover, reconstituting other adhesion-promoting proteins on bilayers matched to the cell type of interest would likely yield similarly suitable adhesion and passivation properties [33].

As for any DNA-PAINT method, a major limitation of DNA-PAINT-SPT is that it cannot be applied to image intracellular targets in live cells. However, we believe that the effort of developing better tools for extracellular SPT is well invested, given the high importance of cell membrane protein dynamics and interactions in cellular signaling and homeostasis. Being able to follow molecules for longer times without significant photobleaching will allow researchers to access biological processes happening at longer timescales and the largely-increased number of trajectories improves statistical certainty for the detection of rare events.

In summary, DNA-PAINT-SPT is a promising technique for quantitative SPT of membrane proteins on both SLBs and live cell membranes while being simple to implement by the single-molecule community: its use of standard protein tags and the commercial availability of a wide range of DNA modifications and fluorophores make it a versatile method. In the future, further improvements of organic dyes [8] and new ways of reducing the background signal in DNA-PAINT experiments in general [34, 35] will directly benefit DNA-PAINT-SPT and allow researchers to visualise protein function in membranes with even higher spatiotemporal resolution.

4.4 Methods

4.4.1 Materials

Chemicals and materials used were HEPES (H3375, Sigma-Aldrich), sodium chloride (310166, Sigma-Aldrich), magnesium chloride (M8266, Sigma-Aldrich), phosphate-buffered saline tablets (P4417, Sigma-Aldrich), pyranose oxidase (P4234, Sigma-Aldrich), catalase (C40, Sigma-Aldrich), Trolox (238813, Sigma-Aldrich), BSA (A9418, Sigma-Aldrich), Uvasol chloroform (1.02447, Sigma-Aldrich), Uvasol methanol (1.06002, Sigma-Aldrich), sulfuric acid (258105, Sigma-Aldrich), hydrogen peroxide (216763, Sigma-Aldrich), Fibronectin (F0895, Sigma-Aldrich), PLL (P4707, Sigma-Aldrich), PLL-PEG-RGD (SuSoS), His-tagged ICAM-1 (IC1-H52H5, ACROBiosystems), B/B homodimerizer (AP20187, Takara Bio), dibenzocyclooctyne-PEG4-maleimide (760676, Sigma-Aldrich), SNAP/CLIP-tag monoclonal antibody (6F9, Chromotek), single-domain antibody (nanobody) against GFP (clone 1H1, Nanotag Biotechnologies), SNAP-Surface Alexa Fluor 647 (S9136S, New England Biolabs), SNAP-Surface ATTO488 (S9124S, New England Biolabs), Tetraspeck Microspheres 0.2 µm (T7280, ThermoFisher Scientific). SNAPtag-ligand Janelia Fluor dyes (BG-JF549i, BG-JF646, BG-JFX650) were kindly provided by Luke Lavis (Janelia Labs, HHMI).

Lipids used were DOPC (850375, Avanti), DGS-NTA-Ni (790404, Avanti), DSPE-RGD (870295, Avanti), DSPE-PEG-cRGDyk (LP096262-2K, Biopharma PEG) and DOPE-ATTO390 (390-161, ATTO-TEC).

All DNA oligonucleotides were obtained HPLC-purified from Eurofins, except for BG-modified docking strands (Biomers) and azide-modified docking strands (Metabion) used for nanobody-DNA conjugation.

Cell biology media and supplements used were DMEM without Phenol Red (12-917F), DMEM with Phenol Red (12-604F, Lonza), RPMI 1640 with Phenol Red (L0500-500, biowest), RPMI 1640 without Phenol Red (11835-030, gibco), Fluorobrite DMEM (A18967-01, gibco), Pen-Strep (15140122, Sigma-Aldrich), Na-Pyruvate (BE13-115E, Lonza), L-Glutamine (25030-024, gibco), FBS (A3160802, gibco), Ultramem (BE12-743F, Lonza), GeneJuice (70967, Sigma-Aldrich).

Molecular biology

pHR-SNAP-CD86-mOrange-FKBP plasmid was a kind gift from Ricardo A. Fernandes. *Tet-pLKO-puro* backbone for tetracycline-inducible was obtained from Addgene (accession number #21915). For live-cell imaging, *pHR-SNAP-CD86-eGFP-FKBP*, *pHR-eGFP-CD86-HaloTag-FKBP* and *Tet-pLKO-puro SNAP-CD86-eGFP-FKBP(f36v)* were created using Gibson assembly. For AP20187-induced homodimerization of FKBP, we introduced a point-mutation ($FKBP^{f36v}$) following previously published protocols [15, 36] and created *pET30-10His-FKBP^{f36v}-SNAP* using Gibson assembly.

Cell biology

Jurkat cells were cultured in RPMI with Phenol Red, supplemented with 10% FBS, 1% PenStrep and 1% Na-Pyruvate. *Tet-pLKO-puro*-transduced Jurkat cells were cultured without tetracycline present in the medium, as the remaining leaky expression was sufficient for single-molecule experiments. HEK cells for lentivirus production were cultured in DMEM with Phenol Red, supplemented with 10% FBS, 1% PenStrep and 1% Glutamax. Phenol-Red free media were used for seeding Jurkat cells into 6-well plates before transfection and labeling.

Transduction of Jurkat T cells

Jurkat cells were transducted using lentiviral transfection: To this end, HEK293T cells were first transfected with the pHR plasmid of interest, psPax and pMD2G using GeneJuice, following the manufacturer's protocol. Viral supernatant was collected after 72h and used for Jurkat transduction.

Nanobody-DNA conjugation

Nanobodies with a single ectopic cysteine at the C-terminus for site-specific conjugation were conjugated similarly to the method described previously [11]. Unconjugated nanobodies were thawed on ice, then 20-fold molar excess of bifunctional maleimide-Peg4-DBCO linker was added and reacted for 2h on ice. Unreacted linker was removed by buffer exchange using Amicon centrifugal filters (10,000 MWCO). Then, two equivalents of azide-functionalized DNA (5') were reacted with the DBCO-modified nanobodies overnight at 4 °C. Unconjugated protein

and free DNA were removed by anion exchange chromatography using an ÄKTA pure system equipped with a Resource Q 1mL column.

Recombinant protein expression

10His-FKBP^{f36v}-SNAP was expressed in *E.coli* (Rosetta strain), purified via its His-tag using an ÄKTA pure system equipped with a HisTrap HP 1mL column, followed by size-exclusion chromatography using a Superdex 200 increase 10/300 GL column.

Small-unilamellar vesicle generation

Lipids were dissolved in chloroform (to dissolve DSPE-PEG-RGD, 10% methanol were added, and the mixture was sonicated for 30 s in a bath sonicator) and stored in 1.5 mL glass vials with PTFE-lined caps at −20 °C. Lipid mixes were prepared from the stock solutions depending on the required bilayer composition (reconstitution experiments: 98.5% DOPC, 1% DGS-NTA-Ni, 0.5% DOPE-ATTO390; live-cell experiments: 89.5% DOPC, 10% DSPE-PEG-RGD, 0.5% DOPE-ATTO390) and 1 mL were transferred to a 50 mL round bottom flask. By gentle swirling and nitrogen flow, the lipid was dried into a thin film onto the flask walls. Once dried, trace amounts of chloroform were removed by desiccating the flask for at least 2h protected from light.

Afterwards, the dried lipid film was re-hydrated in HBS (HEPES 40 mM, pH 7.6, NaCl 140 mM) at a concentration of 2 mg/mL, aliquoted and stored at −20 °C until further use. On the day of the experiment, aliquots were thawed and sonicated for 30 min in a bath sonicator to produce small-unilamellar vesicles (SUVs). SUVs were diluted towards 0.1 mg/mL and used on the same day.

Preparation of imaging chambers

Coverslips with the dimensions 25 x 75 mm, 1.5H (10812, Ibidi) and 22 x 22 mm, 1.5H (631-0851, VWR) were piranha cleaned using H_2SO_4 and H_2O_2 in a 3:1 ratio. After 1h, they were thoroughly rinsed with milliQ water and dried using nitrogen flow. Slides were then air-plasma cleaned for 10 minutes (Harrick Plasma Cleaner PDC-002-HPCE). Chambers were created either by adhering ibidi sticky-slide 8-well or 18-well chambers (80808 or 81818, ibidi) onto pre-treated glass coverslips, or glueing 0.5 mL Eppendorf tubes with the conical part cut off onto cover-

slips, using UV-curable optical adhesive (NOA68, Thorlabs) and a 36 W UV nail dryer (B00R4M0TI0, Nailstar).

Immediately after plasma cleaning and chamber assembly, 50 µL of HBS were added to each chamber. Then, 50 µL of the respective SUV solution (0.1 mg/mL) were added and the samples were transferred to a moisturised box for 30 minutes. Chambers were washed with 2 mL HBS and bilayers were blocked using BSA (1% (w/v) in HBS) for 10 minutes. Chambers were washed again with 2 mL HBS and stored in a dark moisturised box until further use on the same day.

For the screening of surface passivation methods, we used fibronectin (100 µg/mL, 1h incubation), PLL-PEG-RGD (0.8 mg/mL, 2h incubation), PLL (100 µg/µL, 1h incubation) and His-tagged ICAM-1 (20 nM, 1h incubation on SLB containing 1% DGS-NTA-Ni).

Protein labeling and reconstitution in SLBs

$FKBP^{f36v}$was thawed on ice and centrifuged for 1h at 4 °C at 16100 x g. For dual-color experiments, supernatant (2.1 µM) was divided into two aliquots and incubated separately with the respective docking strand (3.6 µM) for 1h at room temperature. Protein-DNA was diluted in HBS with 0.1% BSA and 10 mM $MgCl_2$ and incubated on the prepared lipid bilayers for 1h in a dark moisturised box at room temperature. Chambers were washed with 2 mL HBS and imager strand solution containing 40 nM of the respective imager strands, 5 mM $MgCl_2$, 3.7U/mL pyranose oxidase, 200U/mL catalase, 0.8% glucose, 0.1% (w/v) BSA and 2 mM Trolox-Trolox-quinone (Trolox to Trolox-quinone ratio 10% to 20%, determined via NanoDrop 2000 absorption [37]), were added.

Cell labeling and preparation for microscopy

Cells were incubated with BG-DNA docking strands (1 nM to 10 nM) for Jurkat cell lines with *pHR*-promoter plasmids, 100 nM for Jurkat cell lines with tetracycline-inducible *Tet-pLKO-puro*-promoter plasmids), nanobody-docking strands (5 pM to 10 pM) or BG-fluorophores (1 nM to 10 nM) for 30 minutes at 37 °C, 5% CO_2. Then, cells were washed three times by centrifugation (5 min, 100 x g) and re-suspending in PBS. The final resuspension step was performed in PBS with 5 mM $MgCl_2$ and 0.1% (w/v) BSA and, if applicable, the respective imager strand concentration: DNA-PAINT-SPT experiments were performed with 40 nM imager strands; for DNA single-dye experiments, 100 pM of complementary fluorescently labeled strands were added and washed out after

10 min of incubation. Live-cell measurements were limited to a maximum imaging duration of two hours after removing the cells from the incubator. Cells with labeling densities of around 0.1 μm^{-2} were used for analysis.

TIRF Microscopy

Fluorescence imaging was performed on a custom-built microscope in an objective-type TIRF configuration with an oil-immersion objective (CFI Apochromat TIRF 60x, NA 1.49, Nikon) and a three-color detection scheme. The setup is described in detail in **Chapter 2** and [38].

In brief, a pre-assembled laser combiner was used to provide four excitation wavelengths (C-FLEX laser combiner, Hübner Photonics; 405 nm 140 mW, 488 nm 200 mW, 561 nm 220 mW, 638 nm 195 mW). The excitation beam was delivered to the optical bench via a single-mode polarisation-maintaining fiber (kineFLEX-HPV-P-3-S-405..640-0.7-0.7-P0, Qioptiq). The laser light was re-collimated after the fiber using an achromatic doublet lens (f =50 mm) and directed through an achromatic quarter-waveplate to ensure circular polarisation. The laser beam was spectrally filtered using a quad-line bandpass (ZET405/488/561/-640xv2, Chroma) and then transformed into a collimated flat-top profile using a refractive beam shaping device (piShaper 6_6_VIS, AdlOptica) [39]. The laser beam diameter was magnified by a factor of 2.5 using a telescope assembly (f_1 =100 mm, f_2 =–40 mm). The laser light was focused onto the objective's back focal plane using an achromatic doublet lens (f =250 mm). A stage (KMTS25E/M Motorised Translation Stage, Thorlabs) translated the excitation beam off-axis to switch between wide-field, HILO or TIRF imaging. A short penetration depth of the evanescent field was ensured by translating the excitation beam in the back focal plane to the maximum possible value without clipping the beam. The angle of incidence was determined as 76° as previously described [40], resulting in a calculated evanescent field penetration depth ranging from 68 nm (561 nm laser excitation) to 78 nm (638 nm laser excitation).

The excitation beam was directed towards the objective by a four-color notch dichroic mirror (ZT405/488/561/640rpc-UF2, Chroma). Fluorescence emission passing through this dichroic mirror was spectrally filtered with a quad-line notch filter (ZET405/488/561/640mv2, Chroma) and was directed through a tube lens (TTL200-A, Thorlabs). The dichroic mirror, the objective, the tube lens and the quad-band notch filter were all placed in a CNC-milled cube based on the miCube design [41]. This block also supported a piezo stick-slip stage (SLS-5252, Smar-

act) to move the sample in x-y-z. The tube lens formed an image outside of the cube, where a custom-built slit aperture was used to crop the image horizontally to enable simultaneous three-color imaging. In a 4f-system (f =300 mm), the fluorescence emission was split spectrally using two dichroic mirrors (ZT561rdc and ZT640rdc, Chroma), filtered using respective bandpass filters (525/30 Brightline, Semrock; ET595/50m, Chroma; 680/42 BrightLine, Semrock) and imaged on a sCMOS camera (primeBSI, Teledyne Photometrics). Individual lenses (f =300 mm) on the imaging side of the 4f system ensured matching focal planes for all three channels. The imaging setup resulted in an effective pixel size of 108 nm. Focus stabilisation was achieved using a system based on the pgFocus device [42]. An infrared laser (CPS808S, Thorlabs) was attenuated using a neutral density filter (NE13A-B, Thorlabs), coupled into the excitation path using a long pass dichroic mirror (ZT775sp2-2p-UF1, Chroma) and focused onto the back focal plane of the objective using a f =500 mm lens. Using a manual micrometer stage, the infrared laser was brought into total-internal reflection. The back reflection was filtered through a bandpass filter (FB800-40, Thorlabs) and focused (f =200 mm) onto a linescan sensor (TSL1401, Parallax). A feedback loop with the piezo-driven stage moving the sample allowed for focus stabilisation throughout extended measurement durations. The setup was controlled using C# software developed by Marko Seynen (AMOLF, Software Engineering Department).

Imaging conditions

Fluorescence microscopy was performed at room temperature (22 ± 1 °C) in three-color simultaneous imaging mode. To this end, the sCMOS camera readout was cropped to 682 x 2048 pixels, providing a 682 x 682 readout for each channel. The camera was operated at 32.4 ms (in vitro experiments) or 72.4 ms (live-cell experiments) exposure times, with frame rates of 25 or 12.5 per second, respectively. The read-out rate was set to 100 MHz and the dynamic range to 12 bit. We performed experiments at laser excitation powers in the range of 4 mW to 40 mW (measured just before the back focal plane of the objective), which translate to irradiances of 15 W/cm^2 to 150 W/cm^2 in our setup. Laser powers were kept as low as possible while still allowing for robust localization above background levels, resulting in a typical localization precision between 20 nm and 30 nm for all labels. The angle of incidence was 76°, resulting in an evanescent field penetration depth in the range of 68 nm (561 nm laser excitation) to 78 nm (638 nm laser excitation).

Data analysis

Raw data were localized using *picasso* [43]. Optical distortions were determined using a calibration slide with 200 nm Tetraspeck multi-color fluorescently-labeled beads, and corrected using Zernike polynomial gradients [44]. Trajectories were reconstructed from localizations using *trackpy* [45] and *Swift 0.4.3* [46, 47]. Trajectories with durations of less than 10 frames or diffusion constants smaller than 0.01 $\mu m^2/s$ were rejected. For analysis of live cell data, regions of interest were selected in *Fiji* [48] based on the cell outline of a maximum intensity projection of the underlying video or based on the GFP signal of the cell. Colocalization was determined by calculating intramolecular distances between localized molecules in the different color channels, and pairs with distances below 300 nm were identified as colocalized and potentially interacting. With a localization precision ranging between 20 nm and 30 nm and a color channel registration error of 32 nm, the threshold of 300 nm resulted in an expected false negative rate of $< 0.001\%$ [49]. Colocalization events were linked frame-by-frame, with gaps of maximum 6 frames closed. Resulting co-diffusion trajectories were considered as true interactions if their duration exceeded 10 frames (see **Fig. S4.3** for an illustration of the analysis workflow). Integration of the different analysis packages, any further analysis and visualisation of data was performed with custom-written *Python*-code available at github.com/GanzingerLab/SPIT.

4.5 Supplementary Information

4.5.1 DNA sequences

DNA-sequences are in 5'-3' notation.

- DNA-PAINT-SPT sequences

  Imager strand A, Cy3B-conjugated: 4x(GA) - Cy3B
  GAGAGAGA - Cy3B

  Imager strand B, ATTO643-conjugated: 4x(GT) - ATTO643
  GTGTGTGT - ATTO643

  Docking strand A: BG- or azide- conjugated: 37.5x(TC)
  BG/azide - TCTCTCTCTCTCTCTCTCTCTCTCTCTCTCTC
  TCTCTCTCTCTCTCTCTCTCTCTCTCTCTCTCTCTCTCT

  Docking strand B: BG- or azide-conjugated: 37.5x(AC)
  BG/azide - ACACACACACACACACACACACACACACACACA
  CACACACACACACACACACACACACACACACACACACACA

- Single-dye DNA sequences
  We used a single-dye control designed to be of similar size and mass compared to a 50% imager strand-occupied DNA-PAINT-SPT docking strand. The single-dye docking-imager strand pair consists of a 75 nucleotide docking strand and a 35 nucleotide fully complementary imager strand. At our experimental conditions (ionic strength, temperature, timescale), the imager strand is considered to be irreversibly bound to the docking strand.

  Imager strand A:
  ATAATAAGTAATCTACAACAATCGGGTGGGTCAGC - Cy3B

  Imager strand B:
  TAATGAAATGGGAACTAACTCTCGGAAACCTTTAT - ATTO643

  Docking strand A:
  BG - TTTTTTTTTTATAAAGGTTTCCGAGAGTTAGTTCCCA
  TTTCATTATTTTTTTTTTTTTTTTTTTTTTTTTTTT

  Docking strand B:
  BG - TTTTTTTTTTGCTGACCCACCCGATTGTTGTAGATTA
  CTTATTATTTTTTTTTTTTTTTTTTTTTTTTTTTTT

4.5.2 Analytical derivation of dimer concentration for ligand-induced homodimerization

We briefly outline the analytical derivation of the dimer concentration for ligand-induced homodimerization. For a detailed discussion refer to Binder et al., 2021 [17]. We use 2D densities in $1\,\mu m^{-2}$ and convert molar 3D concentrations into $1\,\mu m^{-3}$, where

$$1\,\mu M = \frac{1\times10^{-6}\cdot 6.022\times10^{23}}{1\,L} = \frac{6.022\times10^{17}}{1\times10^{15}\,\mu m^3} = 602.21\,\mu m^{-3}$$

Consider a system with ligands in solution with concentration c_L and protein monomers embedded in a lipid bilayer with surface concentration Γ_M. In this system, the ligands can bind up to two monomers simultaneously. We consider both the equilibrium of a monomer binding to a free ligand **Eq. S4.1** and the equilibrium of a monomer binding to an already bound ligand **Eq. S4.2**:

$$\mathrm{M} + \mathrm{L} \rightleftharpoons \mathrm{ML}, \tag{S4.1}$$

and

$$\mathrm{ML} + \mathrm{M} \rightleftharpoons \mathrm{MLM}. \tag{S4.2}$$

The dissociation constant K_B for a monomer bound to a single ligand, ML, is defined as

$$K_B = \frac{\Gamma_M c_L}{\Gamma_{ML}}, \tag{S4.3}$$

where Γ_{ML} is the surface concentration of ML. The dissociation constant K_X for the ligand-homodimer complex, MLM, is defined as

$$K_X = \frac{\Gamma_{ML}\Gamma_M}{\Gamma_{MLM}}, \tag{S4.4}$$

where Γ_{MLM} is the concentration of MLM.

To derive an expression for Γ_{MLM} that does not include Γ_M or Γ_{ML}, we need the equation for the mass balance of the protein monomer,

$$\Gamma_{M,\mathrm{tot}} = \Gamma_M + \Gamma_{ML} + 2\Gamma_{MLM}. \tag{S4.5}$$

Combining **Eq. S4.3** -**Eq. S4.5** and rearranging, we obtain

$$\Gamma_{MLM} = \frac{K_X(K_B + c_L)^2 + 4K_B\Gamma_{M,\mathrm{tot}}c_L}{8K_Bc_L} - \frac{\sqrt{K_X}(K_B + c_L)\sqrt{K_X(K_B + c_L)^2 + 8K_B\Gamma_{M,\mathrm{tot}}c_L}}{8K_Bc_L}, \tag{S4.6}$$

where we have discarded the second solution in which the second term (containing the square root) is positive, as it leads to negative values of Γ_M and Γ_{ML}.

The density of reconstituted proteins $\Gamma_M = \Gamma_{\text{M, channel 1}} + \Gamma_{\text{M, channel 2}}$ is measured by counting receptors before adding the dimerization ligand, since the random association of magenta and green labeled receptors into same-color and dual-color dimers (total: 25% magenta-magenta, 25% green-green, 50% magenta-green) would otherwise change the apparent receptor density. One hour after adding ligands, the number of dimers is determined by detecting co-diffusion trajectories of dual-color dimers. The number of apparent dimers is multiplied by the quotient of the lower density over the total density of green and magenta receptors: $\Gamma_M \cdot \min\left(\Gamma_{\text{M, channel 1}}, \Gamma_{\text{M, channel 2}}\right)^{-1} \approx 2$. The fraction of dimerized molecules is then fit by **Eq. S4.6** with free parameters K_X, K_B and a correction factor accounting for unlabeled molecules.

4.5.3 Surface passivation

The high concentration of fluorescently labeled imager strands in solution poses two challenges: imager strands bind to the surface via unspecific interactions with the surface or cell debris, and they contribute to a diffuse background, decreasing the signal-to-background ratio. We screened various surface passivation methods (see **Fig. S4.10**) and found lipid bilayers to provide the best passivation efficiency. Cell attachment is ensured by functionalising the bilayers with cell adhesion promoting molecules (RGD, PEG-RGD functionalised lipids or His-tagged ICAM-1 reconstituted on nickelated lipids). Bilayers containing PEG-RGD functionalised lipids or RGD-functionalised lipids had comparable passivation efficiencies, but PEG-RGD functionalised lipids performed better in terms of cell attachment. We also used PLL-PEG-RGD successfully for single-color experiments with Cy3B. When used with ATTO643-labeled imager strands, significant binding of imager strands to the surface was observed, which could at least partially be prevented by adding Trolox/Trolox-quinone as a reductant and oxidant system [37].

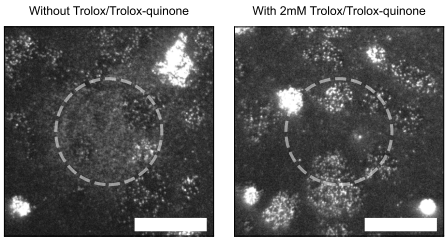

ATTO643 photoreaction on PLL-PEG-RGD with and without Trolox.
Cells labeled with DNA-PAINT and 40 nM ATTO643-labeled imager strands. First frame after illuminating for 1 min in the center circular region, with 2 mM Trolox/Trolox-quinone (left), or without Trolox/Trolox-quinone in the imaging buffer (right). Scale bar: 10 µm.

Surface	Imager strand	Locs. (bg.)	Locs. (cells)	Ratio
BSA	ATTO643	0.67 μm^{-2}	0.78	1.16
	Cy3B	0.25 μm^{-2}	0.37	1.44
Fibronectin	ATTO643	0.30 μm^{-2}	0.35	1.17
	Cy3B	0.17 μm^{-2}	0.22	1.33
PLL	ATTO643	0.17 μm^{-2}	0.30	1.81
	Cy3B	0.04 μm^{-2}	0.15	4.07
PLL-PEG-RGD	ATTO643	0.05 μm^{-2}	0.34	6.48
	Cy3B	0.06 μm^{-2}	0.37	6.45
DSPE-RGD	ATTO643	0.01 μm^{-2}	0.12	9.21
	Cy3B	0.01 μm^{-2}	0.08	11.08
ICAM	ATTO643	0.01 μm^{-2}	0.11	15.04
	Cy3B	0.01 μm^{-2}	0.10	12.34
DSPE-PEG-RGD	ATTO643	0.01 μm^{-2}	0.15 μm^{-2}	13.05
	Cy3B	0.01 μm^{-2}	0.11	16.53

Table 4.1 • Localizations (locs.) on background (bg.) and cells for different surface passivation methods

4.5.4 Supplementary Figures

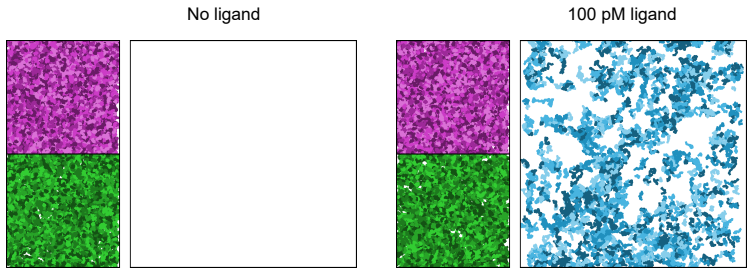

Figure S4.1 • Absence of interaction or crosslinking artifacts introduced by DNA-PAINT-SPT labels

DNA-PAINT-SPT single-molecule trajectories collected during 40 second recordings of reconstituted FKBP proteins with and without dimerization agent AP20187. Small panels (magenta and green) are single-molecule trajectories collected in two color channels and big panel (blue) are detected co-diffusion events that exceed 10 frames (400 ms). The absence of detectable dimers when no ligand is present, suggests that the DNA-PAINT-SPT label itself does not introduce interactions or crosslinking artifacts. Fields of view are 70 µm x 70 µm.

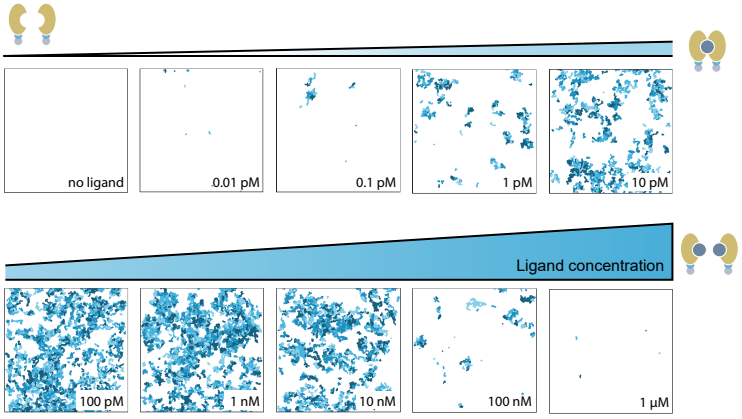

Figure S4.2 • Dimerization of FKBP proteins during ligand-titration experiments from onset to suppression of interaction

Co-diffusion events exceeding 10 frames (400 ms) at increasing concentrations of dimerization agent AP20187, detected by dual-color DNA-PAINT-SPT of reconstituted FKBP proteins. At concentrations above 10 nM, monomers are saturated with ligands and interactions are suppressed. Fields of view are 70 µm x 70 µm, measurement durations are 40 s.

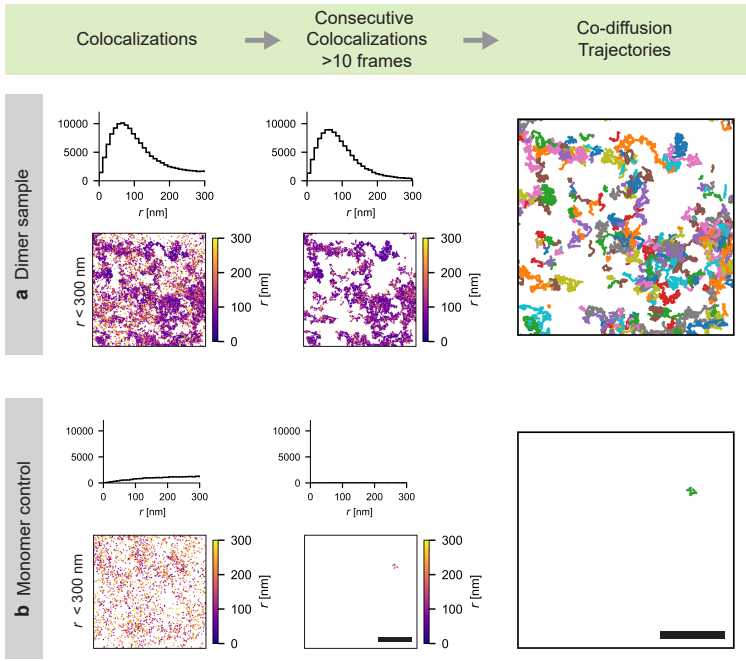

Figure S4.3 • Interaction analysis framework.
Detected colocalizations in a sample of reconstituted FKBP dimers (**a**), top, 100 pM dimerizing agent) and FKBP monomer control (**b**), bottom, no dimerizing agent) during a 20 s measurement. Left column shows colocalizations, color-coded by the distance r of each individual colocalizing pair, and a histogram of their pairwise distances. A colocalization threshold of 300 nm was used. Middle column shows remaining consecutive colocalizations and the respective pairwise distance histogram, after tracking and discarding all trajectories shorter than 10 frames (400 ms). Right column shows co-diffusion trajectories with gaps of up to 6 frames closed, color-coded by their trajectory ID. Scale bar is 10 µm.

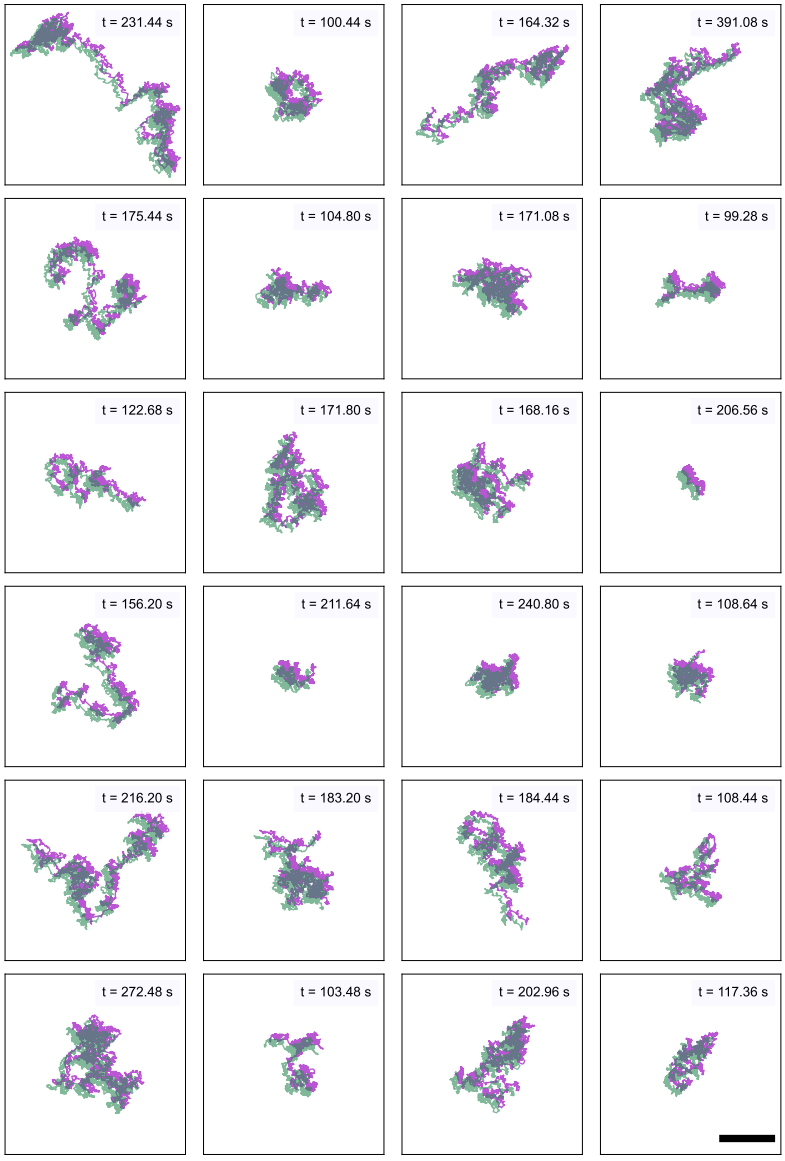

Figure S4.4 • Ligand-induced FKBP dimers detected with dual-color DNA-PAINT-SPT
The longest trajectories (30th-percentile) of co-diffusing AP20187-induced FKBP dimers, labeled with dual-color DNA-PAINT and recorded during a 15 minute TIRFM measurement. For displaying purposes, tracks were moved in opposite x and y directions by 1 µm. Scale bar: 10 µm.

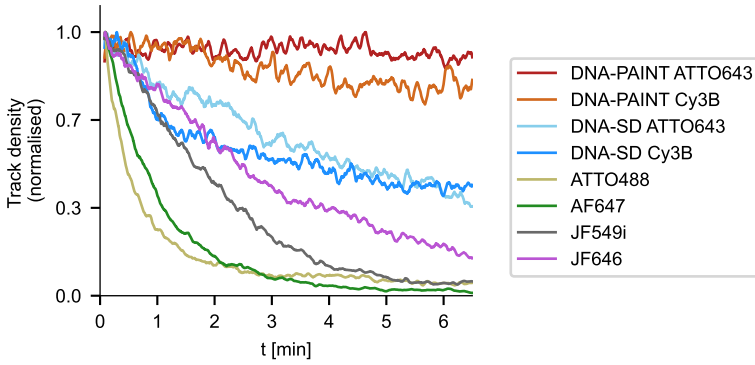

Figure S4.5 • Photostability of different labeling methods and fluorophores in in vitro experiments

Number of trajectories per frame of reconstituted FKBP proteins labeled with DNA-PAINT (ATTO643-imager strands in red, $n_{\text{samples}} = 3$; Cy3B-imager strands in orange, $n_{\text{samples}} = 3$), single-dye DNA (ATTO643-fluorophore in light blue, $n_{\text{samples}} = 4$; Cy3B-fluorophore in dark blue, $n_{\text{samples}} = 4$) or single BG-conjugated fluorophores (ATTO488 in yellow, $n_{\text{samples}} = 2$; AlexaFluor647 in green, $n_{\text{samples}} = 2$; JF549i in gray, $n_{\text{samples}} = 5$; JF646 in magenta, $n_{\text{samples}} = 5$).

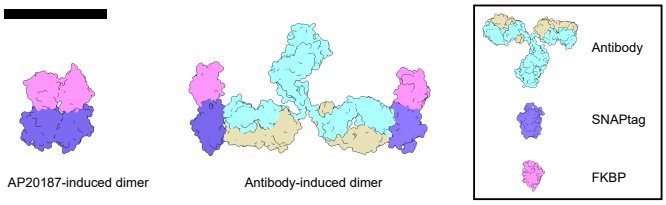

Figure S4.6 • Dimerization geometry for ligand- and antibody-induced dimerization

Size comparison of FKBP-SNAPtag complexes dimerized via the ligand AP20187 and an anti-SNAPtag antibody. Protein structures from PDB (SNAPtag: `3KZY`, FKBP$^{\text{f36v}}$: `1BL4`, Antibody: `1IGT`). Scale bar: 10 nm.

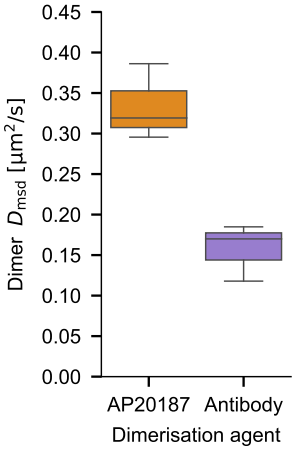

Figure S4.7 • Diffusion constants of dimers for AP20187- and antibody-induced dimerization

Diffusion constants derived from mean-square displacement of co-diffusing trajectories show a two-fold reduction for antibody-induced dimers ($D_{\text{msd, AP20187}} = 0.33 \pm 0.05\,\mu\text{m}^2/\text{s}$, $D_{\text{msd, Antibody}} = 0.16 \pm 0.04\,\mu\text{m}^2/\text{s}$). This effect is likely due to the bigger size and mass of the antibody-induced dimer, and potentially also by the increased coupling of thermal energy to the rotational degree of freedom, as the antibody-induced dimer has a higher moment of rotational inertia compared to the compact ligand-induced dimer. Data from three samples for each condition.

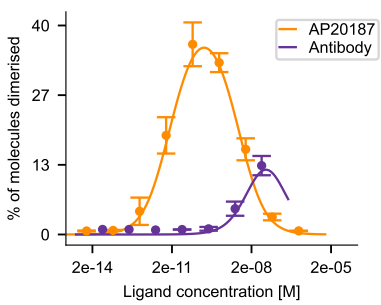

Figure S4.8 • Dimerization curve of ligand-titration experiments measured using DNA-PAINT-SPT

Fraction of dimerized molecules as detected using DNA-PAINT-SPT during ligand-titration experiments. AP20187 or anti-SNAPtag antibody were used to induce dimerization. Labeled fractions according to the fit were $60 \pm 17\,\%$. Error bars denote mean $\pm$ standard deviation of data collected from three field of views of each sample of a titration series for each dimerization agent.

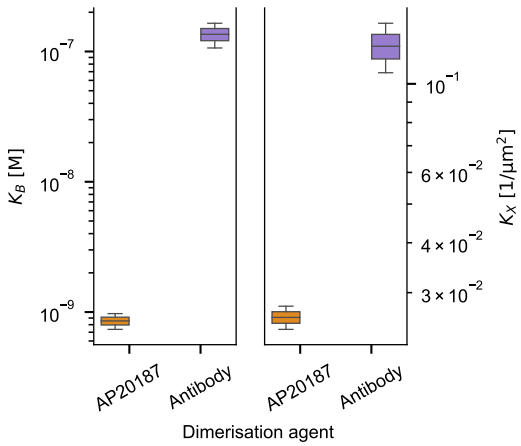

Figure S4.9 • 2D dissociation constants of different dimerization agents measured using DNA-PAINT-SPT

Dissociation constants K_X and K_B of AP20187 and anti-SNAPtag antibody interaction with FKBP^{f36v} as determined from fitting the fraction of dimerized molecules. Labeled fractions according to the fits were 67 ± 16 %. Boxes, line and whiskers show, respectively, 25–75 quartiles, median, and minimum and maximum values of dissociation constants. The data used for fitting was collected from three field of views of each sample of a titration series, prepared in duplicates for each dimerization agent.

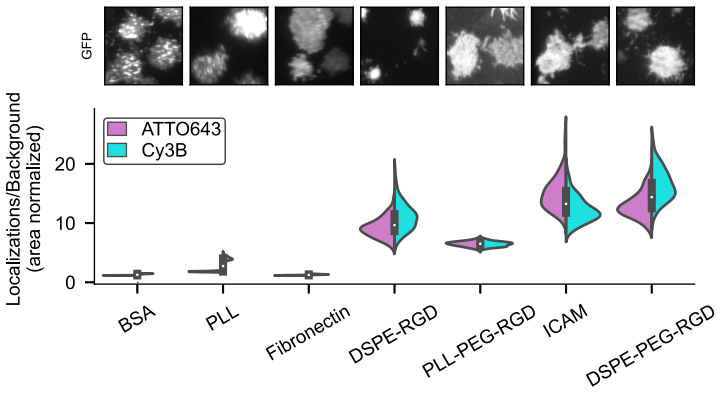

Figure S4.10 • Screening of passivation methods
Ratio of localizations detected on DNA-PAINT labeled cells with 40 nM imager strands (Cy3B- or ATTO643-conjugated) per area versus localizations detected outside of cells per area, for different surfaces. Top row shows GFP signal of adhered cells (field of view: 20 µm). See **??** for video version with single-molecule channels. Data and panels from one representative field of view for each condition.

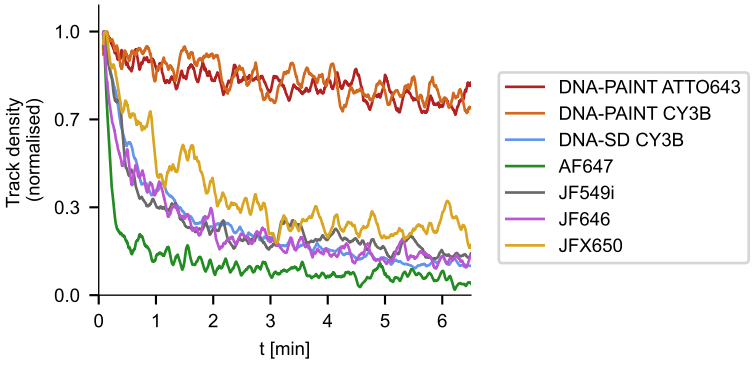

Figure S4.11 • Trajectory density over time for DNA-PAINT labels and single-dye controls
Number of trajectories per frame on individual cells labeled with DNA-PAINT (ATTO643-imager strands in red, $n_{\text{cells}} = 25$; Cy3B-imager strands in orange, $n_{\text{cells}} = 25$), single-dye DNA (Cy3B-fluorophore in blue, $n_{\text{cells}} = 32$) or single BG-conjugated fluorophores (AlexaFluor647 in green, $n_{\text{cells}} = 7$; JF549i in gray, $n_{\text{cells}} = 15$; JF646 in magenta, $n_{\text{cells}} = 6$; JFX650 in yellow, $n_{\text{cells}} = 6$).

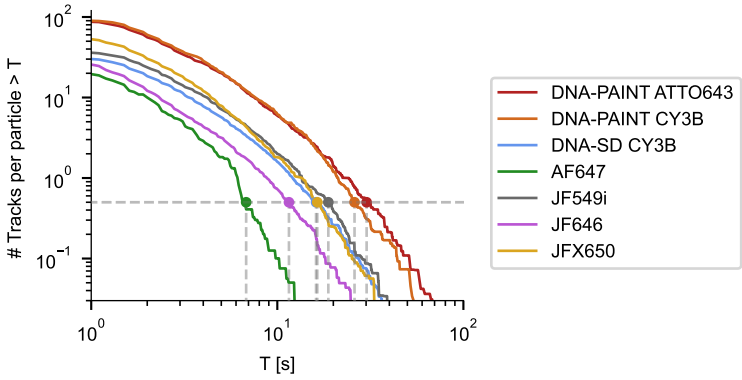

Figure S4.12 • Tracks per particle over time for DNA-PAINT labels and single-dye controls

Single-molecule trajectories with a duration longer than T, normalised to the initial number of trajectories per individual cell. Membrane proteins are labeled with DNA-PAINT (ATTO643-imager strands in red, $n_{\text{cells}} = 25$; Cy3B-imager strands in orange, $n_{\text{cells}} = 25$), single-dye DNA (Cy3B-fluorophore in blue, $n_{\text{cells}} = 32$) or single BG-conjugated fluorophores (AlexaFluor647 in green, $n_{\text{cells}} = 7$; JF549i in gray, $n_{\text{cells}} = 15$; JF646 in magenta, $n_{\text{cells}} = 6$; JFX650 in yellow, $n_{\text{cells}} = 6$).

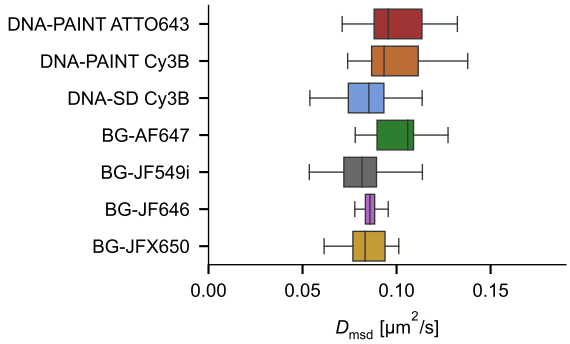

Figure S4.13 • Diffusion constants of membrane proteins labeled with DNA-PAINT and single dye probes

Mean-square displacement derived diffusion constants of membrane proteins on cells labeled with DNA-PAINT (ATTO643-imager strands in red, $n_{\text{cells}} = 25$; Cy3B-imager strands in orange, $n_{\text{cells}} = 25$), single-dye DNA (Cy3B-fluorophore in blue, $n_{\text{cells}} = 32$) or single BG-conjugated fluorophores (AlexaFluor647 in green, $n_{\text{cells}} = 7$; JF549i in gray, $n_{\text{cells}} = 15$; JF646 in magenta, $n_{\text{cells}} = 6$; JFX650 in yellow, $n_{\text{cells}} = 6$).

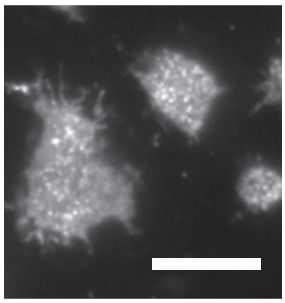

Figure S4.14 • Accessibility of docking strands

Average fluorescence intensity during a 80 s measurement of Jurkat T-cells with densely labeled membrane proteins using DNA-PAINT docking strands and Cy3B-conjugated imager strands, to visualise potential exclusion effects of DNA-labeled proteins from cell-surface contacts.

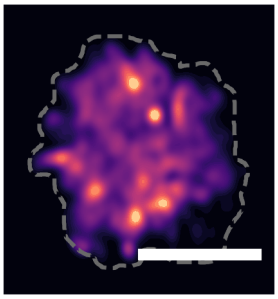

Figure S4.15 • Trajectory density variation across cell surface

Density of single-molecule trajectories across Jurkat T-cell surface during a 400 s measurement for DNA-PAINT docking strand labeled membrane proteins and Cy3B-conjugated imager strands.

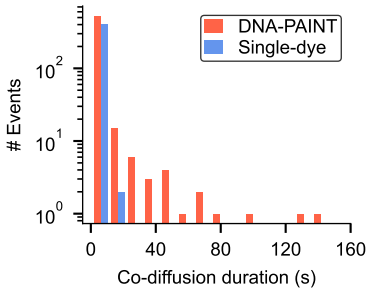

Figure S4.16 • FKBP dimer trajectory durations on live-cells.

Histogram of detected co-diffusion durations of FKBP dimers on live-cells, using Cy3B- and ATTO643 DNA-PAINT-SPT (red, $n = 17$ cells) or BG-JF5449i and BG-AF647 single-dye labeling (blue, $n = 15$ cells) with 10 nM dimerizing agent AP20187. Data collected during three-minute measurements on two identically prepared samples per labeling condition.

References

[1] Christian Niederauer et al. “DNA-PAINT Single-Particle Tracking (DNA-PAINT-SPT) Enables Extended Single-Molecule Studies of Membrane Protein Interactions”. In: *bioRxiv* (2022), p. 503948.

[2] Akihiro Kusumi et al. “Tracking Single Molecules at Work in Living Cells”. In: *Nature Chemical Biology* 10.7 (2014), pp. 524–532.

[3] Carlo Manzo and Maria F Garcia-Parajo. “A Review of Progress in Single Particle Tracking: From Methods to Biophysical Insights”. In: *Reports on Progress in Physics* 78.12 (2015), p. 124601.

[4] Yanqi Yu, Miao Li, and Yan Yu. “Tracking Single Molecules in Biomembranes: Is Seeing Always Believing?” In: *ACS Nano* (2019).

[5] Marlon J Hinner and Kai Johnsson. “How to Obtain Labeled Proteins and What to Do with Them”. In: *Current Opinion in Biotechnology* 21.6 (2010), pp. 766–776.

[6] Peter J. Bosch et al. “Evaluation of Fluorophores to Label SNAP-Tag Fused Proteins for Multicolor Single-Molecule Tracking Microscopy in Live Cells”. In: *Biophysical Journal* 107.4 (2014), pp. 803–814.

[7] Nehir Banaz, Jarno Mäkelä, and Stephan Uphoff. “Choosing the Right Label for Single-Molecule Tracking in Live Bacteria: Side-by-Side Comparison of Photoactivatable Fluorescent Protein and Halo Tag Dyes”. In: *Journal of Physics D: Applied Physics* 52.6 (2019), p. 064002.

[8] Jonathan B. Grimm et al. “A General Method to Optimize and Functionalize Red-Shifted Rhodamine Dyes”. In: *Nature Methods* 17.8 (2020), pp. 815–821.

[9] Florian Stehr et al. “Tracking Single Particles for Hours via Continuous DNA-mediated Fluorophore Exchange”. In: *Nature Communications* 12.1 (2021), p. 4432.

[10] Florian Schueder et al. “An Order of Magnitude Faster DNA-PAINT Imaging by Optimized Sequence Design and Buffer Conditions”. In: *Nature Methods* (2019).

[11] Sebastian Strauss and Ralf Jungmann. “Up to 100-Fold Speed-up and Multiplexing in Optimized DNA-PAINT”. In: *Nature Methods* 17.8 (2020), pp. 789–791.

[12] Benjamin Vermeer and Sonja Schmid. “Can DyeCycling Break the Photobleaching Limit in Single-Molecule FRET?” In: *Nano Research* (2022).

[13] Mirjam Kümmerlin, Abhishek Mazumder, and Achillefs N. Kapanidis. “Bleaching-Resistant, Near-continuous Single-molecule Fluorescence and FRET Based on Fluorogenic and Transient DNA Binding”. In: *ChemPhysChem* n/a.n/a (2023), e202300175.

[14] Jürgen M. Kolos et al. “FKBP Ligands—Where We Are and Where to Go?” In: *Frontiers in Pharmacology* 9 (2018), p. 1425.

[15] Tim Clackson et al. “Redesigning an FKBP–Ligand Interface to Generate Chemical Dimerizers with Novel Specificity”. In: *Proc. Natl. Acad. Sci. USA* (1998), p. 6.

[16] Jonathan B. Grimm and Luke D. Lavis. “Caveat Fluorophore: An Insiders’ Guide to Small-Molecule Fluorescent Labels”. In: *Nature Methods* (2021).

[17] Patrick Binder et al. “Optimal Ligand Discrimination by Asymmetric Dimerization and Turnover of Interferon Receptors”. In: *Proceedings of the National Academy of Sciences* 118.37 (2021), e2103939118.

[18] Laura D. Hughes, Robert J. Rawle, and Steven G. Boxer. “Choose Your Label Wisely: Water-Soluble Fluorophores Often Interact with Lipid Bilayers”. In: *PLoS ONE* 9.2 (2014), e87649.

[19] Tommy Dam et al. “Supported Lipid Bilayers and the Study of Two-Dimensional Binding Kinetics”. In: *Frontiers in Molecular Biosciences* 9 (2022), p. 833123.

[20] Martynas Gavutis et al. “Determination of the Two-Dimensional Interaction Rate Constants of a Cytokine Receptor Complex”. In: *Biophysical Journal* 90.9 (2006), pp. 3345–3355.

[21] Sepehr Fathi et al. “Absolute Ligand Discrimination by Dimeric Signaling Receptors”. In: *Biophysical Journal* 111.5 (2016), pp. 917–920.

[22] David Virant et al. “A Peptide Tag-Specific Nanobody Enables High-Quality Labeling for dSTORM Imaging”. In: *Nature Communications* 9.1 (2018), p. 930.

[23] Hansjörg Götzke et al. “The ALFA-tag Is a Highly Versatile Tool for Nanobody-Based Bioscience Applications”. In: *Nature Communications* 10.1 (2019), p. 4403.

[24] Daniel J. Nieves et al. “tagPAINT: Covalent Labelling of Genetically Encoded Protein Tags for DNA-PAINT Imaging”. In: *Royal Society Open Science* 6.12 (2019), p. 191268.

[25] Stephan Wilmes et al. “Receptor Dimerization Dynamics as a Regulatory Valve for Plasticity of Type I Interferon Signaling”. In: *Journal of Cell Biology* 209.4 (2015), pp. 579–593.

[26] D. Calebiro et al. “Single-Molecule Analysis of Fluorescently Labeled G-protein-coupled Receptors Reveals Complexes with Distinct Dynamics and Organization”. In: *Proceedings of the National Academy of Sciences* 110.2 (2013), pp. 743–748.

[27] Titiwat Sungkaworn et al. “Single-Molecule Imaging Reveals Receptor–G Protein Interactions at Cell Surface Hot Spots”. In: *Nature* 550.7677 (2017), pp. 543–547.

[28] Jan Möller et al. “Single-Molecule Analysis Reveals Agonist-Specific Dimer Formation of μ-Opioid Receptors”. In: *Nature Chemical Biology* 16.9 (2020), pp. 946–954.

[29] Franziska Neubert et al. “Bioorthogonal Click Chemistry Enables Site-specific Fluorescence Labeling of Functional NMDA Receptors for Super-Resolution Imaging”. In: *Angewandte Chemie International Edition* 57.50 (2018), pp. 16364–16369.

[30] Zhiqi Sun, Shengzhen S. Guo, and Reinhard Fässler. “Integrin-Mediated Mechanotransduction”. In: *Journal of Cell Biology* 215.4 (2016), pp. 445–456.

[31] Badriprasad Ananthanarayanan et al. “Neural Stem Cell Adhesion and Proliferation on Phospholipid Bilayers Functionalized with RGD Peptides”. In: *Biomaterials* 31.33 (2010), pp. 8706–8715.

[32] Tobias G. Kapp et al. “A Comprehensive Evaluation of the Activity and Selectivity Profile of Ligands for RGD-binding Integrins”. In: *Scientific Reports* 7.1 (2017), p. 39805.

[33] Pradeep M Nair et al. “Using Patterned Supported Lipid Membranes to Investigate the Role of Receptor Organization in Intercellular Signaling”. In: *Nature Protocols* 6.4 (2011), pp. 523–539.

[34] Kenny K. H. Chung et al. “Fluorogenic DNA-PAINT for Faster, Low-Background Super-Resolution Imaging”. In: *Nature Methods* 19.5 (2022), pp. 554–559.

[35] Edward W. Sanders et al. “resPAINT: Accelerating Volumetric Super-Resolution Localisation Microscopy by Active Control of Probe Emission”. In: *Angewandte Chemie International Edition* (2022).

[36] Huanting Liu and James H Naismith. “An Efficient One-Step Site-Directed Deletion, Insertion, Single and Multiple-Site Plasmid Mutagenesis Protocol”. In: *BMC Biotechnology* 8.1 (2008), p. 91.

[37] Thorben Cordes, Jan Vogelsang, and Philip Tinnefeld. “On the Mechanism of Trolox as Antiblinking and Antibleaching Reagent”. In: *Journal of the American Chemical Society* 131.14 (2009), pp. 5018–5019.

[38] Christian Niederauer et al. “The K2: Open-source Simultaneous Triple-Color TIRF Microscope for Live-Cell and Single-Molecule Imaging”. In: *HardwareX* 13 (2023), e00404.

[39] Florian Stehr et al. “Flat-Top TIRF Illumination Boosts DNA-PAINT Imaging and Quantification”. In: *Nature Communications* 10.1 (2019), p. 1268.

[40] Christian Niederauer et al. “Direct Characterization of the Evanescent Field in Objective-Type Total Internal Reflection Fluorescence Microscopy”. In: *Optics Express* 26.16 (2018), p. 20492.

[41] Koen J. A. Martens et al. “Visualisation of dCas9 Target Search in Vivo Using an Open-Microscopy Framework”. In: *Nature Communications* 10.1 (2019), p. 3552.

[42] Karl Bellve et al. “Design and Implementation of 3D Focus Stabilization for Fluorescence Microscopy”. In: *Biophysical Journal* 106.2 (2014), 606a.

[43] Joerg Schnitzbauer et al. “Super-Resolution Microscopy with DNA-PAINT”. In: *Nature Protocols* 12.6 (2017), pp. 1198–1228.

[44] Kaley A. McCluskey et al. “Global Correction of Optical Distortions in Multicolor Single-Molecule Microscopy Using Zernike Polynomial Gradients”. In: *Optics Express* 29.25 (2021), p. 42251.

[45] Daniel B. Allan et al. *Soft-Matter/Trackpy: Trackpy v0.5.0*. 2021.

[46] M Endesfelder et al. “Swift – Fast, Probabilistic Tracking for Dense, Highly Dynamic Single-Molecule Data”. In: (2022).

[47] Johanna V. Rahm et al. “Diffusion State Transitions in Single-Particle Trajectories of MET Receptor Tyrosine Kinase Measured in Live Cells”. In: *Frontiers in Computer Science* 3 (2021), p. 757653.

[48] Johannes Schindelin et al. “Fiji: An Open-Source Platform for Biological-Image Analysis”. In: *Nature Methods* 9.7 (2012), pp. 676–682.

[49] Verena Ruprecht et al. “Measuring Colocalization by Dual Color Single Molecule Imaging”. In: *Advances in Planar Lipid Bilayers and Liposomes*. Vol. 12. Elsevier, 2010, pp. 21–40.

5 Outlook

In this thesis, I presented the development and application of advanced single-molecule fluorescence microscopy techniques for the study of protein-protein interactions in the context of immunological signaling. The three experimental chapters focus on the creation of an open-source simultaneous triple-color TIRF microscope, the "K2" (**Chapter 2**), the establishment of an experimental platform for single-molecule studies of IL-2/IL-15 receptor assembly kinetics (**Chapter 3**), and the development of DNA-PAINT single-particle tracking (DNA-PAINT-SPT) for live-cell imaging and quantifying protein dimerization (**Chapter 4**).

This outlook chapter aims to provide an overview of the broader context of the work presented in this thesis, particularly with a focus on the importance of open science and the potential for future development and improvement of the techniques discussed. The chapter will also touch upon the feedback we have already received from the scientific community and potential future directions and applications.

5.1 K2 microscope and open science

The K2 microscope's modular design and open-source documentation make it highly adaptable to different scientific and financial needs. We were happy to see that the scientific community's feedback on the project has been very positive [1–5], with several groups stating that they were inspired by our setup, adapted parts of it, or plan to replicate the design. We also plan to reproduce (and advance) the setup in our own laboratory. Since the release of the K2 open-source microscope documentation, we have received valuable technical feedback, enabling refinements to the design and increasing the scope of its applications. It was suggested, for example, to combine our setup with a custom-built (open-source) laser machine [2, 6, 7], to further reduce costs and enhance flexibility.

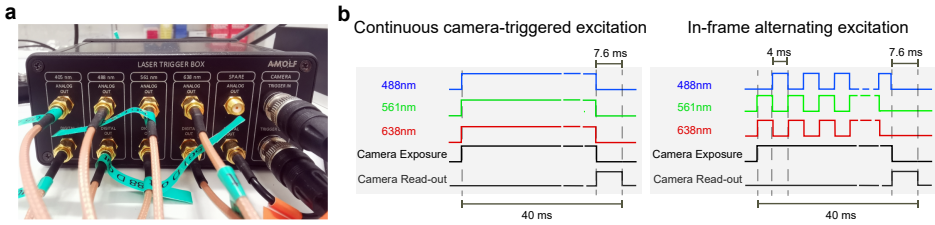

Figure 5.1 • K2 software and electronics update

(a) Laser trigger box with camera trigger in- and outputs and analog and digital outputs for laser triggering. **(b)** The laser trigger box was updated with a field programmable gate array (FPGA) to allow for fast in-frame alternating excitation, which reduces photobleaching of cyanine-dyes induced by co-excitation with 488 nm, and 561 nm and 638 nm laser lines.

As technology advances and new discoveries are made in the field of single-molecule imaging, the K2 open-source microscope can be adapted to incorporate these innovations. After completing the initial setup, several updates have been implemented to enhance its performance: we upgraded the laser trigger box with a field programmable gate array (FPGA) to enable in-frame alternating excitation (see **Fig. 5.1**). This imaging modality reduces excessive photobleaching caused by simultaneous excitation of dyes with the 488 nm, 561 nm and 638 nm laser lines [8], while introducing negligible motion shift between the different channels that would otherwise occur if channels were excited in an alternating frame-by-frame pattern. Moreover, we updated the brightfield LED source to be dimmable, provide a more homogeneous lighting, and integrated its controller into the laser trigger box, enabling software-controlled brightfield illumination (see **Fig. 5.2a**). In the next iteration of the cube replacing the traditional microscope body, we will reduce the distance between the excitation beam port and the dichroic filter cube, enabling the use of TIRF lenses with shorter focal lengths. This adjustment will result in a larger illuminated field-of-view and additional space for incorporating other components. To streamline the alignment process, we will incorporate a through-hole in the cube and mounting holes around the objective (see **Fig. 5.2b-c**).

By continuously addressing and overcoming technical challenges, and importantly, sharing the progress in an open-source fashion (on the website ganzingerlab.github.io/K2TIRF), we promote accessibility to single-molecule microscopy, encourage scientific collaboration and reduce the costs and efforts associated with building custom microscopes.

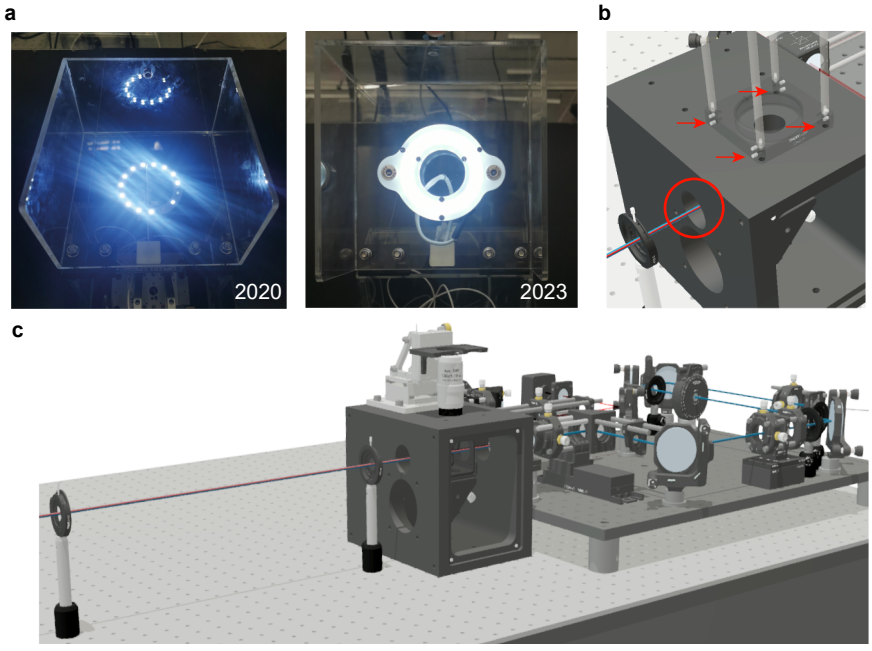

Figure 5.2 • Design iterations and improvements
(a) Left: Initial LED array with manual on/off switch, fixed intensity and low performance LEDs. Right: Improved software-controlled, dimmable LED brightfield source. **(b)** Main cube updates: mounting holes for an alignment cage system centered on the objective thread (red arrows), and a closable through-hole (red circle) to simplify alignment of the excitation laser beam and the main cube. **(c)** Alignment of excitation laser beam and main cube using two irises in line with breadboard holes.

5.2 Future directions for single-molecule studies of IL-2/IL-15 receptor assembly kinetics

The IL-2 and IL-15 membrane receptors play an essential role in immune cell signaling, and understanding their dynamic behavior is critical for developing targeted therapies for immune-related diseases and cancer. In this thesis, we developed an experimental platform to study the receptor assembly kinetics of IL-2 and IL-15 using single-molecule tracking and colocalization analysis. Despite our best efforts, we faced difficulties in characterizing the receptor assembly kinetics of IL-2 and IL-15 in detail. These challenges were likely due to limitations in the quality

of the available ligands, as well as the photostability of the available labeling options, leading to short trajectories that make statistically sound analysis of interaction difficult. To address the photostability issues, we developed a novel labeling method based on DNA-PAINT, which is described in detail in **Chapter 4**. The method involves conjugating a DNA strand to the protein of interest, which serves as a docking site for multiple fluorescent imager strands, significantly improving trajectory lengths compared to traditional single-dye SPT methods. To implement this in our reconstitution assay while maintaining stoichiometric one-to-one site-specific labeling, we will employ sortase-peptides with a DBCO-group and azide-functionalized DNA in the future (see **Fig. 5.3**; similar to [9]). Both molecules are readily available from commercial suppliers. Alternatively, Sfp synthase-mediated labeling presents another promising option by introducing a N-terminal ybbR tag in the interleukin receptor subunit constructs and utilizing coenzyme A-conjugated DNA for labeling [10].

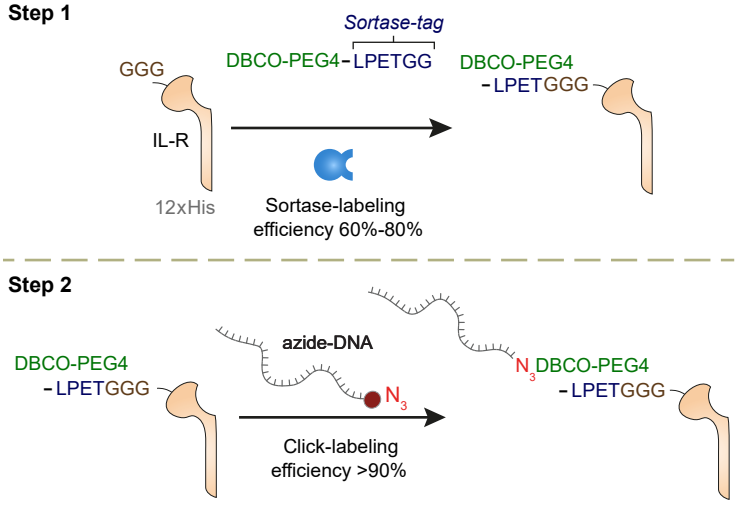

Figure 5.3 • DNA-PAINT-SPT labeling of recombinant proteins
A DNA docking strand is site-specifically conjugated to a recombinantly expressed interleukin receptor subunit. In a first step, the protein is labeled with a DBCO-sortase peptide via sortase-mediated labeling. Sortase and unreacted peptide are removed by Ni-NTA affinity chromatography. Using click-chemistry, azide-DNA reacts with the DBCO group in a second step. Finally, unlabeled protein is removed by size-exclusion chromatography.

Sourcing the ligands from a different supplier offering Good Manufacturing Practice (GMP)-grade products should resolve the issues with ligand quality. Otherwise, an alternative approach is to express the ligands in-house at AMOLF. However, this would necessitate a bio-safety assessment and a considerable time investment, as recombinant interleukin expression and purification can be a complex and labor-intensive process.

With the DNA-PAINT-SPT labeling method and functional proteins in hand, more in-depth investigations can be undertaken. In addition to studying the receptor assembly kinetics as described in **Chapter 3**, it would be interesting to explore the effect of *cis*- versus *trans*-presentation of membrane-bound ligands (see **Fig. 5.4**), or compare ligand binding kinetics of membrane-bound ligands with those in solution in future experiments. The strong optical tweezer expertise available at AMOLF presents an opportunity to investigate the force-stability of the *trans*-presentation configuration of the receptor using optical tweezers. Moreover, it would be valuable to examine the effect of novel, mutated ligands [11–18] on receptor assembly and stability, and relate these findings to their biological effects. Such research could offer insights into how specific changes in ligand structure influence receptor assembly kinetics, illuminating the molecular determinants of receptor activation and signal transduction. These insights are crucial for developing mutated ligands for therapeutic use, as well as for understanding how certain mutations can be oncogenic [19].

Lastly, by combining single-molecule imaging techniques with cellular receptor activation assays, insights about the functional connections between receptor assembly kinetics and the activation of downstream signaling cascades can be gained. Experimentally, this could be achieved by transfecting a cell line to express genetically modified interleukin receptor subunits with extracellular tags (e.g. orthogonal nanobodies [8]) to allow site-specific DNA-PAINT-SPT labeling. Simultaneously, cells could be co-transfected to express genetically modified STAT molecules fused to fluorescent proteins in order to observe their translocation to the nucleus upon receptor activation [20].

Another promising avenue would involve resolving the nanoscopic organization of interleukin receptor assemblies and intracellular signaling molecules by combining DNA-PAINT with the novel protein-PAINT approach, where phosphorylated tyrosine-residues on signaling molecules are visualized using the reversible interaction of phosphotyrosine-binding SH2 domains [21].

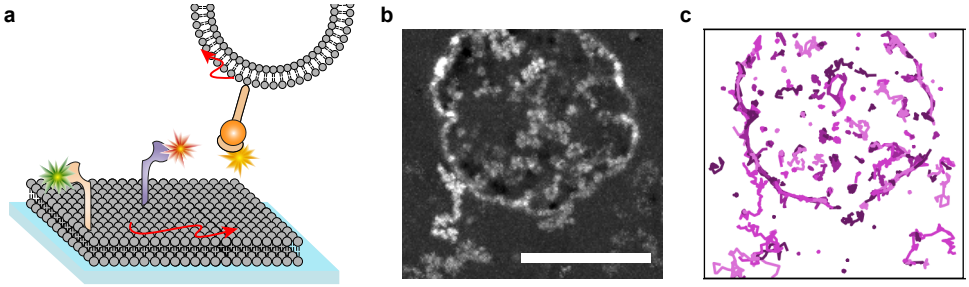

Figure 5.4 • *Trans*-presentation of reconstituted proteins in giant unilamellar vesicle (GUV)-SLB contact

(a) Schematic illustration of IL-15 *trans*-presentation experiments. IL-15Rα is reconstituted on GUVs containing nickelated lipids. IL-15 binds to IL-15Rα, which can then interact with IL-15Rβ and γ_c receptor subunits reconstituted on a SLB. **(b)** Proof of principle experiment with His-SNAPtag fusion proteins reconstituted on GUVs and SLBs. Maximum projection of the first 100 frames of a TIRF movie. Scale bar is 10 µm. **(c)** Detected trajectories on the SLB and GUV shown in **(b)**.

5.3 Future directions for DNA-PAINT-SPT

The DNA-PAINT-SPT method developed and presented in this thesis has the potential to have a significant impact on the broader single-molecule imaging community by providing a versatile platform for studying protein interactions and dynamics at the single-molecule level. DNA-PAINT-SPT overcomes the constraints of fluorophore photobleaching and significantly enhances observation times in in vitro SPT experiments.

In general, since the coupling of fluorophores to DNA is well-established, any developments in fluorophores directly enhance the performance and applicability of DNA-PAINT-SPT. It is simply a matter of acquiring new imager strands with the latest fluorophore generation, minimizing the need for extensive biochemical work. Moreover, advancements in DNA-PAINT sequence design (e.g. [22, 23]) directly benefit DNA-PAINT-SPT by increasing association rates or enabling shorter sequences while maintaining the required binding kinetics, allowing for more compact probes.

Furthermore, the ongoing development of molecular binders can broaden the spectrum of targetable molecules for DNA-PAINT-SPT studies. By generating new probes (e.g. nanobodies [8, 24, 25]) that recognize differ-

ent target proteins or subcellular structures, researchers can investigate a wider variety of biological processes using DNA-PAINT-SPT. Additionally, the development of multiplexed imaging strategies using new fluorophores and orthogonal probes [8, 26] will enable the simultaneous visualization of a wider range of targets within a single experiment, further enhancing the versatility and applicability of DNA-PAINT-SPT.

A remaining challenge is applying the technique to intracellular imaging. DNA docking and imager strands are too large and charged to be readily taken up by cells. While electroporation could potentially introduce these strands [27], they would likely interfere with the cells' normal function. Nevertheless, the reversible binding of fluorophores or fluorophore-carrying molecules can be achieved by a variety of molecules, including intracellularly expressed small peptides [28–34]. By combining these approaches with the expression of multiple binding sites on a single target molecule [35], it should be feasible to achieve continuous replacement of fluorophore labels, similar to DNA-PAINT-SPT, on intracellular targets. This would enable dynamic single-molecule studies of protein interactions within the cellular environment at high spatiotemporal resolution and with extended observation times.

5.4 Concluding remarks

Taken together, the work I presented in this thesis has not only broadened the existing toolbox of single-molecule imaging techniques, but I have also sought to democratize access to these advanced methodologies through various open science practices, such as pre-printing, open-access publication of manuscripts, and sharing detailed technical documentation openly online.

The advancements made in this thesis open up numerous avenues for future research in the field of single-molecule fluorescence microscopy. The continuous development of the K2 microscope, coupled with the integration of new technologies and techniques, will enable researchers to push the boundaries of single-molecule imaging and address increasingly complex biological questions.

Furthermore, the application of these advanced imaging methodologies to study immune cell signaling has the potential to inform the development of novel therapeutic strategies for a wide range of diseases. Novel fluorophores and PAINT probes will further expand the applicability of DNA-PAINT-SPT, enabling researchers to address a wider range of biological questions.

In summary, this thesis has significantly advanced the field of single-molecule fluorescence microscopy, with promising opportunities for continued innovation and applications. I also hope to have emphasized the importance of fostering an innovative and collaborative research environment, not only in the field of single-molecule fluorescence microscopy but also in other scientific domains, for the benefit of scientists and scientific discovery.

References

[1] Andrey Andreev [@aandr314]. *Look at That Crazy-Detailed Writeup from @NiederauerC & Co @kganzinger [...]* Tweet. 2022.

[2] Mario Brameshuber [@MBrameshuber]. *Combining the Hardware Control from the @JonasRies Group with the K2 Microscope from @NiederauerC Sounds like the Perfect Single Molecule TIRF Microscope with Huge Degrees of Freedom [...]* Tweet. 2023.

[3] Marijonas Tutkus [@MTutkus]. *Great Work! Congrats to @NiederauerC and Colleagues. The K2: Open-source Simultaneous Triple-Color TIRF Microscope for Live-Cell and Single-Molecule Imaging [...]* Tweet. 2022.

[4] Johannes Hohlbein [@HohlbeinLab]. *1) #K2 (@NiederauerC / @KGanzinger): "The K2: Open-source Simultaneous Triple-Color TIRF Microscope for Live-Cell and Single-Molecule Imaging" [....]* Tweet. 2023.

[5] John S. H. Danial et al. "Constructing a Cost-Efficient, High-Throughput and High-Quality Single-Molecule Localization Microscope for Super-Resolution Imaging". In: *Nature Protocols* 17.11 (2022), pp. 2570–2619.

[6] Philip R. Nicovich et al. "NicoLase—An Open-Source Diode Laser Combiner, Fiber Launch, and Sequencing Controller for Fluorescence Microscopy". In: *PLOS ONE* 12.3 (2017), e0173879.

[7] Joran Deschamps et al. "MicroFPGA: An Affordable FPGA Platform for Microscope Control". In: *HardwareX* 13 (2023), e00407.

[8] Junel Sotolongo Bellón et al. "Four-Color Single-Molecule Imaging with Engineered Tags Resolves the Molecular Architecture of Signaling Complexes in the Plasma Membrane". In: *Cell Reports Methods* 2.2 (2022), p. 100165.

[9] Valentin Fabricius et al. "Rapid and Efficient C-terminal Labeling of Nanobodies for DNA-PAINT". In: *Journal of Physics D: Applied Physics* 51.47 (2018), p. 474005.

[10] Mario J. Avellaneda et al. "Simultaneous Sensing and Imaging of Individual Biomolecular Complexes Enabled by Modular DNA–Protein Coupling". In: *Communications Chemistry* 3.1 (2020), p. 20.

[11] Alfredo Quijano-Rubio et al. “A Split, Conditionally Active Mimetic of IL-2 Reduces the Toxicity of Systemic Cytokine Therapy”. In: *Nature Biotechnology* (2022).

[12] Junming Ren et al. “Interleukin-2 Superkines by Computational Design”. In: *Proceedings of the National Academy of Sciences* 119.12 (2022), e2117401119.

[13] Aron M. Levin et al. “Exploiting a Natural Conformational Switch to Engineer an Interleukin-2 ‘Superkine’”. In: *Nature* 484.7395 (2012), pp. 529–533.

[14] Fei Mo et al. “An Engineered IL-2 Partial Agonist Promotes CD8+ T Cell Stemness”. In: *Nature* 597.7877 (2021), pp. 544–548.

[15] Ignacio Moraga et al. “Tuning Cytokine Receptor Signaling by Re-orienting Dimer Geometry with Surrogate Ligands”. In: *Cell* 160.6 (2015), pp. 1196–1208.

[16] Jonathan T. Sockolosky et al. “Selective Targeting of Engineered T Cells Using Orthogonal IL-2 Cytokine-Receptor Complexes”. In: *Science* 359.6379 (2018), pp. 1037–1042.

[17] Daniel-Adriano Silva et al. “De Novo Design of Potent and Selective Mimics of IL-2 and IL-15”. In: *Nature* 565.7738 (2019), pp. 186–191.

[18] Liliane Khoryati et al. “An IL-2 Mutein Engineered to Promote Expansion of Regulatory T Cells Arrests Ongoing Autoimmunity in Mice”. In: *Science Immunology* 5.50 (2020), eaba5264.

[19] Stephan Wilmes et al. “Mechanism of Homodimeric Cytokine Receptor Activation and Dysregulation by Oncogenic Mutations”. In: *Science* 367.6478 (2020), pp. 643–652.

[20] Dirk Fahrenkamp et al. “Src Family Kinases Interfere with Dimerization of STAT5A through a Phosphotyrosine-SH2 Domain Interaction”. In: *Cell Communication and Signaling* 13.1 (2015), p. 10.

[21] Megan V. Farrell et al. “Protein-PAINT: Superresolution Microscopy with Signaling Proteins”. In: *Science Signaling* 15.719 (2022), eabg9782.

[22] Sebastian Strauss and Ralf Jungmann. “Up to 100-Fold Speed-up and Multiplexing in Optimized DNA-PAINT”. In: *Nature Methods* 17.8 (2020), pp. 789–791.

[23] Florian Schueder et al. “An Order of Magnitude Faster DNA-PAINT Imaging by Optimized Sequence Design and Buffer Conditions”. In: *Nature Methods* (2019).

[24] Florian Schueder et al. “Nanobodies Combined with DNA-PAINT Super-Resolution Reveal a Staggered Titin Nanoarchitecture in Flight Muscles”. In: *eLife* 12 (2023), e79344.

[25] Hansjörg Götzke et al. “The ALFA-tag Is a Highly Versatile Tool for Nanobody-Based Bioscience Applications”. In: *Nature Communications* 10.1 (2019), p. 4403.

[26] Niclas Gimber et al. “Simultaneous Multicolor DNA-PAINT without Sequential Fluid Exchange Using Spectral Demixing”. In: *Nano Letters* 22.7 (2022), pp. 2682–2690.

[27] Zhongwen Chen et al. “Nanopore-Mediated Protein Delivery Enabling Three-Color Single-Molecule Tracking in Living Cells”. In: *Proceedings of the National Academy of Sciences* 118.5 (2021), e2012229118.

[28] Benjamin Vermeer and Sonja Schmid. “Can DyeCycling Break the Photobleaching Limit in Single-Molecule FRET?” In: *Nano Research* (2022).

[29] Curran Oi et al. “PAINT Using Proteins: A New Brush for Super-Resolution Artists”. In: *Protein Science* 29.11 (2020), pp. 2142–2149.

[30] Curran Oi et al. “LIVE-PAINT Allows Super-Resolution Microscopy inside Living Cells Using Reversible Peptide-Protein Interactions”. In: *Communications Biology* 3.1 (2020), p. 458.

[31] Alexandra S. Eklund et al. “Peptide-PAINT Super-Resolution Imaging Using Transient Coiled Coil Interactions”. In: *Nano Letters* 20.9 (2020), pp. 6732–6737.

[32] Barun Kumar Maity et al. “Peptide-PAINT Using a Transfected-Docker Enables Live- and Fixed-Cell Super-Resolution Imaging”. In: *Small Methods* (2023), p. 2201181.

[33] Maxim M. Perfilov et al. “Highly Photostable Fluorescent Labeling of Proteins in Live Cells Using Exchangeable Coiled Coils Heterodimerization”. In: *Cellular and Molecular Life Sciences* 77.21 (2020), pp. 4429–4440.

[34] Roderick P. Tas, Lorenzo Albertazzi, and Ilja K. Voets. “Small Peptide–Protein Interaction Pair for Genetically Encoded, Fixation Compatible Peptide-PAINT”. In: *Nano Letters* 21.22 (2021), pp. 9509–9516.

[35] Rajarshi P. Ghosh et al. “A Fluorogenic Array for Temporally Unlimited Single-Molecule Tracking”. In: *Nature Chemical Biology* 15.4 (2019), pp. 401–409.

Summary

This thesis titled “Development of Advanced Single-Molecule Fluorescence Microscopy Techniques and their Application for the Study of Protein-Protein Interactions in the Context of Immunological Signaling” aimed to make single-molecule imaging and the study of protein-protein interactions on membranes more accessible to the research community by providing new single-molecule fluorescence microscopy tools and techniques, and sharing them following an open-science approach.

In Chapter 1 of the thesis, I provided an overview of the fundamental concepts of signal transduction, focusing on the molecular mechanisms that underlie membrane receptor signaling. I offered a concise explanation of the thermodynamics and kinetics of protein-protein interactions, highlighting the significance of topology as well as the differences between 3D and 2D interactions. I explored a range of methods for evaluating interactions and discussed the limitations of these techniques in quantifying protein-protein interactions on membranes.

I introduced single-particle tracking of membrane proteins in live cells and reconstituted systems as an effective approach for detecting interactions. Additionally, I presented a comprehensive discussion of the technical aspects of single-molecule fluorescence microscopy, covering optics, labeling approaches, experimental considerations and data analysis, specifically when applied to interaction studies. This introductory chapter laid the foundation for the novel advancements and applications presented in the subsequent chapters, where state-of-the-art single-molecule fluorescence microscopy techniques were developed and employed to examine protein-protein interactions in the context of immunological signaling.

In Chapter 2, I detailed the design, assembly, and characterization of a custom single-molecule TIRF microscope specifically tailored for live-cell and single-molecule imaging applications. The microscope boasts cutting-edge imaging quality and features simultaneous imaging capabilities in up to three colors, an optional bleaching function for FRAP ex-

periments, temperature control, a focus stabilization and uniform TIRF illumination with adjustable TIRF angles. Moreover, it was created with modularity and flexibility in mind and can be upgraded as new technological advancements emerge. Building upon existing open-source projects allowed us to keep the costs low ($\sim$ 100.000 €), in comparison to commercially available setups with similar capabilities.

In order to promote open science practices and assist other researchers in building their own systems or enhancing existing setups, I provided comprehensive building and alignment instructions, a parts list and a CAD model of the entire setup with all optomechanical components.

In Chapter 3, I presented a specialized experimental platform designed for single-molecule analysis of ligand-induced binding, which was employed to investigate purified interleukin-2 and -15 receptors reconstituted on supported lipid bilayers. The chapter elaborated on the purification, labeling, and biophysical characterization of interleukin protein receptor subunits, as well as the implementation and optimization of simultaneous three-color tracking for these subunits.

During the experimental process, various challenges emerged, including issues related to the quality of commercially obtained ligands and the photostability of labeled receptors. I discussed these challenges in depth and examined their implications for data interpretation. To tackle these obstacles, potential solutions were proposed; in regards to photostability, a novel approach was developed and presented in Chapter 4. The thorough analysis of the optimizations executed during the establishment of the reconstitution protocol, f.i. the optimized formation and passivation of the supported lipid bilayers, and the usage of a fluorescently-labeled lipid that does not interfere with the fluorescent imaging of the reconstituted receptor subunits, but allows for a simple quality control by confirming the bilayers' homogeneity and fluidity, not only helps improve the presented experimental platform but also presents valuable tips for other researchers in this field.

In Chapter 4, I presented DNA-PAINT single-particle tracking (DNA-PAINT-SPT), an innovative method designed to extend single-molecule trajectory lengths of membrane proteins in live cells and reconstitution experiments. Utilizing a model membrane protein that forms homodimers, I performed an extensive characterization of protein-protein interactions, and not only observed co-diffusion of dimers over several hundreds of frames, but also quantified 2D dissociation constants of two different dimerization agents via ligand-titration assays. Moreover, I transformed the technique into a valuable tool for the live-cell SPT community by introducing simultaneous dual-color DNA-PAINT-SPT, using SNAPtag ligand- and nanobody-conjugated DNA docking strands

for specifically targeting proteins expressed on the cell membrane. With the capability to concurrently observe multiple targets, dual-color DNA-PAINT-SPT provides a powerful approach for studying protein interactions in a physiologically relevant context.

In the concluding outlook of Chapter 5, I discussed the feedback received from the scientific community regarding the K2 TIRF microscope and explained how the microscope will be continuously developed and updated in the future. I outlined optimal strategies for conducting further research on IL-2/IL-15 receptor binding kinetics, suggesting an approach for applying DNA-PAINT-SPT without requiring new receptor subunit cloning and expression. Moreover, I highlighted the potential for adapting DNA-PAINT-SPT for intracellular imaging in the future.

Overall, the developments and applications presented in this thesis contribute to the advancement of single-molecule fluorescence microscopy techniques and open up new possibilities for investigating protein-protein interactions and immunological signaling in greater detail.

Samenvatting

Dit proefschrift heeft tot doel om beeldvorming van enkelvoudige moleculen (single-molecule microscopy) en de studie van eiwit-eiwitinteracties op membranen toegankelijker te maken voor de onderzoeksgemeenschap door nieuwe single-molecule fluorescentiemicroscopie hulpmiddelen en technieken publiekelijk ter beschikking te stellen van het onderzoeksveld.

In hoofdstuk 1 van het proefschrift gaf ik een overzicht van de fundamentele concepten van signaaltransductie, met de nadruk op de moleculaire mechanismen die ten grondslag liggen aan membraanreceptor signalering. Ik bood een beknopte uitleg van de thermodynamica en kinetica van eiwit-eiwitinteracties, waarbij ik het belang van topologie en de verschillen tussen 3D- en 2D-interacties benadrukte. Ik onderzocht een reeks methoden om interacties te evalueren en besprak de beperkingen van deze technieken bij het kwantificeren van eiwit-eiwitinteracties op membranen.

Als een effectieve benadering voor het detecteren van interacties introduceerde ik enkel-deeltjesvolgen van membraaneiwitten in levende cellen en gereconstitueerde systemen met behulp van microscopie. Daarnaast presenteerde ik een uitgebreide bespreking van de technische aspecten van single-molecule fluorescentiemicroscopie, zoals optica, labelingstrategieën, experimentele overwegingen en data analyse, specifiek toegepast op interactiestudies. Dit inleidende hoofdstuk legde de basis voor de nieuwe ontwikkelingen en toepassingen die in de volgende hoofdstukken werden gepresenteerd, waarbij geavanceerde single-molecule fluorescentiemicroscopie technieken werden ontwikkeld en gebruikt om eiwit-eiwitinteracties in de context van immunologische signalering te onderzoeken.

In hoofdstuk 2 beschreef ik het ontwerp, de montage en de karakterisering van een op maat gemaakte single-molecule TIRF-microscoop, specifiek afgestemd op live-cell- en single-molecule beeldvormingstoepassingen. De opstelling is gemaakt met modulaire opstelling en flexibi-

liteit in gedachten, waardoor het aan verschillende vereisten kan voldoen en diverse experimenten kan uitvoeren. De microscoop beschikt over state-of-the-art beeldkwaliteit en biedt gelijktijdige beeldvormingsmogelijkheden in maximaal drie kleuren, een optie tot FRAP-experimenten, temperatuurcontrole, een focusstabilisatie en uniforme TIRF-verlichting met instelbare TIRF-hoeken. Bovendien kan het worden verbeterd naarmate nieuwe technologische vooruitgang zich voordoet. Door verder bouwen op bestaande open-source projecten konden we de kosten laag houden ($\sim$ 100.000 €), in vergelijking met commercieel verkrijgbare opstellingen met vergelijkbare mogelijkheden.

Om bij te dragen aan open science en andere onderzoekers te helpen bij het bouwen van hun eigen systemen of het verbeteren van bestaande opstellingen, heb ik uitgebreide bouw- en uitlijninstructies, een onderdelenlijst en een CAD-model van de gehele opstelling met alle optomechanische componenten ter beschikking gesteld.

In hoofdstuk 3 presenteerde ik een gespecialiseerd experimenteel platform ontworpen voor single-molecule analyse van ligand-geïnduceerde binding, dat werd gebruikt om interleukine-2 en -15 receptoren gereconstitueerd op gereconstitueerde lipid-membranen te onderzoeken. Het hoofdstuk ging dieper in op de opzuivering, labeling en biofysische karakerisatie van interleukine-eiwitreceptor subeenheden, evenals de implementatie en optimalisatie van gelijktijdige enkel-deeltje-volgen van drie moleculaire soorten in drie kleuren.

Gedurende het experimentele proces kwamen verschillende uitdagingen naar voren, waaronder problemen met betrekking tot de kwaliteit van commercieel verkregen liganden en de fotostabiliteit van gelabelde receptoren. Ik besprak deze uitdagingen diepgaand en onderzocht de implicaties voor datainterpretatie. Om deze obstakels aan te pakken, werden mogelijke oplossingen voorgesteld; met betrekking tot fotostabiliteit werd een nieuwe benadering ontwikkeld en gepresenteerd in hoofdstuk 4. De grondige analyse van de optimalisaties uitgevoerd tijdens de totstandkoming van het reconstitutieprotocol, bijvoorbeeld de geoptimaliseerde vorming en passivering van de gereconstitueerde lipidmembranen, en het gebruik van een fluorescerend gelabeld lipide dat niet interfereert met de fluorescente beeldvorming van de gereconstitueerde receptor subeenheden, maar zorgt voor een eenvoudige kwaliteitscontrole door de homogeniteit en vloeibaarheid van de bilagen te bevestigen, helpt niet alleen het gepresenteerde experimentele platform te verbeteren, maar biedt ook waardevolle tips voor andere onderzoekers in dit vakgebied.

In hoofdstuk 4 presenteerde ik DNA-PAINT enkel-deeltje-volgen (DNA-PAINT single-particle tracking, DNA-PAINT-SPT), een innovatieve me-

thode ontworpen om enkelvoudige moleculen in levende cellen en reconstitutie-experimenten langer te kunnen volgen. Met behulp van een modelmembraaneiwit dat homodimeren vormt, voerde ik een uitgebreide karakterisering uit van eiwit-eiwitinteracties en observeerde niet alleen verlengde co-diffusie van dimeren over enkele honderden frames, maar kwantificeerde ook 2D-dissociatieconstanten van twee verschillende dimerisatieagentia via ligand-titraties. Bovendien heb ik de techniek getransformeerd tot een waardevol instrument voor de levende-cel SPT-gemeenschap door gelijktijdige tweekleurig DNA-PAINT-SPT te introduceren, met behulp van SNAPtag-ligand- en nanobody-geconjugeerde DNA-keten voor specifiek richten op eiwitten die tot expressie worden gebracht op het celmembraan. Met de mogelijkheid om meerdere molecuul soorten tegelijkertijd te observeren, biedt tweekleurig DNA-PAINT-SPT een krachtige benadering voor het bestuderen van eiwitinteracties in een fysiologisch relevante context.

In het afsluitende vooruitblik van hoofdstuk 5 besprak ik de feedback die ik ontving van de wetenschappelijke gemeenschap met betrekking tot de K2 TIRF-microscoop en legde uit hoe de microscoop in de toekomst continu zal worden ontwikkeld en bijgewerkt. Ik schetste optimale strategieën voor het uitvoeren van verder onderzoek naar IL-2/IL-15 receptorbindingskinetiek en stelde een benadering voor om DNA-PAINT-SPT toe te passen zonder dat nieuwe receptor subeenheid kloneren en expressie nodig zijn. Bovendien heb ik het potentieel benadrukt om DNA-PAINT-SPT aan te passen voor intracellulaire beeldvorming in de toekomst.

Over het algemeen dragen de ontwikkelingen en toepassingen die in dit proefschrift worden gepresenteerd bij aan de vooruitgang van single-molecule fluorescentiemicroscopietechnieken en openen ze nieuwe mogelijkheden voor het onderzoeken van eiwit-eiwitinteracties en immunologische signalering in meer detail.

List of Publications

C. Niederauer, M. Seynen, J. Zomerdijk, M. Kamp and K. A. Ganzinger, *The K2: Open-source simultaneous triple-color TIRF microscope for live-cell and single-molecule imaging*, HardwareX 13C, e00404, (2023).

Author contributions:

C. Niederauer built the optical setup, performed characterization experiments and wrote the manuscript. M. Seynen wrote setup control software. J. Zomerdijk designed and built electronic control units. C. Niederauer, M. Kamp and K.A. Ganzinger conceived the optical setup design. K.A. Ganzinger supervised the study. All authors reviewed the manuscript.

C. Niederauer, C. Nguyen, M. Wang-Henderson, J. Stein, S. Strauss, A. Cumberworth, F. Stehr, R. Jungmann, P. Schwille and K. A. Ganzinger *Dual-color DNA-PAINT single-particle tracking enables extended studies of membrane protein interactions*, Nature Communications 14, 4345 (2023)

Author contributions:

C. Niederauer conceived and performed live cell and in vitro experiments, analyzed and interpreted data and wrote the manuscript. C. Nguyen performed live cell and in vitro experiments. M. Wang-Henderson performed initial in vitro experiments. C. Niederauer and M. Wang-Henderson wrote analysis code. J. Stein and F. Stehr performed initial experiments. S. Strauss performed nanobody-DNA coupling and reviewed the manuscript. A. Cumberworth derived analytical homodimerization model. J. Stein, A. Cumberworth, R. Jungmann and P. Schwille interpreted data and reviewed the manuscript. K.A. Ganzinger conceived and supervised the study, interpreted data and wrote the manuscript.

F. Stehr, J. Stein, J. Bauer, **C. Niederauer**, R. Jungmann, K. A. Ganzinger and P. Schwille *Tracking single particles for hours via continuous DNA-mediated fluorophore exchange*, Nature Communications 12, 4432 (2021)

Author contributions:

F. Stehr, J. Stein, R. Jungmann, K.A. Ganzinger and P. Schwille conceived the study. F. Stehr, J. Stein and J. Bauer designed experiments. J. Stein performed the experiments. J. Bauer devised the concept of the tracking handle sequence, prepared DNA origami and performed initial experiments. C.N. performed initial experiments. F. Stehr and J. Stein designed and performed data analysis. F. Stehr wrote the analysis code. F. Stehr, J. Stein, R. Jungmann, K.A. Ganzinger and P. Schwille. wrote the manuscript. K.A. Ganzinger and P. Schwille supervised the study. All authors discussed and interpreted results and revised the manuscript.

Publications not appearing in this thesis:

F. Wruck, J. R. Tait, T. A. Bevers, **C. Niederauer**, A. Mashaghi, A. Sengar, T. E. Ouldridge, K. A. Ganzinger, J. T. B. Overvelde and S. J. Tans *Dynamic DNA origami as a stochastic molecular metamaterial*. In preparation.

C. Niederauer, P. Blumhardt, J. Mücksch, M. Heymann, A. Lambacher, P. Schwille *Direct characterization of the evanescent field in objective-type total internal reflection fluorescence microscopy*. Optics Express 26, 20492-20506 (2018).

Acknowledgments

"Which is more important", asked Big Panda,
"the journey or the destination?"
"The company." said Tiny Dragon.

James Norbury - *Big Panda and Tiny Dragon*

While I kept myself busy studying molecular interactions, I found the real-life interactions in- and outside of the lab to matter the most during my PhD. I had great company throughout all these years, and I would like to acknowledge the invaluable role my colleagues, friends and family played in shaping not only my academic journey but also my personal path.

Kristina, I am immensely grateful for the scientific environment you created, in which I could freely follow my interests and passions and truly be myself. I've always enjoyed our meetings, especially the ones in which we would traverse away from scientific details towards more existential questions of the human experience. While you surely had to deal with a lot of pressure and uncertainty establishing both a lab *and* a family, I can not think of any moment in the last five years where our communication wasn't characterized by empathy and mutual appreciation. Thank you! **Pieter Rein**, your enthusiastic presence and curiosity during the interleukin meetings in the initial years of my PhD were inspiring and a recurrent source of motivation. We were immediately jumping into the deep end of immunology, and lots of scrap paper had to be scribbled on with drawings of T cells, receptors and feedback loops. Thank you for jumping with us and for your encouragement. I would also like to extend my gratitude to the **defense committee** for taking the time to read my thesis and for joining the defense ceremony.

My paranymphs Manuel and Mareike and my partynymphs Kathi and Lucie, thank you for your help in planning and organizing the defense and the party. **Manuel**, I look back at many insightful conversations, touching movies and beautiful trips together. I find it rare for someone

with such an open-minded, non-dogmatic approach towards life, to also be such a caring and considerate friend, like you are for me and many others. Your enthusiasm for life is contagious. How lucky I am to have a friend like you! **Mareike**, when I was still struggling with readjustment after moving from Munich to Amsterdam, you were eager to discover the city and to meet new people. Thanks for carrying me along especially in the beginning! As time went on, I realized how fortunate I was to have met someone who shared my curiosity in uncovering the offbeat and unconventional facets of Amsterdam, of which there luckily are many. I love how you manage to combine your dedication and professionalism with a childlike thirst for action and joy. I am always happy to see you! **Kathi**, your genuine interest in the people surrounding you and your attentive, caring attitude are so precious. Our discussions in the Tiefenpsychologischer Kreis together with Manuel never fail to be both enlightening and thought-provoking. I am happy that you are always down for watching movies that touch the very core. I really love hanging out with you! **Lucie**, I am super happy that we finally became friends after observing each other from a distance for a couple of years. Your openness, curiosity, and profound self-awareness are qualities I deeply admire. The way you balance calm and introspective sides of your personality with being outgoing and fun, inspires me. Seeing you brightens my day!

One of the best parts of doing a PhD for me was being able to supervise students. They were all so different, and I learned from all of them. **Louis**, when you started, I still had no clue about building a microscope. Your relaxed attitude made working with you through all the trials and errors fun. **Thomas**, our supported lipid bilayers now are mobile and defect-free all the time!! I am sorry that you had to spend months optimizing the protocol. Kudos to your persistence. **Miles**, the lab still benefits from the framework you set up for the analysis of single-molecule interactions. It was an absolute pleasure to work with you and I am very happy that we have a paper together. **Elia**, what a coincidence having you working on a setup named after the mountain your dad climbed as the French premiere. Your scientific project was less dangerous, but surely also high-risk. Thank you for taking up on that challenge, you did a great job.

Besides the students I supervised, I was lucky to work with many amazing colleagues. **Rob** - I remember late evening climbing in between microscopy sessions, ambitious (and not always completed) DIY projects with scrap wood from the AMOLF containers, your incredible enthusiasm, curiosity and sense for adventure. May your bare feet carry you wherever you want to go in life. **Lori**, I was very happy when you joined the lab. Finally someone to share the ups and downs that working in a

young and small research group brings with it. I really enjoy your humor, and I think we did a decent job developing a welcoming and inclusive lab culture for all our students. **Laura** and **Sharon**, once you joined, and together with Rob, the lab was suddenly alive. First group meetings, coffee breaks, scientific and non-scientific discussions. And besides all that, you laid the foundation for two different research lines in the Ganzinger group. **Tom**, it was great to have you joining the interleukin project and working on it from a completely different, computational angle. Your findings were super interesting and I wish I could have explored the implications experimentally more deeply. **Elisa**, thanks for all the hard work in the wet labs. It was great to team up with you to deal with the misbehaving AKTA or cranky insect cell lines. **SaFyre**, I was inspired by how free and brave you are when it comes to talking about and experiencing insecurities and doubts, and nevertheless not being held back by them. Also, what a great idea to introduce R.A.D.A.R. to our lab meetings! Thank you for the atmosphere of positivity and appreciation you carry with you. **Helena**, we still need to go to De School together one day! I really enjoyed your willingness to be open, and your playful attitude. It was fun to share an office with you. **Guusje**, thanks for the positive and chill vibes you brought with you, even though you were working hard in- and outside of the lab. Happy to run into you at Polder anytime soon! **Chi**, seeing you always put a smile on my face. It was great to watch how you grew as a scientist, from starting your master project and taking it to Canada, to becoming a PhD student and now even supervising your own Postdoc ;-) Your ability to maintain a positive and forward-oriented attitude in challenging situations, and your dedication to work hard are very special. I am really grateful that you took over a considerable part of the work when things got tough with the DNA-PAINT-SPT paper. **Nebojsa**, your ability to switch from absolute existential, life decision kind of talk, to light discussions about how cucumbers are related to courgettes, amazed me. I thoroughly enjoyed having both kind of conversations with you. Please never stop enriching all our lifes with your bizarre collection of fun facts and serbo-croatian proverbs. *Umiljato jagnje dve ovce sisa.* **Marcel**, thanks for the countless tries with the click-chemistry protocol that never worked and for all your support in the ML1 lab. **Raquel**, I am so happy that the K2 microscope project is being continued and improved by such a capable, joyful and curious scientist. Have fun with it! **Rhythm**, sorry for always making you wait for lunch time. I loved joking around with you. Enjoy the premium seat at the window.

I would like to thank the people in the bio department within AMOLF for creating a supportive and pleasant work atmosphere. **Vanda**, I know you will be slightly embarrassed to read all these positive comments following, but I can't help it. Chatting with you in between running purifications and SDS gels was fun and gave me lots of new ideas and perspectives, both scientifically but more importantly, personally. I loved hearing your unobstructed point of view on many topics, often spiced with some sarcasm, below which I could always sense a lot of kindness towards the people around you. **Sander**, when Kristina was on her first maternity leave, you became my interim supervisor for a few months. I deeply enjoyed our lunch meetings and appreciated the fresh insights and your critical questions. Thank you for never hesitating to provide unsolicited words of encouragement and recognition. Ramon, Lennard and Jeff from **0.16**, you welcomed me so nicely in your all-Dutch office. We didn't stay together for long in this configuration, but the few times we had drinks together were legendary. **Lennard**, engaging in conversations - and often laughing together - about lab challenges or life's obstacles with you added a sense of lightness to everything. Thank you for sharing your cheerful attitude with us. I was sad when your lab moved to Delft. Thanks **Jeff** for your work in the wet lab and taking it on against the AKTA! **Ramon**, as if loosing Jeff and Lennard in the office wasn't bad enough, your seat was also empty throughout most of Corona times. I missed hearing your thoughts on politics and society. Thank you for introducing me to 80s movies of high educational value and, indirectly, the Ecstatic Dance boat Odessa. **Kim**, I love how you're always finding the positive and good in other people. I thoroughly enjoyed our coffee and lunch conversations and I'm very happy we made it to Ruigoord together this summer. **Xuan**, thanks for your warm smile and enthusiastic hand-wave whenever we met in the AMOLF hallways or the ML2 lab. **Max**, there is always an interesting topic to discuss with you, be it uterus organoids or German cloud rap. Also, it felt pretty good to not be the only person working at unusual times (cheers Fotis) in the ML2 lab. **Fotis**, your friendly and slightly conspiratorial nod helped to feel a bit less weird during the night shifts at AMOLF. I admire your dedication as a scientist! **Yvonne**, thank you for keeping the ML2 lab so well-organized and supporting our cell culture endeavours. **Jack**, I enjoyed our imaging sessions for the DNA origami project. **Luca**, we never managed to put any of our project ideas to fruition. Geeking out over the right gardening conditions in the DUWO flats was anyway more fun. **Alex**, thanks for your contribution to the DNA-PAINT-SPT paper. I've always enjoyed your company and I admire the level of consideration you approach many aspects in life with. **Kasper**, I am looking forward to run into you again in the gym or sauna.

Also outside of the bio department, there is a lot of interesting science happening at AMOLF, and I was lucky to have some points of contact with people in solar cell, robotics and photonics research. Meeting scientists working on completely different topics, but sharing the same curiosity, and often, similar struggles, was truly enriching. **Lukas**, too bad we had to leave our jungle office 0.16 after only a few months. I learnt a lot from you in the past years, thank you for sharing your knowledge and your many talents, and for being such a dependable, gentle and fun friend. **Nasim**, I appreciate the trust you've placed in me when I was cat-sitting Luna. Thank you for being a sweet, honest and compassionate friend. **Tzeni**, we hit it off just before you had to leave Amsterdam, sadly, but I hope to be one of the first guests in your green agritourism business! **Agustin** and **Bram**, thanks for your culinary support during my writing phase and all the dance moves, laughter and special moments we shared on festivals and parties. With you, I am always having a good time! **Giada**, I admire the way you speak up for your convictions. Thanks for taking me to some more offbeat places in Amsterdam. **Sofija**, **Marco**, **Mario**, **Giorgio**, **Andrea**, **Imme**, **Rene**, **Dhawal**, **Pascal**, **Daan**, **Age**, **Evan**, **Alexander**, **Harmen**, **Timo**, **Florian**, **Marloes**, **Carolyn** and many others that I forget to mention now here - it was a pleasure to see you at the institute or at parties.

Especially for the first part of my PhD, the construction of a TIRF microscope, I was fortunate to work with a group of very capable and approachable engineers. It was such a relief to share some of the responsibility. **Marko**, thank you for your guidance with the design of the K2 and many useful practical tips for setting up and aligning the system. **Marco**, I want to thank you for the diligence with which you approached the software development for the K2 setup. You implemented so many special wishes, were always available for short notice bug fixes and patiently explained how things work on the software level. I found your way of calmly but persistently working on the tasks at hand extremely pleasant. **Jan**, you did a great job designing the qgFocus, I really enjoyed working with you. Thank you **Henk-Jan** for truly thinking along with my design ideas and transforming them into elegant CADs. It was such a relief knowing that this is something I don't have to worry about. Thanks also for having an (actual) open-door policy and extremely clear and efficient communication. **Hinco**, thanks for fixing all sorts of infrastructure issues, and especially, for suggesting improvements to some of my makeshift provisional solutions (and promptly implementing them).

Thanks to all the current and past members of the **Personeelsvereniging**, you organized amazing events and outings that made it easy for me getting to know my colleagues in a very fun way! Thank you for taking time out of your work day to make social life at AMOLF more vibrant.

I would also like to thank **Clyde**, **Inkoop**, **Precision Manufacturing**, **Electronics**, the **Receptie** team, **Wiebe**, **Richard** and the rest of **ICT** for ensuring a smooth-running and welcoming working environment. Thanks to the **cleaning staff** for keeping the labs and offices tidy and never complaining about dead leafs on the ground, spilled water or soil from our many office plants.

Science luckily is team work, and while AMOLF is a fantastic place for research, some projects could only be pulled off in collaboration with people outside of the green building. **Johannes**, **Florian** and **Ralf**, I am grateful for all your input on the DNA-PAINT project, for your words of encouragement and your support. **Patrick**, thank you for teaching us how to purify proteins from insect cells and for producing a few milligrams of those precious proteins. Your level of expertise and the quality of your work was inspiring.

Was für den Vogel die Kraft der Schwingen,
das ist für den Menschen die Freundschaft.
Zenta Maurina

Niklas, almost every time I visited home in the first summers and falls of my PhD, we managed to meet up and go for a multipitch climb, which would then bring me through another couple of weeks of no exposure in the flatlands. I am grateful for those memories. I am even more grateful for how our friendship developed later on. Even though living hundreds of kilometers apart, I feel very close to you. **Max**, we spent many hours talking to each other via the AMOLF landline, exchanging thoughts, encouragement and perspectives on life. I truly value your openness and vulnerability, our friendship means a lot to me. **Hannes**, I love how our friendship takes us on many fun adventures. At the same time, I deeply appreciate how you engage with the melancholic, contemplative side of life. Thank you for pushing me out of my comfort zone at times. Through you I learnt how freeing it can be to share thoughts and stories and stop minding what other people could think of it. Hab dich lieb! **Philipp**, being with you feels like being home. Despite all the life events and moves, our friendship remained one of the few things unchanged. Thank you for being such a loyal friend for almost 20 years. **Uschi** and **Steff**, thank you for always welcoming me, spontaneously (or, rarely, planned) in Ottobrunn and Munich. I am happy you come visiting me wherever I move to. **Barbara**, listening to your voice messages in Bavarian dialect, sent out from France, Spain, Portugal or Morocco, warms my heart and makes me feel home anywhere for a moment. **Santosh**, too bad you never moved to Amsterdam for your job, we would have had lots of fun. **Lise**, I am deeply grateful for what we shared together. Your degree of

second degré is unmatched and I admire the sincerity and love reflected in the connections with the people around you. I am very happy our paths crossed. **Daniel**, I felt sad leaving our flat in Munich after we had just moved in together, had become good friends and a well-rehearsed Seilschaft. I'm happy I could score a few more Pause climbs with you before you are done with the list. Thanks for the things you taught me, for keeping us safe and for the great company along the way. **Lizzy**, I always enjoy your surprise phone calls. Our paragliding classes together were definitely a highlight of the last couple of years! I celebrate your sense of adventure and fearlessness. **Hella**, meeting you just before starting to write my thesis made me fly through the whole process. Your late night shifts and my late night writing sessions perfectly aligned.

Julian, meeting you in the first months after arriving in Amsterdam was a real gift. I look back at climbing trips with just the right balance between safe and sketchy, an unforgettable five hour boat ride through Amsterdam and many fun evenings and nights you invited me to. I admire your openness, how you constantly welcome and integrate new people into your circle of friends, and that you fight for affordable housing in a city with one of the toughest rental markets. **Chiara**, we connected over climbing but I am happy that our friendship extends beyond that, to USC sauna sessions, walks in Oost and insightful discussions about life and love. **Sara**, a large part of my PhD journey in Amsterdam, especially during the Corona time, I spent with you. I am grateful for the time we shared and happy that we managed to keep in touch after our paths diverted. I (tried to) take inspiration in the well-organised and rigorous way you approached your PhD. Grazie. **Laura**, my tea-drinking friend, hanging out with you is always so relaxing. Thanks for being such a hospitable person. **Maxime**, actually I don't really like board games. Somehow, you are one of the few persons with whom I enjoy playing. Thank you for being a welcoming host on many occasions, and for explaining the rules for the tenth time when everyone else forgot. **Abishek**, I am happy that we managed to stay in touch over all the years, your performances and creations are an ever-welcome change of perspective for me. **Fleur**, what you are creating in Anna's Tuin en Ruigte is wonderful. The hands-on construction and garden work has been a pleasant contrast to my mostly sedentary office job as a PhD student. **Hiro**, quite nice that we managed to rekindle our friendship once you moved to Utrecht. Oerol with you and Marion will remain a special memory. **Philipp B.**, I am happy you encouraged me to do my PhD in Kristina's group in Amsterdam. Thank you for giving me a kick start with the TIRF setup and generally sharing your advice throughout the way.

Throughout all these years spent abroad, I could always count on my family for encouragement and support in any kind of situation. Thank you for letting me go and explore the world without hesitation, for being curious and compassionate about my experiences, and for welcoming me at home with unconditional joy and warmth.

Stefan und **Kerstin**, danke, dass ihr immer für mich da seid. Die Einblicke ins Leben dahoam mit **Paul** haben mir so manch verregneten Tag in Amsterdam verschönert. **Mama**, wie schön dass wir trotz der Distanz so nah an unsrer beider Leben teilhaben. Vielen Dank für deine Unterstützung, für deine Offenheit und das Gefühl bei dir und **Hubert** immer uneingeschränkt willkommen zu sein. **Papa**, für deinen optimistischen und neugierigen Blick auf die Welt und die Menschen um uns herum bin ich dir unendlich dankbar. Ich hätte gerne noch mehr Zeit mit dir geteilt.

About the author

Christian Niederauer was born on September 30, 1992, in Berlin, Germany. The curiosity for the world was instilled in him by his parents, who encouraged him to explore and learn throughout his life. This led him to pursue a degree in Physics at the Ludwig-Maximilians-University in Munich. During his studies, Christian developed a keen interest in Biophysics and finished with a Bachelor's thesis on pH gradients in the context of the origin of life.

Seeking to broaden his academic and cultural horizons, Christian embarked on a research stay in Pune, India. Developing a passion for these new experiences, he followed his time in India with a semester abroad at the Boğaziçi University in Istanbul, Turkey, where he studied Physics and Philosophy.

Upon returning to Germany, Christian completed his Master's thesis at the Max-Planck Institute of Biochemistry, working in the group of Prof. Dr. Petra Schwille. During this time, he developed a novel method for measuring light fields in total internal reflection fluorescence microscopy.

It was at the Max-Planck Institute where Christian crossed paths with Dr. Kristina Ganzinger, who was in the process of transitioning from a postdoctoral position to becoming a new group leader at AMOLF, Amsterdam. Intrigued by the opportunity to work in a new lab and contribute to its development from the ground up, Christian once more decided to take a step out of his comfort zone and moved from his beloved mountains to Europe's flattest country.

Once Christian had relocated to Amsterdam, he eagerly embraced the freedom and responsibility that came with being the first student in a newly established lab. His journey thus far had not only prepared him for the challenges ahead but also fostered a passion for scientific discovery that would drive his contributions to the field of single-molecule biophysics.